

Fast determination of fatigue properties of metals during fatigue tests at 20kHz by using in situ time-resolved X-ray diffraction.

Vincent Jacquemain

▶ **To cite this version:**

Vincent Jacquemain. Fast determination of fatigue properties of metals during fatigue tests at 20kHz by using in situ time-resolved X-ray diffraction.. Mechanics of materials [physics.class-ph]. HESAM Université, 2022. English. ⟨NNT : 2022HESAE050⟩. ⟨tel-03832241⟩

HAL Id: tel-03832241

https://pastel.hal.science/tel-03832241v1

Submitted on 27 Oct 2022

HAL is a multi-disciplinary open access archive for the deposit and dissemination of scientific research documents, whether they are published or not. The documents may come from teaching and research institutions in France or abroad, or from public or private research centers.

L'archive ouverte pluridisciplinaire **HAL**, est destinée au dépôt et à la diffusion de documents scientifiques de niveau recherche, publiés ou non, émanant des établissements d'enseignement et de recherche français ou étrangers, des laboratoires publics ou privés.



HAL Authorization

HESAM UNIVERSITÉ

Arts et Métiers Sciences et Technologies

ÉCOLE DOCTORALE SCIENCES ET MÉTIERS DE L'INGÉNIEUR

PIMM - Campus of Paris

THESIS

presented by : **Vincent JACQUEMAIN**

defended on : **07 October 2022**

to obtain the status of : **Doctor from HESAM University**

prepared at : **Ecole Nationale Superieure d'Arts et Metiers**

Specialty : **Mechanics of materials**

Fast determination of stored energy of metals during fatigue tests at 20kHz by using in situ time-resolved X-ray diffraction

PhD supervised by : RANC Nicolas

Jury

M. Pierre-Olivier RENAULT	University of Poitiers	President
M. Cedric DOUDARD	ENSTA Brest	Reviewer
M. Henry PROUDHON	MINES Paris	Reviewer
M. Jonathan CORMIER	ENSMA Poitiers	Examinator
M. Olivier CASTELNAU	ENSAM Paris	Examinator
M. Cristian MOCUTA	Synchrotron SOLEIL	Examinator
M. Nicolas RANC	ENSAM Paris	Examinator

THÈSE

Acknowledgments

Cette thèse s'est déroulée au Laboratoire PIMM, dans le cadre du projet ERC FastMat porté par Nicolas Ranc. Je tiens donc à remercier en premier le Conseil Européen de Recherche pour avoir financé mes travaux de thèse à travers l'accord de financement No 725142.

Mes remerciements sont naturellement adressés à Nicolas Ranc ensuite, qui ne fut autre que mon directeur de thèse pendant ces 3(+0,5) années. M'ayant contacté bien avant que je fasse le choix de me tourner vers la recherche, il a surement participé à éveiller en moi la curiosité nécessaire pour que je me lance. Je ne le remercierai jamais assez de m'avoir épaulé dans l'avancée de mes travaux, depuis mon stage recherche en Master MAGIS, jusqu'à la rédaction du manuscrit et la préparation de la soutenance. Sa rigueur et sa vision globale du projet ont été extrêmement bénéfiques pour moi. Grâce à lui, je sors de cette thèse avec bien plus qu'une expertise en mécanique des matériaux. Son retour fait sur mon travail et ma personne à la fin de la soutenance m'ont particulièrement ému ; il n'aura fallu attendre que 3 ans pour connaitre son point de vue sur la question... mais ça valait clairement le coup ! Son amour inconditionnel pour le chocolat, que je partage, ont potentiellement aidé à ce que tout se passe sous les meilleurs auspices !

Je me dois de remercier toute l'équipe FastMat puisque ce travail fut avant tout collectif. Je tiens d'abord à saluer le travail acharné qu'a fourni Christophe Cheuleu en tant qu'ingénieur électronicien, sans qui le projet n'aurait pas pu être porté si loin. Merci à ce collègue devenu un ami, pour les moments de détente qu'il m'a apporté tout au long de ma thèse, qui ne furent clairement pas de trop ! Son infatigable humour aura eu raison de tous mes coups de mou. Je me demande comment on peut être aussi compétent et faire autant l'imbécile (toujours avec classe !)... A bientôt Christophe, futur associé d'une belle aventure à venir.

J'adresse aussi mes remerciements à Olivier Castelnau pour l'aide apportée, sur les problématiques de diffraction des rayons X et pour le développement de simulations microstructurelles, qui a été indispensable à la complétion de ce travail. Sa vision m'a également été grandement bénéfique dans la rédaction de mon manuscrit. Merci égale-

ment pour ta bonne humeur et nos échanges toujours agréables !

Je tiens à remercier Véronique Favier et Vincent Michel pour leur soutien scientifique et moral qu'ils ont pu m'apporter tout au long de ces années, et particulièrement pendant les campagnes synchrotron réalisées ! Merci également à Taylan Ors et Doriana Vinci, post-doctorants sur le projet FastMat, pour leur très agréable collaboration et tous les bons moments partagés avec eux ! Je n'oublie pas Marc Fivel qui a participé au projet FastMat depuis le laboratoire SIMAP à Grenoble, mais dont la présence pendant les campagnes d'essais et réunions fut très appréciée.

Comment rédiger mes remerciements sans parler du synchrotron SOLEIL, et plus particulièrement de la ligne de lumière DiffAbs (bien cachée à l'arrière de l'anneau). Tout ce travail n'aurait tout simplement pas pu être réalisé sans leur étroite et très appréciée collaboration. Je m'estime heureux d'avoir pu y réaliser de nombreuses campagnes synchrotron avec l'équipe FastMat ! Je salue principalement la gentillesse et le professionnalisme du responsable de la ligne Dominique Thiaudière et je le remercie pour les temps de faisceau qu'il nous a accordé. Je salue l'aide technique apportée par Philippe Joly (toujours le mot pour rire), et le support de Solenn Reguer lors des dernières campagnes. Enfin, je remercie tout particulièrement Cristian Mocuta, scientifique de la ligne, pour sa collaboration sans faille, et son aide qui fut extrêmement précieuse dans mes travaux. Sans son expertise et ses idées toujours pertinentes, le développement de la méthode expérimentale n'en serait qu'à ses balbutiements. Et si en plus de ça il était vraiment bienveillant et drôle, on ne me croirait pas !

Je tiens à adresser un grand merci à Cédric Doudard et Henry Proudhon qui ont accepté de lire mon manuscrit et d'estimer mon travail de thèse. Je remercie de même Pierre-Olivier Renault pour avoir fait un excellent président de jury ainsi que Jonathan Cormier pour avoir accepté d'en faire partie. Leurs retours et discussions ont été particulièrement enrichissants pour moi. Leur appréciation de mon travail fut à la fois pertinente et bienveillante, ce qui m'a placé dans les meilleures conditions pendant la soutenance. Merci également à Olivier Castelnau et Cristian Mocuta pour leur participation à ce jury. Vos retours en ce jour particulier m'ont beaucoup touché, et je dois dire que je ne m'y attendais pas. Merci aussi à Laurent Berthe et Diogo Queiros Condé d'avoir pris le temps d'évaluer mes travaux en cours de thèse.

Merci également à celles et ceux qui ont fait le déplacement pour me voir soutenir. Votre présence fut très appréciée !

Je tiens à exprimer ma gratitude à tout le laboratoire PIMM dans lequel j'ai effectué ma thèse dans des conditions exemplaires. Plus particulièrement aux doctorants

et permanents avec qui j'ai pu partager de nombreuses collaborations ou moments de convivialité dans l'espace détente (avant et après sa rénovation...). Ces moments passés au PIMM furent plus déterminants qu'ils n'en avaient l'air et je ne suis pas près de les oublier. Je pense particulièrement à Shawn Lee Kiser, membre avec Christophe et moi-même du meilleur bureau de la halle 3, que je remercie pour son soutien et pour la bonne humeur qu'il m'a apporté depuis son arrivée (mais toujours pas en français...) ainsi que sa bienveillance et son humour dont je suis très friand. Je ne le remercierai jamais assez d'avoir pris le temps de corriger mes rédactions en anglais ! Merci également à Marc Rebillat, pour l'aide qu'il a apporté à Christophe (qui en avait bien besoin d'après lui) et pour avoir été un soutien externe au projet. Merci à Marine S.B. de m'avoir invité à une superbe campagne synchrotron sur Psiché, où j'ai constaté la décadence de son papillon, hélas. Je remercie Marc Raffestin (une daube qui n'est pas assez présente au PIMM, ce qui est peut être un bien pour notre productivité), Nassim (qui est pour le coup un peu trop présent au PIMM), Grégoire (l'allemand infiltré), Hadrien (que je trouve un peu trop attaché à la Corse pour un parisien), Arthur (plutôt très sympa pour un Gad'z de Metz) et Quentin (qui est sans doute mon frère caché) pour les échanges très « corporate » et très extra-professionnels que nous avons pu avoir ; ainsi que Lucas, Sebastian, Guilherme et les autres membres du PIMM que j'ai côtoyé mais sans doute oublié (veuillez me pardonner...).

Tout ce travail n'aurait jamais eu lieu sans le soutien de mes parents, qui m'ont aidé à bien des niveaux : depuis ma naissance (si je me souviens bien) jusque dans mes études supérieures, et ce sans ménagement. Leur présence, bien qu'épisodique du fait de la distance qui nous sépare, fut une véritable force pour me motiver à donner le meilleur de moi-même. Je les remercie d'ailleurs pour le déplacement qu'ils ont fait pour me voir soutenir ! La fierté que j'ai pu lire en eux en ce jour m'a énormément touché. Je ne suis pas forcément doué avec les mots pour dire à quel point je tiens à eux, mais j'espère qu'ils mesurent à quel point ils comptent pour moi et ô combien ils m'inspirent. J'ai une pensée également pour ma sœur et mes 4 nièces, qui m'offrent une parenthèse bien appréciée à chaque fois que je leur rend visite.

Je tiens également à remercier mes amis de toujours Alexis et Florine pour avoir été présents pour moi, à distance et plus ponctuellement physiquement. L'affection que je leur porte est sans limite, et je leur suis reconnaissant d'avoir toujours été là et de m'avoir écouté et épaulé lors des moments de doutes tout au long de cette épreuve de plus de 3 ans (et depuis bien avant d'ailleurs !). A chaque retour au pays, rien n'a changé et c'est parfait ainsi : les choses sont simples entre nous et c'est ça que j'aime par dessus tout.

Viennent ensuite les Hiboux, deux précieux amis que je remercie pour m'avoir appris

à découvrir mes talents de sculpteur dans le but d'ériger de jolies créations ensemble... en parallèle de ma thèse. L'un des hiboux refuse d'être prolétaire et l'autre vie en marge de la société moderne mais je compte faire en sorte que notre amitié ne se défasse pas avec les années !

Merci à Cathy (a.k.a. Catch), Mathilde (Une âme bienveillante et sincère), Sébastien (une âme tout aussi bienveillante quoi qu'un peu cupide...), Anna (dont le coup de crayon va toujours à fond les ball's), Quiman (un compagnon de « chasse » hors-pair), Guillaume et Ratou (dont l'amitié m'est plus précieuse qu'il n'y parait) pour les très très bons moments passés en leur compagnie et pour leur présence dans ma vie, qui a, je dois l'admettre, changé depuis que je les connais ! Mon âme est certes absente, mais votre présence comble bien plus que ça !

"Last but clearly not least", Merci à Romane, pour son soutien indéfectible et pour avoir réussi à me supporter pendant aussi longtemps, et ce quotidiennement : un grand bravo ! Et bon courage car ce n'est pas près d'être terminé ! Elle n'a certes pas pu (ni souhaité d'ailleurs) m'aider dans mes travaux directement, mais sa présence et son abnégation à mon égard ont rendu les choses beaucoup plus simples, notamment pendant les derniers mois de ma thèse. Merci d'être restée toi-même tout ce temps et d'avoir tissé ta vie à la mienne pour écrire une aussi belle histoire.

Abstract

The objective of this thesis is to develop a methodology to quickly determine the fatigue properties of materials, from the evolution of the stored energy with respect to the stress amplitude and number of cycles applied. This evolution is estimated during fatigue tests conducted at high frequency and for very high number of cycles. The understanding of the link between the evolution of stored energy and the activation of fatigue damage mechanisms would help to improve the credibility of the methodology. The stored energy is estimated by establishing an energy balance from the difference between the mechanical work that is brought to the material and the energy that is dissipated as heat. The mechanical work is estimated from in situ time resolved X-ray diffraction measurements and the dissipated energy from thermographic measurements. To study the very high fatigue lives, fatigue tests are conducted by using an ultrasonic fatigue machine working at 20 kHz. On the first hand, the results show that the stored energy decreases with the number of cycles, down to reach a stabilized regime. On the other hand, the stored energy increases with the stress amplitude. In the case of copper, the evolution of the stored energy with respect to the stress amplitude is also correlated to the appearance of slip bands, which are precursors of fatigue damage.

Keywords : Very high cycle fatigue, Ultrasonic fatigue machine, Energetic balance, Mechanical work, In situ time-resolved X-ray diffraction, Dissipated energy, Infrared thermography, Copper single crystal, C70 pearlitic steel.

Résumé

L'objectif de cette thèse est de développer une méthode de détermination rapide des propriétés des matériaux en fatigue, à partir de l'évolution de l'énergie stockée en fonction de l'amplitude de contrainte et du nombre de cycles appliqués. Cette évolution est estimée pendant des essais de fatigue menés à haute fréquence et pour des très grands nombres de cycles. La compréhension du lien entre l'évolution de l'énergie stockée et l'activation des mécanismes d'endommagement en fatigue permettrait de renforcer la crédibilité de la méthode. L'énergie stockée est estimée en réalisant un bilan d'énergie, qui correspond à la différence entre le travail mécanique apporté au matériau et l'énergie qu'il dissipe sous forme de chaleur. Le travail mécanique est estimé par diffraction des rayons X in situ résolue en temps et l'énergie dissipée par thermographie. Pour étudier le domaine des très grands nombres de cycles, un machine de fatigue ultrasonique fonctionnant à 20 kHz est utilisée. Les résultats des mesures montrent d'une part que l'énergie stockée décroit avec le nombre de cycles, jusqu'à atteindre un régime stabilisé et d'autre part qu'elle augmente avec l'amplitude de contrainte. Dans le cas du cuivre, l'évolution de l'énergie stockée en fonction de l'amplitude de contrainte semble également être corrélée à l'apparition de bandes de glissements, précurseurs de la formation d'endommagement en fatigue.

Mots-clés : Fatigue à très grand nombre de cycles, Machine de fatigue ultrasonique, Bilan d'énergie, travail mécanique, Diffraction des rayons X in situ résolue en temps, Energie dissipée, Thermographie infrarouge, Cuivre monocristallin, Acier C70 perlitique.

Table des matières

Acknowledgments **3**

Abstract **7**

Résumé **9**

List of tables **18**

List of figures **27**

Glossary **29**

Nomenclature **31**

Introduction **33**

1 State of the art **39**

1.1 Context of fatigue of materials 40

1.1.1 Industrial context and origins 40

1.1.2 Methodologies to characterize and design structures in fatigue . . 42

1.1.2.1 1st approach : test structures at their scale 42

1.1.2.2 2nd approach : test structures at a small scale 43

1.1.2.3 3rd approach : test structures at a small scale faster with a complementary characterization 45

1.2 Fatigue design with SN (Stress-Number of cycles to failure) diagrams . . 45

1.2.1 SN diagram concept 45

1.2.2 Fatigue machines to conduct small-scale tests 47

1.2.3 Experimental results : SN diagrams to study the behavior of materials in the HCF and VHCF domains . . . 48
1.3 Fatigue design from interrupted tests . . . 53
1.3.1 Thermographic approaches . . . 53
1.3.2 Estimation of the dissipated energy . . . 56
1.3.3 Stored energy as a marker of fatigue damage ? . . . 59
1.3.4 Conclusion of the section . . . 63
1.4 Mechanisms of fatigue damage . . . 64
1.4.1 Fatigue damage mechanisms in the HCF domain . . . 64
1.4.1.1 Cyclic slip irreversibility . . . 64
1.4.1.2 Dislocation structures and Persistent Slip Bands (PSB) . . . 65
1.4.1.3 PSBs leading to fatigue failure in the HCF domain . . . 68
1.4.2 Fatigue damage mechanisms in the VHCF domain . . . 69
1.4.2.1 Fatigue failure in VHCF for type I materials . . . 70
1.4.2.2 Fatigue failure in VHCF for type II materials . . . 75
1.4.3 Conclusion of the section . . . 77
1.5 Conclusion of the chapter . . . 77

2 Contribution to the development of an experimental methodology to estimate the stored energy during fatigue tests at 20kHz 79
2.1 Introduction . . . 80
2.2 Tested materials . . . 82
2.2.1 Pure copper single crystal . . . 83
2.2.2 Pearlitic (C70) steel . . . 84
2.3 Ultrasonic fatigue tests . . . 87
2.3.1 Functioning in conventional mode . . . 87
2.3.1.1 Principle of the ultrasonic fatigue machine . . . 87
2.3.1.2 Characterization of the ultrasonic fatigue machine . . . 90
2.3.1.3 Control of the ultrasonic fatigue machine . . . 92
2.3.1.4 Design of fatigue specimens . . . 92
2.3.1.5 Estimation of the stress amplitude in fatigue specimens . . . 96
2.3.2 Functioning in synchronized mode . . . 101

2.4 Time-resolved methodology to estimate the mechanical work 102
2.4.1 Estimation of the total strain 102
2.4.2 Estimation of the stress 104
2.4.2.1 Principle of X-ray diffraction 104
2.4.2.2 Treatment of XRD patterns 109
2.4.2.3 Uncertainties on the treatment of XRD patterns 111
2.4.2.4 Determination of the stress 113
2.4.2.5 Uncertainties on the estimation of the XEC 115
2.4.2.6 Experimental setup 116
2.4.2.7 Accuracy of the measurements 118
2.4.3 Development of an experimental time-resolved methodology . . . 120
2.4.3.1 Time-resolved measurements - Pump-probe methodology 120
2.4.3.2 Principle of data acquisition for uniform and pulsed modes 122
2.4.3.3 Experimental setup - uniform mode 124
2.4.3.4 Experimental setup - single-bunch mode 125
2.4.3.5 Periodic evolutions of diffraction peaks 127
2.4.3.6 Estimation of stress and strain evolutions 129
2.4.3.7 Estimation of the mechanical work 130
2.4.3.8 Influence of the experimental setup on the estimation of the time shift 131
2.4.4 Conclusion of the section 135
2.5 Measurement of the temperature to estimate the dissipated energy 135
2.5.1 Principle of experimental measurements 135
2.5.2 Temperature measurements during ultrasonic fatigue tests 136
2.5.3 Estimation of the dissipated energy 138
2.6 Conclusion of the chapter 140

3 Experimental results and discussions **143**

3.1 Estimation of the stress amplitude from in situ time-resolved X-ray diffraction 144
3.1.1 Estimation of the stress - case of copper 144
3.1.1.1 Experimental protocol of the tests - case of copper . . . 144

3.1.1.2 Experimental estimation of the XEC for copper 147
3.1.2 Estimation of the stress - case of steel 148
3.1.2.1 Experimental protocol of the tests 148
3.1.2.2 Estimation of the stress amplitude for steel specimens . 150
3.1.2.3 Variability of the XEC for steel 151
3.1.3 Conclusion of the results 152
3.2 Estimation of the stored energy : case of copper single crystal 152
3.2.1 Estimation of the mechanical work evolution with the stress amplitude and number of cycles 152
3.2.1.1 Influence of the stress amplitude and number of cycles on the time shift 153
3.2.1.2 Influence of the stress amplitude and number of cycles on the mechanical work 155
3.2.2 Estimation of the dissipated energy evolution with the stress amplitude 158
3.2.2.1 Experimental protocol for dissipative measurements . . . 158
3.2.2.2 Influence of the stress amplitude on the dissipated energy 159
3.2.3 Evolution of the stored energy with the number of cycles and the stress amplitude 161
3.2.3.1 Estimation of the stored energy 161
3.2.3.2 Influence of the number of cycles on the stored energy . 162
3.2.3.3 Estimation of the cumulative stored energy until the fracture of a specimen 163
3.2.3.4 Influence of the stress amplitude on the stored energy . . 163
3.3 Estimation of the stored energy : case of C70 pearlitic steel 169
3.3.1 Estimation of the mechanical work evolution with the stress amplitude and number of cycles 169
3.3.1.1 Experimental protocol of the tests 169
3.3.1.2 Influence of the stress amplitude and number of cycles on the mechanical work 170
3.3.2 Estimation of the dissipated energy evolution with the stress amplitude 171
3.3.2.1 Experimental protocol for dissipative measurements . . . 171

3.3.2.2 Influence of the stress amplitude on the dissipated energy 172
3.3.3 Estimation of the stored energy evolution with the stress amplitude and number of cycles 173
3.3.4 Conclusion of the discussions 177

Conclusion and perspectives **179**

References **185**

List of tables

1.1 Cumulative stored energy estimated experimentally on polycrystalline materials from fatigue tests. 61

1.2 Stored energy per cycle estimated from experimental measurements on polycrystalline materials. SMA = Shape Memory Alloys. 61

2.1 Chemical composition of pure copper single crystal studied (% weight). . 83

2.2 Mechanical properties of single crystal pure copper. 83

2.3 Chemical composition of the C70 steel studied (% weight). 84

2.4 Mechanical properties of the C70 steel studied. 85

2.5 Anti-resonance and resonance frequencies of various configurations of the resonant system in its conventional functioning - "Co." = piezoelectric converter and "Bo." = booster. 89

2.6 Longitudinal stress amplitudes of the steel specimen (in the **x** direction) for a displacement amplitude applied of 1 µm. 98

2.7 Longitudinal stress amplitudes of both copper specimens (in the **x** direction) for an applied displacement amplitude of 1 µm. 100

2.8 Resolved shear stresses for the respective slip systems of the copper specimen (in the **x** direction) for a displacement amplitude applied of 1 µm. . 100

2.9 Example of parameters of the Pearson VII asymmetrical fit function for the peak showed in Figure 2.24. Two widths and two shape factors are considered to fit both sides of the peak. The area and peak position is the same for both sides. - Case of C70 steel, Energy = 18 keV. 110

2.10 XEC of the two diffraction peaks studied for the pure copper single crystal. 115

2.11 XEC of the three diffraction peaks studied for the C70 pearlitic steel. . . 115

2.12 Total time shift induced on the reconstructed stress and strain signals in both Synchrotron modes. 131

2.13 Total time shift and total jitter induced on the reconstructed stress and strain signals in both Synchrotron modes. 134

2.14 Overview of the parameters selected to conduct XRD experiments on C70 steel (case of 110 diffraction ring of the ferrite phase) and copper single crystal (case of the $2\bar{2}6$ diffraction ring). 141

3.1 Characteristic of "Cu1" and "Cu2" studied diffraction peaks in uniform mode. The uncertainties are computed as the standard deviation of 50 acquired diffraction peaks. Beam energy of 18 keV. 146

3.2 Characteristic of C70 steel diffraction peaks in uniform mode. The uncertainties are computed as the standard deviation of 50 diffraction peaks. Beam energy of 18 keV. 150

3.3 XEC of ferrite for 110 lattice strain, estimated from experimental results - case of C70 steel. Theoretical value is $XEC_{110} = -1.32 \times 10^{-6}\text{MPa}^{-1}$. . 151

3.4 Characteristic of ferrite 110 diffraction peak studied in single-bunch mode. The uncertainty is computed as the standard deviation of 50 acquired diffraction peaks - case of C70 steel, specimen "C70-P6-SB"; beam energy of 18 keV. 170

List of figures

1.1 Image of a broken plane fuselage (owing to a fatigue crack) [Jacek and Gieras, 2013]. 41

1.2 Example of a fatigue test conducted on the wing of a plane in which the real loading conditions are reproduced to assess the mechanical part behavior under fatigue - case of the wing of an Airbus^{TM} A380. 42

1.3 Example of a small-scale test rig : a hydraulic fatigue machine (from NASA). 44

1.4 Experimental results reported in SN diagram in the case of a fully pearlitic steel with 0.8 wt% C. Figure adapted from [Dollar et al., 1989]. 46

1.5 Experimental results reported in SN diagram in the case of a pearlitic steel with 0.58 wt% C. Figure adapted from [Li et al., 2019]. 46

1.6 Schematic representation of the four types of SN diagrams obtain from experimental results : a) continuous decrease, b) decrease with a knee point, c) horizontal asymptote and d) decrease after horizontal asymptote. 48

1.7 Experimental results of SN diagrams showing a continuous decrease behavior for a) high-strength steel 100Cr6 [Sonsino, 2007] and b+c) aluminum/magnesium alloy + aluminum 2024-T531 [Sharma et al., 2020]. . . . 49

1.8 Experimental results of SN diagrams showing a knee point for a) copper (99.95% purity) [Phung et al., 2013], b) cast iron [Sonsino, 2007] and c) aluminum alloys [Sonsino, 2007]. 50

1.9 Experimental results of SN diagrams reaching a plateau after $10^6/10^7$ cycles for a) low carbon steel [Zettl et al., 2006], b) dual phase steel (DP600) [Torabian et al., 2017] and c) inconel 718 [Chen et al., 2005]. . . 51

1.10 Experimental results of SN diagrams showing a decrease after a horizontal asymptote a) high-strength steel [Furuya et al., 2002], b) high carbon steel [Wang et al., 2012] and c) titanium alloy TC21 - adapted from [Baohua et al., 2018]. 52

1.11 Evolution of the mean temperature elevation during a short interrupted fatigue test [Munier et al., 2014]. 54

1.12 Self-heating curves of an aluminum alloy specimen for three stress amplitudes. 54

1.13 Self-heating temperature increase for an XC55 steel. The fatigue limit is determined from the interception of the asymptotes of both regimes in the temperature evolution ; adapted from [Luong, 1995]. 55

1.14 Intrinsic dissipation computed from temperature measurements conducted at the surface of the specimen - polycrystalline copper [Blanche et al., 2015]. 57

1.15 Experimental self-heating curves, namely average intrinsic dissipation per cycle versus stress amplitude, obtained for a ferritic steel for different loading ratios [Mareau et al., 2012]. 58

1.16 Evolution of stored with respect to the number of cycles - case of a shape memory alloy loaded in LCF [Zhang et al., 2019]. 62

1.17 Cyclic stress-strain curve with associated dislocation pattern in 3 stages (with a plateau at which PSBs are forming) - case of a copper single crystal [Li et al., 2011]. 66

1.18 Schematic representation of a) dslocation aggregates in veins (patches) structure and b) dislocation walls in PSB after [Haasen et al., 1980]. . . . 68

1.19 Shape of predicted surface relief of an emerging PSB [Polák and Man, 2015]. 69

1.20 Schematic representation of SN curve to explain the fatigue behavior of type I materials [Mughrabi, 2006]. 71

1.21 Process of fatigue crack initiation at the surface in VHCF : a) initial state of the material, b) surface roughening and small intrusions forming and c) PSB nuclei forming at these steep intrusions [Mughrabi, 2006]. 72

1.22 SN diagram of polycrystalline copper fatigued with an ultrasonic fatigue machine in the VHCF domain. Appearance of first slip bands and PSB is reported on this curve [Stanzltschegg et al., 2007]. 73

1.23 Micrographs of the three types of slip markings observed on polycrystalline copper during fatigue loading : a) type I, b) type II and c) Type III [Phung, 2012]. 74

1.24 Schematic representation of SN curve to explain the fatigue behavior of type II materials. Differentiation is made between external and internal fatigue crack initiation [Mughrabi, 2006]. 75

1.25 Experimental observation of the dislocation structures characteristics of strain localization : dislocation pile ups at grain boundaries. Case of a duplex stainless steel subjected to 5×10^9 cycles at a loading amplitude $\Delta\sigma = 345$MPa [Fu et al., 2021]. "PB" stands for phase boundary. 76

2.1 Principle of the estimation of mechanical work from the estimation of stress and strain for one loading cycle. 81

2.2 Micrography of the C70 pearlitic steel taken from SEM at a magnification of 3000. The interlamellar spacing S_p is represented [Yahiaoui, 2013]. . . 85

2.3 SN curve of C70 pearlitic steel in the HCF and VHCF domains. A fatigue limit is determined from 10^7 to 10^{10} cycles at 402 MPa. 85

2.4 Fracture surface of the C70 steel in case of a fatigue loading conducted at 20 kHz for a) 406 MPa during 10^7 cycles ; internal crack initiation forming a fish-eye and b) 413 MPa during 2×10^6 cycles ; crack initiation at the surface. 86

2.5 Ultrasonic fatigue machine a) principle, b) picture. 88

2.6 a) Schematic representation of the experimental setup used to measure the displacement amplitude at the edge of the sonotrode and b) evolution of the displacement amplitude measured at the free end of the horn, with respect to the voltage amplitude applied to the piezoelectric converter. . 89

2.7 Characterization of the piezoelectric converter : a) Transfer function gain , b) phase and c) displacement vs. frequency [Jacquemain et al., 2021]. . 91

2.8 Geometry of a C70 steel fatigue specimen designed to vibrate at an ultrasonic frequency. 93

2.9 Evolution of the frequency with respect to the shaft length of a C70 steel specimen modeled by using Abaqus^{TM}. 93

2.10 Specimen geometry in the case of a) steel specimen reserved for XRD parallelepipedic shape, b) steel specimen for building an SN diagram and c) copper single crystal specimen for XRD. 94

2.11 Configuration of the copper single crystal specimens with their largest surface oriented perpendicular to the a) [113] and b) [1$\bar{1}$1] directions. . . 95

2.12 a) Longitudinal stress amplitude along the specimen central axis and b) longitudinal stress amplitude field (applied displacement amplitude $1\mu m$; loading frequency of 20232Hz) [Jacquemain et al., 2021]. 97

2.13 Longitudinal stress amplitude distribution within the specimen cross-section, in the center of the specimen for an applied displacement of 1 µm - case of steel specimen with parallelepipedic shape for a frequency of 20 232 Hz. 98

2.14 Evolution of the stress at the center of the specimen vs. the applied displacement to its screwed end - case of a C70 steel specimen. 99

2.15 Longitudinal stress amplitude distribution within the specimen cross-section, in the center of the specimen for an applied displacement of 1 µm - case of copper specimen a) with its larger central surface oriented perpendicular to the $[1\bar{1}3]$ direction, for a frequency of 20 269 Hz and b) with its larger central surface oriented perpendicular to the $[1\bar{1}1]$ direction, for a frequency of 20 267 Hz. 100

2.16 Schematic representation of the process of synchronization of the fatigue loading at the frequency of the synchrotron. 102

2.17 Schematic representation of the experimental configuration for the measurement of the total strain. 103

2.18 Bode diagram of the signal conditioner : a) gain and b) phase vs. frequency of the signal read by the conditioner. 104

2.19 Diffraction principle on a perfect crystallite in Bragg's condition (i.e. in diffraction condition). The crystallographic planes of the perfect crystal have their normal ($\boldsymbol{K_{hkl}}$) that is oriented along the $[hkl]$ direction. 105

2.20 Bragg's law and experimental configuration with respect to a specimen. Case of crystallographic planes that are in diffraction condition and their respective orientation with the coordinates system of the specimen. . . . 105

2.21 Bragg's law and experimental configuration with respect to a specimen. Examples of two diffracting dots corresponding to the contribution of two crystallites' orientations. 106

2.22 XRD pattern characteristic : a) pure copper single crystal diffraction "spot" and b) polycrystalline C70 steel continuous diffraction ring. 107

2.23 Bragg's law and experimental configuration with respect to a specimen. Only a portion of the diffraction cone is captured by the detector which represents the grains oriented parallel (or almost) to the surface of the specimen. 108

2.24 Organigram of the methodology to obtain a diffraction peak from a diffraction pattern. Case of C70 steel ; XPAD S140 total exposure time of 1 s ; energy of the beam : 18 keV. 110

2.25 Determination of the SNR from the study of a diffraction peak - case of ferrite 110 diffraction peak of C70 steel with an time exposure of 2 seconds ; energy of the beam : 18 keV. 112

2.26 a) Evolution of the Signal-to-Noise ratio with the time exposure and b) Random error on the estimation of 2θ positions and FWHM with the time exposure (estimated through the fitting of 50 diffraction peaks). . . 113

2.27 Picture of the experimental setup that was installed on the diffractometer at the DiffAbs beamline, SOLEIL Synchrotron. 117

2.28 Influence of the vertical beam drift on the measured position of the diffracted beam with the XPAD S140 detector. 119

2.29 Assessment of the vertical beam drift with the use of a Basler camera settled in front of the X-ray beam. The specimen is taken down to allow a direct exposure of the camera to the direct beam. 119

2.30 Principle of data acquisition based on a pump-probe approach. Adapted from Wang et al., 2013 120

2.31 Main difference in achievable time resolution between the two synchrotron modes of interest. 121

2.32 Principle of reconstruction of the sampled cyclic evolution of the total strain from acquired strain gauge values. 123

2.33 a) Experimental setup (acquisition loop) developed to acquire strain and stress evolutions during fatigue loadings at $20kHz$ and b) principle of data acquisition triggered by a threshold on the voltage signal - example of the acquisition of one value of the strain gauge signal. 125

2.34 a) Schematic representation of the acquisition loop used to acquire data which was adapted to the pulsed (single-bunch) mode at SOLEIL Synchrotron and b) principle of data acquisition triggered by the TimBel signal - acquisition of one value of total strain. 127

2.35 Peak position evolution reconstructed from the fitting of the integrated $2\bar{2}6$ diffraction peak - case of copper single crystal for stress amplitudes of respectively a) 30 MPa and b) 80 MPa. 128

2.36 FWHM evolution reconstructed from the fitting of the integrated $2\bar{2}6$ diffraction peak - case of copper single crystal for stress amplitudes of respectively a) 30 MPa and b) 80 MPa. 128

2.37 Stress and strain signal reconstructed through the stroboscopic principle. Both signals are acquired with the same time basis which allows one to estimate a time shift between the two signals - case of the copper single crystal at a loading amplitude of 80 MPa ; These cycles were reconstructed in uniform mode. 129

2.38 Reconstructed hysteresis loop showing the evolution of stress with respect to strain - case of the copper single crystal at a loading amplitude of 80 MPa. 130

2.39 a) Recall of the experimental setup and b) associated time shift of the signals at several stages of the process of data acquisition - case of uniform mode. 132

2.40 a) Recall of the experimental setup and b) associated time shift of the signals at several stages of the process of data acquisition - case of single-bunch mode. 133

2.41 Experimental setup developed to measure the dissipated energy from specimen under a fatigue loading. 136

2.42 Example of an image recorded by the IR camera during a fatigue test conducted on a steel specimen. 137

2.43 Self-heating (temperature increment) curve versus time during an ultrasonic fatigue test at 228 MPa - case of the C70 steel. 137

2.44 Zoom on the self-heating curve of the C70 steel (Fig. 2.43). Calculation of the speed of cooling as the slope at the end of the test. 138

2.45 Dissipated energy estimated with respect to the applied stress amplitudes to a) pure copper single crystal and b) C70 steel. 140

3.1 Loading history of specimens put in vibration with the ultrasonic fatigue machine during XRD measurements : specimens a) "Cu1" and b) "Cu2". Measurements were conducted by using strain gauge. 145

3.2 Diffraction profile (intensity versus 2θ) of the diffraction ring $2\bar{2}6$ of copper - case of specimen "Cu1", not loaded. 146

3.3 Evolution of the strain amplitude measured from lattice deformation using XRD with respect to the stress amplitudes measured calculated from total strain measured using strain gauge - case of copper single crystal, specimens "Cu1" and "Cu2". 147

3.4 Loading history of specimens put in vibration with the ultrasonic fatigue machine during XRD measurements : specimens a) "C70-A9" and b) "C70-P9". 149

3.5 Procedure of treatment of the ferrite 110 diffraction peak allowing the convenient study of the cementite 102 peak - case of specimen "C70-A9", not loaded. 149

3.6 Evolution of the strain amplitude measured from lattice deformation using XRD (from diffraction peaks of cementite and ferrite phases) with respect to the stress amplitudes measured calculated from total strain measured using strain gauge - case of C70 steel specimens "C70-19" and "C70-P9". 150

3.7 Stress and strain cycle reconstructed with respect to the time delay of the acquisitions. The time shift is measured between stress and strain signals - case of copper single crystal, specimen "Cu1" at a stress amplitude of 80 MPa. 153

3.8 Evolution of the time shift between stress and strain with respect to the applied stress amplitudes - case of copper single crystal, specimen "Cu1". For each stress amplitude, the values measured for three reconstructed cycles are reported. For one stress amplitude, the three points corresponds to the time shift evaluated for cycles respectively reconstructed after 8.46×10^6, 1.69×10^7 and 2.54×10^7 loading cycles. 154

3.9 Evolution of the time shift between stress and strain with respect to the applied stress amplitudes - case of copper single crystal, specimen "Cu2". For each stress amplitude, the values measured for three reconstructed cycles are reported. For one stress amplitude, the three points corresponds to the time shift evaluated for cycles respectively reconstructed after 8.46×10^6, 1.69×10^7 and 2.54×10^7 loading cycles. 154

3.10 Evolution of the Mechanical work with respect to the applied stress amplitudes - case of copper single crystal, specimen "Cu1". For one stress amplitude, the three points correspond to the mechanical work evaluated for three cycles successively reconstructed. 156

3.11 Evolution of the Mechanical work with respect to the applied stress amplitudes - case of copper single crystal, specimen "Cu2". For one stress amplitude, the three points correspond to the mechanical work evaluated for three cycles successively reconstructed. 157

3.12 Loading history of specimens put in vibration with the ultrasonic fatigue machine during temperature measurements - case of copper single crystal, specimen "Cu1". 158

3.13 Evolution of temperature imcrement (θ_s) with respect to the applied stress amplitudes - case of copper single crystal, specimen "Cu1". 159

3.14 Evolution of dissipated energy with respect to the applied stress amplitudes - case of copper single crystal, specimen "Cu1". 160

3.15 Evolution of the both mechanical work (for the third reconstructed cycle) and dissipated energy with respect to the stress amplitude applied to the specimen - case of copper single crystal, specimen "Cu1". 161

3.16 Evolution of the stored energy with respect to the number of loading cycles applied to the specimen for a loading amplitude of 80 MPa maintained during 1.02×10^8 cycles - case of copper single crystal, specimen "Cu1". 162

3.17 Evolution of the stored energy with respect to the stress amplitude applied to the specimen - case of copper single crystal, specimen "Cu1". Results are shown for the third reconstructed cycle, for which the stored energy is considered stabilized. 164

3.18 Threshold (nominal macroscopic) stress for appearance of microstructural mechanisms in pure copper single crystals : Peierl's [Nabarro, 1997], Frank-Read [Madec et al., 2000], slip markings [Stanzltschegg et al., 2007], PSB [Mughrabi, 1978]. 164

3.19 Evolution of the FWHM of the $2\bar{2}6$ diffraction peak (copper single crystal) with respect to the applied delay to acquire the data. The cyclic evolution of the FWHM is acquired cycle per cycle. Their representation one after the other is made for sake of simplicity. Yet, it does not mean that these reconstructed cycles are successive as they are each reconstructed over 8.46×10^6 cycles. The strain measured by the strain gauge provide an element of comparison to the cyclic evolution of the FWHM. The FWHM are plotted for stress amplitudes of a) 16 MPa, b) 30 MPa, c) 48 MPa, d) 55 MPa, e) 61 MPa, f) 69 MPa, g) 77 MPa and h) 80 MPa. 166

3.20 Evolution of parameters A_w, B_w and C_w with respect to the stress amplitudes - case of copper single crystal, specimen "Cu1". 167

3.21 Loading history of specimens put in vibration with the ultrasonic fatigue machine during XRD measurements : specimen "C70-P6-SB". Stress amplitudes has been estimated by using strain gauge. 169

3.22 Evolution of the Mechanical work with respect to the applied stress amplitudes - case of C70 steel. For each stress amplitude, the values measured for three reconstructed cycles are reported. For one stress amplitude, the three points corresponds to the mechanical work evaluated for cycles respectively reconstructed after 1.1×10^8, 2.2×10^8 and 3.3×10^8 loading cycles. 171

3.23 Loading history of specimens for temperature measurements during ultrasonic fatigue tests - case of C70 steel, specimen "C70-P6-SB". 172

3.24 Evolution of temperature imcrement (θ_s) with respect to the applied stress amplitudes - case of C70 steel, specimen "C70-P6-SB". 172

3.25 Evolution of dissippated energy with respect to the applied stress amplitudes - case of C70 steel, specimen "C70-P6-SB". 173

3.26 Evolution of the stored energy with respect to the stress amplitude applied to the specimen - case of C70 steel, specimen "C70-P6-SB". Results are shown for the a) first, b) second and c) third reconstructed cycles. 174

3.27 Evolution of the FWHM of the 110 diffraction peak with respect to the applied delay to acquire the data. The cyclic evolution of the FWHM is acquired cycle per cycle. Their representation one after the other is made for sake of simplicity. Yet, it does not mean that these cycles are successive as they are each computed over 1.1×10^8 cycles. The strain measured by the strain gauge provides an element of comparison to the cyclic evolution of the FWHM. The FWHM are plotted for stress amplitudes of a) 35 MPa, b) 100 MPa, c) 180 MPa, d) 230 MPa and e) 253 MPa. 175

3.28 Evolution of parameters A_w, B_w and C_w with respect to the stress amplitudes - case of C70 steel, specimen "C70-P6-SB". 176

Glossary

SN	Stress versus Number of cycle (Diagram or curve)
LCF	Low Cycle Fatigue
HCF	High Cycle Fatigue
VHCF	Very High Cycle Fatigue
XRD	X-ray Diffraction
RVE	Representative Element of Volume
PSB	Persistent Slip Band
CSSC	Cyclic Stress-Strain Curve
TEM	Transmission Electron Microscope
FCC	Face Centered Cubic
BCC	Body Centered Cubic
OR	Orthorombic
ASTM	American Society for Testing and Materials
FEA	Finite Element Analysis
FWHM	Full Width at Half Maximum
SNR	Signal-to-Noise Ratio
PLL	Phase-Locked Loop
XEC	X-ray Elastic Constant
MS	Mega Sample
LFG	Low Frequency Generator
IR	InfraRed
CCD	Charge-Coupled Device

Nomenclature

N_f	Number of cycles to failure
Δe	Specific internal energy variation
T	Temperature
ρ	Density
C	Specific heat energy
σ	Stress
ε	Total strain
$\dot{\varepsilon}$	Strain rate
$s_{coupling}$	Coupling sources
E_{diss}	Dissipated energy
W_{mech}	Mechanical Work
E_{st}	Stored energy
S_p	Interlamellar spacing (microstructure)
E_{is}	Isothermal Young's modulus
Re	Yield stress
Rm	Ultimate tensile stress
$A\%$	Elongation
C_{ij}	Compliances constants
S_{ij}	Stiffness constants
d_{int}	Intrinsic dissipation
s_{the}	Thermoelastic sources
f	Loading frequency
τ_{0D}	Characteristic time of heat losses (case of a zero-dimensional model)
θ_s	Saturation temperature increment
$H(jw)$	Transfert function (in the case of a harmonic calculation)
u	Voltage
u_0	Voltage amplitude
i	Current
i_0	Current amplitude
w	Angular frequency
$\phi_{machine}$	Phase shift between voltage and current

L_s	Shaft length
L_c	Centre length
S_s	Shaft section
S_c	Central section
R	Curvature radius
$\varnothing_s$	Diameter of the shaft
$\varnothing_c$	Diameter of the centre
k_i	Coefficient between stress and displacement
K_{hkl}	Diffraction vector
λ	Wavelength
d_{hkl}	Inter-reticular distance
θ_{hkl}	Reference angular position of the diffracted beam
θ	Angular position of the diffracted beam
ϕ_{drx}	Reference angle of the diffraction vector
ψ	Reference angle of the diffraction vector
ε_{hkl}	Lattice strain
$P_{7,i}$	Pearson VII function
$H(\theta)$	Heaviside function
A	Area under the diffraction peak
B	Baseline of the diffraction peak
m	Shape factor of the diffraction peak
W	Full Width at Half Maximum
I_{max}	Maximum intensity of diffraction peak
$I_{noise,mean}$	Mean intensity of the baseline of diffraction peak
s_{ijkl}	X-ray elastic constant
E	Beam energy
ΔE	beam energy variation
$\Delta\varepsilon$	Total strain amplitude
$\Delta\sigma$	Stress amplitude
ϕ	Time shift between stress and strain
$XEC_{theo,i}$	XEC from theoretical calculation
$XEC_{exp,i}$	experimentally estimated XEC
E_{st}	Stored energy per cycle
$E_{st,cum}$	Cumulated stored energy per cycle
A_w	Parameter A of FWHM fit function
B_w	Parameter B of FWHM fit function
C_w	Parameter C of FWHM fit function

Introduction

Context of fatigue phenomenon and industrial impact

Since the XIXth century, numerous accidents are caused in metallic structures (railways, planes, ...) by an unanticipated failure that is owing to fatigue of materials. The fatigue phenomenon is the action of cyclic repeated loading on a mechanical component. This loading induces a deformation that accumulates over numerous repetitions (one repetition is classically referred to as one cycle). The process of fatigue failure relies on the accumulation of a small deformation which leads to the weakening of the matter and later to its failure. In fact, a cyclic loading can lead to failure even when the applied stress is smaller than the elastic limit of the material.
Even in current industrial applications, the fatigue of materials seems to be an underestimated concern. As a matter of fact, in 2021 the right engine of a Boeing 777 caught fire during a flight [Guardian, 2021]. This dramatic incident happened due to the damage to one of the blades of the engine. This damage was later attributed to the fatigue of the deficient blade after more than two billions of cycles.

To ensure safety, to be economically sustainable and also to reduce their ecological footprint, the objective of industrials starts to be directed towards structures that can last for a very high number of cycles. Then, fatigue lives of mechanical components that outcome billions of cycles will become even more common. It is currently necessary to direct the investigations toward very high fatigue lives (i.e. higher than 10^7 cycles). Such lifespans correspond to the Very High Cycle Fatigue (VHCF) domain.

To explore the domain beyond 10^7 cycles with reasonable test duration, fatigue machines were developed based on a new technology : piezoelectric devices. The properties of piezoelectric ceramics were used to apply a fatigue loading by making a material vibrate. This technology is referred to as ultrasonic fatigue machines, which works at frequencies close to 20 kHz. They permit to reach 10^9 cycles in only 14 hours, allowing to reach the gigacycle fatigue regime in short test durations whereas with a conventional fatigue machine working at 10 Hz, it would take more than three years. With ultrasonic fatigue machines, the investigation of the VHCF domain is then accessible.

Fatigue design

Design against fatigue failure requires strong knowledge and a substantial experience in both structural and mechanical engineering and materials science. One can report various approaches to fatigue design, with different degrees of life inssurance for mechanical parts. A common approach is based on an experimental assessment of the fatigue properties of materials. By ”fatigue properties”, one should understand the fatigue lifespan experienced by a material for a given loading state.

The determination of the fatigue properties has been carried out by the conduction of fatigue tests up to failure. For one loading condition, the lifelength of the material

under various conditions can be estimated. This approach is time-consuming and not viable when it concerns fatigue lives exceeding 10^8 cycles or more. Ultrasonic fatigue machines allow to study of the VHCF domain, but studying the fatigue behavior of materials subjected to more than 10^{11} cycles remain long.

To accelerate the process of fatigue design, the measurement of the temperature field on the surface of a specimen during short interrupted tests was studied. It is commonly referred to as the "thermographic method". For this method, a temperature variation during an interrupted cyclic loading of a material can be associated with a number of cycles to failure. This non-contact and non-destructive technique offers the possibility to determine the fatigue properties of metals by considerably reducing the testing durations, which reinforced its popularity. In addition, this methodology provides consistent results for many materials, but its application remains not feasible for all. In fact, the abovementioned thermal effect is associated with the energy dissipated in the material. This energy is not directly linked to microstructural changes, such as the formation of persistent slip bands from which fatigue damage can nucleate. This is why the application of the thermographic methodology requires modelling at the microscopic scale to allow the determination of the fatigue properties of metals from temperature measurements.

Another methodology, proposed in this Ph.D., is to estimate and follow the energy that is stored in the material during cyclic loading. Indeed, the stored energy is directly correlated to the non recoverable microstructural changes of the material when it is subjected to a mechanical loading. For instance, the stored energy is sensitive to a change in dislocation density or the formation of dislocation structures (such as persistent slip bands for instance) in the material. Thus, the stored energy is a good candidate to be measured during short interrupted tests to determine fast the fatigue properties of metallic materials. Nevertheless, the estimation of stored energy remains a very difficult task compared to the estimation of the dissipated energy, especially during a fatigue test conducted in the VHCF domain. In addition, the development of models could be required as well to indubitably interpret the evolutions of stored energy.

Scientific objectives of the Ph.D.

The aim of the work performed during this Ph.D. is threefold :

- Determine fast the fatigue properties of materials, at a very high number of cycles, from the evolution of stored energy.
- Estimate the evolution of stored energy with respect to the number of cycles and the applied stress amplitude during ultrasonic fatigue tests.
- Understand the link between the stored energy evolutions and the fatigue damage mechanisms.

The work of this Ph.D. was conducted in the framework of the European research project H2020 FastMat (fast determination of fatigue properties of materials beyond one billion cycles) funding by the European Research Council (ERC) (grant agreement No 725142).

Scientific approach

The work conducted in this Ph.D. focused on the development of a methodology based on an energy balance to determine the stored energy from the difference between the mechanical work provided to the loaded material and the energy dissipated as heat. Both measurements were conducted independently. On the first hand, the estimation of the dissipated energy was conducted through temperature measurements at the surface of the specimen. On the other hand, the mechanical work was estimated by means of an in situ time-resolved X-ray diffraction methodology which was conducted by using a Synchrotron X-ray source. This work was conducted in a collaboration with the DiffAbs beamline at Synchrotron SOLEIL. The development of this methodology required the use of the synchrotron X-ray source during 60 days, corresponding to at least ten experimental campaigns that were carried out at DiffAbs. It underlines the highly iterative character of this development to ensure the reliability of the methodology. Indeed, the correct association of the developed experimental setup and the beamline apparatus was mandatory.
In addition, this study requires the use of an ultrasonic fatigue machine, to establish the energy balance during fatigue tests conducted in the VHCF domain in reasonable testing durations.

Both methodologies were applied to two materials to validate their performance. The materials of interest are C70 fully pearlitic steel and pure copper single crystal. The pure copper single crystal is a perfect candidate to validate the process of the methodology. Indeed, its application to X-ray diffraction measurements is convenient owing to its simple crystalline structure. The C70 steel is a rather classical material for engineering studies as it can be used to manufacture railways for instance. Hence, this material is a good candidate to test the method : validation of the methodology, when applied to a material that has industrial applications, would reinforce its credibility.

Organization of the manuscript

This Ph.D. manuscript is divided into three chapters :

- The first chapter corresponds to a state of the art that defines the current stakes of fatigue design and presents the methodologies that are employed to determine the fatigue properties of metals. The focus is made first on the SN diagram and

its difficult construction when it comes to fatigue lives in the VHCF domain. Recent methodologies allowing a fast determination of fatigue properties from temperature measurements are then exposed as well as their limitations in terms of interpretation of the results. It underlines the requirement for a methodology that takes into account the understanding of the microstructural phenomenon that takes place in the material. Such methodology is believed to be associated with the estimation of the stored energy, representative of the microstructural change occurring in a material during the application of a loading. The mechanisms responsible for microstructural changes in a fatigued metal are then reviewed.

- The second chapter provides an overview of the contribution of this work in terms of the experimental methodology that was developed, applied and optimized to allow an estimation of the stored energy in metals during a fatigue test in the VHCF domain, conducted with an ultrasonic fatigue machine (working at 20 kHz). The chapter starts with the presentation of both materials of interest and carries on with the presentation of the ultrasonic fatigue machine and its specific use. Then, the focus is made on the experimental approach developed to estimate the mechanical work from an in situ time-resolved X-ray diffraction method. The last section describes the experimental approach that was employed to determine the dissipated energy. For each methodology, first results are provided.

- Finally, the third chapter presents the results obtained from the application of the methodologies that were presented in the second chapter. The measurements of dissipated energy, mechanical work and stored energy will be discussed, especially their evolution with respect to the stress amplitude and the number of cycles applied to the materials of interest.

Chapitre 1

State of the art

This chapter provides an overview of the fatigue phenomenon and how important it is for industries to design mechanical components or structures. The objective of this chapter is to describe the fatigue of materials, how this phenomenon is understood, the methodologies considered to design mechanical parts, and what are the main characteristics and questionning which rise when applying these methodologies. As fatigue life of components tend to increase, this work is concentrated around the Very High Cycle Fatigue (VHCF) domain, which corresponds to fatigue life length above 10^7 cycles. The main difficulty arises when it comes to the determination of the fatigue properties[1] of materials for fatigue lives above 10^9 cycles. In particular, the challenge is to maintain reasonable test durations for the experimental determination of these properties.

In the first section, the focus is made respectively on the stakes of fatigue design and the different methodologies developed over the past decades to be able to study the fatigue of materials. Then, an analysis of the fatigue properties determined experimentally for various metallic materials is conducted in the second section. This analysis reveals the difficulty related to the determination of fatigue properties. Next, the third section overviews new methodologies to design structures in fatigue that are based on energetical measurements during interrupted fatigue tests. Finally, the microstructural mechanisms responsible for fatigue damage and crack initiation, especially in the VHCF domain are exposed in the last section. It enhances the application of the new methodologies presented in the third section.

1.1 Context of fatigue of materials

1.1.1 Industrial context and origins

To put things in their context, fatigue of materials was at first studied in the XIXth century by [Albert, 1837] who reported the failure of mine host chains, made of iron, arising from repeated loadings. Most of the studies of this phenomenon, at that time, were directed towards metallic materials experiencing failure because of repeated loading, even at stress amplitude below their yield strength[2]. The cyclic loading effect on materials was called "fatigue of materials" by [Poncelet, 1841] for the first time. The expansion of the knowledge of fatigue of materials made great progress owing to the

1. As "fatigue properties", one should understand the life length of a component respectively to the external load applied to it.

2. The notion of yield strength was first approached by Leonardo Da Vinci at the end of the XVth century as he conducted experiments on the resistance of iron cables. The yield strength corresponds to the stress value below which the relationship between stress and strain is linear and for which the material can bend elastically ; this concept was shown by Robert Hooke in 1660.

development of railways [Wöhler, 1867]. [Wöhler, 1870] was interested in railroad axles and summarizes his work into one major conclusion : he stated that to conduct a reliable design of a mechanical part, the consideration of the cyclic stress applied to a material was more important than the peak stress (corresponding to a monotonous applied stress). Since this period, fatigue has become of increasing interest for the rail industry and transportation industries in general. In fact, at least 80% of the mechanical parts and structures are designed to resist fatigue, essentially in the transport and energy production industries.



FIGURE 1.1 – Image of a broken plane fuselage (owing to a fatigue crack) [Jacek and Gieras, 2013].

Fatigue damage occurs in mechanical parts because of the repeated deformation applied to the material. One can refer to fatigue damage as the unrecoverable microstructural changes in a material that will not be recovered when rested ; damage is associated with the appearance of cracks in the material. Indeed, a fatigue crack originates from damage mechanisms at a microscopic scale and propagates slowly (in a stable manner) in a component, as observed by Sir James Alfred Ewing in 1903. Such crack is not dangerous but can become lethal for a structure as soon as it has reached a sufficient length. It then starts to propagate in an unstable manner until the global failure of the component or the structure.

Fatigue damages affect metallic parts in heavily loaded components which are critical in terms of the reliability of the structure to which they belong. Rotating parts of thermal engines in the car industry, turbine blades in turbojets and power plants are the most common components subjected to fatigue failure. Such incident was frequent in the XXth century, as illustrated by the plane incident of Aloha Airline Flight 243 in 1988 where the fuselage fractured in-flight due to fatigue failure originating from multiple corroded

rivet holes (see Figure 1.1). In fact, this failure originated from the bad knowledge of the fatigue behavior of the materials constituting the fuselage surrounding the rivets.

In-use loading conditions might be different from what has been considered to conduct fatigue design, leading to the formation of fatigue cracks. The presence of a fatigue crack is not necessarily detrimental, especially if it is detected early in the fatigue lifetime of the structure. Maintenance phases enable to detect small cracks and follow their advance during the structure lifecycle. The occurrence of the maintenance phases is thus critical and is determined by the knowledge of the fatigue properties of a material. This underlines the importance of the determination of fatigue properties of metallic materials.

1.1.2 Methodologies to characterize and design structures in fatigue

Nowadays, there are several ways in the literature to conduct fatigue design of a structure. These ways are presented in this section ; their advantages and drawbacks are presented.

1.1.2.1 1st approach : test structures at their scale

Impressive test rigs can be developed to test a full structure in real conditions. Figure 1.2 shows an example of a full-scale fatigue test conducted on a plane wing where the real loading conditions are reproduced.



FIGURE 1.2 – Example of a fatigue test conducted on the wing of a plane in which the real loading conditions are reproduced to assess the mechanical part behavior under fatigue - case of the wing of an Airbus^{TM} A380.

The frequency of application of the load, the stress amplitude, the loading path, or even the temperature and pressure of the environment can be reproduced to conduct the test of the structure. These experiments are usually conducted up to fracture. Thus, the results obtained from such tests are interesting to predict how the structure will react after several thousand or millions of cycles, what is the weakest part of the structure or how fatigue cracks appear, etc. However, such machines are very expensive, very specific to a single structure, sometimes in a single representative loading condition and the process is time-consuming as it takes months to develop one test rig.

1.1.2.2 2nd approach : test structures at a small scale

The second approach consists in testing only a small representative element of the volume of the material constitutive of the structure. The objective is to characterize the material instead of the structure. This approach was proposed by [Wöhler, 1870] and relies on the determination of the fatigue properties of a material through fatigue tests conducted up to its failure. It requires the use of small-scale fatigue machines : Figure 1.3 shows an example of a conventional hydraulic fatigue machine that can be used. Ultimately, the fatigue properties obtained through the application of successive small-scale tests are commonly integrated into a Finite Element Model (FEM) that models the structure to be designed. A calculation of the structure stress state according to its in-use conditions, its material parameters and its fatigue properties will validate its design.

The abovementioned tests are governed by standards that have been established to guarantee their repeatability, independently of the machine or the person who conduct the test [ASM-E606, 2001, ISO-12107, 2012, DIN-50100, 2016, ASM-E466, 2021]. The standards provide the basics to design the fatigue sample (with an advised shape that should be either dog-bone or hourglass according to [ASM-E466, 2021]), which fatigue machine to use, the set of parameters to tune, etc.

Such small-scale tests are advantageous in the way that they allow one to consider the complex stress state of the specimen loaded. Triaxial tests can be conducted to account for stress triaxiality (if only it is possible to assess such stress state during the loading)[3]. The loading parameters, that generally limits to a certain number (such as the amplitude, the mean or the frequency of the applied load), are key parameters to control a test and personalize the loading to fit the in-use conditions. The effect of each parameter can be tested independently or combined with other parameters. For instance, it is possible to study the effect of an overload during one cycle or to test the influence of the mean loading amplitude. The type of cyclic loading applied to the material is

3. To our knowledge, this type of test is not constrained by any standards up to now.

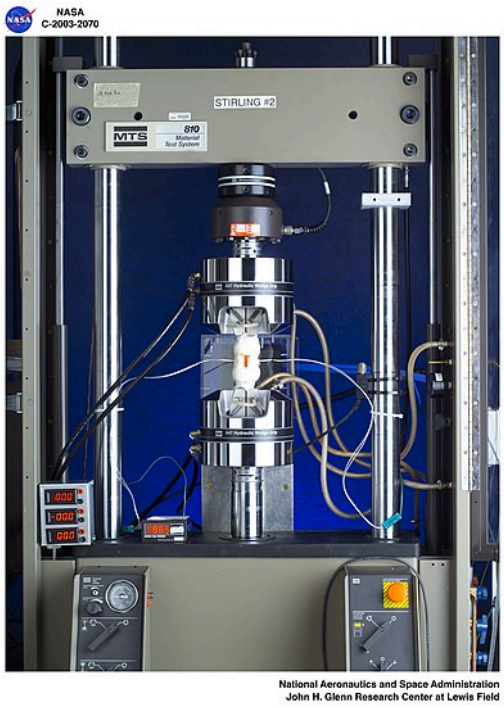


FIGURE 1.3 – Example of a small-scale test rig : a hydraulic fatigue machine (from NASA).

generally quite simple : from triangular (to obtain a constant strain rate) to sinusoidal (easier to apply and study). With small-scale tests, fatigue damage mechanisms can be studied, which enhances the development of models at a microscopic scale to explain the formation of fatigue damage.

However, this methodology has its drawbacks. First, a size effect is an unavoidable confounding factor [Furuya, 2011, Tridello et al., 2021]. If two specimens, one larger than the other, are tested, the larger one will show a smaller life length, which comes from the higher probability to find critical defects in the larger specimen. In addition, fatigue of material is not a stochastic but a probabilistic phenomenon. This difference is explained by the difference in microstructure between the two specimens. To counter this probabilistic aspect, numerous tests are required to obtain a statistically reliable estimation of the fatigue properties. The results of the small-scale tests are usually expressed with a probability of failure.

1.1.2.3 3rd approach : test structures at a small scale faster with a complementary characterization

The procedure to determine the fatigue properties of materials from the second methodology is time-consuming. Thus, this third approach was developed to accelerate the process. This methodology requires the use of small-scale machines but consists in realizing short interrupted tests (instead of tests until fracture). In fact, these interrupted fatigue tests are coupled to complementary measurements that allow one to measure alternative quantities such as the temperature at the surface of the specimen for instance [Luong, 1995, Rosa and Risitano, 2000]. The measurements take place during a short test and are sufficient in themselves to provide information on the material state evolution. In the case of temperature measurements on specimens loaded in fatigue, the temperature can be assessed during the first thousands of cycles applied in a short interrupted test. By extrapolation of these results, several empirical approaches have been developed to understand the link between the temperature increase and the number of cycles to failure (N_f).

1.2 Fatigue design with SN (Stress-Number of cycles to failure) diagrams

The present section details the application of the second methodology presented previously. It is based on the concept of SN curve also called Wöhler curve [Wöhler, 1870].

1.2.1 SN diagram concept

The SN curve plots the stress amplitude with respect to the corresponding number of cycles to failure (N_f). One point on the curve corresponds to one fatigue test conducted up to failure, at a constant stress amplitude. Two examples are presented in Figure 1.4 and 1.5 for a pearlitic steel with respectively 0.58 wt % C and 0.8 wt % C. This material is close, in terms of composition, to the C70 steel on which this Ph.D. work will focus. Figure 1.4 characterizes fatigue life lower than 10^7 cycles whereas Figure 1.5 characterizes fatigue life up to 10^9 cycles. It is shown that the life length increases with a decreasing stress amplitude. A horizontal scatter is generally seen for every stress amplitude. From Figure 1.5, it appears that the tested steel could fail at 450 MPa after 1.1×10^5 or after 5×10^5 cycles. Additionally, when looking at the fatigue curve of Fig. 1.5, a hypothetical horizontal asymptote is identified at a stress of 430 MPa between 10^6 and 2×10^8 cycles.

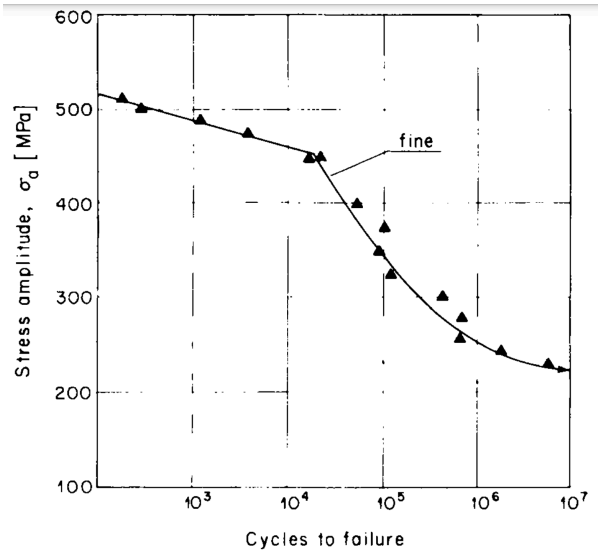


FIGURE 1.4 – Experimental results reported in SN diagram in the case of a fully pearlitic steel with 0.8 wt% C. Figure adapted from [Dollar et al., 1989].

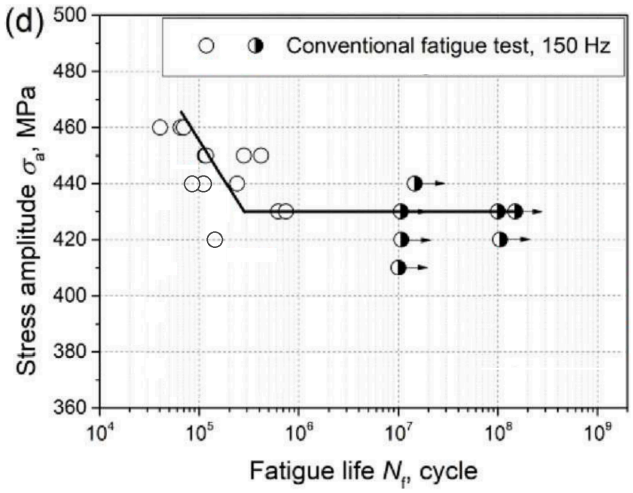


FIGURE 1.5 – Experimental results reported in SN diagram in the case of a pearlitic steel with 0.58 wt% C. Figure adapted from [Li et al., 2019].

When considering such a curve, it is possible to identify three domains. First, one can identify the Low Cycle Fatigue (LCF) domain which corresponds to stress amplitudes, in the order of the yield stress of the material, and thus very low fatigue life ; that is up to 10^4 cycles (it is well represented on the left of Fig. 1.4). This domain is characterized by a macroscopic plastic activity of the material when it is loaded to such stress amplitudes [Xu, 2017]. Then, there is the High Cycle Fatigue (HCF) domain. This one represents the fatigue life longer than 10^4 cycles and shorter than 10^7 cycles. This

domain was limited to such fatigue lives because fatigue lives above 10^7 cycles were considered almost infinite in many industrial applications. In addition, reaching more than 10^7 cycles with fatigue machines working at low-frequency would induce too long test durations. This domain corresponds to failure occurring for stress amplitudes in the order of half the yield stress (it is well represented on the right of Fig. 1.4). The HCF domain is characterized by a localized plastic activity, which takes time to develop and to produce a fatigue crack leading to failure [Mughrabi, 2012]. Recently, the Very High Cycle Fatigue (VHCF) domain was defined as the fatigue life domain which goes further than 10^7 cycles from the constatation of the possible failure of components at such number of cycles [Mughrabi et al., 1979, Puškár, 1993a, Mughrabi, 2006, Zettl et al., 2006]. The VHCF domain can also be referred to as the gigacycle fatigue regime for fatigue lives longer than 10^9 cycles. Fatigue tests conducted in the VHCF domain are representative of stress (and strain) levels that are very small, i.e. lower than half the yield stress.

1.2.2 Fatigue machines to conduct small-scale tests

For many decades, fatigue tests were conducted with conventional fatigue machines that could either be hydraulic or electro-mechanic [Wöhler, 1867, Sakai et al., 2002]. Those machines could load specimens at frequencies from 10 to 30 Hz. This type of fatigue machine allows to reach 10^7 cycles in less than a day but it would require too much time to reach higher fatigue lives with such means. Fatigue design was confined to fatigue lives of 10^7 cycles at maximum and remained in the HCF or LCF domains owing to long test durations.

During the last decades, the focus was directed towards higher load frequencies in order to reach higher fatigue lives faster. The development were oriented towards vibrophores, also called resonant testing machines [Nicholas, 2002, George, 2004]. These machines rely on a mechanical vibration system : a spring-mass functions as an electromagnetically driven oscillator. This type of machine is particularly adapted to study the HCF domain. It is to be noted that vibrophores are commonly found on the market of fatigue machines and exhibit frequencies around a few hundred of hertz. Frequency up to 1.8kHz has been reached with such machines [Nicholas, 2002]. In parallel, [Morgan and Milligan, 1997] and [Zimmermann and Christ, 2007] developed vibrophores with a frequency reaching 1kHz and load capacity up to 600N.

Notwithstanding, for several decades the focus is oriented towards piezo-electric converters whose control has been improved, allowing the development of ultrasonic fatigue machines. This type of machine was initially proposed in the 1950s by Mason [Mason, 1958]. Such machines are less cumbersome than conventional machines. For ul-

trasonic machines, the principle is relatively simple : it loads a specimen[4] (considered itself as a mass-spring system) by making it vibrate in its first longitudinal mode of vibration. The loaded specimens are designed to reach a vibration frequency close to 20kHz [Fischer et al., 2011, Schmidt et al., 2010] and up to 30kHz [Marines, 2003], depending on the setup. The development of such machines enables to reach faster the very high fatigue lives and thus to investigate the VHCF domain with acceptable test durations. The functioning of ultrasonic fatigue machines will be described later in this work.

1.2.3 Experimental results : SN diagrams to study the behavior of materials in the HCF and VHCF domains

The results obtained when plotting an SN diagram in the HCF and VHCF domains are very different when comparing all metallic materials. In fact, they can be regrouped into four categories [Pyttel et al., 2011] :

- continuous decrease ;
- decrease with a knee point ;
- horizontal asymptote ;
- decrease after horizontal asymptote.

The four categories of the SN diagram are schematically represented in Figure 1.6.

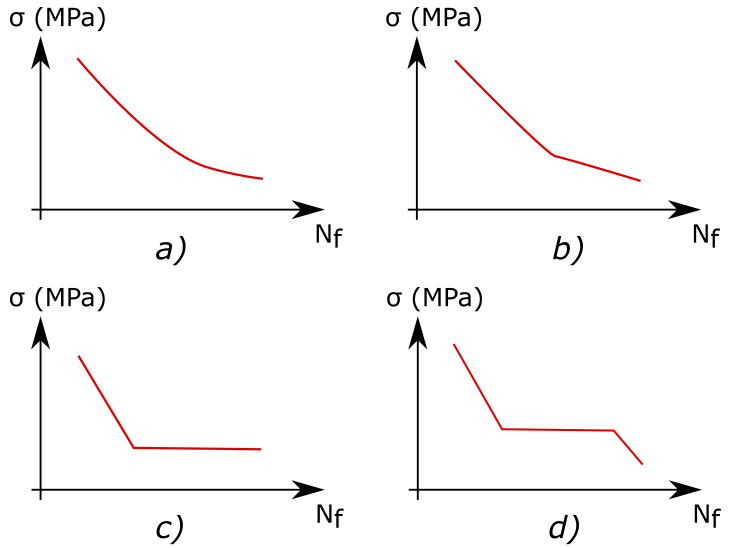


FIGURE 1.6 – Schematic representation of the four types of SN diagrams obtain from experimental results : a) continuous decrease, b) decrease with a knee point, c) horizontal asymptote and d) decrease after horizontal asymptote.

4. Ultrasonic fatigue specimens have a length that is typically smaller than 700 mm.

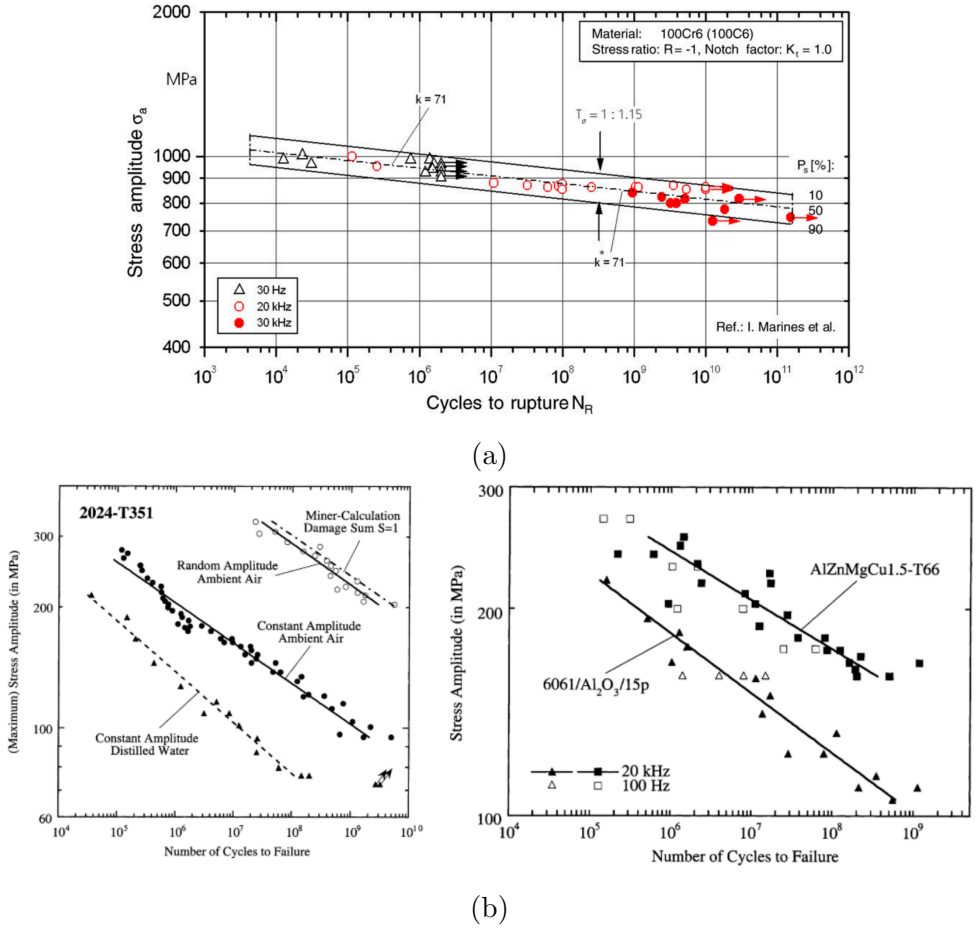
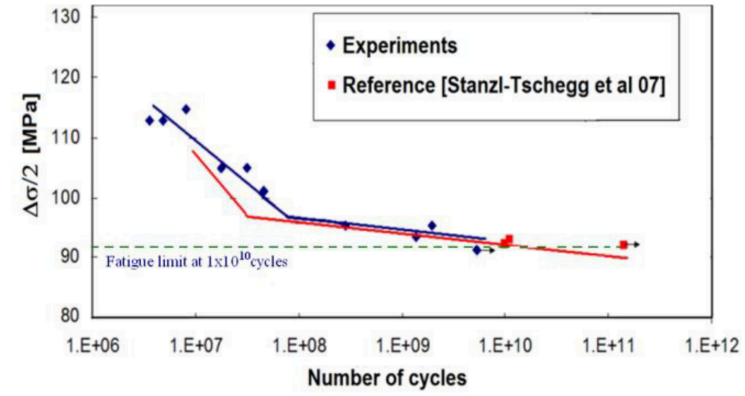


FIGURE 1.7 – Experimental results of SN diagrams showing a continuous decrease behavior for a) high-strength steel 100Cr6 [Sonsino, 2007] and b+c) aluminum/magnesium alloy + aluminum 2024-T531 [Sharma et al., 2020].

Figure 1.7 shows experimental results for a high-strength steel 100Cr6 and two aluminum alloys. The SN diagrams show a continuous decrease : the fatigue life length continuously increases with the decreasing stress amplitude. The log scale that is used for stress amplitudes in Fig. 3.1a, compared to Fig. 3.1b, does not influence the continuous decrease observed for the SN diagram, it just emphasizes it.



(a)

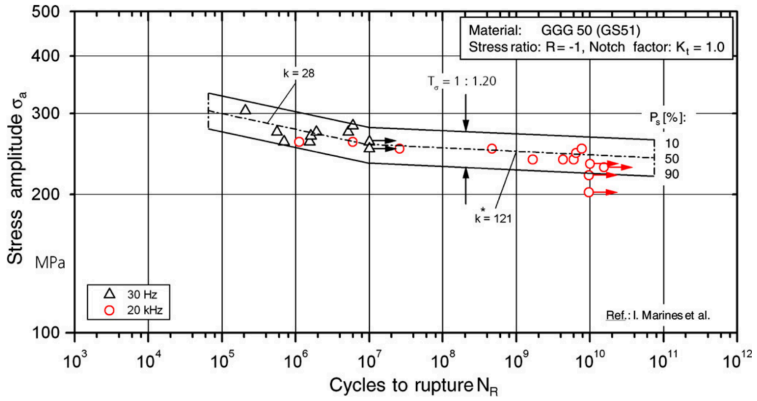
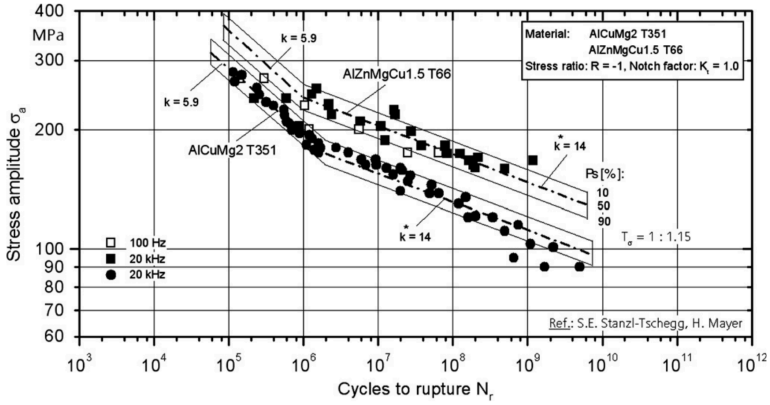


Fig. 7. SN-curve of a cast iron up to the giga-cycle regime.

(b)



(c)

FIGURE 1.8 – Experimental results of SN diagrams showing a knee point for a) copper (99.95% purity) [Phung et al., 2013], b) cast iron [Sonsino, 2007] and c) aluminum alloys [Sonsino, 2007].

The continuous decrease is sometimes found to exhibit two distinct slopes. In these cases, a knee point is identified : the slope of the increasing life length with the decreasing stress changes and becomes flatter, generally between 10^6 and 10^8 cycles. Figure 1.8 shows experimental results for pure copper, cast iron and aluminum alloys exhibiting a knee point. Fig. 1.8b and 1.8c, compared to Fig. 1.8a, show a knee point whose slopes are smaller in log scale and would thus be more remarkable in linear scale.

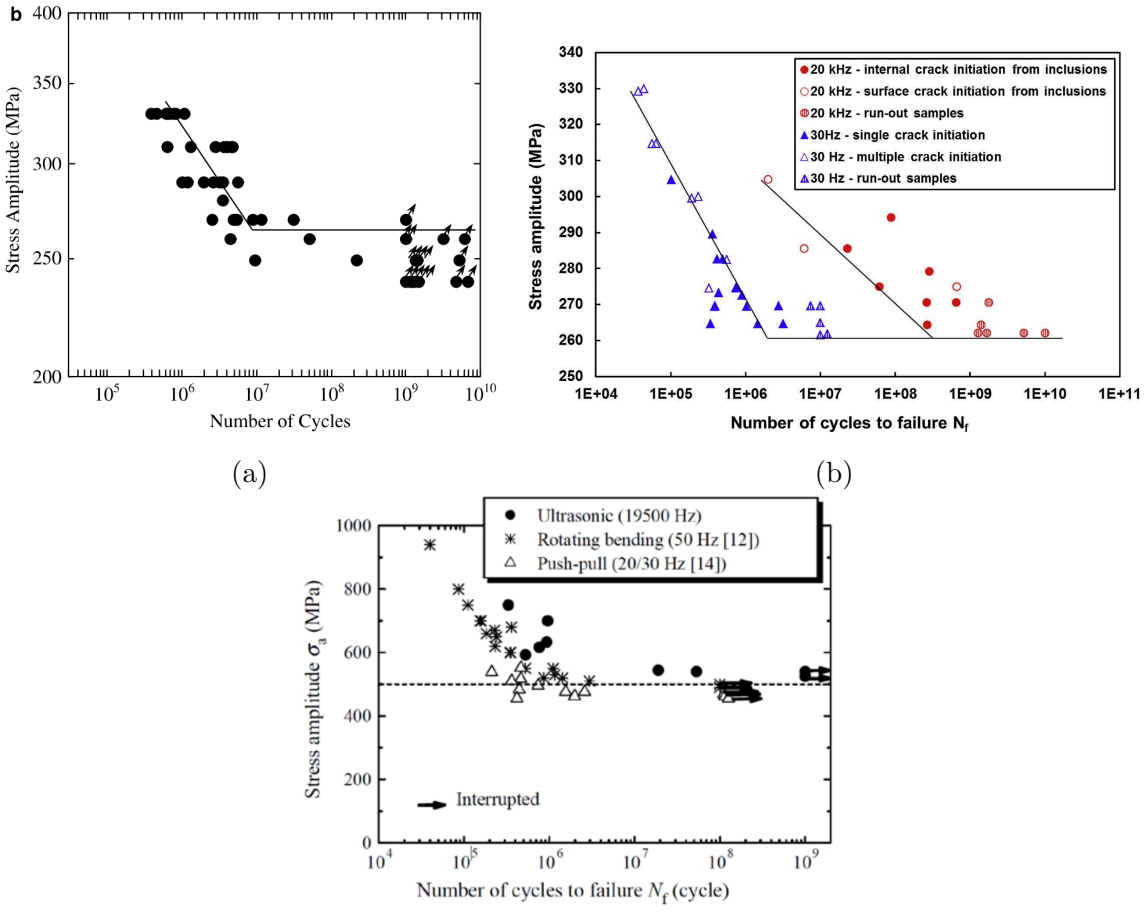


FIGURE 1.9 – Experimental results of SN diagrams reaching a plateau after $10^6/10^7$ cycles for a) low carbon steel [Zettl et al., 2006], b) dual phase steel (DP600) [Torabian et al., 2017] and c) inconel 718 [Chen et al., 2005].

The SN diagrams built with conventional fatigue machines often reached a plateau around 10^7 cycles (see Fig. 1.5). According to the ASTM-E468 standard [ASM-E468, 2011], the horizontal asymptote close to 10^7 cycles is considered the "fatigue limit" of the material. The standard states that a test conducted at a stress amplitude inferior to this limit would never lead to failure. This concept of infinite life can not be verified expe-

rimentally because an infinite life length has no experimental meaning. Instead, fatigue tests must be conducted to very high fatigue lives to study the VHCF domain and obtain crucial information on the fatigue behavior of materials in this domain. In some cases, SN diagrams can show a plateau corresponding to a prolongation of the concept of a horizontal asymptote in the VHCF domain, up to fatigue lives of 10^{10} cycles. Some examples are provided in Figure 1.9 for low carbon steel, dual phase steel (DP600) and inconel 718. In the case of Fig. 1.9a, compared to Fig. 1.9b and 1.9c, the plateau is not influenced by the log scale.

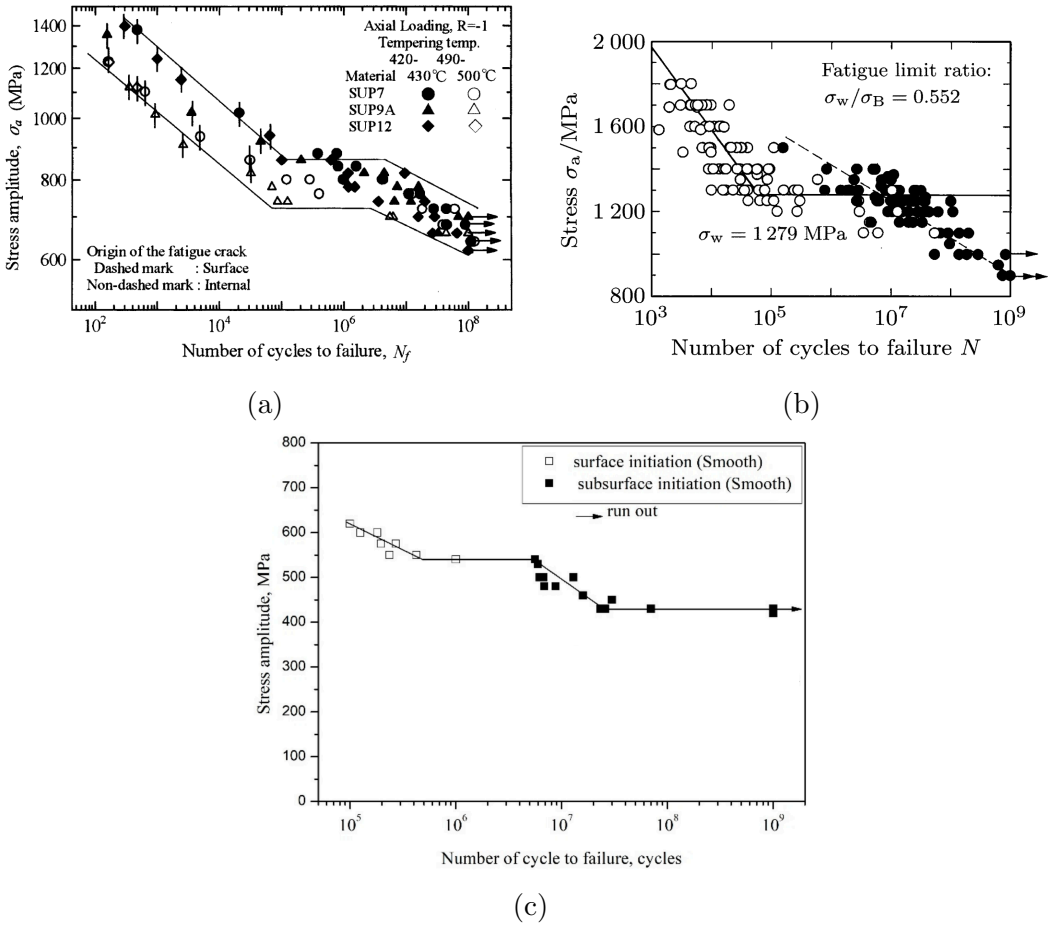


FIGURE 1.10 – Experimental results of SN diagrams showing a decrease after a horizontal asymptote a) high-strength steel [Furuya et al., 2002], b) high carbon steel [Wang et al., 2012] and c) titanium alloy TC21 - adapted from [Baohua et al., 2018].

Notwithstanding, several materials do not show a prolongation of the horizontal asymptote. Failures happen for fatigue life in the VHCF domain and stress below the horizontal asymptote that is identified around 10^7 cycles. It means that the concept of fatigue limit, as an extrapolation of the horizontal asymptote identified from an SN

diagram, is experimentally proved wrong as a unifying criterion. Figure 1.10 shows SN diagrams exhibiting a decrease after horizontal asymptote for high-strength steel, high carbon steel and titanium alloy TC21. The log scale seen on Fig. 1.10a, compared to Fig. 1.10b and 1.10c, slightly understated the SN shape to make the plot clearer.

1.3 Fatigue design from interrupted tests

Experimental small-scale tests can be emphasized by complementary measurements to follow the evolution of the temperature of the tested specimen. Such methodology corresponds to the third fatigue design methodology presented in Section 1.1.2.

1.3.1 Thermographic approaches

When a material is subjected to a cyclic loading, its temperature raises. This phenomenon is called self-heating and corresponds to the activation of heat sources in the material. The increase of the temperature increment[5] can be measured at the surface of the fatigued specimens by using either thermocouples fixed on the specimen's surface or an InfraRed (IR) camera to measure a temperature field. Figure 1.11 provides a schematic representation of the self-heating phenomenon in the case of a dual phase steel [Boulanger, 2004, Doudard et al., 2010, Munier et al., 2014].

During a fatigue test, the temperature evolves in two ways. It evolves in a reversible manner during one cycle, and the mean temperature increases over several cycles [Berthel et al., 2008]. The reversible evolution of the temperature during one cycle is associated with thermo-elasticity. It is reported as the sinusoidal evolution of temperature in the bottom left of Figure 1.11 and corresponds to the reversible dilatation of the material. The increase of the mean temperature is associated with dissipative heat sources that are always positive and cumulative with each loading cycle. Generally, the temperature increment stabilizes after a certain time and reaches a plateau.

The temperature increment depends on the loading amplitude. As shown in Figure 1.12 in the case of an aluminum alloy, the higher the stress amplitude, the higher the temperature increment increase. However, in the event of failure of the tested specimen, the temperature increment increases strongly when the fatigue crack propagates. It is shown in Fig. 1.12 for the aluminum alloy that failed at a stress amplitude of 55 MPa. In the case of failure, the temperature at the surface of the specimen becomes spatially heterogeneous, i.e. the temperature is higher at the location of the fatigue crack.

5. The temperature increment is noted θ. It corresponds to the difference between the temperature of the specimen at a given time and its initial temperature before the loading.

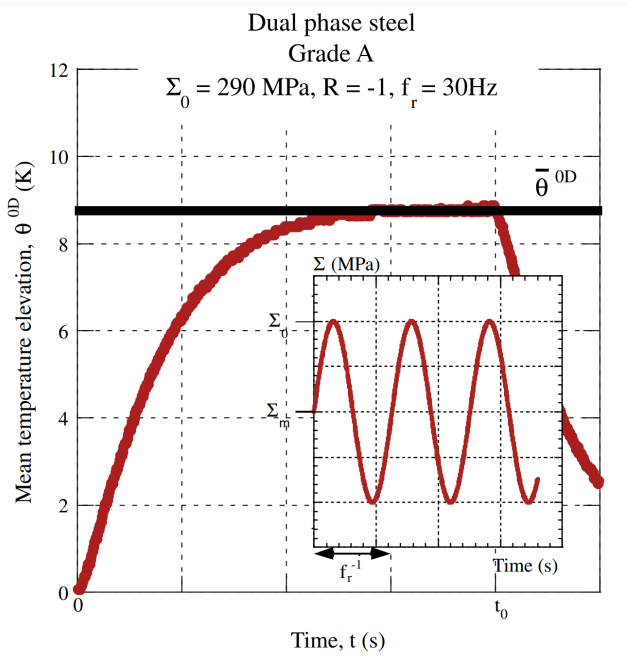


FIGURE 1.11 – Evolution of the mean temperature elevation during a short interrupted fatigue test [Munier et al., 2014].

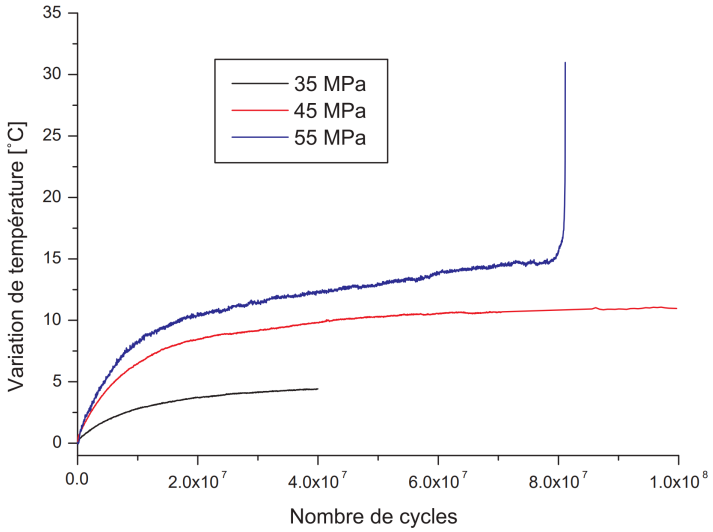


FIGURE 1.12 – Self-heating curves of an aluminum alloy specimen for three stress amplitudes.

It is worth noting that a fatigue test conducted at high frequency will induce a higher temperature increase per unit of time [Blanche et al., 2015, Favier et al., 2014]. Indeed, for very low-stress amplitudes applied (of about 10% of the yield stress associated with

the VHCF domain) quantifiable temperature increments can be detected with a sufficient signal-to-noise ratio when the fatigue loading is conducted at ultrasonic frequencies (in the order of 20 kHz) [Ranc, 2014].

Self-heating curves are plotted for loading sequences conducted at different stress amplitudes. A temperature increment associated with one loading condition is measured when the temperature has reached a stabilized value during the test. Several tests are conducted, leading to a plot showing the evolution of the temperature increment with respect to the stress amplitude. [Luong, 1995] was the first to propose a method to use this type of curve to experimentally determine the fatigue limit of materials. Figure 1.13 shows the abovementioned curve in the case of an XC55 steel specimen.

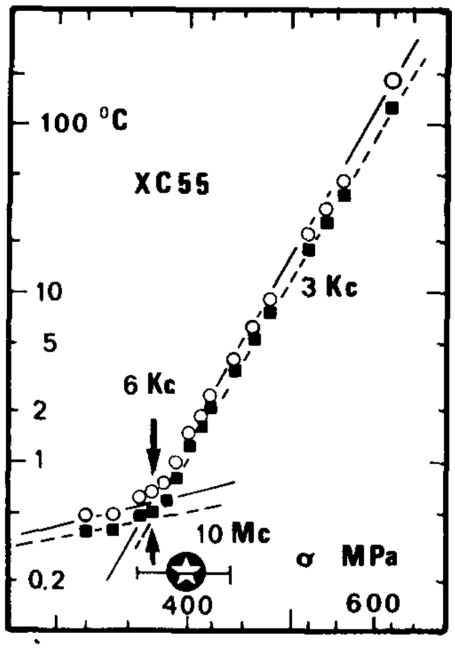


FIGURE 1.13 – Self-heating temperature increase for an XC55 steel. The fatigue limit is determined from the interception of the asymptotes of both regimes in the temperature evolution ; adapted from [Luong, 1995].

When plotted in a semi-logarithmic scale, the temperature increment exhibits two increasing slopes with respect to the stress amplitude. The first slope corresponds to a low increase in temperature and the second slope shows a sharp increase in temperature. The sharp increase is believed to be associated with plasticity which starts to appear in the material. [Luong, 1995], [Luong, 1997], [Rosa and Risitano, 2000] defined (in an arbitrary way) the fatigue limit as the intersection between the two slopes. This methodology works for several materials, but particularly for high strength or dual phase steels [Doudard et al., 2005].

Such methodology is interesting as it enables to only load from one to three specimens with conventional fatigue machines, working in the range of 30 Hz, to provide an estimate of the fatigue limit of a material in a few hours.

[Munier et al., 2014] has shown that this method gives good results to estimate the fatigue limit for a large variety of steels whereas [Krapez et al., 2000] has shown that the self-heating method gives an underestimation of the fatigue limit in the case of the stainless steel 316L under a tension–tension cyclic loading.
Besides, inconsistencies were found between the fatigue limit determined from self-heating measurements and the fatigue limit determined by an SN diagram, respectively on DP600 steel [Torabian et al., 2016] and pure copper polycrystalline [Phung, 2012].
Additionally, the results found using the thermographic methods based on the two tangent slopes of the temperature increment increase are strongly dependent on the way the tangents of the slopes are defined and on the number of points gathered to plot the curve. Indeed, the number of points to plot a self-heating curve is commonly small, in general less than twenty according to the results found in the literature. Thus, the accuracy of the slope computation might not be guaranteed.
For aluminum alloys, for instance, the temperature increments are very weak and it is difficult to distinguish the two regimes of temperature increment increase leading to a difficult estimation of the fatigue limit [Krapez et al., 2000]. Additionally, for a given stress amplitude, the temperature evolution of aluminum alloys does not reach a stable regime and the self-heating curve becomes complex to plot [Wagner et al., 2012].

The previous paragraph corroborates the fact that the temperature evolution is difficult to interpret. It can be influenced by the surrounding environment (i.e. by conduction and convection) and does not directly allow to study the sole contribution of the material behavior to the increase of the temperature increment. It is thus difficult to consider the temperature evolution to determine the fatigue limit as such evolution is not only correlated to the fatigue damage.

1.3.2 Estimation of the dissipated energy

The fatigue behavior of the material can not be directly deduced from the self-heating data, and it would be preferable to base the estimations directly on the heat sources that activate in the material [Doudard et al., 2010], [Connesson et al., 2011a], [Blanche et al., 2015], [Favier et al., 2014], [Crupi et al., 2016], [Furuya, 2019].

To estimate the heat sources, an inversion of the heat equation is used. It considers the measurement of the temperature increment (presented in the previous section) as an input. When conducting such estimation, the main difficulty comes from the noise observed in the temperature measurement which can induce instability in the inversion

of the heat equation. This instability is due to the differential operators involved in this inversion, i.e. the derivative of the temperature with respect to time and the second derivative of temperature with respect to the spatial coordinates. Some adapted solutions, such as filtering of the data, can be found in the literature [Ranc et al., 2015].
Besides, the heat equation in three dimensions is generally too complex to be used directly and several hypotheses must be found to employ a simplified form of the heat equation, as discussed in [Boulanger, 2004, Blanche et al., 2015]. It allows one to conduct the estimation with a 1-Dimension heat equation (or even a 0-Dimension heat equation [Jongchansitto et al., 2019]), considering that the heat sources are homogeneously distributed along the section of the specimen.
As mentioned previously, the heat sources can be either thermo-elastic or dissipative. The thermo- elastic sources are believed to be null over one loading cycle (see previous section). On the contrary, the dissipative sources are associated with the intrinsic dissipation and are related to the viscoelastic and plastic behavior of the material [Boulanger, 2004].

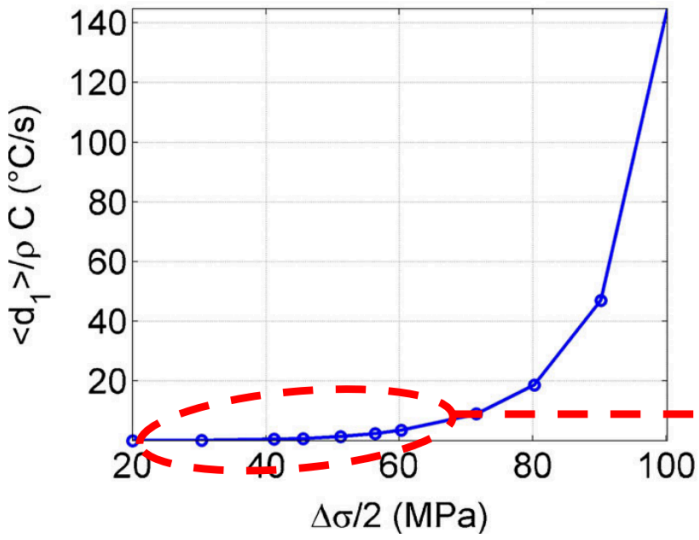


FIGURE 1.14 – Intrinsic dissipation computed from temperature measurements conducted at the surface of the specimen - polycrystalline copper [Blanche et al., 2015].

During an ultrasonic fatigue test, the time integration with an infrared camera corresponds, at best, to twenty cycles and do not allow observation of the thermo-elastic source. This is not a problem as these sources are reversible and does not dissipate any energy [Boulanger, 2004]. However, the average intrinsic dissipation (associated with the energy dissipated as heat) that would occur during many cycles can still be estimated. Figure 1.14 shows the evolution of the intrinsic dissipation measured during ultrasonic fatigue tests conducted on polycrystalline copper. The shape of the evolution of the

intrinsic dissipation is generally quadratic.

The abovementioned determination of the heat sources is conducted macroscopically, at the scale of the specimen. To understand the link between the heat sources and the fatigue damage mechanisms taking place in the matter, scale transitions micro-macro models are required [Mareau et al., 2012]. Figure 1.15 shows the evolution of the intrinsic dissipation per cycle with respect to the stress ampltiude. Mareau shown that the dissipative mechanisms are different depending on the stress amplitude [Mareau et al., 2009]. In fact, the material behavior is seen to transition from an anelastic to an inelastic regime. Both notions can be defined as follows [Maquin and Pierron, 2009] [Mareau et al., 2012] :

- For low-stress amplitudes, in the anelastic regime, the dissipation is independent on the loading ratio and is due to an anelastic mechanism, i.e. the strain is irreversible but recoverable from a mechanical point of view. It corresponds to no fatigue damage and no microstructural change of the material [Golovin, 2008, Torkabadi et al., 2016].
- For high-stress amplitudes, the dissipative mechanism is inelastic, i.e. the strain is irreversible and unrecoverable. It is associated with microstructural changes occurring in the material and possibly to fatigue damage starting to form [Szczepiński, 2001].

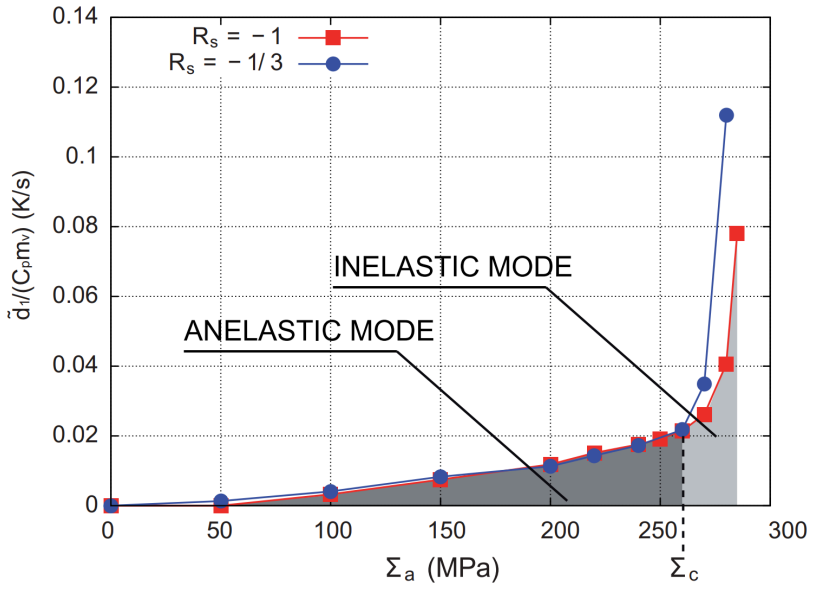


FIGURE 1.15 – Experimental self-heating curves, namely average intrinsic dissipation per cycle versus stress amplitude, obtained for a ferritic steel for different loading ratios [Mareau et al., 2012].

Although the high potential of the estimation of the dissipative sources to determine the fatigue behavior of metallic materials, the method is also sensitive to the applied

process. It might depend on the fatigue testing conditions, the environment and the material state ; it may also depend on the order of the loading steps conducted (with an increasing or decreasing stress amplitude) [Maquin and Pierron, 2009]. According to [Chrysochoos et al., 2008], a specimen that has already been loaded, even at lower stress than the current applied stress, will dissipate less energy (at a macroscopic scale) than the unloaded one. This suggests that the history of fatigue loading should be taken into account for tested specimens with methods based on temperature measurements.

In consequence, the correlation between the involved damage mechanisms and the evolution of the dissipation is not completely understood [Lebedev, 1999] [Favier et al., 2016]. The estimation of dissipated energy is a convolution of visco-elasticity (anelasticity) and micro-plasticity (inelasticity) contributions [Maquin and Pierron, 2009]. Those contributions are unequal, which induces the interpretation of dissipated energy estimation to require the be completed with models at the microscopic scale [Maquin and Pierron, 2009] [Ghuzlan, 2001].

1.3.3 Stored energy as a marker of fatigue damage ?

The focus is now directed toward the stored energy. This energy is suposed to be representative of the microstructural changes occurring in the material during a cyclic loading, referred to as fatigue damage [Wauthier-Monnin et al., 2015].

Historically, it has been decades since which stored energy is estimated in metallic materials to account for microstructural changes [Clarebrough et al., 1952]. Two methods have been identified to estimate the energy stored in materials owing to their deformation. The first one relies on the comparison between calorimetric measurements of the heat released when heating at a very high temperature a deformed sample and an annealed sample. The second one is based on the computation of the difference between the mechanical work provided to deform the material and the energy dissipated as heat during the deformation.
Previous works by [Farren and Taylor, 1925], [Quinney and Taylor, 1937] present an application of the second methodology that is based on an energy balance computed from calorimetric measurements. It relies on the combination of the first and the second principles of thermodynamics ; equation 1.1 shows the complete formulation.

$$\underbrace{\int_{cycle} \rho \dot{e} dt}_{\rho \Delta e} = \underbrace{\int_{cycle} \sigma \dot{\varepsilon} dt}_{W_{mech}} + \underbrace{\int_{cycle} \rho C \dot{T} dt}_{\rho C \Delta T} - \int_{cycle} s_{the} dt - \underbrace{\int_{cycle} d_{int} dt}_{E_{diss}} . \tag{1.1}$$

where ρ is the density of the material and C is its specific heat energy, Δe is the specific internal energy, W_{mech} is the volumetric mechanical work brought to the material from the exterior, $\dot{T}$ is the temperature variation of the material between the begining and

the end of the cycle, E_{diss} is the volumetric energy dissipated in the material and s_{the} is associated with the heat source from thermo-elastic effects.

Notwithstanding, in the case of a fatigue loading conducted in the VHCF domain, this equation can be simplified into an unidimensional problem in the case of a transformation corresponding to one full loading cycle in the steady-state regime, see equation (1.2). The assumptions made to get this simplified expression are reported below [Chrysochoos et al., 2008, Ranc, 2014] :

- the thermo-elastic coupling source is considered fully reversible during one loading cycle, i.e. the mean value of the source over one cycle is null. Thus, the term associated with the integral of the thermo-elastic coupling sources during one cycle is neglected compared to the other terms.
- the temperature of the material increases during a fatigue loading but stabilizes in few thousands of cycles. Besides, it is believed not to significantly change during one loading cycle so that the calorific term is considered negligible compared to the other terms.

One can thus consider the simplified energy balance as :

$$E_{st} = W_{mech} - E_{diss}. \tag{1.2}$$

where E_{st} corresponds to the variation of specific internal energy (also referred to as stored energy).

[Clarebrough et al., 1952, Bever, 1973] studied the stored energy which they referred to as cold work energy. It is associated with microstructural changes obtained at low temperature, only by applying a mechanical load. The stored energy is known to increase with the applied strain or stress [Williams, 1964, Rönnpagel and Schwink, 1978]. Besides, the energy that is stored in the material increases with an increasing dislocation density [Bailey, 1963, Bever, 1973, Ungar et al., 1984] [Benzerga et al., 2005] [Čebron and Kosel, 2014] [Chen et al., 2019]. It is worth noting that no work was conducted to determine the energy that corresponds to a given arrangement of dislocations but only a correlation between dislocation density and stored energy was determined through Discrete Dislocation Dynamics [Manole et al., 2009].

The stored energy was estimated experimentally during fatigue tests in a few works. Tables 1.1 and 1.2 provide the results that were reported in the literature. The two tables report respectively the cumulative stored energy and the stored energy per cycle. Such measurements were only conducted in LCF and at low-frequency to obtain a sufficient time resolution[6] on the estimation of the stored energy.

6. The time resolution is limited by the sampling frequency of the apparatus that are used to assess the mechanical work and dissipated energy during each cycle of the fatigue test.

TABLE 1.1 – Cumulative stored energy estimated experimentally on polycrystalline materials from fatigue tests.

Reference	Material	Strain/Stress amp.	N_{cycles}	E_{st} $(J.m^{-3})$
Clarebrough et al., 1957	Copper	172MPa	2.5×10^4	4.5×10^6
		69MPa	10^6	1.13×10^6
Martins et al., 2020	Bainitic steel	0.006	10^4	1.08×10^{10}
		0.008	10^4	1.49×10^{10}
		0.01	10^4	1.65×10^{10}
Connesson et al., 2011b	Low carbon steel	85MPa	10	0.4×10^4
		”	60	1.95×10^4
		”	120	3.5×10^4

TABLE 1.2 – Stored energy per cycle estimated from experimental measurements on polycrystalline materials. SMA = Shape Memory Alloys.

Reference	Material	Strain/Stress amp.	N_{cycles}	E_{st} $(J.m^{-3}.cycle^{-1})$
Martins et al., 2020	Bainitic steel	0.007	150	6.6×10^6
		0.007	10^3	$6. \times 10^6$
		0.01	150	13.5×10^6
		0.01	10^3	12.6×10^6
Zhang et al., 2019	NiTi SMA*	473MPa	<1	3×10^6
		”	10	1×10^6
		”	50	0
Seelan et al., 2020	316L steel	150	1	0.7×10^4
		”	10	1.5×10^4
		”	30	3.2×10^4
		”	100	0.8×10^4
		”	300	0.3×10^4
Jirandehi and Khonsari, 2020	Al. 7075-T6	330MPa	150	4.7×10^3
		510MPa	/	5.4×10^5
	Steel AISI 1018	410MPa	/	2×10^5
		425MPa	/	3.45×10^5
Hu et al., 2021	Al. alloy LY12	359	/	3.28×10^4
		584MPa	/	5.36×10^6
	Al. alloy LC9	383MPa	/	3.48×10^4
		589MPa	/	5.52×10^6

From the results displayed in table 1.1, it is seen that the cumulative stored energy increases with the number of cycles applied to the specimen Connesson et al., 2011b. It

also increases with the stress amplitude [Clarebrough et al., 1957, Martins et al., 2020]. In Table 1.2, two tendencies are observed. The energy stored per cycle increases with the stress amplitude [Martins et al., 2020, Jirandehi and Khonsari, 2020]. Martins even reported an increase in stored energy per cycle when a fatigue crack is starting to propagate.

The energy stored per cycle also decreases with the number of cycles [Zhang et al., 2019, Martins et al., 2020]. The explanation for this observation would be that the stored energy saturates after a certain number of cycles for a prescribed stress amplitude [Seelan et al., 2020]. An example of this behavior is shown in Figure 1.16 in the case of a shape memory alloy loaded during 60 cycles.

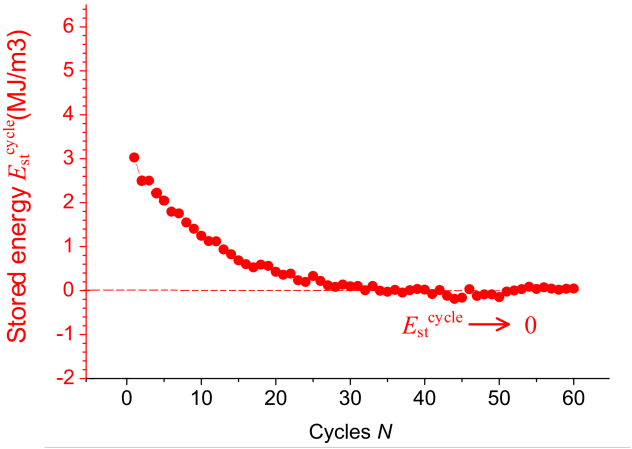


FIGURE 1.16 – Evolution of stored with respect to the number of cycles - case of a shape memory alloy loaded in LCF [Zhang et al., 2019].

1.3.4 Conclusion of the section

In this section, the methodologies based on the use of small-scale fatigue machines were reviewed. It appeared that SN diagrams are a powerful tool to determine experimentally the fatigue properties of metallic materials. This methodology comes with a counterpart that numerous fatigue tests must be carried out inducing a time-consuming construction of SN diagrams, especially when studying the VHCF domain. The methodology based on energy measurements during short interrupted fatigue tests is in turn of great interest as it could help to reduce the duration of the determination of fatigue properties of metals. The methodologies based on the estimation of dissipated or stored energy are both based on the estimation of a quantity that is an image of what happens in the material. The understanding of their evolution is only possible through simulations or additional characterization.
In this work, stored energy is believed to be more representative of the fatigue damage occurring in the material during a cyclic loading and its interpretation is considered easier. Unfortunately, very few results were reported in the literature to discuss the stored energy evolution during a fatigue loading.

1.4 Mechanisms of fatigue damage

The origin of the initiation of fatigue failure in crystalline materials is commonly related to some sort of slip irreversibility in the bulk that leads to unreversed microstructural evolutions. The accumulation of small irreversible microstructural evolutions observed during each loading cycle will ultimately form damage[7] [Mughrabi, 2006]. The significance of slip irreversibilities, their origin, magnitude and how they contribute to fatigue damage must be investigated in order to relate the slip irreversibilities to the fatigue life of metals. The microstructural mechanisms responsible for fatigue damage in the HCF and VHCF domain both arise from cyclic slip irreversibility but do not rely on the same microstructural mechanisms.

This section is split into two parts. The first part recalls the basics of the fatigue crack initiation mechanisms taking place for loadings in the HCF domain and introduces the notion of cyclic slip irreversibility, which is at the root of fatigue damage initiation in both HCF and VHCF domains. The second part is dedicated to the presentation of the microstructural mechanisms that are representative of the VHCF domain.

1.4.1 Fatigue damage mechanisms in the HCF domain

1.4.1.1 Cyclic slip irreversibility

Cyclic slip irreversibilities are associated with any outbreak of plasticity as a microstructural or physical change in the material. Cyclic slip irreversibility was quantitatively defined as the fraction p of irreversible plastic shear strain (in a microstructural sense), referred to the total plastic shear strain [Mughrabi, 2009, Mughrabi, 2013]. This quantity is thus expected to depend on the plastic strain amplitude and it is commonly consider that $0 \leq p \leq 1$. Estimates of p are not easily obtained. Few experimental assessments were possible by using atomic force microscopy [Risbet et al., 2003] or electronic microcopy [Weidner et al., 2010]. The p parameter can vary from 10^{-1} (measured in a PSB) for loadings in the HCF domain of FCC[8] metals, down to 10^{-5} for pure copper loaded in the VHCF domain after more than 10^{10} cycles [Mughrabi, 2009] [Mughrabi, 2015]. In consequence, the lower the stress (or plastic strain) amplitude, the smaller p and the higher the fatigue life. The p parameter could have been used to predict the number of cycles to failure but the difficulty arising to conduct an estimation of this parameter made this technique not viable for industrial applications. Few microstructural mechanisms, that can be associated with cyclic slip irreversibilities in the sense that forward

7. Fatigue damage is associated with the appearance of micro-cracks in the material.
8. Face Centered Cubic (crystallographic structure).

and reverse glide of dislocations do not occur along identical paths, were brought to light by [Mughrabi, 2009] :

- cross-slip of screw dislocations in the case of body centered-cubic (BCC) metals, implying that forward and reverse glide of dislocations do not occur on the same slip planes. Cross-slip events are estimated to have higher chances to happen for higher stress amplitudes but can occur for stress amplitudes of few tens of MegaPascals in copper [Bonneville and Escaig, 1979] [Couteau et al., 2011]) ;
- mutual annihilation of unlike screw and unlike edge dislocations : whenever a dislocation is annihilated, this marks the end of its glide path, implying that reverse deformation cannot occur along the same glide path ;
- so-called slip plane asymmetry in the case of bodycentered-cubic (bcc) metals : in this case, forward and reverse glide of dislocations occur on different glide planes in tension and compression ;
- random to and fro glide of dislocations.

Irreversibilities can only occur if the applied stress is sufficient. Namely, dislocations starts to move when the nominal stress applied is in the order of 0.2 MPa, in pure copper [Peierls, 1940, Nabarro, 1997]. The chance for a dislocation to induce an irreversible change in the microstructure of the material is also increased as soon as the applied stress is high enough to trigger the Frank-Read mechanisms responsible for dislocation multiplications. It corresponds to a nominal stress higher than 5 MPa in copper [Madec et al., 2000] and 32 MPa in steel [Callister, 1994]. For higher stress amplitudes, the formation of irreversible dislocation structures strongly contributes to the cyclic slip irreversibilities happening in the material.

To put it simply, the irreversible character of the movement of dislocations enables one to understand the microstructural mechanisms that are responsible for damage initiation in the HCF but also in the VHCF domains. In the VHCF domain, cyclic slip irreversibilities can be accumulated for a very high number of cycles until a micro-crack initiates.

1.4.1.2 Dislocation structures and Persistent Slip Bands (PSB)

In fatigue, and for the first cycles of loading, the plastic strain amplitude evolves when the stress amplitude is imposed. In a reversed way, the stress amplitude evolves when it is the plastic strain that is imposed. This corresponds to cyclic softening or hardening, depending on whether the material is annealed or has been pre-deformed. The cyclic loading generally stabilizes after a few cycles. The stress and strain amplitudes of the loading are measured on the stabilized cyclic stress-strain curve.

The so-called cyclic stress-strain curve (CSSC) was presented by [Li et al., 2011]. It

was built in the case of a pure copper single crystal (whose orientation corresponds to the activation of a single glide system of dislocations). This curve, shown in Figure 1.17, plots the resolved shear stress amplitude (measured along the crystallographic direction of the studied crystal) with respect to the plastic resolved shear strain that is imposed. Both quantities were measured when the loading was stabilized (i.e. after the eventual softening/hardening). Micrographs from the work of [Woods, 1973], [Winter, 1974], [**?**] and [Cheng and Laird, 1981] are represented to illustrate the corresponding dislocation structures that develop at each range of plastic resolved shear strain.

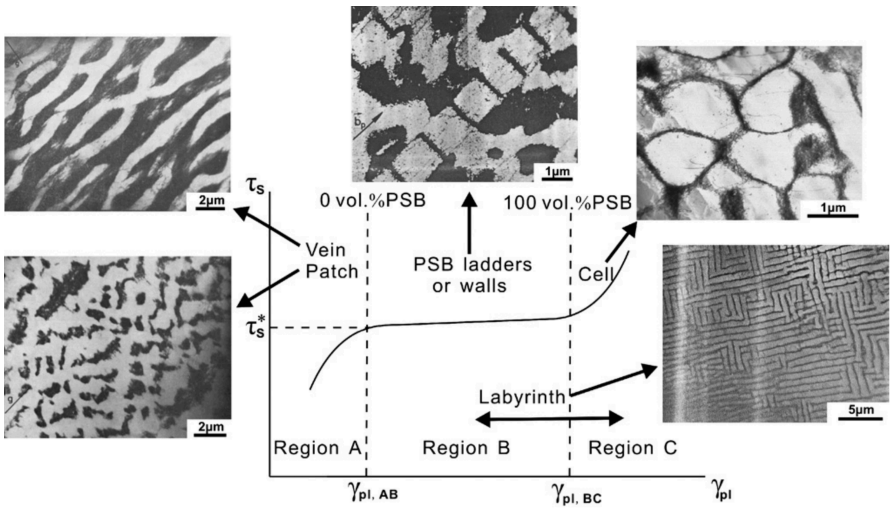


FIGURE 1.17 – Cyclic stress-strain curve with associated dislocation pattern in 3 stages (with a plateau at which PSBs are forming) - case of a copper single crystal [Li et al., 2011].

Three regions are identified on this curve :

- Region A : is characterized by plastic resolved shear strain inferior to $\gamma_{pl,AB} = 6 \times 10^{-5}$. For an increasing plastic strain amplitude, the measured resolved shear stress increases as well. In this domain, screw dislocations will annihilate whereas edge dislocations of opposite signs are trapped in dipolar configurations called "patches" [Buchinger et al., 1985]. These patches are separated by regions of low dislocation density called channels. The combination of channels and loop patches is referred to as "veins" structure [Mughrabi, 2015]. Figure 1.18a shows a schematic representation of this type of structure. Between the patches, screw dislocations can glide freely. To minimise the internal energy of the crystal, dislocations of opposite signs rearrange along a Taylor network oriented at 45° of finite size [Neumann, 1986]. This region corresponds to fatigue loading representative of the VHCF domain. When a "veins" structure is subjected to a fatigue loading, the distance between two dislocations will increase under the positive part of

the cyclic loading and come back to its initial value during the unloading. It is worth noting that [Shih et al., 2010] also reported similar dislocation structures in steels.

- Region B : is marked-out by plastic resolved shear strain that are higher than $\gamma_{pl,AB} = 6 \times 10^{-5}$ but lower than $\gamma_{pl,BC} = 7.5 \times 10^{-3}$. It is characterized by a plateau at which the resolved shear stress is independent of the plastic strain applied. The plateau corresponds to a plastic resolved shear stress $\tau_s^* = 28\,\text{MPa}$ along the activated glide system [Mughrabi, 1978, Buchinger et al., 1985]. The dislocation structures observed in region B have a ladder-like structure. This type of structure is referred to as "persistent slip bands" (PSB)[9]. The formation of PSBs is conditoned by the stability of the "veins" structures. [Neumann, 1986] showed that from a certain stress amplitude (corresponding to region B), "veins" structures become unstable and start to break down locally and make room for dislocation walls to appear. [Buchinger et al., 1985] evidenced it with micrographs of the evolution of the veins into ladder-like structures. The walls are separated by zones of low dislocation density, as shown in Figure 1.18b. Such structure is even more stable than the "veins" structure. First observation of a ladder-like structure (constituted of walls and zones with low dislocation content) was conducted by [Laufer and Roberts, 1964]. Region B is particular as it corresponds to the cohabitation of PSB that lies within a "matrix" exhibiting a structure in "veins" or "patches". The dislocation density is strongly heterogeneous in these dual structure : it is concentrated in the PSB because they easily accommodate the plastic strain[10]. The plastic shear strain in PSB is estimated at 8×10^{-3} whereas it lies at 6.5×10^{-5} in the matrix. Consequently, the resolved shear strain remains constant in region B for an increasing plastic strain which corresponds to an increase of the volumic fraction of PSB in the crystal [Finney and Laird, 1975, Mughrabi, 1978]. This region is associated with the HCF domain as the damage initiation in HCF strongly relies on PSBs. The minimum loading at which PSBs occur is defined as the PSB-threshold. This threshold is estimated at 56 MPa in terms of axial stress amplitude and at 2.5×10^{-5} in terms of plastic strain amplitude [Essmann and Mughrabi, 1981].
- Region C : corresponds to plastic resolved shear strain larger than to $\gamma_{pl,BC} = 7.5 \times 10^{-3}$. The plastic strain increase also corresponds to an increase in the stress amplitude. This domain is characterized by the appearance of dislocation

9. [Thompson et al., 1956] evidenced that slip bands are persistent when they reappear at the exact same location when the material is fatigued again after the previously formed slip bands had been polished away.

10. It appears that dislocation density is also heterogeneous in PSBs as well, where dislocations are gathered in walls [Laird et al., 1981].

structures in "cells" and "mazes" [Llanes et al., 1993]. This region would be representative of the LCF domain.

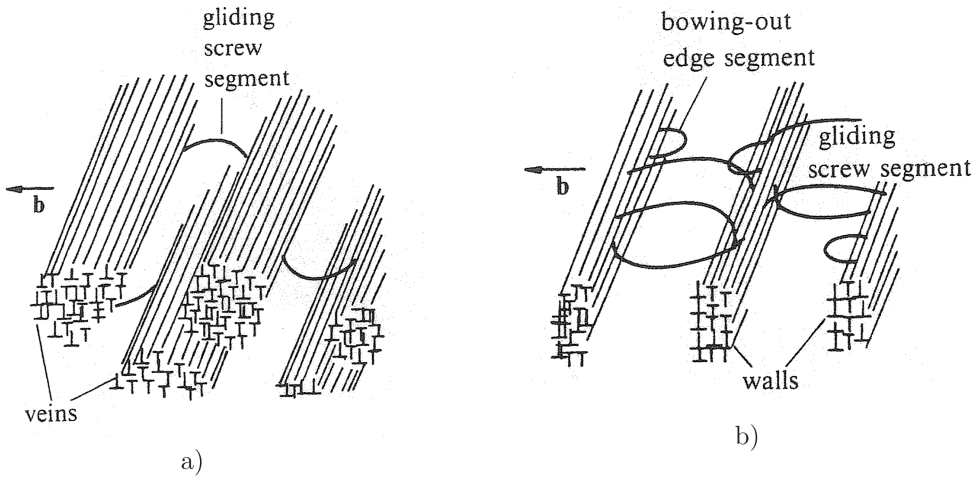


FIGURE 1.18 – Schematic representation of a) dslocation aggregates in veins (patches) structure and b) dislocation walls in PSB after [Haasen et al., 1980].

1.4.1.3 PSBs leading to fatigue failure in the HCF domain

The HCF domain corresponds to plastic resolved shear strain in the order of region B on Figure 1.17. At a sufficient plastic strain amplitude, and thus at a sufficient stress amplitude, PSBs appears in the material along the slip planes for which the plastic resolved shear strain is the highest. The plastic strain is concentrated in the PSBs and lead to a strong irreversible movement of the dislocations inside them. The dislocations that are highly mobile in the PSBs transmit the plastic deformation to the surface [Lukáš and Kunz, 2004]. When PSBs meet the surface, it leads to irreversible small steps/marches [Obrtlík et al., 1994] called slip markings. The cyclic character of the loading leads to an increasing surface roughening throughout the fatigue life. The accumulation of plastic strain at the surface generates extrusions (positive steps) and intrusions (negative steps). Extrusions formed by PSBs are produced by the diffusion of vacancies which was highlighted by [Essmann and Mughrabi, 1981] and retrieved by [Polák and Man, 2015]. In HCF, the surface of the tested material is generally covered with numerous slip markings whose heigth and width are increasing with the number of cycles [Stanzltschegg et al., 2007]. This cyclic contribution to slip markings induces an increase in the depth of intrusions. These intrusions act as critical stress risers (equivalent to a notch) at which fatigue micro-cracks initiate. In HCF, the fatigue limit is estimated to be twice higher than the PSB-threshold [Mughrabi, 2015]. This is explained

by the fact that the stress amplitude corresponding to the PSB-threshold is not sufficient to propagate the cracks that could initiate at the PSBs. It is the further development of PSBs that are responsible for fatigue failure in the HCF domain.

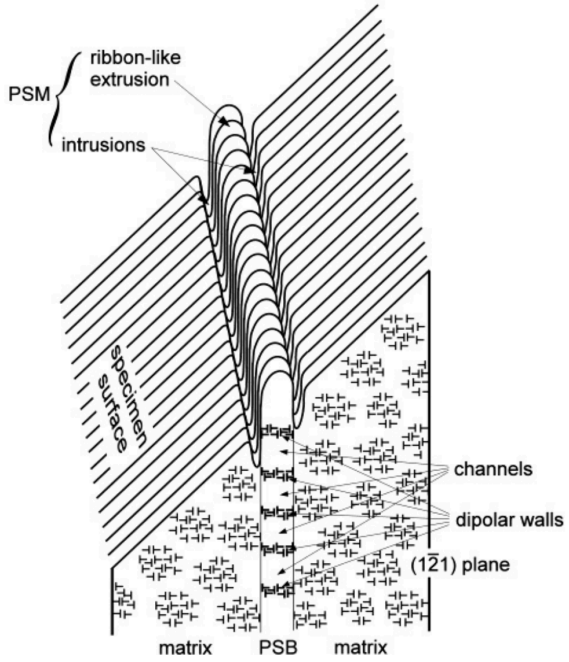


FIGURE 1.19 – Shape of predicted surface relief of an emerging PSB [Polák and Man, 2015].

1.4.2 Fatigue damage mechanisms in the VHCF domain

In the HCF domain, the fatigue failure originates at the roughening that is induced by slip markings through the emergence of PSBs at the surface of the material. In light of the experimental SN diagrams of various metals presented in Section 1.2.3, it was noticed that failure can occur in the VHCF domain, i.e. after 10^7 cycles for loading amplitudes below the horizontal asymptote characteristic of the HCF domain. A question remains for these failures occurring in the VHCF domain : does a failure occurring in VHCF necessarily originate from a PSB ? The answer to this question was found to be "no". Indeed, fatigue failures were found to occur even under the PSB-threshold but happen generally after a very high number of cycles in the VHCF domain because of accumulated slip irreversibilities [Stanzltschegg et al., 2007, Mughrabi, 2015]. The process of fatigue failure in the VHCF domain must thus be based on different mechanisms than in HCF. A first proposition was made by [Mughrabi, 2002] to classify the materials into two types

according to the behavior they exhibit in VHCF :

- Type I : are homogeneous materials and single phase alloys, that are ductile and do not contain precipitates or internal inclusions. It is the case of pure metals with face centered cubic structure such as copper.
- Type II : are metals and alloys with a heterogeneous microstructure, which have several phases and might also contain precipitates or internal inclusions. High-strength steels are an example of such materials.

Mughrabi proposed two SN diagrams to represent the fatigue behavior of materials of both types. The case of materials showing a horizontal asymptote that remains in the VHCF domain is not treated and simply corresponds to a prolongation of the HCF behavior for higher fatigue lives. As Mughrabi focuses on the cyclic irreversibility of the movement of dislocations, the SN diagrams are provided as Coffin-Manson plots with the plastic strain amplitude for the vertical axis instead of the stress amplitude.

1.4.2.1 Fatigue failure in VHCF for type I materials

Pure (polycrystalline) copper is the best example to illustrate type I materials. Figure 1.20 shows the evolution of plastic strain amplitude with respect to the number of cycles until failure. This curve is divided into four characteristic domains [Mughrabi, 2002] :

- domain "I" : is characteristic of the LCF domain for which the plastic strain amplitude is very high.
- domain II : is representative of the HCF domain, with the horizontal asymptote characteristic of the high scatter in fatigue lives. This domain is associated with the PSB-threshold [Lukás et al., 1974].
- domain "III" : corresponds to the domain that is below the PSB-threshold but still above the irreversibility threshold. This corresponds to the beginning of the VHCF domain where the fatigue life is longer than in HCF but not infinite.
- domain IV : is represented by a horizontal asymptote corresponding to an irreversibility threshold. It is considered that under this plastic strain amplitude, the deformation is reversible. It was thus considered that no irreversibility would lead to no fatigue damage and therefore that no fatigue failure would occur. However, this can not be proven experimentally.

Cracks initiated at plastic strain amplitude corresponding to domains "III" (i.e. in the VHCF domain) are propagating slowlier than in the HCF domain ; the focus will be made on this domain in this subsection [Stanzl-Tschegg and Schönbauer, 2010].

It was seen that dislocation structures can form at stress amplitudes lower than the PSB threshold. This underlines the existing plastic activity occuring in the material. To explain the mechanisms of fatigue crack initiation, Mughrabi [Mughrabi, 2006]

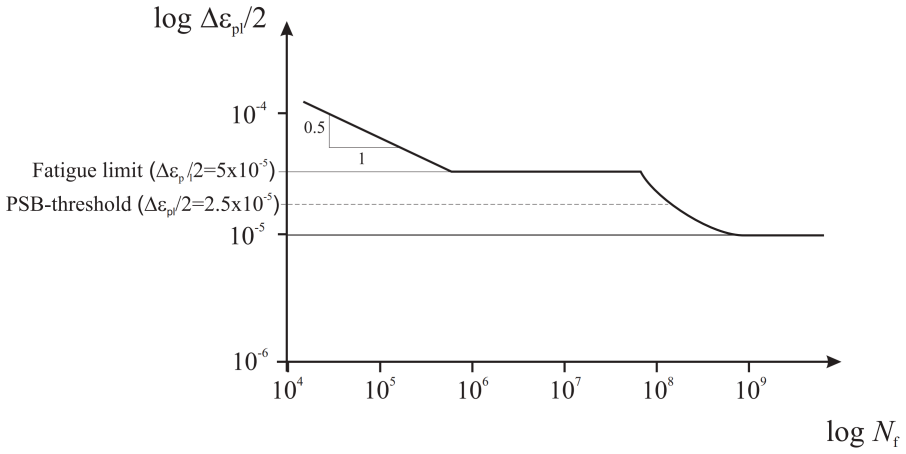


FIGURE 1.20 – Schematic representation of SN curve to explain the fatigue behavior of type I materials [Mughrabi, 2006].

proposed that the plastic activity evolves with the number of loading cycles to form a surface roughness which can also induce the initiation of a crack. However, in this case, the surface roughness (induced by prolonged slip markings) must reach a critical state [Mughrabi, 2006]. At this point, few valleys in the surface roughness profile can act as strong stress raisers if they are sufficiently steep. The local stress will thus locally exceed the PSB-threshold and PSB nuclei will be formed. Only a few PSB nuclei are formed in VHCF owing to the very localized plastic activity. The process is schematized in Figure 1.21. Such a PSB will only extend to a small depth into the material. Nevertheless, the cyclic strain starts to be localized in the PSB nuclei and the equivalent notch at which the PSB occurred will increase in depth with the increasing number of cycles. The depth increase will lead to the initiation of a fatigue micro-crack that could further propagate and lead to failure if the loading amplitude is high enough.

The typical slip markings of the VHCF domain, that are observed for low-stress amplitudes, are isolated and not numerous on the contrary to what can be observed in the case of higher stress amplitudes [Stanzltschegg et al., 2007]. This is associated with the orientation of the grains that is not favorable for all of them to activate a slip system and then provoke slip markings at the surface [Macdonald, 1976]. Thus, only a few grains exhibit slip markings. As the slip markings are more isolated in the case of a loading typical of the VHCF domain, this explains why a fatigue crack would initiate later than in the HCF domain [Stanzl-Tschegg and Schönbauer, 2010]. In fact, the larger the stress amplitude applied, the more intense and generalized the plastic activity.

To challenge the behavior proposed by Mughrabi for type I materials in the VHCF, Stanzl-Tschegg explored experimentally the irreversibility threshold evidenced by Mugh-

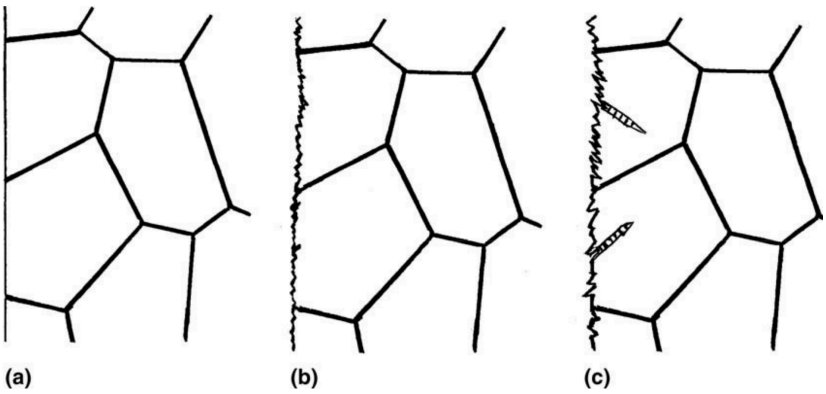


FIGURE 1.21 – Process of fatigue crack initiation at the surface in VHCF : a) initial state of the material, b) surface roughening and small intrusions forming and c) PSB nuclei forming at these steep intrusions [Mughrabi, 2006].

rabi in the case of a polycrystalline copper specimen loaded with an ultrasonic fatigue machine [Stanzltschegg et al., 2007]. Stanzl-Tschegg *et al.* identified a PSB-threshold in terms of plastic strain amplitude that is lower than the one expressed by Mughrabi. In fact, they detected early ladder-like structures that are associated with PSB precursors [Wang and Laird, 1988, Llanes et al., 1993] at plastic strain amplitude of 6.1×10^{-6} after 2×10^6 cycles (corresponding to an axial stress amplitude of 62.6 MPa). The difference between the PSB-threshold value found by Stanzl-Tschegg *et al.* (during tests at 20 kHz) and that found by [Mughrabi, 2015] (during tests at 0.15 Hz) was believed to be attributed to the very high frequency of the loading which could have led to a hardening that is more pronounced [Stanzltschegg et al., 2007]. However, [Buchinger et al., 1985] applied as well an ultrasonic fatigue loading to copper single crystal specimens and reported that PSB appeared for stress amplitudes similar to what was found by [Mughrabi, 2015] after 10^6 cycles. Consequently, the threshold reported by [Stanzltschegg et al., 2007] would be specific to polycrystalline copper and does not necessarily prove the findings of Mughrabi to be wrong.

Figure 1.22 shows the SN curve of pure polycrystalline copper on which are reported the first appearance of slip markings and PSB that are representative of the irreversible character of the cyclic deformation. The work of Stanzl-Tschegg evidenced that the appearance of PSBs is not only governed by a threshold. It is dependent on the number of cycles that are applied to the material and not only on the plastic strain (or stress) amplitude applied to the material. [Phung et al., 2013] confirmed that the lower the stress amplitude, the higher the number of cycles necessary to observe the earliest slip markings on the surface of the specimen. This result could explain the lower estimate of the stress value at which PSBs were first identified by [Stanzltschegg et al., 2007].

Even below the PSB-threshold, irreversible cyclic slip still operates and fatigue-induced slip band features were detected for stress (or plastic strain) amplitudes approximately 50% lower than the PSB-threshold level [Stanzl-Tschegg and Schönbauer, 2010]. In fact, slip markings were observed at stress amplitudes of 34 MPa after 10^{10} cycles. These slip markings do not exhibit the ladder-like structure that is typical of PSBs but still are a manifestation at the surface of the irreversibility of the deformation taking place in the bulk of the material [Phung, 2012].

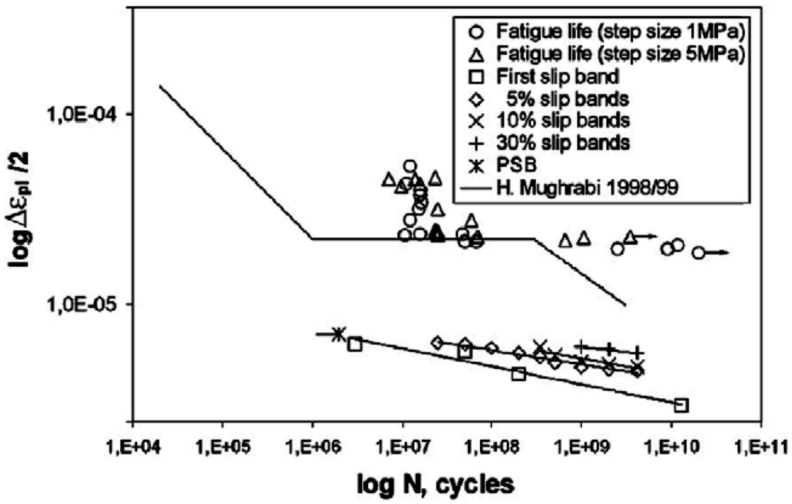


FIGURE 1.22 – SN diagram of polycrystalline copper fatigued with an ultrasonic fatigue machine in the VHCF domain. Appearance of first slip bands and PSB is reported on this curve [Stanzltschegg et al., 2007].

The appearance and the evolution (with the number of cycles) of the slip markings in the VHCF regime for a wide range of stress amplitude from 38 to 115 MPa in the case of polycrystalline copper was studied by [Phung et al., 2013]. The fatigue loading was conducted with an ultrasonic fatigue machine working at 20 kHz. Three types of slip markings were identified : type I, type II and type III. They differ in their morphology and their location within the microstructure. Figure 1.23 shows an example of the three types of slip markings. The three types of slip markings were identified as persistent because they reappeared at the same site when fatigue was resumed after the surface was electropolished.

Slip bands of type I are typically formed of tens of bands that are straight, long and parallel. They are generally entirely crossing grains in which they appear. Type II slip bands are long and straight but are generally isolated which differentiates them from type I bands. Type II bands appear generally along grain boundaries. Type I and II slip bands are exhibiting approximately the same height. The third type of slip bands (type III) have a smaller height but are constituted of an ensemble of fine bands that

are very close to each other. These slip bands are very localized and usually appear close to grains or twins boundaries. This observation is corroborated by the findings of [Llanes and Laird, 1992], [Peralta et al., 1999]. Slip bands close to type II were reported by [Obrtlík et al., 1994] and slip markings close to type III were evidenced by [Stanzltschegg et al., 2007] during ultrasonic fatigue loadings. Typically, slip markings of type III are generally attributed to fatigue loading at low-stress amplitudes (in the order of 34 to 57 MPa), in the VHCF domain and appear after very large number of cycles (namely above 10^8 cycles) [Stanzltschegg et al., 2007], [Phung, 2012]. In addition, type I and II slip markings that appear early (namely below 10^7 cycles) are gradually steeper with an increasing number of cycle [Phung, 2012], [Stanzl-Tschegg, 2017].

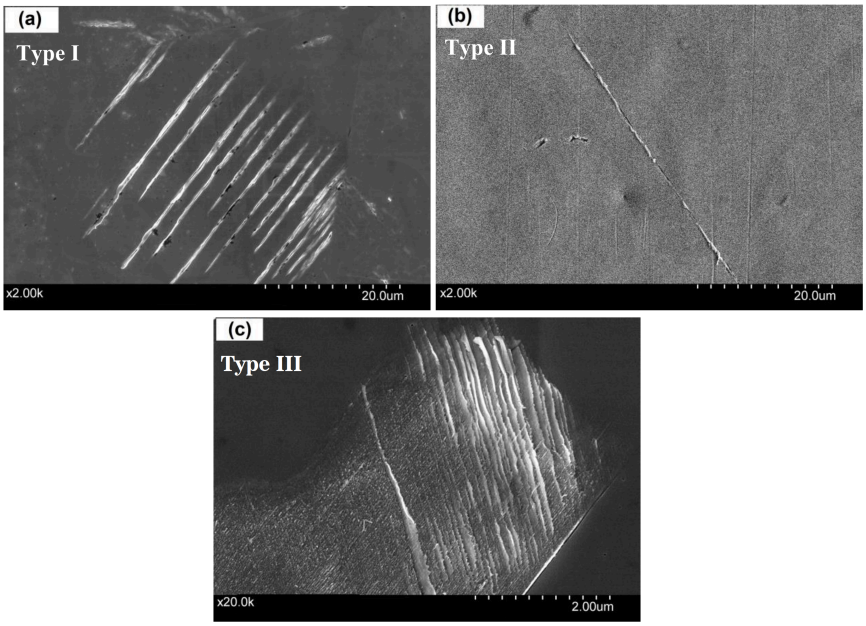


FIGURE 1.23 – Micrographs of the three types of slip markings observed on polycrystalline copper during fatigue loading : a) type I, b) type II and c) Type III [Phung, 2012].

The findings detailed above concerning the slip markings observed in copper under HCF and VHCF loadings demonstrate slip markings that are straight and sometimes appear at grain boundaries of the material. The study of other materials such as α-brass and α-iron loaded in the VHCF domain by [Favier et al., 2016] evidenced several conclusions. First, there is a threshold in stress amplitude above which slip markings are observed on the surface of α-brass and this threshold decreases for an increasing number of cycles. Also, the slip markings that are observed in α-brass are similar to those of copper whereas slip markings observed in α-iron are wavy and fully cover few grains. [Mughrabi et al., 1979], [Munier, 2012] reported similar observations of wavy slip

markings in α-iron. This wavy character was attributed to the cross-slip of dislocations that is easier in BCC metals [Favier et al., 2016].

1.4.2.2 Fatigue failure in VHCF for type II materials

The focus is now made on type II materials. Typical type II materials would be high-strength steel containing non-metallic inclusions. Figure 1.24 shows a schematic representation of the evolution of a multi-stage Wöhler-type S–N plot for this type of material. This curve is divided into four characteristic domains that are similar to those in the case of type I material. The transitions between the different ranges will of course not be sharp but gradual with some scatter and overlap. The most interesting feature of this work is attributed to the differentiation between surface and internal crack initiation. In the LCF (stage I) and HCF (range II), fatigue failures are initiated in most cases at the surface. The conventional "fatigue limit" associated with HCF (stage II) is also found for type II materials. The HCF regime is terminated with the onset of the VHCF (stage III) in which fatigue failures occur at stresses below the horizontal asymptote. For such fatigue failure, the cracks originate in most cases from internal defects. Consequently, Mughrabi proposed to estimate that at sufficiently low-stress levels, there might exist a true fatigue limit at which no fatigue failure will occur [Mughrabi, 2002, Nishijima and Kanazawa, 1999] which would correspond to stage IV.

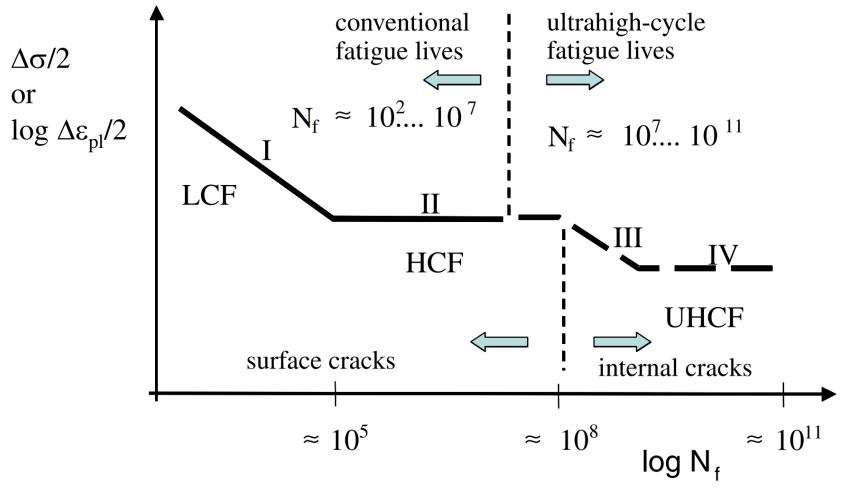


FIGURE 1.24 – Schematic representation of SN curve to explain the fatigue behavior of type II materials. Differentiation is made between external and internal fatigue crack initiation [Mughrabi, 2006].

Fatigue cracks often occur in the interior of type II materials subjected to fatigue loading characteristics of the VHCF domain. Such crack is generally found to initiate at in-

ternal stress concentration sites such as non-metallic inclusions or pores. The micro-crack initiation arise from the accumulation of dislocations corresponding to a strong localized plastic activity at these locations [Krupp et al., 2010, Bathias et al., 2013]. It was also observed that fatigue crack can initiate at grain boundaries or even at phase boundaries in the bulk of materials that do not contain non-metallic inclusions [Krupp et al., 2016, Tofique, 2016, Fu et al., 2021]. Even in VHCF, the plastic strain which is induced in the bulk of the material can also be high but then very localized. The dislocations interactions with microstructural barriers is decisive. If the dislocations meet soft barriers and can outcome them, they can then pursue their displacement. On the contrary, when they meet a strong barrier, such as grain boundaries, the dislocations accumulate and form dislocations pile-ups [Antolovich and Armstrong, 2014, Fu et al., 2021]. Figure 1.25 shows Transmission Electron Microscope (TEM) micrographs of dislocation pile-ups in the case of a duplex stainless steel subjected to fatigue loading in the gigacycle fatigue regime. The pile-ups induce a higher plastic activity and thus a higher strain at the grain (or phase) boundary. [Fu et al., 2021]. If the stress amplitude applied to the material is sufficient, the dislocation activity will induce a crack nucleation at the grain (or phase) boundary, in the VHCF regime (corresponding to stage III of Fig. 1.24). Stage IV in Fig. 1.24 would thus correspond to stress amplitudes at which dislocations are not accumulated enough at microstructural barriers or are not subjected to a sufficient plastic strain amplitude to lead to failure.

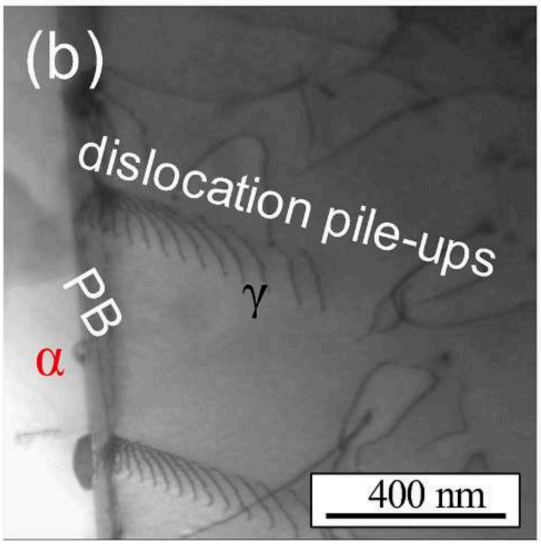


FIGURE 1.25 – Experimental observation of the dislocation structures characteristics of strain localization : dislocation pile ups at grain boundaries. Case of a duplex stainless steel subjected to 5×10^9 cycles at a loading amplitude $\Delta\sigma = 345$MPa [Fu et al., 2021]. "PB" stands for phase boundary.

1.4.3 Conclusion of the section

Cyclic irreversibility is a key factor to study the behavior of metals in HCF and VHCF domains. The irreversibility is usually characterized by the microstructural mechanisms that are activated at a certain level of plastic strain. These irreversibilities influence the localization of the plastic strain and can induce failure even at loading amplitudes below the PSB-threshold. Hence, a fatigue test conducted at a fatigue loading at which slip bands are created (but not PSB) might ultimately lead to failure but at a number of cycles that can't be reached experimentally. The cyclic slip irreversibility could have been a relevant parameter to determine the existence of a fatigue limit if only this parameter was easy to measure. Consequently, alternative investigations must be conducted to provide convenient and reliable methodologies to determine fast the fatigue properties of metallic materials, especially in the VHCF domain. The focus should still be made on the cyclic slip irreversibility but with an alternative manner to estimate its magnitude and progression under a fatigue loading.

1.5 Conclusion of the chapter

The industrial stakes, aiming at increasing the fatigue life of structures and components, require the use of powerful methodologies to determine accurately, reliably and rapidly the fatigue properties of materials. The behavior of metals when subjected to low-stress amplitudes and thus for very long fatigue lives (more than 10^7 cycles) must be understood to acquire a complete knowledge of the VHCF domain and design safer structures. Such methodologies were reviewed in this chapter. The focus was first made on SN diagrams. They constitute a powerful tool that is required to study the fatigue behavior of materials from experimental results and observations. However, such a design tool is limited when it comes to the study of fatigue lives above 10^{11} cycles. Indeed, experimental means can not provide results in test durations that are short enough, even when using ultrasonic fatigue machines. The focus was then directed towards alternative methodologies based on energetic measurements during short interrupted fatigue tests. The measurement of the dissipated energy is a convenient method to study the evolution of the behavior of fatigued materials but is not completely correlated with microstructural changes in the matter. The use of dissipated energy thus requires to model what happens in the material. Microstructural mechanisms occurring in a material loaded in the VHCF regime, namely at low-stress amplitudes, rely on the irreversibility of the dislocation movement leading to specific structures in which plastic strain is concentrated. This plastic strain accumulates during the cyclic loading, leading ultimately to the nucleation of a micro-crack. The stored energy accounts for such irreversibilities developing

in a cyclically loaded material. Thus, this quantity could be used to develop a criterion to allow the fast determination of the fatigue properties of metallic materials. The interpretation of stored energy evolutions compared to those of the dissipated energy are believed to be more suitable but still requires the use of modelisation to be completely understood.. Although its interesting potential, the estimation of this quantity remains a difficult task according to the very few experimental results found in the literature. Consequently, an innovative methodology to reliably estimate the energy that is stored in metals (even for fatigue loadings in the VHCF domain) is missing.

Chapitre 2

Contribution to the development of an experimental methodology to estimate the stored energy during fatigue tests at 20kHz

This chapter is devoted to the presentation of the contribution of this Ph.D. work to provide an experimental methodology to complete the estimation of stored energy during an ultrasonic fatigue test in the VHCF regime.
The first section presents the methodology and the objective of its development. The materials that were studied in this work are described in the second section. Then, the third section defines the ultrasonic fatigue machine functioning principle and the key parameters to understand its use. From this knowledge, the two experimental methodologies and setup that were developed to conduct the estimation of the mechanical work and of the dissipated energy are presented in two separate sections. The validation of both methodologies is presented in keeping with the respective methodologies.

2.1 Introduction

The main target of this work is to estimate the energy stored in a metallic material during a fatigue loading, in the VHCF regime, in the course of tests performed at 20 kHz. Consequently, an experimental methodology to carry on with the estimation of the stored energy, in such conditions, must be developed. The choice was made to estimate the stored energy from an energy balance during one cycle (see Section 1.3.3). This balance will be completed through the estimation of two quantities, as to know :

- the energy dissipated per cycle by the material, from temperature measurements ;
- the mechanical work provided to the material, during one cycle, through stress measurement using an in situ time-resolved X-ray diffraction (XRD) methodology and total strain measurement using strain gauge.

The dissipated energy is estimated from an inverse resolution of the heat equation that relies on the measurement of the temperature increase on the specimen surface during an ultrasonic fatigue test. The methodology relies on the use of an infrared (IR) camera to acquire a temperature field at the surface of the specimen.

The mechanical work estimation relies on the estimation of the stress and the total strain rate during one cycle. The calculation of the mechanical work is given by equation (2.1) :

$$W_{mech} = \int_{cycle} \sigma \dot{\varepsilon} dt \tag{2.1}$$

It also corresponds to estimating the area of the hysteresis loop to obtain an estimation of the mechanical work during one cycle, as represented in Figure 2.1.

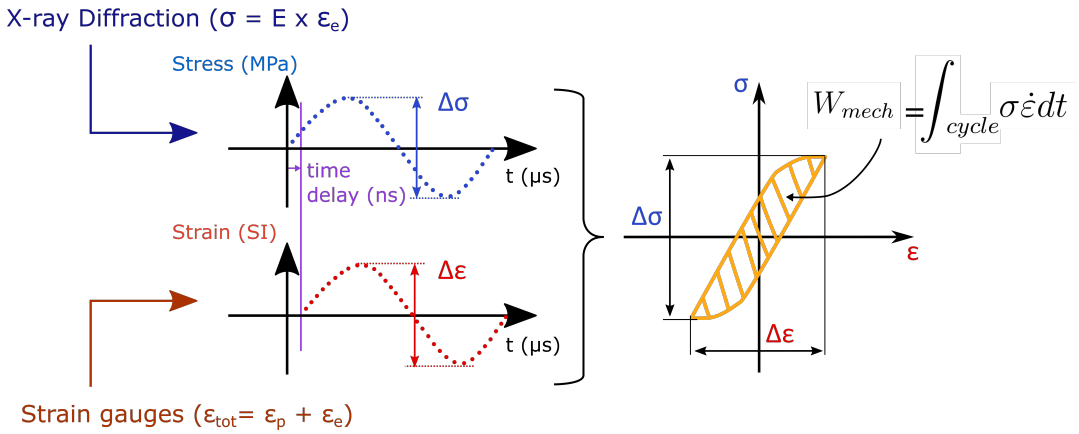


FIGURE 2.1 – Principle of the estimation of mechanical work from the estimation of stress and strain for one loading cycle.

To be able to draw the hysteresis loop and estimate the mechanical work, the evolutions of stress and strain, during one cycle, must be measured. During a cyclic loading, the stress can be estimated by either measuring the total strain (with strain gauge) or by measuring the displacement applied to the specimen (with a laser vibrometer). These methods rely on the assumption of a linear elastic behavior of the material[1], corresponding to a hysteresis loop that is closed. Thus, the mechanical work can not be estimated.
A third method must be considered, namely X-ray diffraction (XRD), which is independent of the elastic assumption and allows one to directly estimate the elastic strain applied to the material. From the elastic strain, the stress is estimated and the hysteresis loop area can be determined. In consequence, the mechanical work can be estimated. Indeed, the estimation of the total strain is conducted by using strain gauge and the estimation of the stress by employing XRD.

The methodology relies on a good correlation of the stress and strain estimation with time. In fact, the time shift between the stress and strain which determines directly the hysteresis loop aperture is about 10 ns in metals[2] [Ono, 2020].
To ensure such time resolution, several conditions must be fulfilled :

- Acquire a significant number of stress (and strain) values during the cyclic loading to correctly describe one cycle ;
- Achieve an accurate temporal positioning of the measured values of stress (and strain) ;

1. By neglecting the plastic deformation, the total strain can be identified with the elastic strain, and thus stress can be estimated.
2. This time shift is associated with the characteristic time of the viscous damping of metals.

- Settle an integration time that is small enough to limit the variation of the signal during the acquisition. It should be in the order of 1 µs down to 0.1 ns ;
- Reduce the noise level to limit its influence compared to the amplitude of the signals.

Fulfilling these conditions is possible by reducing the influence of the noise on the acquired XRD images (from which the stress is computed). It is equivalent to increasing the Signal-to-Noise ratio of these images. This is achievable by using an X-ray source that has high brilliance such as a Synchrotron source. Nevertheless, the current brilliance of synchrotrons does not allow them to meet such requirements on their own. Consequently, a stroboscopic method must be employed as well.

The methodology presented here is original as no one ever tried to estimate the stored energy evolution during a fatigue tests conducted at 20 kHz in the VHCF domain. Its development was thus difficult and highly iterative : it required the conduction of 10 experimental campaigns at the DiffAbs beamline, at SOLEIL Synchrotron. The development of the methodology sometimes required to make a backwards step to characterize the experimental setup before keeping up with the application of the methodology to the two studied materials. In this manuscript, the presentation of the development of the methodology is depicted as linear. In fact, non essential aspects of this work were cut off from the manuscript to make its reading more comfortable.

2.2 Tested materials

This work focuses on the fast determination of the fatigue properties of two materials :

- A pure copper single crystal with an orientation along the crystallographic [110] direction. The study of single crystals provides data on the behavior of materials by freeing ourselves of the effect of grain boundaries[3] and focus only on the dislocation structures and their effect on the fatigue behavior of the material. Moreover, the VHCF behavior of single grains was rarely studied in the literature which underlines the exploratory character of this work. This could open further interpretations as copper has widely been studied in terms of evolution of dislocation structures.
- A polycrystalline C70 steel, fully pearlitic, composed of ferrite and cementite phases in a lamellar microstructure. Its interest is to validate the methodology

3. The stress concentration owing to different elastic stiffness between grains with different orientations can not be considered as well.

on a more complex material, that is closer to those employed in the industry. A second interest lies in the fact that this material has two phases, helping to validate the use of the methodology to get a reliable estimation of macroscopic stress from XRD data on both phases.

Both materials are presented in the next subsections : their composition and their mechanical properties are provided. A brief overview of their fatigue behavior in the VHCF domain is discussed as well.

2.2.1 Pure copper single crystal

The crystalline structure of copper single crystal is Face-Centered Cubic (FCC). The composition of the present copper is given by the manufacturer (namely GoodFellow^{TM}) as shown in Table 2.1.

TABLE 2.1 – Chemical composition of pure copper single crystal studied (% weight).

Cu	Others
99.999	Balance

The mechanical properties of all copper single crystals mostly depend on the level of purity of the material. In the case of our material, its properties can be found in the literature. [Ledbetter and Naimon, 1974] compared almost twenty experimental measurements on copper specimens with various purity contents. The mean value of the elastic constants of copper and the standard deviations over the twenty results are reported in Table 2.2.

TABLE 2.2 – Mechanical properties of single crystal pure copper.

C_{11} (GPa)	C_{12} (GPa)	C_{44} (GPa)
169.1 ± 0.2	122.2 ± 0.3	75.4 ± 0.5

Three single crystals were received, as built, in cylinder rods with the crystallographic orientation [110] lying along the cylinder length, with an accuracy of 1 to 3°[4]. This cylinder orientation was chosen among two, including also the longitudinal orientation [100]. The choice was made to consider only the [110] cylinder rods in the first place as this orientation allows to design fatigue specimens that have dimensions close to those of steel specimens and as eight slip systems can possibly activate in this crystal, corresponding to a plastic activity that is closer to what can be observed in polycrystalline materials. As the single crystal rods were not numerous, very few fatigue specimens

4. These single crystals were manufactured using the Bridgman technique to reach a crystal size of a few centimeters. The raw crystals were 50 mm long with a diameter of 10 mm.

could be manufactured : at least two for crystals with longitudinal orientation [110]. The equivalent Young's modulus of the specimen in its longitudinal direction is estimated to be $E_{110} = 130.3 \pm 0.3GPa$ from the elastic constants.

It is to be noted that no results are found in the literature concerning the determination of the fatigue properties of copper single crystals. However, [Buchinger et al., 1985] discusses the behavior of copper single crystal in the VHCF domain, in terms of the evolution of dislocation structures, through ultrasonic fatigue tests.

2.2.2 Pearlitic (C70) steel

The composition of the polycrystalline fully pearlitic C70 steel is given in Table 2.3.

TABLE 2.3 – Chemical composition of the C70 steel studied (% weight).

C	Si	Mn	S	P	Ni	Cr	Mo	Cu	Al	Sn	Fe
0.68	0.192	0.846	0.01	0.01	0.114	0.16	0.027	0.205	0.042	0.016	balance

This material was studied after a heat treatment which has been applied to the raw rods of steel. The heat treatment was conducted as follows : austenitization at 1050°C during 7 min followed by a cooling in air. The heat treatment led to a fully lamellar pearlitic microstructure. The cooling stage was realized in a blown air environment which resulted in a microstructure of the material with interlamellar spacings Sp (between cementite lamellae) of 170 nm. Figure 2.2 shows a micrography of the microstructure of the steel and showing the interlamellar spacing. The volume percentage of ferrite in the pearlite was estimated with X-ray diffraction and is about 89%. Therefore, the volume percentage of cementite is 11%. The crystalline structure of ferrite is centered cubic (CC) and that of cementite is orthorhombic (OR).

Mechanical properties of C70 steel are exposed in Table 2.4. The density ρ of the material was measured by double weighing. The longitudinal elastic modulus, here denoted E_{is} was measured with ultrasound wave propagation method with 5 MHz frequency[5]. The interlamellar spacing Sp as well as other conventional parameters (Re, Rm and A%) of this material were taken from the literature [Özdemir, 2012, Yahiaoui, 2013].

The experimental SN diagram of the C70 fully pearlitic steel is plotted in Figure 2.3. This SN diagram was built from several fatigue tests conducted with the ultrasonic

5. The isothermal modulus, for an adiabatic and reversible transformation, is considered here as the study is based on ultrasonic fatigue (i.e. dynamic) tests considered adiabatic due to very short loading period (50µs). It is worth noting that only a small discrepancy is observed between the isentropic and isothermal modulii. They are related with the following formula $E_{is} = 1/(1/E_T - T_0\alpha^2/\rho C)$ where C is the volumetric heat capacity, T_0 the ambient temperature and α the thermal expansion coefficient.

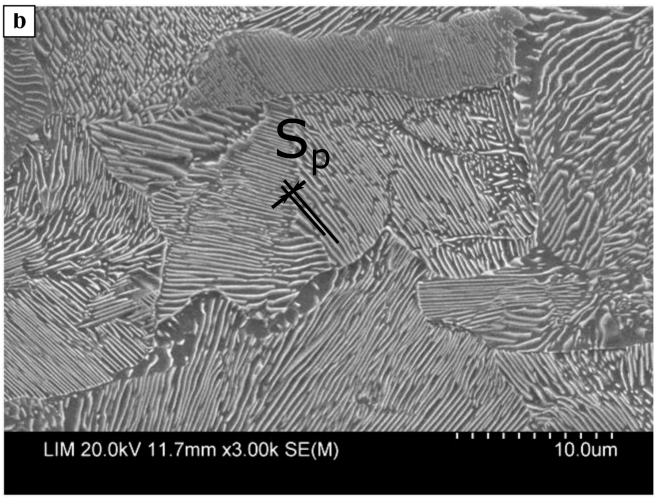


FIGURE 2.2 – Micrography of the C70 pearlitic steel taken from SEM at a magnification of 3000. The interlamellar spacing S_p is represented [Yahiaoui, 2013].

TABLE 2.4 – Mechanical properties of the C70 steel studied.

Material	Sp (nm)	ρ (kg/m^{-3})	E_{is} (GPa)	Re (MPa)	Rm (MPa)	A (%)
C70 pearlitic steel	170 ± 25	7800 ± 140	206 ± 4	462	799	14

fatigue machine in the HCF and VHCF regimes. It shows a fatigue limit estimated at 402 MPa. Below 402 MPa, no failure occurred for tests conducted up to 10^{10} cycles. In addition, a strong variability is observed for stress amplitudes between 401 and 404 MPa with specimens failing after a few 10^6 cycles or not failing until 10^{10} cycles.

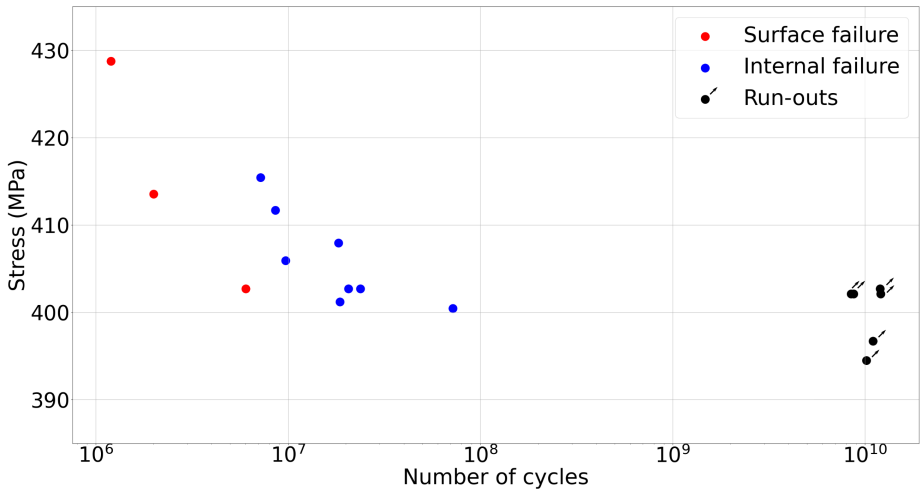
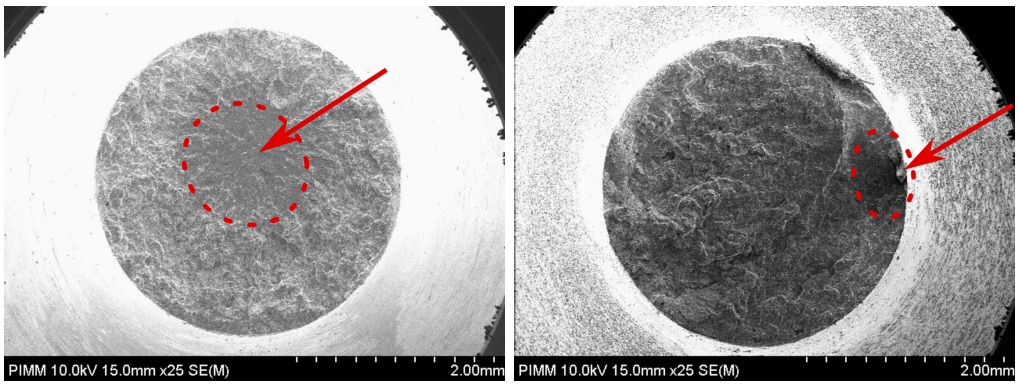


FIGURE 2.3 – SN curve of C70 pearlitic steel in the HCF and VHCF domains. A fatigue limit is determined from 10^7 to 10^{10} cycles at 402 MPa.

It was observed that fatigue cracks initiate essentially at the surface of steels at rather high-stress amplitudes and low fatigue lifelength (namely below 10^7 cycles). In the case of lower stress amplitudes and thus higher lifelength (namely above 10^7 cycles), an internal crack initiation and growth was observed. These results are represented in different colors in Figure 2.3. The fracture surfaces are provided in Figure 2.4. Cracks are generally found to be initiating at a phase boundary between ferrite and cementite phases[6] in VHCF as discussed by [Bach et al., 2016]. According to its behavior, the present C70 steel is associated with type II materials (see Section 1.4.2).



(a) (b)

FIGURE 2.4 – Fracture surface of the C70 steel in case of a fatigue loading conducted at 20 kHz for a) 406 MPa during 10^7 cycles ; internal crack initiation forming a fish-eye and b) 413 MPa during 2×10^6 cycles ; crack initiation at the surface.

6. It might also be encountered that this material experiences internal initiation at grain boundaries [Bayraktar et al., 2006].

2.3 Ultrasonic fatigue tests

To carry out time-resolved X-ray diffraction for stress measurements, the ultrasonic machine was used in two modes :

- the conventional (or standard) mode where the frequency of the machine is adapted in real time to minimize the supplied power ;
- the synchronized mode where the machine vibrates at a fixed frequency imposed by an external source, like a synchrotron master clock for instance.

Initially, the ultrasonic fatigue machine works with a standard power supply from Branson^{TM}. However, to allow the machine to work in synchronized mode, a power supply was developed during this Ph.D., and used to fatigue specimens.

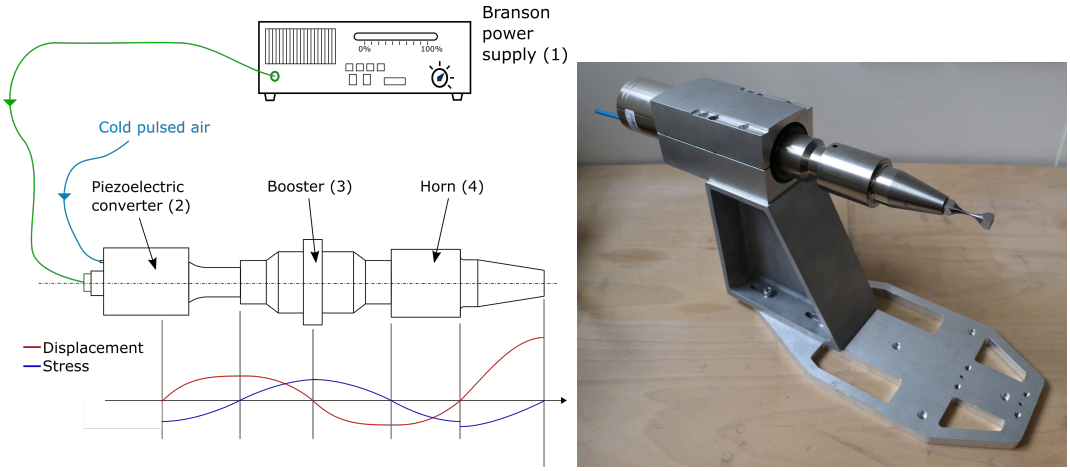
2.3.1 Functioning in conventional mode

2.3.1.1 Principle of the ultrasonic fatigue machine

The history of the development of fatigue machines was directed towards increasing frequencies to reach faster the very high number of cycles and study the VHCF domain. The evolution of the machines evolved from conventional hydraulic or electronic fatigue machines at rather low-frequency (in the order of 10 Hz), through vibratory machines which showed frequencies lying close to 1000 Hz, up to ultrasonic fatigue machines with frequencies ranging from 20 kHz to 40 kHz[7]. Due to their very high frequency, this type of machine can reach 10^9 cycles within only 14 hours and thus to investigate the VHCF domain with convenient tests durations. The use of ultrasonic fatigue machine has been precisely described in the dedicated ASTM standard [ASM et al., 2000]. It provides, among other things, the type of machine that should be used and methods to conduct fatigue tests at 20 kHz.

In the present work, an ultrasonic fatigue machine is used to load specimens at 20kHz. This machine is based on the original design of Bathias and coworkers [Wu et al., 1994] using Branson^{TM} components, see Figure 2.5. The horizontal shelf was developed during this Ph.D. to facilitate its installation and use on the synchrotron diffractometer. The machine is composed of a power supply (1) from Branson^{TM}, a high power piezo-electric converter (2) from Branson^{TM} (referenced as "2000 Series Model CR-20" constituted of six stacks of piezoelectric material, whose power is estimated at 3000 W) and which converts the electrical signal into mechanical vibrations, a booster (3) and an amplifying acoustic horn (4) which amplifies the displacement by a ratio which varies according to the horn shape.

7. At such frequency, the period of the loading is ranging from 50 to 25 µs.



(a) (b)

FIGURE 2.5 – Ultrasonic fatigue machine a) principle, b) picture.

In consequence, it is possible to obtain a steady wave in the system with a frequency close to 20 kHz. It induces displacement and stress whose amplitude vary along the system length, as shown with red and blue curves respectively in Figure 2.5a. As can be seen in this figure, there are places where the amplitude of vibration is zero in the resonant system. Such points are called vibration nodes and it is at these locations that the resonant system is fixed to the equipment frame. Our machine is settled by clamping the central part of the booster. When working, the converter is continuously refreshed with a cold air flux to maintain the temperature of the piezoelectric stacks constant and close to the ambient.

The piezoelectric converter works at a frequency corresponding to its first longitudinal eigenmode of vibration[8]. The other components (booster and horn) are designed so that their eigenfrequency is close to the frequency at which the converter works [Bruchhausen et al., 2013]. The ASTM standard [ASM et al., 2000] details the horn shapes and specimen geometries that can be designed to be used on an ultrasonic fatigue machine.
In practice, when considering a booster and a horn assembled with the piezoelectric converter, the system vibrates at a frequency that is slightly different from that of the converter alone[9]. This specific frequency is called anti-resonance frequency. Table 2.5 displays the anti-resonance frequency of the system in various configurations. This frequency corresponds to the working point at which the minimum power is supplied to the

8. At this working point, the power supplied to the machine is minimized ; piezo-electric converters are described independently in [Prokic, 2004]

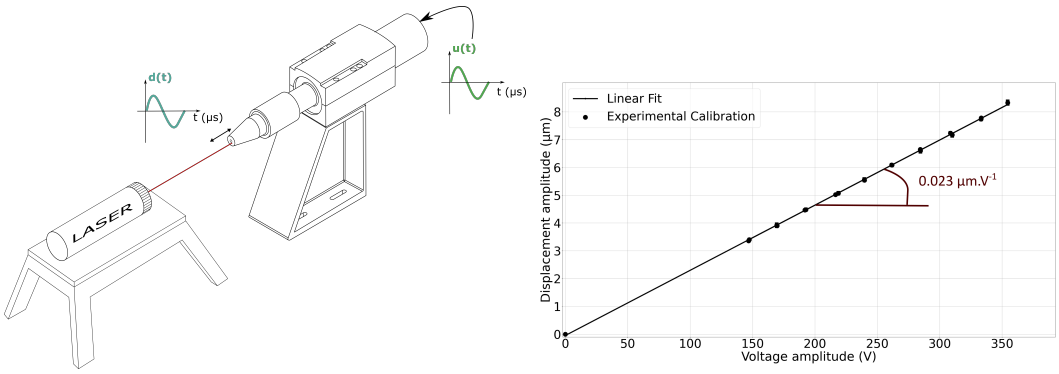
9. The shape and material (elastic) properties of a mechanical vibratory part define its vibration properties, namely its longitudinal eigenmode frequency.

machine. A specimen can likewise be screwed at the free end of the horn to be fatigued, but in this subsubsection we first characterize the behavior of the machine itself with no specimen attached to it.

TABLE 2.5 – Anti-resonance and resonance frequencies of various configurations of the resonant system in its conventional functioning - "Co." = piezoelectric converter and "Bo." = booster.

Configuration	anti-res. frequency (Hz)	Disp. amp. range (µm)	Slope ($\mu m/V$)
Converter (Co.) alone	20740	0.05-12	/
Co. + Booster (Bo.) x1	20190	0.05-12	/
Co. + Bo. x1 + Horn x2.65	20232	0.15-30	0.023
Co. + Bo. x1 + Horn x10	20029	0.6-120	0.086

The adding of a specific mechanical part (booster or horn) is conditioned by the objective of the test in order to reach rather low or high displacement amplitudes (reported in Table 2.5) [Prokic, 2004]. In the case of a configuration of the system being constituted of {converter + booster x1 + horn x2.65}, the displacement was measured at the free end of the horn, by using a laser vibrometer, as shown in Figure 2.6a. Figure 2.6b shows the experimental results representing the displacement amplitude with respect to the voltage amplitude supplied to the piezoelectric converter. A linear correlation is evidenced between the displacement and voltage amplitudes, with a slope lying close to 0.023 µm/V. The plotted error bars are attributed to the uncertainty associated with the measure conducted with the laser vibrometer (for further details, see [Jacquemain et al., 2021]). In addition, the displacement ranges provided by the system in different configurations are reported in Table 2.5.



(a) (b)

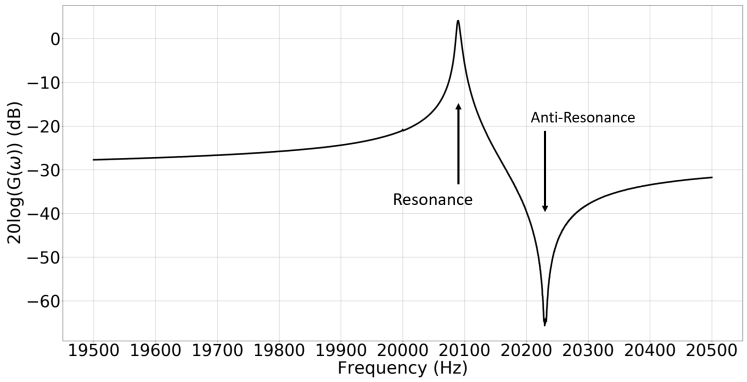
FIGURE 2.6 – a) Schematic representation of the experimental setup used to measure the displacement amplitude at the edge of the sonotrode and b) evolution of the displacement amplitude measured at the free end of the horn, with respect to the voltage amplitude applied to the piezoelectric converter.

2.3.1.2 Characterization of the ultrasonic fatigue machine

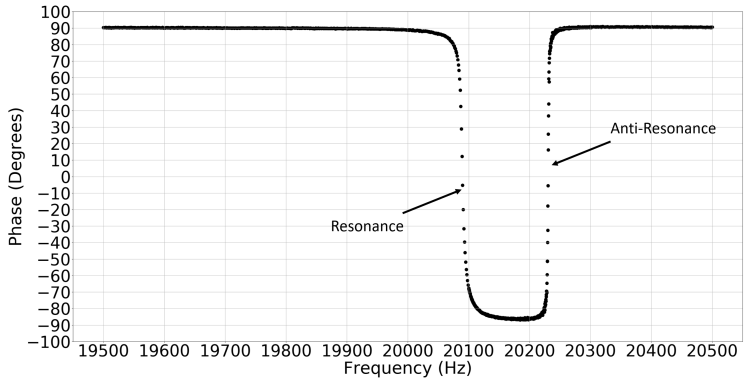
The input of the converter is a sinusoidal voltage signal $u(t) = u_0 \sin(\omega t)$ imposed by the voltage generator (where ω is the angular frequency). The current $i(t) = i_0 \sin(\omega t + \phi_{machine})$ and the displacement signals of the end of the horn $d(t) = d_0 \sin(\omega t + \phi_{machine,2})$ are the two outputs. The measurement of the current and displacement were conducted for a voltage amplitude of $u_0 = 15$V, specifically in the case of the system being composed of {converter + booster x1 + horn x2.65} presented in Figure 2.5. Therefore, the electrical transfer function of the piezo-electric system $H(t) = \frac{i(t)}{u(t)}$ was determined experimentally. In the case of a harmonic evolution, this allows one to define the gain of the transfer function $G(\omega) = \frac{i_0}{u_0}$ as a function of ω, which is represented on Figure 2.7a with respect to the frequency. On this curve, two extrema can be observed : the maximum (4dB) at a frequency of 20090Hz and minimum (-65dB) at 20232Hz defined respectively as the resonance and the anti-resonance of the system. At the anti-resonance, the mean energy rate supplied by the generator corresponds to the smallest amount of power to work. The provided power compensates exactly the energy dissipated by the system.

The phase $\phi_{machine}$ between the current and voltage supplied to the system is plotted in Figure 2.7b with respect to frequency, for a voltage amplitude of 15V. Sharp evolutions are noticed very close to the resonance and the anti-resonance frequencies.

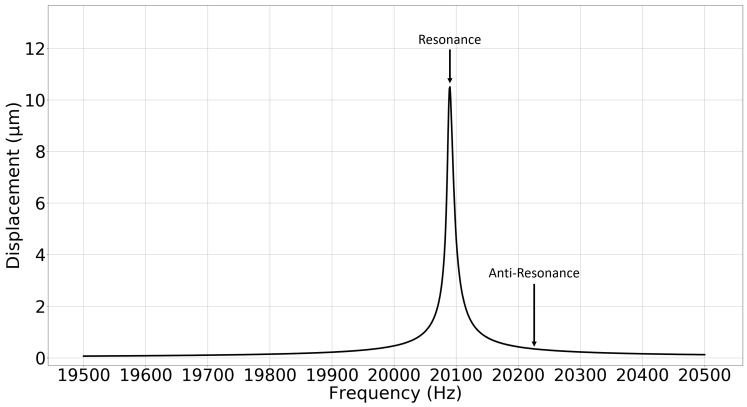
The speed of displacement at the free end of the horn was measured using a Polytec^{TM} HSV 2001 laser vibrometer and is converted into displacement amplitude. The variation of displacement amplitude is plotted in Figure 2.7c with respect to the frequency for a voltage amplitude of 15V. The closer frequency is to the resonance, the larger the displacement amplitude provided but the larger the amount of current required to obtain such displacement. On that account, there are several benefits of working at a frequency close to the anti-resonance : it leads to a smaller amount of power required to work and thus less energy that is dissipated in the piezoelectric converter corresponding to a better thermal stability. In addition, the displacement amplitude is less sensitive to frequency shifts (a property that is useful to carry out mechanical tests under precisely controlled conditions), even though a smaller displacement amplitude is accessible at the anti-resonance : at least 0.25µm at 20232Hz for a voltage amplitude of 15V.



(a)



(b)



(c)

FIGURE 2.7 – Characterization of the piezoelectric converter : a) Transfer function gain , b) phase and c) displacement vs. frequency [Jacquemain et al., 2021].

2.3.1.3 Control of the ultrasonic fatigue machine

Remote control of the machine is necessary to make sure that it works continuously at a frequency close to the anti-resonance frequency of the system[10]. To do that, the phase plays a key role in controlling the machine because the anti-resonance is characterized by a strong phase change as shown in Figure 2.7b. The target phase value is zero degrees correponding to a working frequency of 20232Hz. During a sweeping of the frequency (from 20500 to 19500Hz) at a small voltage amplitude input, the highest frequency corresponding to the phase being equal to zero degrees is identified and stored. It corresponds to the anti-resonance of the system. Then, using a phase locked loop (PLL), the controlling system adjusts the frequency during the fatigue loading so that the phase stays close to the value $\phi_{machine} = 0°$. When the anti-resonance frequency is reached, the system amplifies the input voltage to apply a significant displacement amplitude at the free end of the horn. This process takes in general 100ms to complete.

2.3.1.4 Design of fatigue specimens

Having characterized the machine response the next step is to design the specimen so that the machine and the specimen[11] can vibrate independently in their own vibration mode. This guarantees then the decoupling between the whole system and the specimen ; in other words, no stress exists at the interface between them. To assure these conditions, the specimen must vibrate in its first longitudinal mode of free vibration with a frequency close to the anti-resonance frequency of the machine [Puškár, 1993b, Mayer, 1999, Wagner et al., 2012, Bruchhausen et al., 2013, Marti et al., 2015]. The main objective of the design is therefore to determine all specimen dimensions that correspond to the target eigenfrequency.

Every specimen designed in this work is based on an hourglass shape for which a smooth gaussian stress gradient appears along the longitudinal direction, the maximum stress being located at the specimen center (in the gauge zone).

The design process has been presented in detail in [Jacquemain et al., 2021]. It considers the study case a specimen made of pearlitic C70 steel[12] that is also considered in the present section. The dimensions of the specimen (as shown in Figure 2.8) are chosen

10. The anti-resonance frequency can change if the fatigue specimen experiences self-heating of if a crack appears in it.

11. To be fatigued, a specimen is usually screwed to the free end of the horn. In our work, the system is designed such that the acoustic waves induce a perfect tension-compression loading to the specimen with a loading ratio $R = -1$.

12. In this reference, the design procedure was detailed in the case of a steel specimen but it is the same for every mechanical parts of the system (namely boosters or horns). The steps of the process is also identical for any specimen shapes or material.

to be fixed, except the shaft length L_s. The objective is to identify the value of L_s at which the eigenfrequency of the specimen coincides with the anti-resonance frequency of the ultrasonic fatigue machine (that was estimated at 20 232 Hz). This length is gradually changed through a modal calculation conducted on a Finite Element Analysis (FEA) simulation[13]. Figure 2.9 shows the evolution of the eigenfrequency of the specimen with respect to the shaft length L_s in the case of a steel specimen. From Figure 2.9, the optimal L_s value was identified to be $L_s = 17.5$ mm.

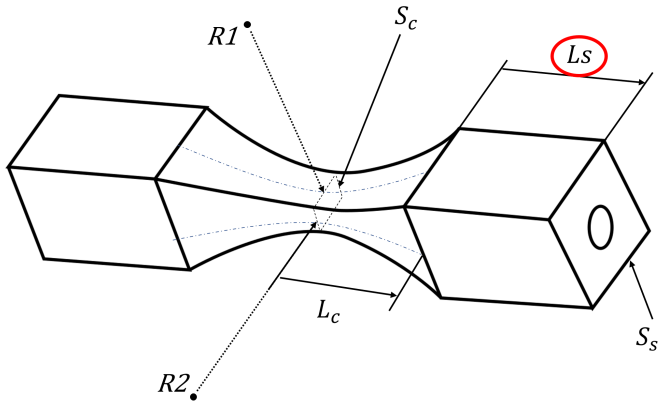


FIGURE 2.8 – Geometry of a C70 steel fatigue specimen designed to vibrate at an ultrasonic frequency.

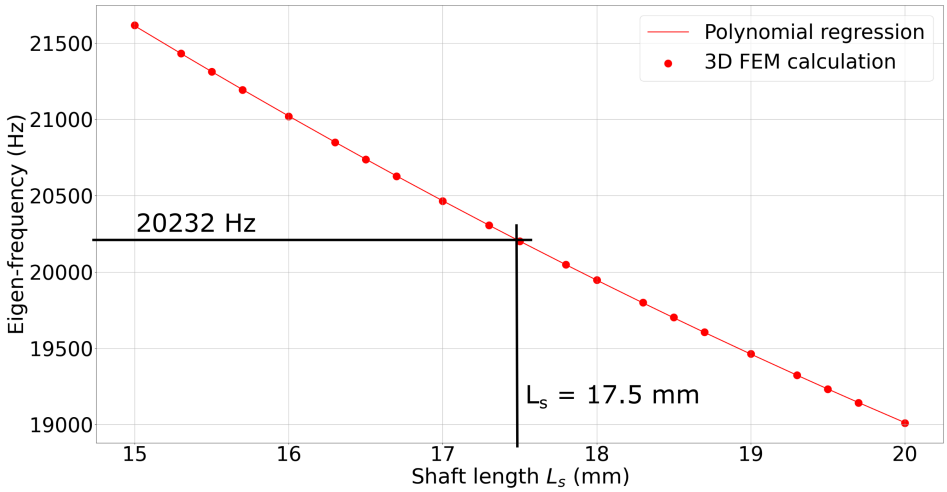
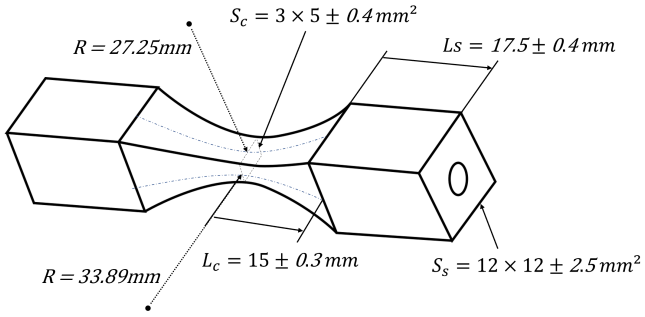


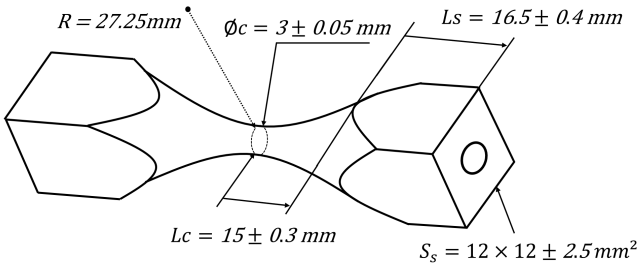
FIGURE 2.9 – Evolution of the frequency with respect to the shaft length of a C70 steel specimen modeled by using Abaqus^{TM}.

13. The mesh size that was chosen in the FEA model was fixed at 0.4 mm, for which the results were independent of the mesh.

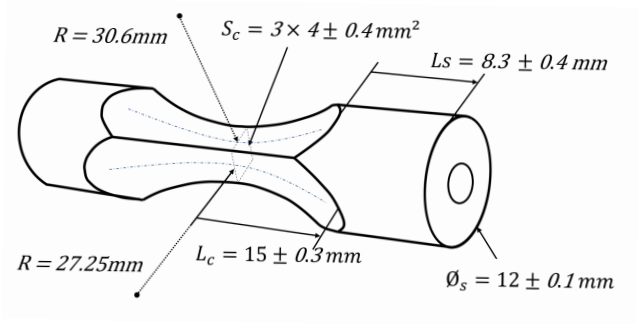
The specimen design procedure was applied to pure copper single crystal and C70 steel specimens. The fact that the studied pure copper was a single crystal made the specimen design process a bit more complex than what is presented above. As this material is anisotropic, its elastic properties depend on the crystal orientation. The FEA model must account for the anisotropy of the single crystal which is easily achieved in Abaqus^{TM}. Concerning the C70 steel, its behavior being isotropic, the calculation was straightforward.



(a)



(b)



(c)

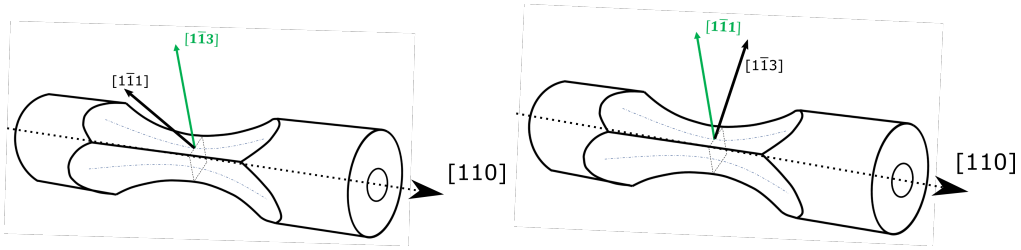
FIGURE 2.10 – Specimen geometry in the case of a) steel specimen reserved for XRD parallelepipedic shape, b) steel specimen for building an SN diagram and c) copper single crystal specimen for XRD.

Specimens were designed in this study to have different shapes. In some cases, a rectangular cross-section is considered. This geometry allows one to conduct XRD measurements on the largest, almost flat, surface at the center of the specimen [14]. A circular cross-section is considered for specimens that are used for plotting SN diagrams [15] for instance. The final design of the copper and steel specimens are shown in Figure 2.10.

Figure 2.10 shows as well the tolerance intervals associated with each dimension of all specimens. The tolerance intervals are associated with a maximum frequency uncertainty of ±204 Hz. This uncertainty in frequency arises from the uncertainty observed when estimating the materials properties. The tolerance intervals are determined from a sensitivity analysis that ensures that the variation of frequency induced by each dimension of the specimens remains smaller than the maximum uncertainty of ±204 Hz. The sensitivity of the first longitudinal eigenfrequency of a fatigue specimen, with respect to geometrical and material parameters, was investigated with a modal calculation by using a 3D FEA model ; more details can be found in [Jacquemain et al., 2021].

The fatigue specimens are manufactured by electro erosion wire-cutting. This ensures that the surface integrity of the specimen is preserved. The last point is mandatory for pure copper single crystals that are very soft.

Copper specimens have been manufactured with their larger central surface being perpendicular to a specific crystallographic direction of the crystal. In fact, two cases were considered, one specimen whose larger surface is oriented perpendicular to the $[1\bar{1}1]$ direction and one specimen whose larger surface is oriented perpendicular to the $[1\bar{1}3]$ direction. Both cases are represented in Figure 2.11.



(a) (b)

FIGURE 2.11 – Configuration of the copper single crystal specimens with their largest surface oriented perpendicular to the a) $[1\bar{1}3]$ and b) $[1\bar{1}1]$ directions.

14. [Zhigachev, 2013] demonstrated that circular cross-sections are not optimal to conduct XRD leading to the selection of almost flat surfaces in this work.

15. Circular cross-sections are preferred to reduce the stress concentration zones by removing the specimen edges.

2.3.1.5 Estimation of the stress amplitude in fatigue specimens

In the literature, two conventional methods are reported to estimate the stress amplitude from a fatigue test conducted at 20 kHz. The application of both methodologies is based on the assumption that the material exhibits a purely macroscopic elastic behavior :

- The first one requires the use of strain gauge to estimate the stress from the measurement of the total strain. This technique is straightforward and only requires the precise knowledge of the elastic properties of the material [Brugger et al., 2017].
- The second one requires the use of a laser vibrometer to estimate the stress and is conducted in two steps [Bathias, 2006]. First, the speed of displacement of the free end of the specimen is estimated with the vibrometer and converted into a displacement amplitude from the knowledge of the frequency of vibration. The specimen is then modeled in FEA (using the Abaqus^{TM} software with the same elements size than exposed in the previous section) to carry out a harmonic calculation (considering a linear elastic behavior of the material). The calculation considers an external load[16] symbolised by a displacement amplitude applied to one end of the specimen (that is fixed to $1\mu m$), the other end remaining free. This calculation allows the determination of the k coefficient that links the longitudinal stress amplitude to the applied displacement.

In this section, the choice is made to focus on the second method (using laser vibrometer and FEA) as it allows one to estimate the stress distribution in the whole specimen.

From the FEA calculation, the stress is estimated at the surface of the specimen, along its length. Figure 2.12 presents the FEA model of a C70 steel specimen as well as the heterogeneous stress repartition along its length for an applied displacement of 1 µm. Fig. 2.12a focuses on the central part as both specimen ends show a stress that is null. The stress is higher in the center of the specimen (in the gauge zone) and remains above 99% of its maximum in a zone of ±0.5 mm around the center.

16. In the model, the specimen is considered to vibrate at the frequency of its first longitudinal eigenmode.

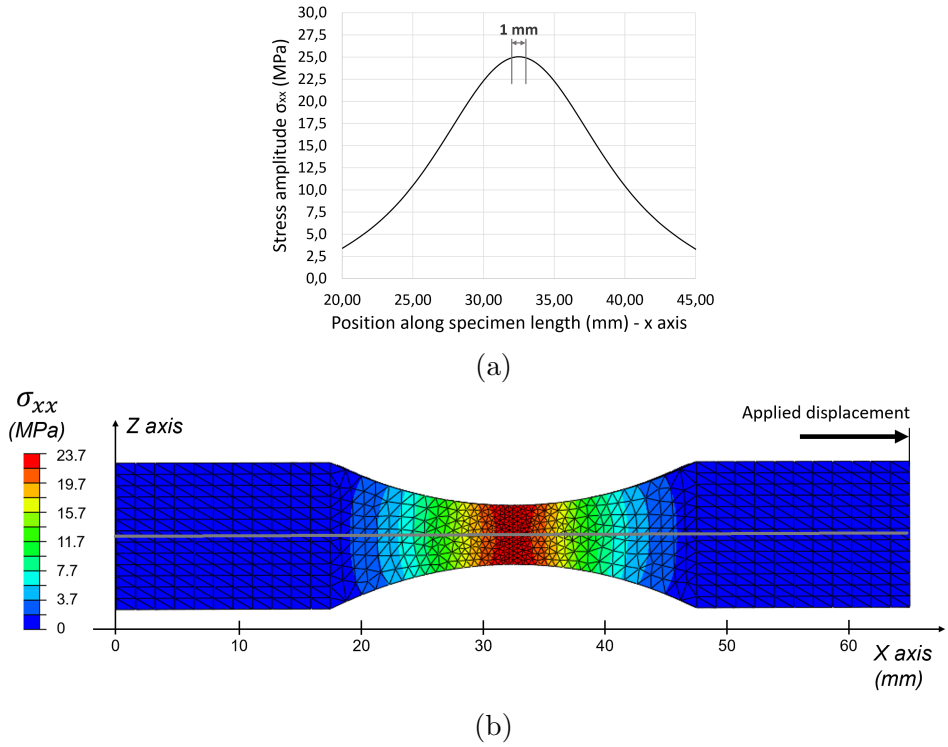


FIGURE 2.12 – a) Longitudinal stress amplitude along the specimen central axis and b) longitudinal stress amplitude field (applied displacement amplitude $1\mu m$; loading frequency of 20232Hz) [Jacquemain et al., 2021].

The abovementioned calculation enables to identify a non negligible stress gradient throughout the cross-section of a specimen. The heterogeneity of the longitudinal stress in the central cross-section of the specimen is shown in Figure 2.13 for steel. A stress concentration is found at the four edges of the cross-section and might be arising from an edge effect. Table 2.6 shows the stress amplitudes reached in the specimen central cross section for the steel specimen. The k_{C70} coefficient corresponds to the stress value measured at the surface of the specimen (for an applied displacement of 1 µm), which is shown by a black dot[17] on Figure 2.13. It is found to be $k_{C70} = 24.2\,\text{MPa/µm}$. This value corresponds to the maximum stress in Figure 2.12a.

17. The k coefficient is estimated at this specific place because stress measurements from XRD are conducted at the same location, on the surface of the specimen. This allows a consistent comparison between both estimations of stress.

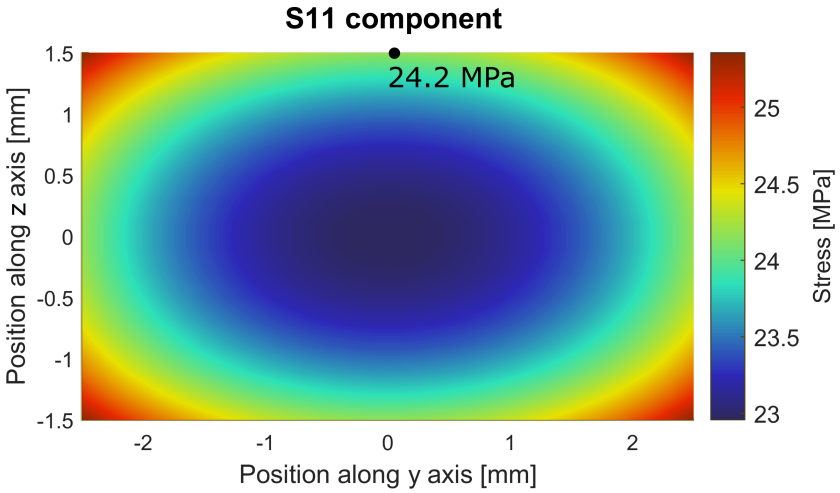


FIGURE 2.13 – Longitudinal stress amplitude distribution within the specimen cross-section, in the center of the specimen for an applied displacement of 1 µm - case of steel specimen with parallelepipedic shape for a frequency of 20 232 Hz.

	σ_{11} (MPa/µm)			
	min.	max.	mean	surface
C70 Steel	23.1	25.3	23.6	24.2

TABLE 2.6 – Longitudinal stress amplitudes of the steel specimen (in the **x** direction) for a displacement amplitude applied of 1 µm.

Results obtained from the application of the abovementioned methods to estimate the stress amplitude (at the center of the specimen), in several loading conditions, are reported in Figure 2.14 with respect to the displacement amplitude imposed by the machine (measured experimentally). The measurements based on the use of the laser vibrometer (from which the stress amplitude is considered at the center of the specimen) are in great agreement with those obtained with the strain gauge glued on the specimen (at its center). The calculation is considered valid as the relative difference between both linear fits is lower than 5%. The linear curve shows a slope that corresponds to the k_{C70} coefficient.

The process of stress estimation by using the laser vibrometer was conducted once with one specimen to build such a curve. Then, the present curve combined with the curve from Figure 2.6 will be used during the fatigue tests to obtain an approximation of the stress amplitude applied to specimens with respect to the input voltage of the machine that is adjusted.
In practice, the frequency at which the specimen vibrates is generally different from the frequency at which the calculation has been conducted. For instance, for a difference of

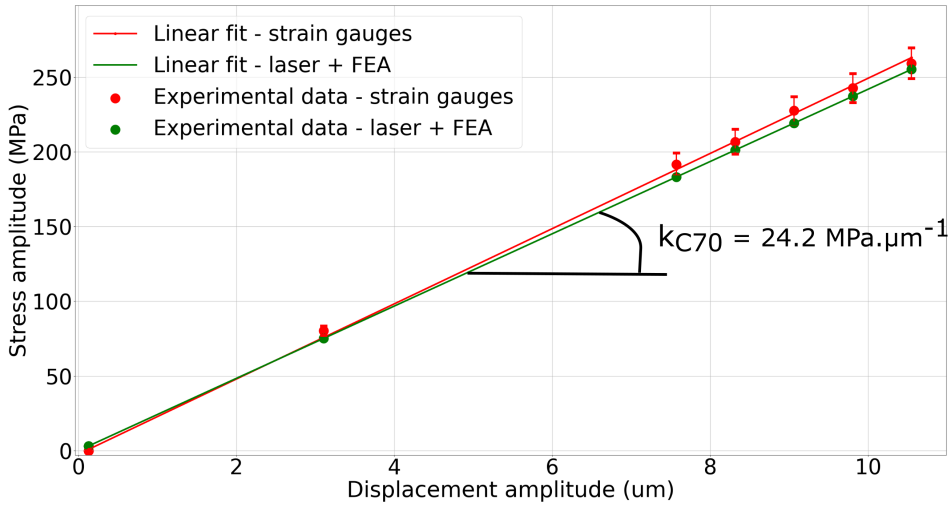
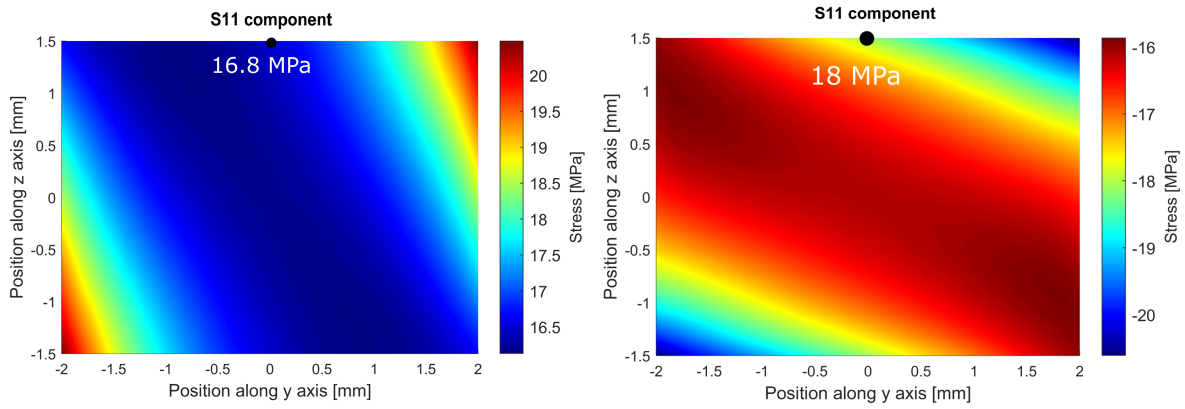


FIGURE 2.14 – Evolution of the stress at the center of the specimen vs. the applied displacement to its screwed end - case of a C70 steel specimen.

10 Hz between both frequencies (owing to the self-heating of the specimen), the difference in stress between the value estimated and the value underwent by the specimen is in the order of 0.2 MPa, which is negligible. On top of that, strain gauge will be used to experimentally estimate the total strain underwent by the specimen and estimate in-situ the applied load during all experiments.

In the case of copper single crystal, the FEA calculation is conducted by taking into account the anisotropic character of the specimen. The specimen's longitudinal direction is oriented along the [110] direction and its largest central surface is respectively perpendicular to the $[1\bar{1}1]$ and $[1\bar{1}3]$ directions for the two orientations of specimens. The stress heterogeneity along the length of the specimen is similar in terms of shape between copper and steel. In addition, the anisotropy in copper single crystal induces a stress concentration that is localized at the opposite edges of the cross-section, as shown in Figure 2.15 for both specimens' orientations. In this figure, the coefficient k_{cu} is identified in the same manner than what was done previously for steel. The k coefficients are estimated at $k_{cu,1\bar{1}3} = 16.8\,\text{MPa}/\mu\text{m}$ and $k_{cu,1\bar{1}1} = 18.0\,\text{MPa}/\mu\text{m}$. Table 2.7 provides the values of the longitudinal stress amplitudes obtained in the central cross-section of both copper specimens.



(a) (b)

FIGURE 2.15 – Longitudinal stress amplitude distribution within the specimen cross-section, in the center of the specimen for an applied displacement of 1 µm - case of copper specimen a) with its larger central surface oriented perpendicular to the $[1\bar{1}3]$ direction, for a frequency of 20 269 Hz and b) with its larger central surface oriented perpendicular to the $[1\bar{1}1]$ direction, for a frequency of 20 267 Hz.

Orientation	σ_{11} (MPa/µm)			
	min.	max.	mean	surface
$(1\bar{1}3)$	16.1	20.5	17.0	16.8
$(1\bar{1}1)$	15.9	20.6	16.9	18.0

TABLE 2.7 – Longitudinal stress amplitudes of both copper specimens (in the **x** direction) for an applied displacement amplitude of 1 µm.

Orientation	Resolved shear stress (MPa/µm)					
	B4			C1		
	min.	max.	mean	min.	max.	mean
$(1\bar{1}1)$	6,46	8,42	6,75	6,46	8,42	6,75
$(1\bar{1}3)$	6,44	8,36	6,80	6,44	8,36	6,80

Orientation	Resolved shear stress (MPa/µm)					
	B2			C3		
	min.	max.	mean	min.	max.	mean
$(1\bar{1}1)$	6,32	8,42	6,75	6,32	8,42	6,75
$(1\bar{1}3)$	6,46	8,36	6,81	6,46	8,36	6,81

TABLE 2.8 – Resolved shear stresses for the respective slip systems of the copper specimen (in the **x** direction) for a displacement amplitude applied of 1 µm.

According to the orientation of the specimen longitudinal direction, which corresponds to the [110] direction, four slip systems were identified : B2, B4, C1 and C3. These possibly active slip systems were determined from the calculation of the Schmid factor of each slip system. The resolved shear stress that is measured on the glide plane of each slip system was estimated from the post-treatment of the abovementioned harmonic calculation (using Abaqus) and the results are shown in Table 2.8. The maximum resolved shear stress is localized at the opposite edges of the cross-section, as well as the longitudinal stress (see Fig. 2.15).

2.3.2 Functioning in synchronized mode

In synchronized mode, the frequency at which the machine vibrates is imposed by an external reference signal provided by the master clock of the synchrotron. The frequency of this external signal is imposed on the machine to enable the application of a new methodology that was developed in this Ph.D.

The machine can work in synchronized mode only if the frequency that is imposed on the system is close to its anti-resonance frequency. In fact, the farther the working frequency from the anti-resonance frequency of the system, the higher the power supplied to the machine up to the limit of the power supply. In addition, the dissipated power in the piezoelectric converter is higher in such a detrimental configuration, inducing its heating. The output of the converter then tends to derivate with time. To limit these negative effects, new horns and specimens were designed to have their longitudinal eigenfrequency the closest to the target frequency allowing the whole system to vibrate at a frequency close to the imposed frequency.

The process of synchronization of the fatigue loading at the frequency of the external signal is schematized in Figure 2.16. This process relies on a power supply that was designed especially for this application by Christophe Cheuleu, engineer in mechatronics. It is constituted of a signal generation board, a synchronization board and an amplification board. Its operation can be summarized as follows : the electronic board reads the reference signal and generates a sinusoidal signal at a frequency that is the same as that of the reference signal ; the synchronization board then synchronizes both signals in phase ; the amplifying board finally amplifies the output signal to supply the piezoelectric converter with a sufficient voltage amplitude of a few hundreds of volts.

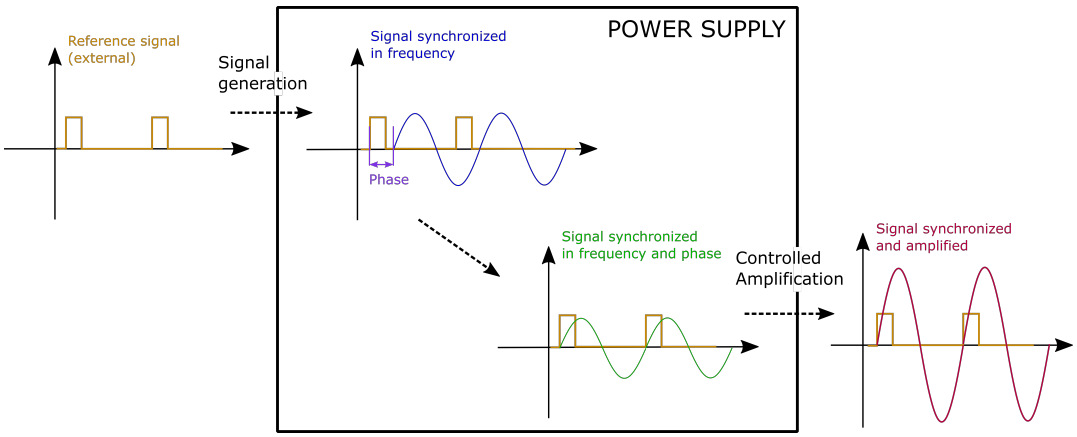


FIGURE 2.16 – Schematic representation of the process of synchronization of the fatigue loading at the frequency of the synchrotron.

2.4 Time-resolved methodology to estimate the mechanical work

The estimation of the evolution of stress and total strain rate allows one to draw the hysteresis loop of one loading cycle in order to estimate the mechanical work.

2.4.1 Estimation of the total strain

Strain gauge are used to measure the total longitudinal strain in the center of the specimens loaded at 20 kHz. Thus, two gauge (*KYOWA KFG-1N-120-C1-11*) are glued facing each other on opposite surfaces of the central cross-section. The size of those gauge is 1mm × 0.64mm and there are oriented along the specimen length. These gauge can measure strain level of 10^{-6}. Gauge are put in a full wheatstone bridge circuit. Two additional gauge are glued on a second (dummy) not loaded specimen of the same material to fully compensate for any change in room temperature[18]. A Kyowa^{TM} (CDV-900A) signal conditioner is used to power the bridge and to amplify the output voltage. The experimental configuration is presented in Figure 2.17.

18. Strain gauge are themselves thermally compensated to account for the self-heating of the specimen, i.e. their gain remains constant when their temperature changes, up to 100 °C.

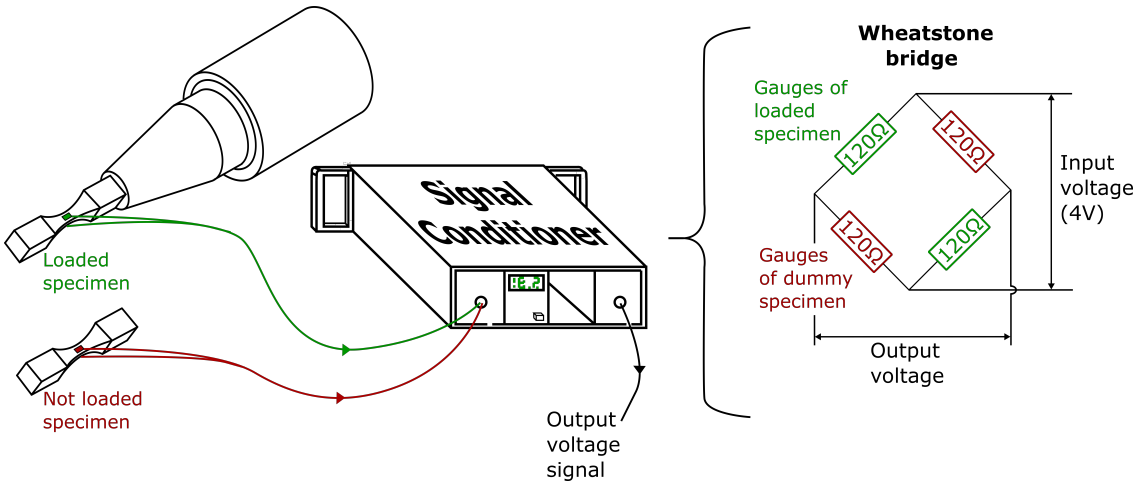
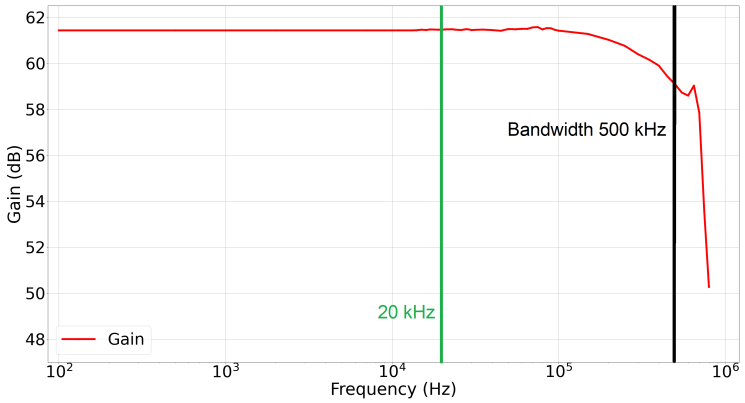
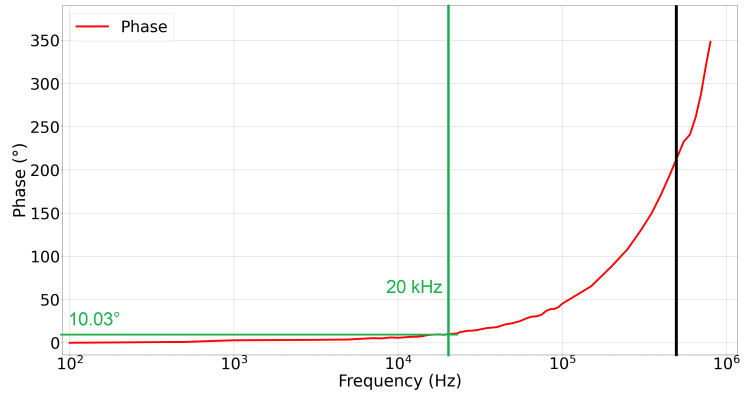


FIGURE 2.17 – Schematic representation of the experimental configuration for the measurement of the total strain.

The acquisitions of the values of the wheatstone bridge signal output are conducted over time. The time resolution achieved in the estimation of the strain evolution under a fatigue loading is dependent on the signal conditioner characteristics and on the sampling frequency of the acquisition board (used to acquire strain gauge values). The characteristics of the signal conditioner were determined through the construction of a Bode diagram. Both gain and phase evolutions with respect to the frequency are given in Figure 2.18. It is seen that when the signal conditioner is used with an input signal at a frequency of 20 kHz, the output signal is not attenuated ; the bandwidth at $-3dB$ is at 500 kHz. However, a phase shift of the output signal compared to the input signal is measured to be approximately $10.03 \pm 0.5°$, corresponding to a time shift (that is a constant offset) of 1392 ± 69ns when brought back to the period of the fatigue loading.



(a)



(b)

FIGURE 2.18 – Bode diagram of the signal conditioner : a) gain and b) phase vs. frequency of the signal read by the conditioner.

2.4.2 Estimation of the stress

The stress applied to the specimen during ultrasonic fatigue tests is estimated by using X-ray diffraction (XRD).

2.4.2.1 Principle of X-ray diffraction

Metallic materials are defined by their lattice structure, which is intrinsic to a material. Such structure is characterized by the organization and position of the constitutive atoms. Besides, metallic materials are composed of several thousands of grains. In a grain, the lattice structure is generally oriented (in a polycrystalline material, grains are randomly oriented). This orientation defines the identification of specific crystallographic planes that are defined by their Miller indexes (hkl). In an unstressed state, the inter-reticular spacing between (hkl) planes is noted d_{hkl}. According to Bragg's law

(equation (2.2)), the X-rays diffracted by crystallographic planes having Miller indexes (hkl) and distant of d_{hkl} are aligned with a half-apex angle of θ with respect to the incident beam :

$$\lambda = 2d_{hkl}\sin(\theta_{hkl}). \tag{2.2}$$

Figure 2.19 schematizes the Bragg's law in the case of a perfect crystallite in diffraction condition. Each grain with (hkl) planes has its corresponding diffraction cone at a unique 2θ angle.

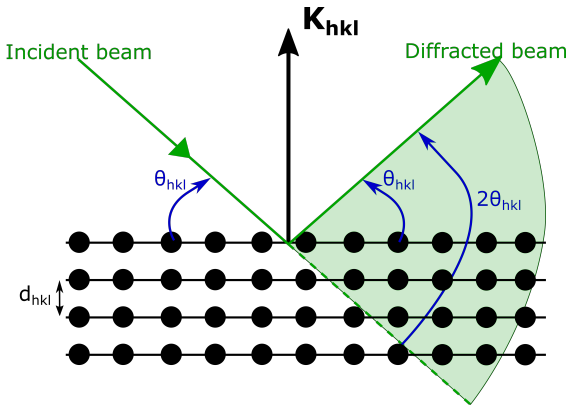


FIGURE 2.19 – Diffraction principle on a perfect crystallite in Bragg's condition (i.e. in diffraction condition). The crystallographic planes of the perfect crystal have their normal $(\boldsymbol{K_{hkl}})$ that is oriented along the $[hkl]$ direction.

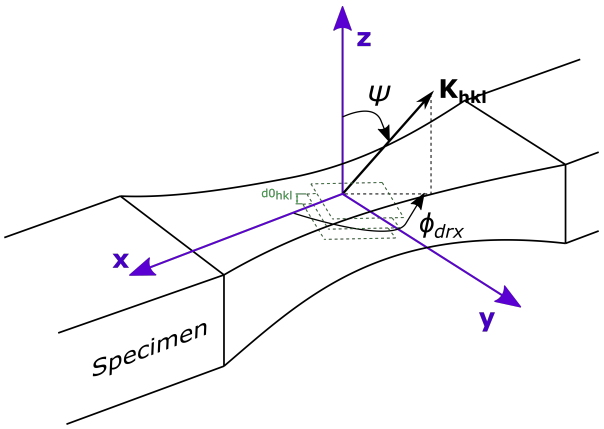


FIGURE 2.20 – Bragg's law and experimental configuration with respect to a specimen. Case of crystallographic planes that are in diffraction condition and their respective orientation with the coordinates system of the specimen.

The diffraction configuration to study a fatigue specimen by using XRD is depicted in Figure 2.20. The vector $\boldsymbol{K_{hkl}}$ is the normal vector to the represented (hkl) crystallographic planes. The two angles ψ and ϕ_{drx} are defined to determine the position of

$\boldsymbol{K_{hkl}}$ with respect to the specimen orientations, whose main directions are **x**, **y** and **z**. In the setting of this Ph.D., the grains which are observed have their crystallographic planes lying almost parallel to the surface exposed to X-rays. In such configuration, $\psi = \phi_{drx} = 0°$. This symmetrical configuration is called $\theta - 2\theta$. In fact, the incident beam makes an incident angle with the surface of the specimen which is equal to θ and the angle between the incident beam and the diffracted beam is equal to 2θ. This configuration is depicted in Figure 2.21 and guarantees a compromise between the intensity of the diffracted beam and its spatial resolution.

A single grain that is in diffraction configuration contributes to one single diffracted spot. If several grains (with the same (hkl) orientation) are considered, their contribution corresponds to several diffracted spots. Figure 2.21 shows an example in the case of two grains in diffraction conditions. In the figure, the green contribution is associated with planes that are parallel to the specimen surface whereas the purple contribution is associated with planes that have a ψ angle that is not null. In a sufficiently large diffraction volume, the contributions of numerous grains is observed. All the contributions are aligned along a diffraction cone. A continuous diffraction cone represents the contribution of all grains (with the same (hkl) orientation) that are in diffraction condition, i.e. that have their diffraction vector $\boldsymbol{K_{hkl}}$ oriented with a specific 2θ angle with respect to the X-ray beam.

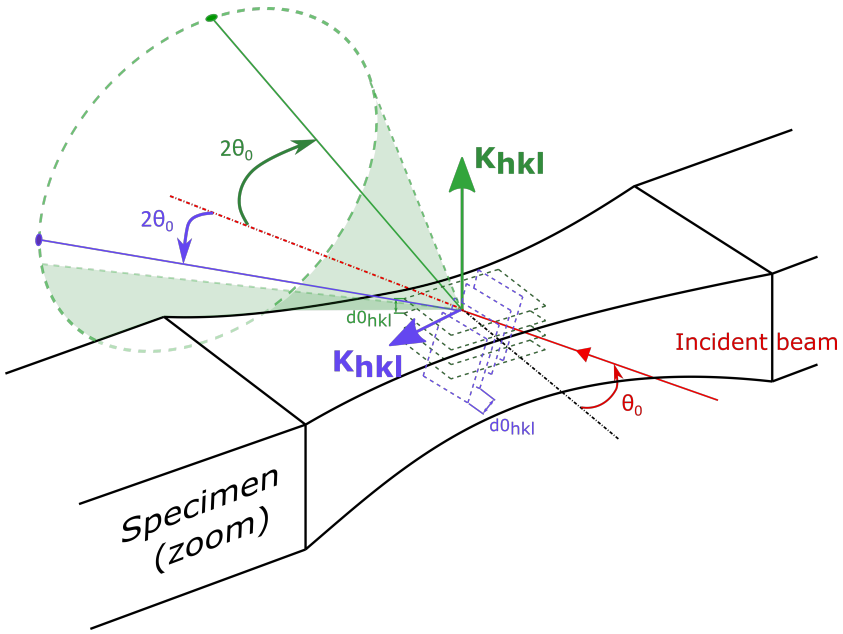
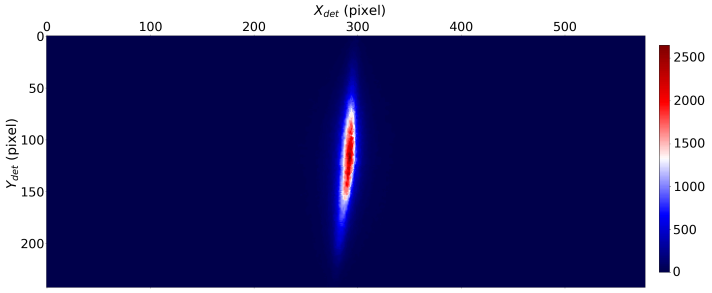
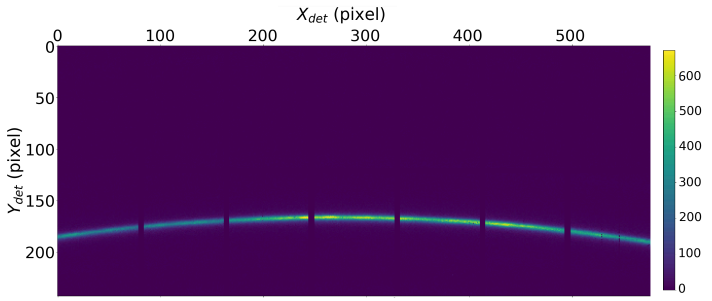


FIGURE 2.21 – Bragg's law and experimental configuration with respect to a specimen. Examples of two diffracting dots corresponding to the contribution of two crystallites' orientations.

Figure 2.22a shows an example of a diffraction pattern from a copper single crystal captured by a 2D detector. This diffraction pattern is not exactly a circular spot because of the slight misorientations present in the crystal that contributes to increasing the azimuthal size of the spot. Figure 2.22b shows an example of a continuous diffraction cone from C70 polycrystalline steel whose portion was captured by a 2D detector. The crystallites, contributing to this ring portion exposed, have the normal of their crystallographic planes oriented such that $\phi_{drx} = 90°$ and $-2° \leq \psi \leq 2°$, i.e. the crystallographic planes that are parallel or almost to the surface of the specimen. The size of the diffracting volume[19] should be sufficient to account for numerous grains and obtain a diffraction cone that is statistically representative of numerous crystallites.



(a)



(b)

FIGURE 2.22 – XRD pattern characteristic : a) pure copper single crystal diffraction "spot" and b) polycrystalline C70 steel continuous diffraction ring.

19. The size of the diffraction volume depends on the X-ray beam size, the beam divergence, its spectral width and its penetration depth (the penetration depth in turn depends on the material and the beam energy).

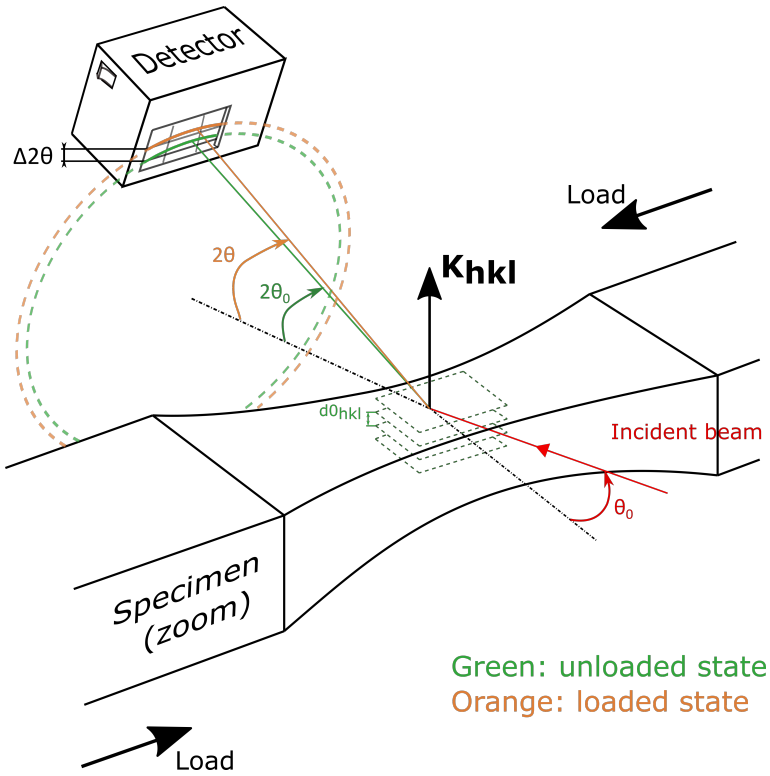


FIGURE 2.23 – Bragg's law and experimental configuration with respect to a specimen. Only a portion of the diffraction cone is captured by the detector which represents the grains oriented parallel (or almost) to the surface of the specimen.

Under a macroscopic elastic strain, the inter-reticular distance d_{hkl} of the crystallographic planes of crystallites is modified [Brenner et al., 2009, Lebensohn et al., 2011, Gu et al., 2017]. This variation is noted Δd_{hkl}. The elastic strain underwent by the grains is referred to as lattice strain[20] and is expressed by the relative variation of d_{hkl}, as shown in equation (2.3) :

$$\varepsilon_{hkl} = \frac{\Delta d_{hkl}}{d_{hkl}} = -\frac{\Delta 2\theta}{2\tan(\theta_{hkl})}. \tag{2.3}$$

Through Bragg's law, it is possible to link the variation of d_{hkl} and the variation of the diffraction cone angle θ_{hkl} (called a shift). θ_{hkl} corresponds to the position of the diffraction cone when the material is not loaded. Figure 2.23 shows an example of the positive variation of the angular position θ_{hkl} of the diffraction cone when a specimen is subjected to a macroscopic longitudinal compression load.

20. The elastic strain is heterogeneous at the grain scale owing to the anisotropic elastic behavior of the crystal.

2.4.2.2 Treatment of XRD patterns

To estimate the lattice strain, the observed diffraction cone is intercepted with the 2D detector which only sees one ring (see Figures 2.23). The acquired XRD image (see Fig. 2.24a) is replotted in a new coordinates system, 2θ vs. ψ, in which the ring portion appears to be straight (see Fig. 2.24b). This operation is conducted by an azimuthal regroupment performed using pyFAI[21] [Kieffer and Karkoulis, 2013]. This hkl diffraction ring is then integrated along its length and is represented as a 1D hkl diffraction peak in an 'intensity versus 2θ position' plot (see Fig. 2.24c). For further details, the complete procedure is reported in [Ors et al., 2019].
The azimuthal integration along the ring length provides a diffraction peak that is representative of the average behavior of numerous grains, which contributed to the studied portion of the diffraction cone.

To exploit the information contained in the experimental diffraction rings, the integrated diffraction peaks must be fitted. The fitting of the peaks is done with an asymmetrical Pearson VII distribution. The formula of the Pearson VII function used is given by equation (2.4).

$$P_7(2\theta) = \frac{A}{\left[1 + 4(2^{\frac{1}{m}} - 1)\frac{(2\theta - 2\theta_{hkl})^2}{W^2}\right]^m} + B. \tag{2.4}$$

where $2\theta_{hkl}$ is the position of the maximum of the peak, W the full-width at half maximum (FWHM) of the peak, A is the area under the peak, B is the baseline of the peak and m is its shape factor. This Pearson VII distribution is used in two halves, one for each side of the peak to account for the peak asymmetry [Howard and Preston, 1989]. A Heaviside function is implemented such that :

$$I(2\theta) = P_{7,left}(2\theta)H(-\theta + \theta_{hkl}) + P_{7,right}(2\theta)H(\theta - \theta_{hkl}). \tag{2.5}$$

The fitting procedure finds the best fit relying on the least-squares method.
The fitting parameters are identified from Figure 2.24c, in the case of steel. They are reported in Table 2.9.

21. pyFAI is a Python library with which diffraction data treatment is commonly conducted.

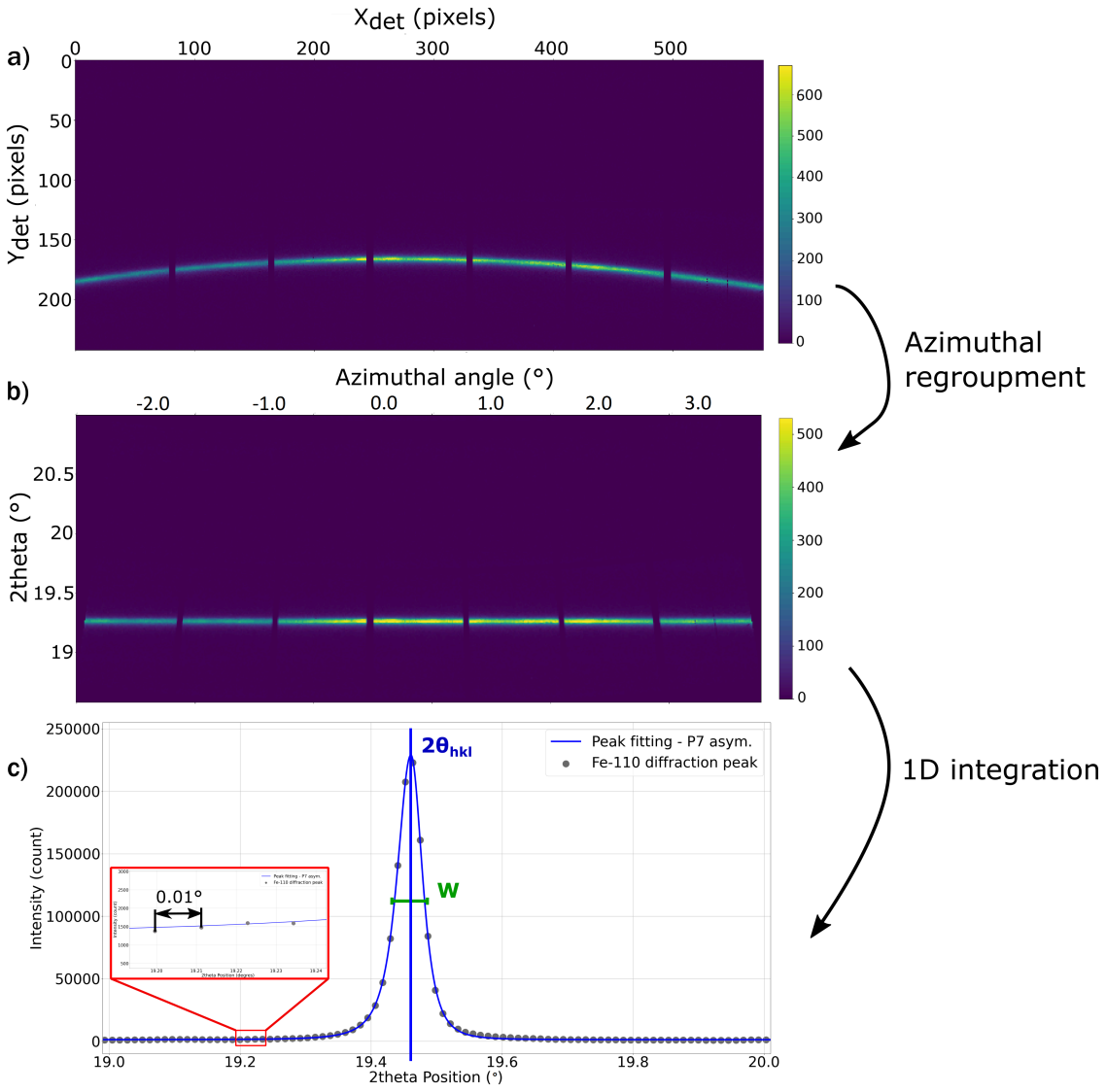


FIGURE 2.24 – Organigram of the methodology to obtain a diffraction peak from a diffraction pattern. Case of C70 steel ; XPAD S140 total exposure time of 1 s ; energy of the beam : 18 keV.

TABLE 2.9 – Example of parameters of the Pearson VII asymmetrical fit function for the peak showed in Figure 2.24. Two widths and two shape factors are considered to fit both sides of the peak. The area and peak position is the same for both sides. - Case of C70 steel, Energy = 18 keV.

Parameter (hkl)	2θ (°)	A	W_{left} (°)	W_{right} (°)	m_{left}	m_{right}	B
Value	19.46	2.27×10^5	4.1×10^{-2}	4.9×10^{-2}	1.78	1.63	1.28×10^3

The elastic lattice strain that takes place in the grains can be estimated from the shift of the diffraction peak. Besides, the peak broadening can as well be studied [Berkum et al., 1996, Ungár, 2004, Vashista and Paul, 2012]. The diffraction peak width, referred to as Full-Width at Half Maximum (FWHM) is representative of the stress heterogeneity[22], the dislocation structures and the material microstructural state [Berkum et al., 1996]. The contributions to the broadening of a diffraction peak are the grain boundaries, the dislocation density and the mosaicity[23] of the crystallites of the material as well as the elastic anisotropy. In addition, the FHWM of diffraction peaks (and their evolution under a loading or a heat treatment for instance) has even been used to estimate dislocation densities in metals [Ungár, 2001, Groma and Szekely, 2006].

The function in equation (2.5) allows one to correctly fit the peaks that are themselves asymmetrical, which is the case of diffraction peaks of numerous materials. The asymmetry of a diffraction peak can arise from the experimental and optical setup that is used but also from the material's microstructural state. In fact, the asymmetry arising from the material state generally depends on material defects such as dislocations, stacking faults, twins faults, boundaries, impurities, etc. [Krivoglaz, 1996]. For the steel, the stronger the difference between the width and shape factor of each side of the peak, the stronger the asymmetry.

2.4.2.3 Uncertainties on the treatment of XRD patterns

Uncertainties are estimated on the estimation of the diffraction peak angular positions 2θ and FWHMs. These uncertainties account for the noise observed on XRD images and the fitting procedure on the determination of the parameters of the peak. To compute the uncertainties experimentally, 50 XRD images of the same diffraction peak were successively recorded (with the same time aperture) while the specimen was not loaded. The acquired peaks are thus supposed to have the exact same position and width. A standard deviation was measured on the overall 2θ positions and FWHMs of the 50 peaks. This standard deviation will act as the random error for the position (and width) of a single peak. This uncertainty depends strongly on the quality of the images, i.e. on the signal-to-noise ratio (SNR) of the images. The SNR of an image is calculated as defined in equation (2.6) and the principle is exposed in Figure 2.25 (for a time aperture of the detector of 2 s) :

$$SNR = \frac{I_{max}}{I_{noise,mean}}. \tag{2.6}$$

22. The stress heterogeneity arises from the fact that each dislocation induces a heterogeneous stress state in the crystal.
23. The mosaicity widens the diffraction peak in the azimuthal direction but not in the 2θ direction.

with I_{Max} the maximum intensity of the peak and $I_{noise,mean}$ is the background noise which is estimated as the range of fluctuation of the diffraction baseline measured a few degrees apart from the peak on the 'Intensity versus 2θ' profile. The deterministic quantity of the SNR is the maximum intensity. In the case of a 1 second exposure of the XPAD S140 detector, I_{max} is about 110000 (resp. 2300000) counts for steel (resp. copper single crystal) with respect to a baseline that is around 6300 (resp. 2000) counts for steel (resp. copper single crystal).

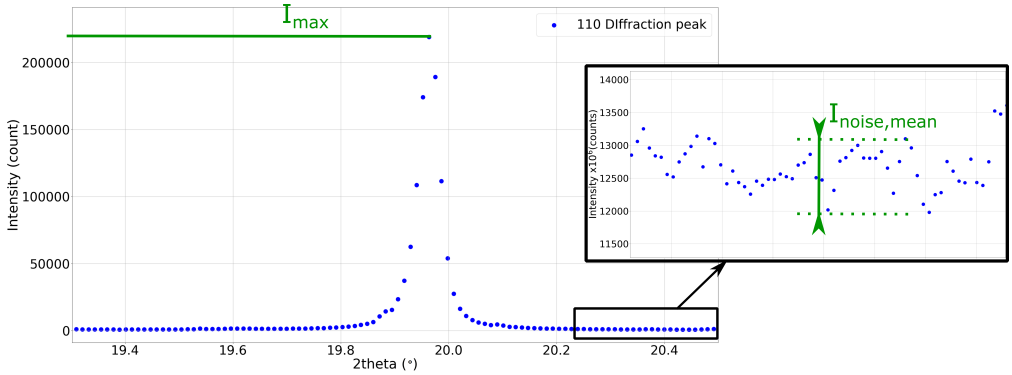
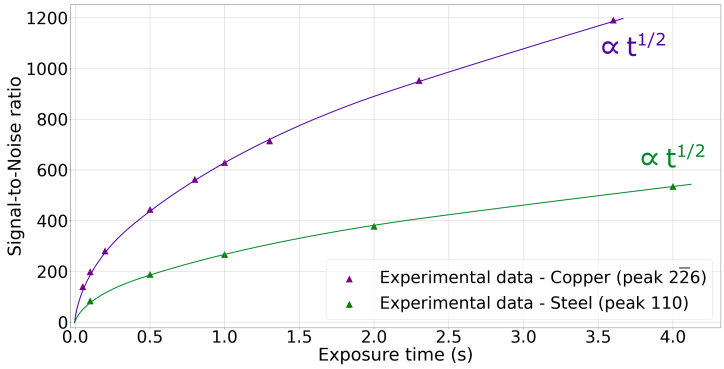


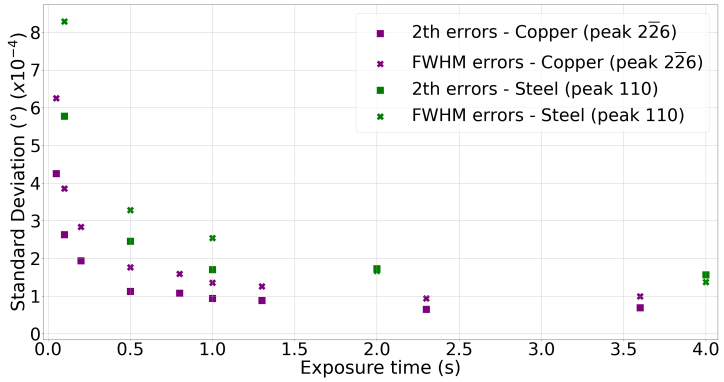
FIGURE 2.25 – Determination of the SNR from the study of a diffraction peak - case of ferrite 110 diffraction peak of C70 steel with an time exposure of 2 seconds ; energy of the beam : 18 keV.

The abovementioned statistical study was conducted in the case of the diffraction ring 110 of the ferrite phase of C70 steel and diffraction spot $2\bar{2}6$ of copper. The evolution of the SNR with the exposure time of an XRD image is plotted in Figure 2.26a. The SNR increases (in a squareroot evolution) with the exposure time of the XRD images ; the higher the time exposure, the higher the number of photons to hit the surface of the detector. The SNR is twice higher for copper owing to its single crystal structure that increases the intensity of the diffraction spot compared to the background of the XRD image. In addition, Figure 2.26b shows the evolution of the random error measured on the estimation of the peak position and width with respect to the exposure time. These errors take into account the effect of the noise on the XRD images and the bias introduced by the fitting procedure. The respective errors of both quantities are decreasing with the time exposure in an inverse exponential trend. Errors are smaller for copper, owing to the better SNR of its diffraction pattern.

Copper diffraction peaks usually show an angular displacement higher than $10^{-2\circ}$ for stress amplitudes higher than 50 MPa whereas steel peaks show displacement in the order of $4 \times 10^{-3\circ}$ for stress amplitudes above 100 MPa (and under an X-ray beam settled at an energy of 18 keV). Thus, to reduce the influence of the random error on



(a)



(b)

FIGURE 2.26 – a) Evolution of the Signal-to-Noise ratio with the time exposure and b) Random error on the estimation of 2θ positions and FWHM with the time exposure (estimated through the fitting of 50 diffraction peaks).

the amplitude of displacement of the peaks (to be lower than 5% for instance), the SNR should be higher than 200 for copper and steel. This corresponds to a time exposure of X-ray diffraction images of 0.1 s for copper and 2 s for steel.

2.4.2.4 Determination of the stress

The objective is to link the lattice strain, measured by XRD from the diffraction peak shifting, with the equivalent macroscopic stress that is applied to the specimen. This link is established through scale transition models. Such a model requires the identification of a parameter called X-ray elastic constant (XEC) to be computed. Specimens are oriented such that the external stress is applied along direction **x** and the lattice strain is measured along direction **z**[24]. Thus, the macroscopic longitudinal stress is calculated

24. This direction is parallel to the $[hkl]$ direction of the observed crystallites.

from the lattice strain and is expressed as :

$$\sigma_{xx} = \frac{\varepsilon_{hkl}}{s_{xxzz,hkl}}. \tag{2.7}$$

where s_{xxzz} is the XEC that relates the lattice strain (estimated in grains with (hkl) crystallographic planes diffracting) and the equivalent macroscopic stress applied along the longitudinal direction of the specimen. Each grain with (hkl) orientation has a corresponding XEC value. The estimation of XECs depends on the material microstructure and its elastic properties.

In the case of a copper single crystal oriented along the [110] direction, the estimation of the XEC is straightforward and consists in a calculation based on the elastic constants of the material. The compliance constants are estimated from the elastic constants exposed in Table 2.2 as :

$$S_{11} = \frac{C_{11} + C_{12}}{(C_{11} - C_{12})(C_{11} + 2C_{12})} = 0.01499 GPa^{-1}. \tag{2.8}$$

$$S_{12} = -\frac{C_{12}}{(C_{11} - C_{12})(C_{11} + 2C_{12})} = -0.00628 GPa^{-1}. \tag{2.9}$$

$$S_{44} = \frac{1}{C_{44}} = 0.01326 GPa^{-1}. \tag{2.10}$$

Then, accounting for an elastic cubic behavior at the scale of the grain and by considering that the loading is applied in the [110] direction (also corresponding to direction **x** of the specimen) one can link the stress and strain through the involvement of the deformation tensor such as :

$$\left[\varepsilon\right] = \frac{1}{2}\begin{bmatrix} \frac{1}{2}(S_{11}+S_{12}) & \frac{1}{2}S_{44} & 0 \\ \frac{1}{2}S_{44} & \frac{1}{2}(S_{11}+S_{12}) & 0 \\ 0 & 0 & 2S_{12} \end{bmatrix} \times \frac{1}{\sigma_{xx}}. \tag{2.11}$$

This strain is projected along the direction of the measurement (i.e. the direction of the diffraction vector K_{hkl}) such that :

$$K_{hkl} \otimes K_{hkl} = \begin{bmatrix} h \\ k \\ l \end{bmatrix} \otimes \begin{bmatrix} h \\ k \\ l \end{bmatrix} = \begin{bmatrix} h^2 & hk & hl \\ kh & k^2 & kl \\ lh & lk & l^2 \end{bmatrix}. \tag{2.12}$$

Then, the calculation of an XEC (expressed in MPa^{-1}) can be formulated as follows

from the multiplication of both matrixes from equations (2.11) and (2.12) :

$$s_{xxzz}(hkl) = \frac{1}{h^2+l^2+k^2} \times \left(S_{11}\frac{k^2+h^2}{2} + S_{12}\left(\frac{k^2+h^2}{2}+l^2\right) + S_{44}\frac{hk}{2} \right). \quad (2.13)$$

Tables 2.10 provides the XEC of the pure copper single crystal specimens in their two orientations.

TABLE 2.10 – XEC of the two diffraction peaks studied for the pure copper single crystal.

Diffraction peak (hkl)	$2\bar{2}6$	$5\bar{5}5$
s_{xxzz} (MPa^{-1})	-4.966×10^{-6}	-1.403×10^{-6}

However, in the case of the polycrystalline steel, the estimation of the XECs requires the use of modelisation. The XECs are estimated similarly to what was exposed previously in the case of a single crystal ; that is according to a cubic elastic behavior at the grain scale. However, because the set of crystallites under diffraction condition (i.e. in "the diffraction volume") is only part of the whole specimen, scale transition models, which bridge the grain deformation with the macroscopic strain are necessary to express the relationship between ε_{hkl} and σ_{xx}. A micro-macro Self-Consistent (SC) model [Hershey, 1954] [Kröner, 1978] is used to estimate the XECs for the studied material [Vermeulen, 2001, Faurie et al., 2009, Vermeulen et al., 2019]. It relies on an homogeneisation scheme consisting in the simulation of randomly mixed crystallites with random orientations in an equivalent representative volume element (RVE). The model considers the elastic properties of each phase (ferrite and cementite) of the modeled material as well as the average grain size (and shape) and the specimen microstructure. Tables 2.11 provides the XEC of the studied crystallites from both phases of the C70 steel, computed from a SC model.

TABLE 2.11 – XEC of the three diffraction peaks studied for the C70 pearlitic steel.

Diffraction peak (hkl)	Fe 110	Fe 220	Fe_3C 102
s_{xxzz} (MPa^{-1})	-1.32×10^{-6}	-1.32×10^{-6}	-1.29×10^{-6}

2.4.2.5 Uncertainties on the estimation of the XEC

For copper, the uncertainties on the estimation of the XEC are estimated from the uncertainties on the elastic properties of the materials. These uncertainties are in the order

of 1% of the value of the XEC for $1\bar{1}3$ and $1\bar{1}1$ crystallites [Ledbetter and Naimon, 1974].

For steel, the uncertainties on the estimation of the XEC are considered as extremum variations from the consideration of extreme limits determined with Voigt and Reus models. From such estimation, the XEC of ferrite and cementite phases were both varying from -8% to +12% of the estimated values. The uncertainties observed for steel are bigger than those of copper. In fact, it is considered that the homogenization scheme can introduce bias in the estimation.

2.4.2.6 Experimental setup

The experimental developments were conducted at the DiffAbs beamline at SOLEIL Synchrotron in France. The use of a synchrotron X-ray source is required to acquire diffraction images that show a sufficient SNR (see the previous sections). The characteristics and capacities of the DiffAbs beamline are presented in [Thiaudière et al., 2012]. This review is ten years old but is still mostly up to date. The work of [Gallard, 2019] gives an update of the beamline characteristics up to the current time of this Ph.D. work. The most important parameters of the beamline are recalled here after :

- Energy span of the beamline : 3.5 to 23 keV. The beam was settled at 18 keV here.
- Energy resolution of $\frac{\Delta E}{E} = 10^{-4}$ with a monochromatic beam.
- The beam size at the specimen level is about 180×240 µm^2 (FWHM, Vertical $\times$ Horizontal) in all our experiments.
- The photon flux on the specimen is 10^{12} to 10^{13} $photons/$s.

To conduct XRD measurements during a fatigue loading, the ultrasonic fatigue machine was settled on the 6-circles diffractometer at the DiffAbs beamline. The experimental setup is showed in Figure 2.27. The specimen is positioned such that its central part is in the direct beam. The fatigue machine loads the specimen in its first longitudinal mode of free vibration (the loading ratio being R=-1). The vibration induces a strong stress and strain state in its center but no displacement. Therefore, the continuous observation of this zone at the surface of the specimen is possible with XRD and enables one to assess the stress state of the specimen during its loading, i.e. in situ. A 2D detector is used to acquire XRD images. Such a detector is mounted on an independent arm that can be rotated horizontally and vertically to observe all the diffraction rings of crystalline materials. The six circles diffractometer, and especially its connector board on which the machine is mounted, could be moved and tilted to induce an incident angle of the specimen. This allows one to always conduct XRD measurements in a $\theta - 2\theta$ symmetrical configuration for all diffraction rings to be studied.

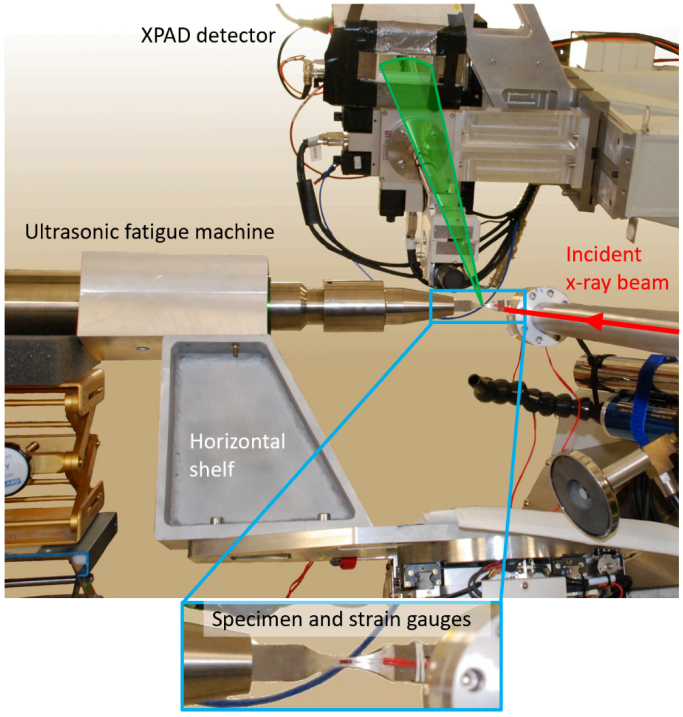


FIGURE 2.27 – Picture of the experimental setup that was installed on the diffractometer at the DiffAbs beamline, SOLEIL Synchrotron.

The DiffAbs beamline is equipped with hybrid pixel detectors, which are adapted to conduct fast X-ray analysis [Boudet et al., 2003, Basolo et al., 2008, Le Bourlot et al., 2012]. This type of detector is composed of multiple chips, which are small plates on which 80×120 pixels (each have a $130 \times 130 \mu m$ size) are fixed and bumped to high-speed reading electronics. This detector is called a single photon detector because every pixel is independently connected to an electronics reading element and can count each photon that hits the pixel. Also, the reading time of such a detector is very short : about a few milliseconds. The electronic shutter used in such a detector allow for very small detector opening, as small as 100 ns [Berar et al., 2009, Buton et al., 2014]. The XPAD S140 hybrid pixel detector available at the DiffAbs beamine was used to conduct the XRD measurements. It is composed of two modules constituted of seven chips each, accounting for a total surface of 134400 pixels [Dawiec et al., 2016]. The pixels of the XPAD detector have a counter depth that is of 12-bit dynamics but can be extended up to 16 or 32-bit through the use of an overflow bit (see [Dawiec et al., 2016]).

2.4.2.7 Accuracy of the measurements

To study X-ray diffraction and to precisely follow a diffraction cone during short acquisitions, such a detector must exhibit a very fine angular resolution. The angular resolution of the diffraction peak[25] integrated from XRD images depends on the experimental configuration. It is expressed in degree per pixel and depends on the size of the pixels and on the distance between the detector and the specimen which diffracts. For instance, the XPAD S140 detector was commonly placed at a distance of 640 to 720 mm of the specimen, which corresponds to a resolution of the XRD images ranging between 0.0116 and 0.0103 °/pixel.

For instance, for a loading of 100 MPa applied to a steel specimen (under an X-ray beam settled at an energy of 18 keV), the shift of the angular position of the diffraction cone of the 110 ferrite crystallites is about $2 \times 10^{-3\circ}$. Thus, a sub-pixel resolution is required. Such resolution is achieved by fitting the diffraction peak with the procedure detailed above. It is to be noted that the diffraction peak FWHM (in the case of steel) is four times higher than the abovementioned resolution (see Table 2.9).

During the measurements carried out on the beamline, the X-ray beam was seen to drift[26]. The beam drifts influence the results of the diffraction measurements. Indeed, a change in the incident beam position corresponds to a change of the position of the diffracted beam as well[27]. This effect is schematically represented in Figure 2.28. Thus, a shift of the angular position of a diffraction cone could be seen by the detector whereas it is not related to a change in the material stress state, in the case of prolonged acquisitions.

The drifts of the beam have been characterized during this work and were measured with a camera[28] that is fixed to the diffractometer of the beamline in front of the direct beam. The position of the beam was continuously assessed during several hours and a drift could be seen in its horizontal position but more importantly in its vertical position. Typically, the beam drifts vertically of 50 µm/h. A drift of 50 µm of the vertical beam

25. The angular resolution of a diffraction peak corresponds to the space between two points on the integrated peak (see Fig. 2.24).

26. The X-ray beam can drift for various reasons. It might come from a temperature change in the monochromator where it is focused, from a slight change in the bunches of electrons in the storage ring of the synchrotron or from any change in the optical alignment that conditions the beam until its projection towards the specimen. The true reason is still unknown and the reasons mentioned above are only considered and not verified.

27. The drift might also influence the FWHM of the diffraction peak, but this correlation has not been evidenced by the experimental results.

28. The Basler camera square pixels are 16 µm wide. Its fine resolution allows one to measure a change in the beam position of at least two microns when interpolating the image it acquires.

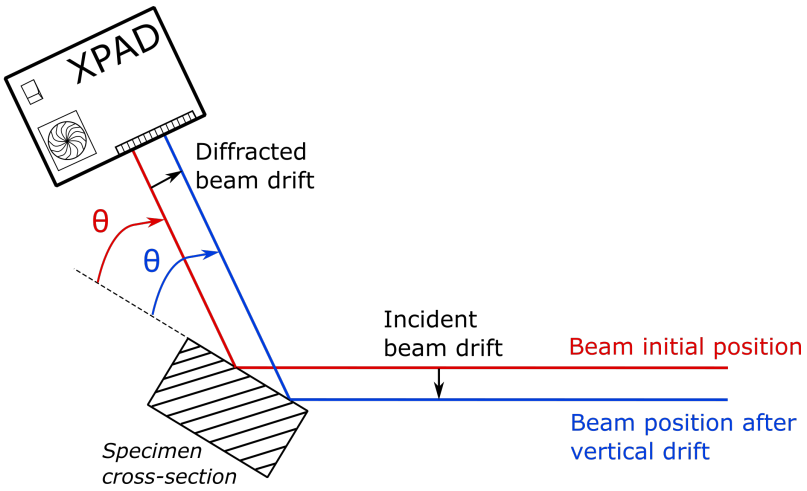


FIGURE 2.28 – Influence of the vertical beam drift on the measured position of the diffracted beam with the XPAD S140 detector.

position will induce a drift of the diffracted beam of $-2.5 \times 10^{-4\circ}$ on the XPAD detector. For copper (res. steel) subjected to a stress of 50 MPa (resp. 100 MPa), its diffraction peaks show angular displacement higher than $10^{-2\circ}$ (resp. $2 \times 10^{-3\circ}$). Thus, during a one hour assessment of the position of diffraction peaks of copper (resp. steel), the beam drift would correspond to 2.5% (resp. 12.5%) of the nominal peak angular displacement. C70 steel is thus more subjected to the influence of the beam drift.

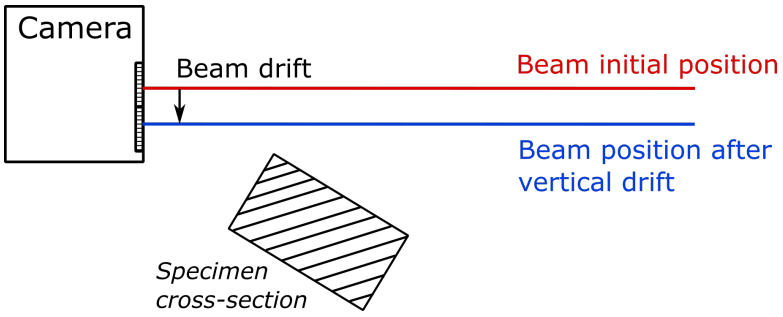


FIGURE 2.29 – Assessment of the vertical beam drift with the use of a Basler camera settled in front of the X-ray beam. The specimen is taken down to allow a direct exposure of the camera to the direct beam.

The beam position can be corrected manually. Yet, this correction only helps to put the beam back in its initial position and does not guarantee that it will not drift further. Genuinely, the drifts can only be assessed to confirm that a continuous change in a diffraction ring angular position is due to the drifts and not to a change in the stress (or thermal) state of the material.

2.4.3 Development of an experimental time-resolved methodology

2.4.3.1 Time-resolved measurements - Pump-probe methodology

Historically, pump-probe methods represent the rudiments for time-resolved XRD experiments. In short, a pump applies an external load to a material. To be fast enough, pumps are generally optical such as laser pulses [Inogamov et al., 2010, Zhu et al., 2017]. The probe, which is generally composed of a (pulsed) light source and a detector, acquires data to study the material state evolution during the application of the load [Neutze and Hajdu, 1997, Rehn et al., 1990, Elzinga et al., 1987]. The pump-probe process is iterated and allows one to follow a material evolution under an external repeated load. Figure 2.30 shows the principle for the pump and the probe activation with signals represented versus time. The pump (a laser for instance) is triggered at a given time and triggers a pulse which is shot at the material and makes its state change locally. The trigger signal of the probe (an optical or XRD detector for example) happens after a certain time delay to observe the material state. The most important characteristic of this methodology is to be able to finely tune the delay between the pump and the probe to be able to observe the desired state of the material. Considering the temporal domain, a pump-probe technique can measure deterministic processes with a time resolution determined by the pulse duration of the light source or the detector time opening observed in typical multiframe imaging. Thus, a pump-probe method can show a time resolution as fine as a few femtoseconds [French, 1996].

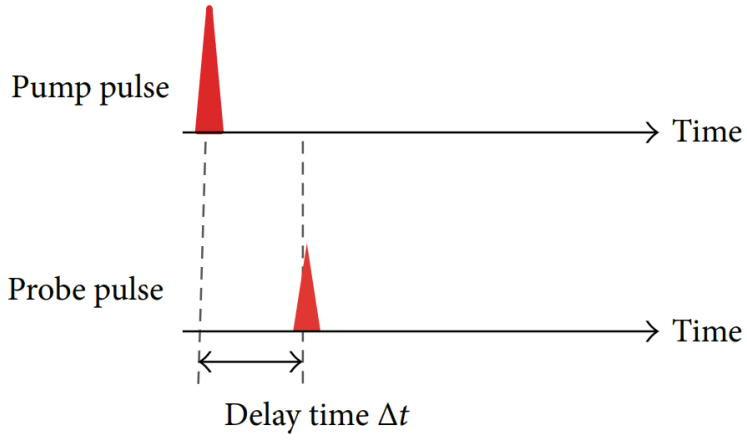


FIGURE 2.30 – Principle of data acquisition based on a pump-probe approach. Adapted from [Wang et al., 2013].

Several intrinsic ultrafast processes were developed by applying very fast measurements using optical, x-ray and electron or photon pulses [Neutze and Hajdu, 1997]

[Bargheer et al., 2006] [Berera et al., 2009] [Yang et al., 2010, Graber et al., 2011]. Nevertheless, the basic developments of pump-probe methods used large X-ray beams and were not able to reach a very fine spatial resolution to study the dynamics of heterogeneity which concerns many fundamentally important and currently relevant phenomena. Synchrotron facilities have the advantage to provide a highly brilliant X-ray beam that can be tuned in a small beam and keep a very high intensity [Ludwig et al., 2010, Rössle et al., 2022].

During this Ph.D., a pump-probe multiframe methodology was developed in which the fatigue machine is the pump and the X-ray source combined with the XPAD detector constitues the probe [Ors et al., 2019, Jacquemain et al., 2021]. This methodology, based on in situ time-resolved XRD measurements, has been applied to two SOLEIL Synchrotron modes : uniform and single-bunch modes. Figure 2.31 shows the representation of the beam intensity with respect to time for each mode. The uniform mode exhibits an X-ray source considered continuous. It corresponds to the contribution of 416 electrons bunches that are revolving in the storage ring of the synchrotron, with a revolution period of 1.1812 µs. The single-bunch mode corresponds to a pulsed X-ray source, for which only one bunch revolves in the storage ring with the same revolution period.

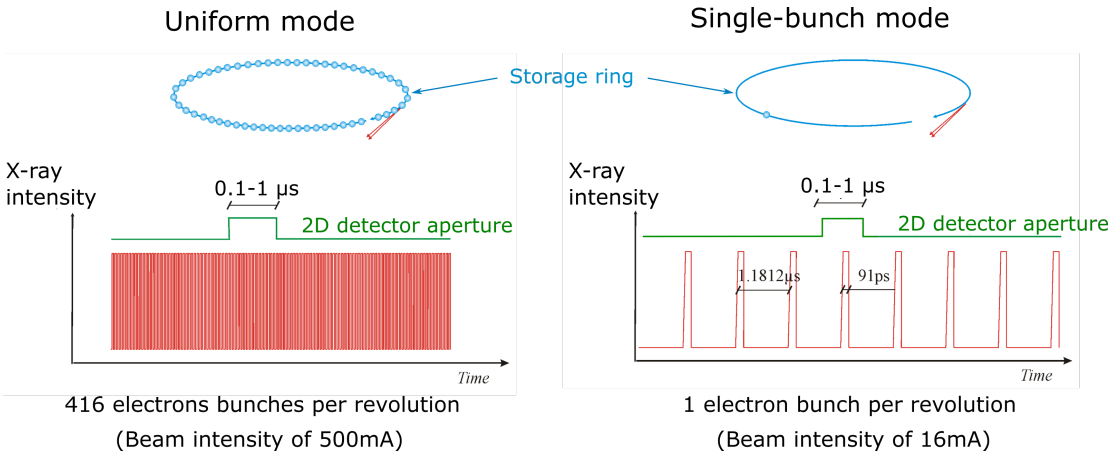


FIGURE 2.31 – Main difference in achievable time resolution between the two synchrotron modes of interest.

2.4.3.2 Principle of data acquisition for uniform and pulsed modes

The principle of measurement of stress and strain, conducted in situ during ultrasonic fatigue tests, is addressed in this section.

The longitudinal stress is computed from the measurement of the evolution of the diffraction peak position through the treatment of XRD images whereas the total strain is measured by using strain gauge. During the fatigue loading, the longitudinal stress and the total strain evolve cyclically. The loading frequency being 20 kHz, the measurements must be conducted at a high sampling frequency by using a stroboscopic approach. The measurement of stress and strain signals is then referred to as reconstruction. The principle of signal reconstruction is depicted in Figure 2.32 and can be defined as follows in the case of total strain :

1. First, a reference time position is chosen on the cyclic loading evolution, i.e. when it crosses zero in an increasing slope for instance.
2. One value of total strain is acquired every cycle during several thousands of cycles in a stroboscopic approach, i.e. at a fixed delay compared to the chosen time position. The average value over the thousands of acquired values corresponds to one point on the signal reconstruction, plotted with respect to the time delay. The accumulation of strain gauge values allows to improve the statistics of the measurement and improve the quality of the strain gauge signal reconstruction.
3. The XRD and strain gauge data are then stored.
4. Then, a different time delay is applied and different values of total strain are acquired during several thousands of cycles as well. This provides a second point on the signal reconstruction
5. The process is repeated with a time delay that evolves to sweep the entire cyclic evolution and acquire different values. This leads to the reconstruction of one sampled cycle as shown in the bottom part of Figure 2.32.
6. Once one cycle is reconstructed, the delay generator resets the time delay at zero and a second cycle is reconstructed following the same procedure.

During the strain gauge values acquisitions, XRD frames are acquired as well by the XPAD detector. The accumulation of XRD frames over thousands of cycles provides a final XRD image with a sufficient SNR (see Section 2.4.2.3). From the final XRD image obtained at each time delay, the estimation of the stress is conducted from the determination of the diffraction peak position. It allows one to reconstruct the sampled cyclic evolution of stress in the same manner as what was exposed for total strain.

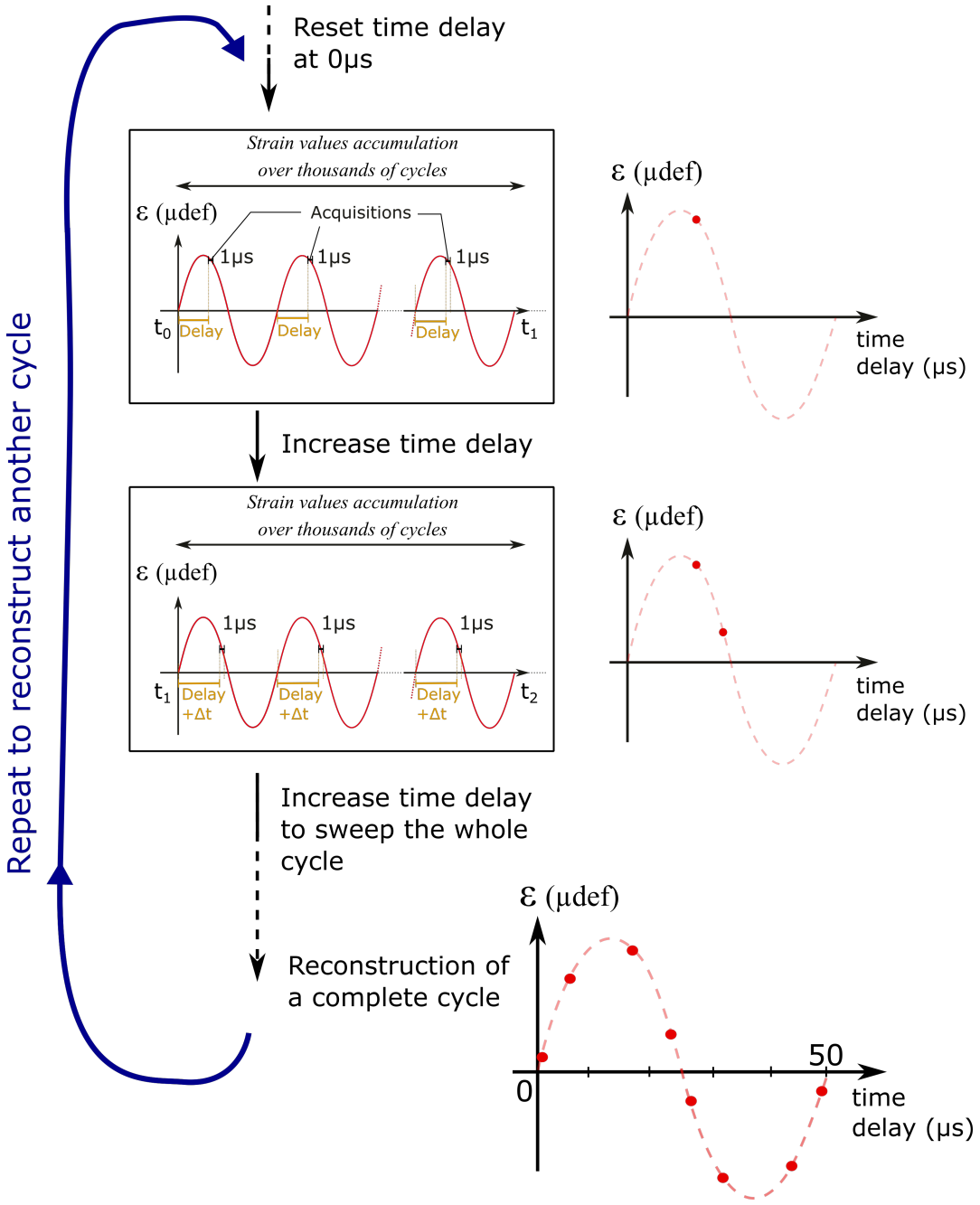


FIGURE 2.32 – Principle of reconstruction of the sampled cyclic evolution of the total strain from acquired strain gauge values.

Each Synchrotron mode requires a specific experimental setup to enable the acquisition of strain gauge values and XRD images.
In uniform mode, the fatigue machine works in its standard mode. The acquisitions are triggered from a threshold value on the input voltage signal of the ultrasonic fatigue

machine. The trigger sets the initial time position on the cyclic evolution (associated with the reconstruction of the first point at a time delay $\Delta t = 0$).
In single-bunch mode, the fatigue machine is synchronized in frequency and phase with the Synchrotron through the use of a master clock board (called "TimBel"). The frequency at which the machine vibrates is that of the electron bunch revolution (in the storage ring) divided by 42, i.e. 20 158 Hz. This specific frequency was chosen to obtain a loading period that is close to that of the machine in its standard mode of functioning. Data acquisitions are triggered by the TimBel board and are synchronized with the X-ray pulses.

The methodology adapted to the uniform mode was already developed and reliable before the start of the Ph.D [Ors et al., 2019]. However, during the course of this Ph.D., this methodology was diverted to be applied to copper single crystal specimens and the methodology adapted to the single bunch mode was completely developed.

2.4.3.3 Experimental setup - uniform mode

The acquisition of data is conducted with an experimental setup constituted of several apparatus, as shown in Figure 2.33a. This setup is constituted of :

- The ultrasonic fatigue machine and its standard power supply to load the specimen. The frequency of vibration is controlled by a PLL (see Section 2.3.1.3).
- A delay generator (namely a T560© digital delay generator) is used to trigger the data acquisitions. It imposes a delay on the output trigger signal to perform acquisitions at different time positions along the cyclic evolutions. It allows one to acquire many points to reconstruct cycles.
- The X-ray detector XPAD S140 to acquire XRD images. The aperture time opening of the detector is controlled by the width of the pulse signal that is imposed upstream by a low-frequency generator (LFG). The LFG is synchronized with the trigger signal coming from the delay generator.
- The strain gauge, whose output signal is read and amplified by a signal conditioner.
- A data acquisition board (namely, an SAI-DAQ acquisition card with a sampling frequency of 2 MS/s) is used to acquire the values of the strain gauge signal.

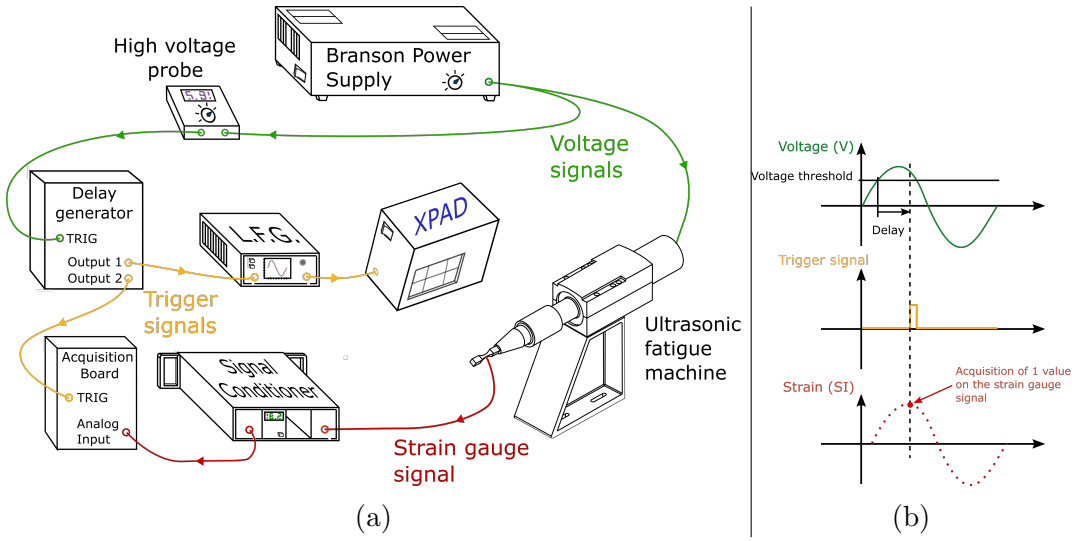


FIGURE 2.33 – a) Experimental setup (acquisition loop) developed to acquire strain and stress evolutions during fatigue loadings at $20kHz$ and b) principle of data acquisition triggered by a threshold on the voltage signal - example of the acquisition of one value of the strain gauge signal.

In uniform mode, the acquisitions are triggered by a threshold on the input voltage of the fatigue machine (see Figure 2.33b). Each time the threshold is exceeded by the voltage signal, one value of total strain and one XRD frame are acquired. The process is repeated over 2000 up to 20000 times for one fixed delay. The delay is evolving by steps of 1 µs to sweep the complete period. Thus, the number of points to reconstruct one cycle is settled at 50.

In addition, the time resolution of the methodology is directly correlated to the detector aperture time in uniform mode [Ors et al., 2019, Jacquemain et al., 2021]. Typically, the integration time of the hybrid pixel detector was set at 1 μs. A detector aperture time of 1 µs corresponds to a compromise between the small variation of the diffraction peak angular position when XRD images are acquired and a sufficient amount of photons hitting the detector during the exposure.

2.4.3.4 Experimental setup - single-bunch mode

In single-bunch mode, the beamline only lights the studied material for a duration of 91 ps during regular pulses. This duration becomes predominant compared to the detector aperture opening and thus corresponds to the achievable time resolution in this approach. In addition, XRD frames must now be acquired at the exact time of the X-ray pulses occurrence. To ensure this synchronization, the 2D detector is generally opened

during a few hundreds of nanoseconds (generally 300 ns) with a window centered around the time position of the X-ray pulse to easily capture the short pulse. This is possible by using the TimBel synchronization board that generates a signal that is synchronized with the revolution of the single electron bunch in the storage ring [Ricaud et al., 2011].

An experimental setup adapted to the single-bunch mode of SOLEIL Synchrotron was developed and is represented in Figure 2.34a. It is composed of :

- The TimBel board is used to synchronize the vibration of the fatigue machine with a multiple of the frequency of the synchrotron (i.e. at a frequency of 20 158 Hz). It also triggers the acquisitions of data at the same frequency.
- A T560© delay generator is still used to trigger the data acquisitions. It imposes a delay on the output trigger signal of the TimeBel board.
- The developed power supply that takes the output square signal of the TimBel board as an input and generates a synchronized sinusoidal signal to power the piezoelectric converter of the ultrasonic fatigue machine.
- The XPAD S140 detector is used to acquire XRD frames. Its aperture time is tuned by the width of the pulse sent by a low-frequency generator.
- The strain gauge, whose output signal is read and amplified by a signal conditioner.
- The acquisition board used to acquire the values of the strain gauge signal is a RedPitaya STEMlab 125-14 board with a sampling frequency of 125 MS/s.

The stroboscopic principle is obviously applied in single-bunch mode as well. The acquisition of one XRD frame is triggered every 42 bunches, i.e. once per loading cycle, by the TimBel board. The delay is evolving by steps of 1.1812 µs to sweep the complete period and conduct XRD frame acquisitions at the times when the X-ray pulses light the specimen. In parallel, values of the strain gauge signal are acquired as well following the same process. Finally, the number of points to reconstruct one cycle is limited to 42.

The methodology was adapted to the single-bunch mode to cope with the strong influence of noise on the XRD measurements conducted on steel. The diffraction peaks that are studied for steel are showing low angular displacement under loading, compared to that of a copper diffraction peak. In addition, the intensity captured in one detector opening in single-bunch mode is smaller than that of the uniform mode. In fact, the duration of the detector exposure was brought from 1 µs to 91 ps and the intensity of the X-ray beam from 500 to 16 mA. Thus, the number of frames to accumulate is more important in single-bunch mode to reach a sufficient SNR on the final XRD images. It is typically larger than 800000. The number of strain gauge values accumulated is about 1500 and is limited by the RedPitaya board. This leads to cycle reconstructions that are longer, i.e. more subjected to beam drift influence. However, the low time resolution

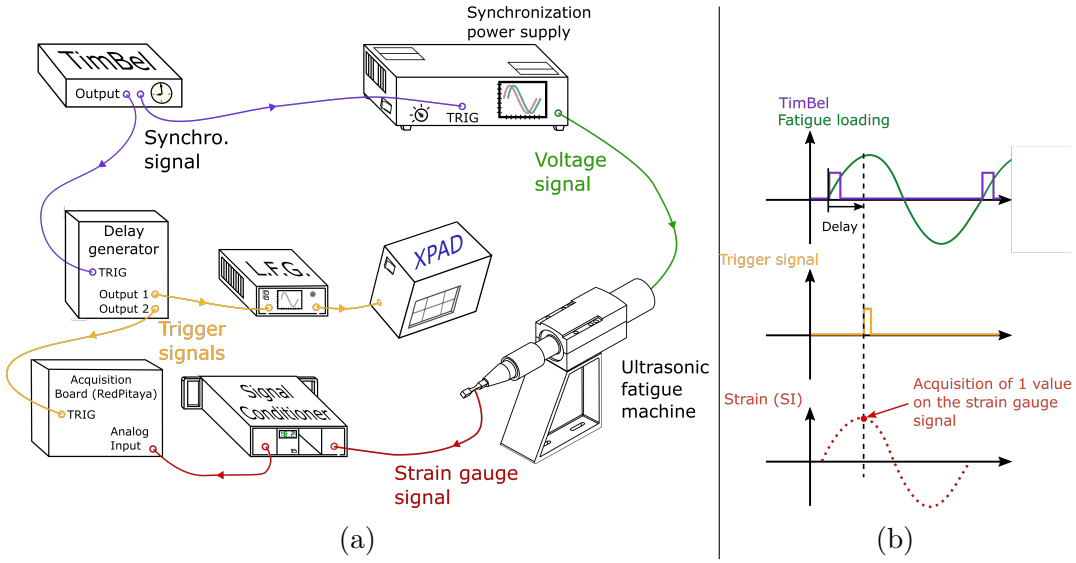


FIGURE 2.34 – a) Schematic representation of the acquisition loop used to acquire data which was adapted to the pulsed (single-bunch) mode at SOLEIL Synchrotron and b) principle of data acquisition triggered by the TimBel signal - acquisition of one value of total strain.

achieved in single-bunch mode improves the time accuracy of the reconstructions and reduces the influence of the image noise on the cycle reconstructions.

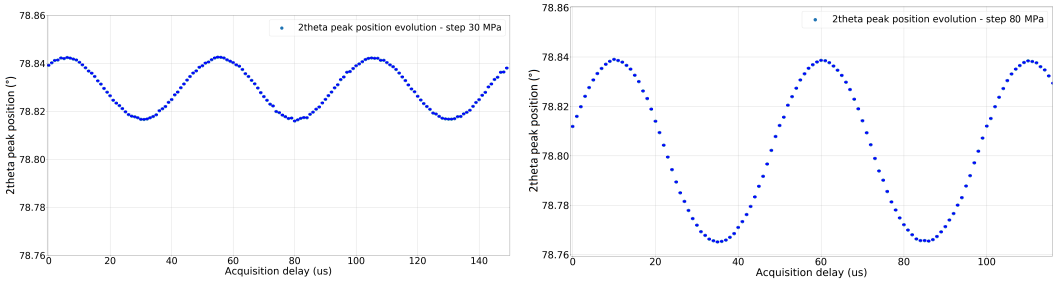
2.4.3.5 Periodic evolutions of diffraction peaks

The abovementioned measurements were conducted in uniform mode on a copper single crystal and the focus was made on diffraction peak $2\bar{2}6$ that shows an SNR of 500. XRD images were acquired in situ during the fatigue loading and were then post-treated. From the fitting of the diffraction patterns observed on these images, the periodic evolutions of the peak shifting and peak broadening are reconstructed. These evolutions, are respectively plotted in Figures 2.35 and 2.36 for stress amplitudes of 30 and 80 MPa.

The plots contain at least two cyclic evolutions of 2θ positions and FWHM. Both reconstructed cycles were acquired successively and for each, the corresponding delay applied to conduct the measurements point by point was ranging from 0 to 50 µs. However, for sake of clarity, the reconstructed periodic evolutions are plotted one after the other with respect to an equivalent time delay.

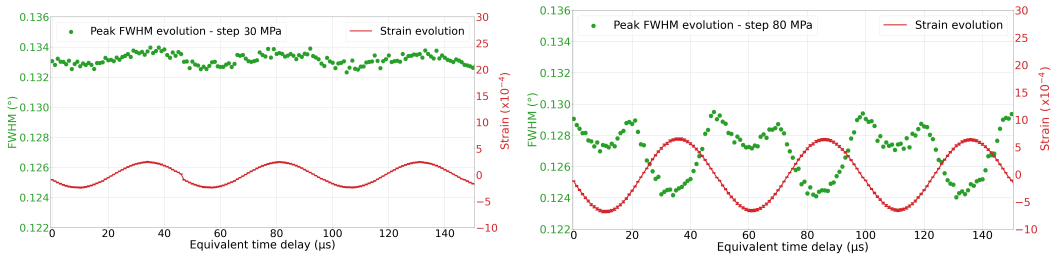
The variation on the 2θ position of the diffraction peak shows a sinusoidal evolution with time. The evolution of the FWHM is sinusoidal for stress amplitudes in the range of 30 MPa. For higher stress amplitudes, in the order of 80 MPa, the FWHM shows a

more complex evolution. Similar evolutions of the diffraction peak FWHM are generally encountered in polycrystalline materials. These evolutions can be modelled by a function like "$A + B \times \sin(\omega t) + C \times \sin(\omega t)^2$" where parameters A, B and C are related to the stress heterogeneity between grains of the matter and to residual stress.



(a) (b)

FIGURE 2.35 – Peak position evolution reconstructed from the fitting of the integrated $2\bar{2}6$ diffraction peak - case of copper single crystal for stress amplitudes of respectively a) 30 MPa and b) 80 MPa.



(a) (b)

FIGURE 2.36 – FWHM evolution reconstructed from the fitting of the integrated $2\bar{2}6$ diffraction peak - case of copper single crystal for stress amplitudes of respectively a) 30 MPa and b) 80 MPa.

The uncertainties, arising from the fitting procedure of the peaks and the noise on XRD images, are estimated following the method presented in Section 2.4.2.3. The error bars made on the estimation of both quantities are smaller than the dot size in both Figures.
From the statistical study of the $2\bar{2}6$ diffraction peak positions, the noise is estimated at $8 \times 10^{-4\circ}$ which corresponds to 5% (resp. 1%) of the amplitude of evolution of the 2θ position for a stress amplitude of 30 MPa (resp. 80 MPa). Thus, the lower the peak displacement, the stronger the influence of the random error on the reconstructed signals.

The amplitude of variation of the peak position and of the peak width (between two reconstructed points on the evolutions) are smaller than the angular resolution of the

experimental configuration (that is estimated to be in the order of 0.011 °/pixel). These results underline the requirement of the fitting procedure to be able to track such small variations of the parameters of diffraction peaks during the fatigue loading.

2.4.3.6 Estimation of stress and strain evolutions

From the evolution of the peak shifting and from the strain gauge values acquired to reconstruct one cyclic evolution, the stress and strain signals can be determined. The stress and strain evolutions are plotted as two discrete signals of 50 points per cycle, in the same time basis, as shown in Figure 2.37. The stress and strain are found to have an evolution with time that is sinusoidal. Concerning the error bars of the stress signal, the corresponding uncertainty, arising from the peak fitting and the noise of the XRD images, was quantified to be close to 3 MPa. The uncertainty on the strain measured by the strain gauge is estimated at 1% (see [Jacquemain et al., 2021]). A time shift ϕ is observed between both signals.

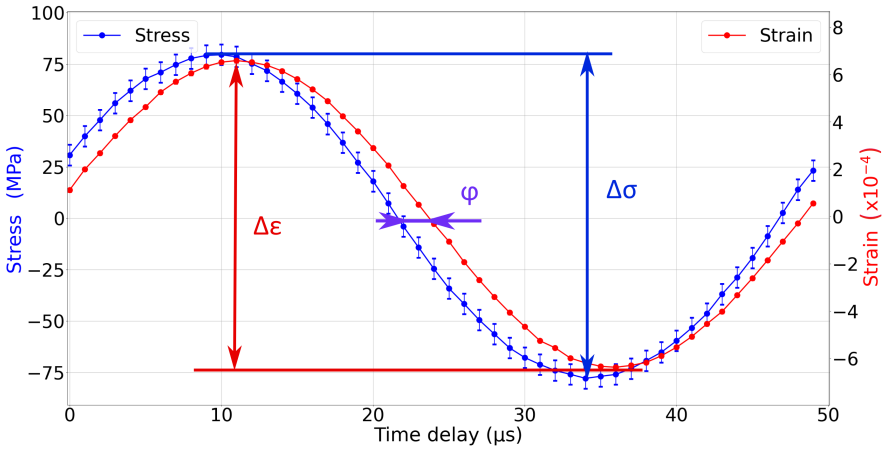


FIGURE 2.37 – Stress and strain signal reconstructed through the stroboscopic principle. Both signals are acquired with the same time basis which allows one to estimate a time shift between the two signals - case of the copper single crystal at a loading amplitude of 80 MPa ; These cycles were reconstructed in uniform mode.

The cyclic evolution of stress with respect to strain is plotted as a hysteresis loop in Figure 2.38. The evolution shows a hysteresis loop that is elliptic with a clear opening. The opening is proportional to the time shift between stress and strain.

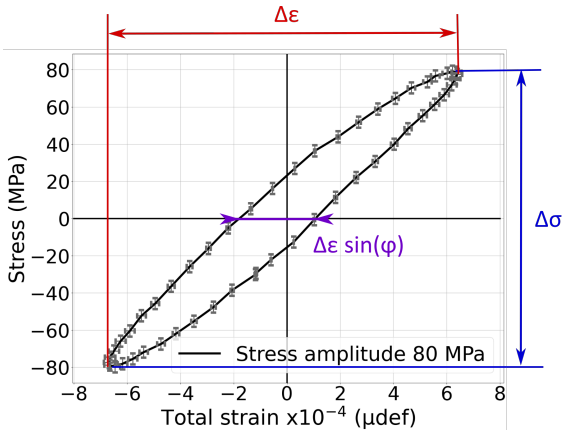


FIGURE 2.38 – Reconstructed hysteresis loop showing the evolution of stress with respect to strain - case of the copper single crystal at a loading amplitude of 80 MPa.

2.4.3.7 Estimation of the mechanical work

From the estimation of stress and strain, it is possible to compute the mechanical work from equation 2.14 :

$$W_{mech} = \int_{cycle} \sigma \dot{\varepsilon} dt. \tag{2.14}$$

From the reconstructions of the cyclic evolutions of stress and strain evidenced in Figure 2.37, their evolution is considered sinusoidal such that :

$$\sigma = \Delta\sigma \sin(\omega t). \tag{2.15}$$

$$\varepsilon = \Delta\varepsilon \sin(\omega t + \phi). \tag{2.16}$$

A time shift between stress and strain is considered. It is associated with the opening of the hysteresis loop, as shown in Figure 2.38. Thus, the mechanical work that is brought to the material can be estimated by the following equation :

$$W_{mech} = \int_{cycle} \sigma \dot{\varepsilon} dt = -\pi \frac{\Delta\sigma}{2} \frac{\Delta\varepsilon}{2} \sin(\phi). \tag{2.17}$$

From this formula, it is only required to accurately estimate the stress and strain amplitudes as well as the time shift between both signals. The stress and strain amplitudes are prone to uncertainties that were discussed in the previous section.
The time shift between stress and strain is generally small. An error committed in the determination of its value has important consequences on the estimation of the mechanical work. Consequently, the uncertainties made when estimating the time shift are particularly important to measure.

2.4.3.8 Influence of the experimental setup on the estimation of the time shift

The time shift ϕ between stress and strain is measured as the difference between the respective time shifts of the stress and strain reconstructed signals, as shown in Figure 2.37. In this particular case, i.e. for copper single crystal loaded at 80 MPa, the time shift between stress and strain is estimated at ϕ =1753 ns. This time shift contains the contribution of the experimental setup[29] (induced by the apparatus and cables employed to acquire the data) and of dissipative effects associated with the viscoelastic/plastic behavior of the material.

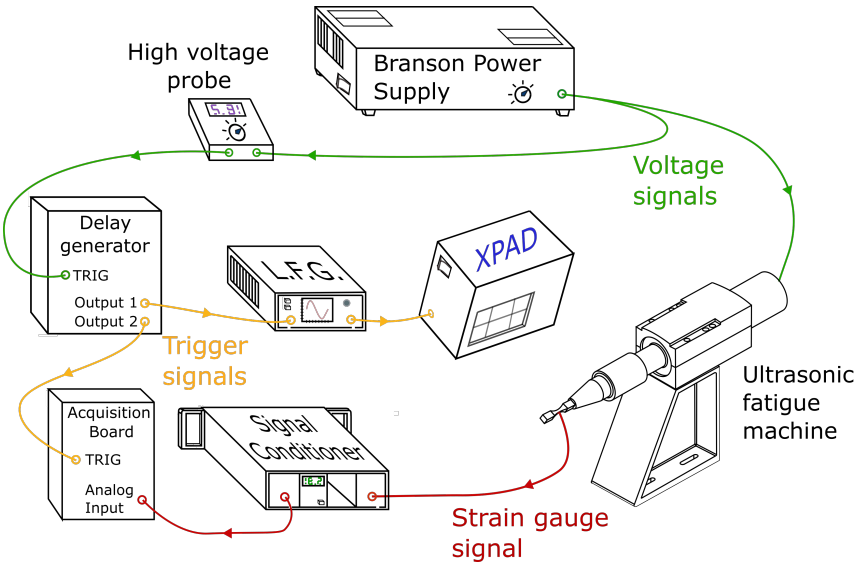
The time shifts induced from the measuring chain were quantified experimentally (before conducting fatigue tests), for the application of the methodology in both modes of SOLEIL Synchrotron. The time shift was measured at each step of the data acquisition setup, especially in each branch of XRD images and strain gauge values respective acquisitions. Figures 2.39 and 2.40 show the experimental contributions to the induced time shift, at several stages of the measuring chain, respectively for the setup in uniform and single-bunch modes. From these measurements, the contribution to the time shift between stress and strain that is induced by the measuring chain is quantifiable. Table 2.12 shows the results of its quantification. The contribution of the measuring chain to the time shift between stress and strain is in the order of 1643 ns as measurements were conducted in uniform mode.

Synchrotron mode	Induced time shift (ns)		Time shift offset (ns)
	Stress signal	Strain signal	
Uniform	13334	14977	1643
Single Bunch	13100	15020	1920

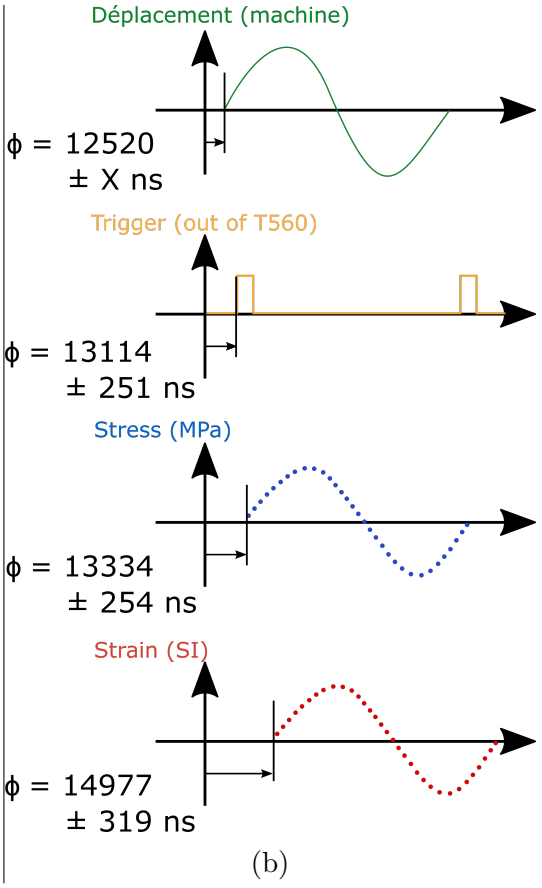
TABLE 2.12 – Total time shift induced on the reconstructed stress and strain signals in both Synchrotron modes.

From Figure 2.37 and in the case of copper single crystal loaded at 80 MPa, it appears that the time shift induced by the measuring chain represents a major contribution to the estimated time shift between stress and strain and that the material only contributes to a time shift in the order of 110 ns.

29. The experimental setup is also referred to as measuring chain.



(a)



(b)

FIGURE 2.39 – a) Recall of the experimental setup and b) associated time shift of the signals at several stages of the process of data acquisition - case of uniform mode.

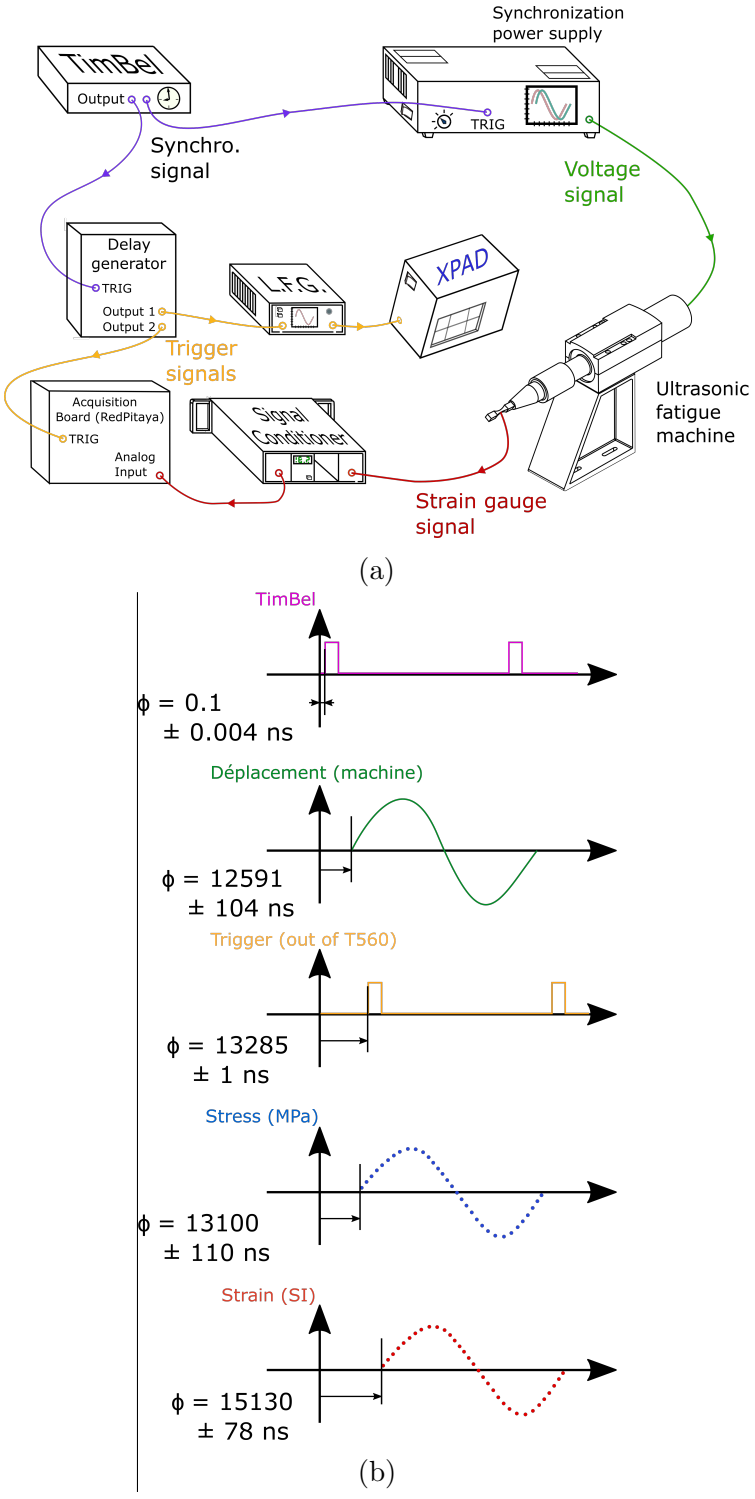


FIGURE 2.40 – a) Recall of the experimental setup and b) associated time shift of the signals at several stages of the process of data acquisition - case of single-bunch mode.

In the following, the time shift between stress and strain will be estimated as a relative evolution to only account for the contribution of the material. The time shift induced by the material is considered to be zero for low-stress amplitudes. Thus, a reference phase shift will be computed for low-stress amplitudes and considered as the reference value only induced by the experimental setup. The relative evolution of the phase shift will be estimated with respect to this reference value.

The types of equipment employed also introduce a jitter[30] on the signals at all steps of the measuring chain ; that corresponds to the uncertainties on the time shift offsets in Figures 2.39 and 2.40. In our case, the jitter will act as an uncertainty on the reconstruction of stress and strain signals and therefore on the estimation of their respective amplitudes and time shifts.

The total jitter, as an envelope, that is introduced by the apparatus constitutive of the measuring chain, can be computed as the sum of the envelopes of the jitters introduced by all apparatus. For instance, the respective jitter on the acquisition of one strain gauge value and one XRD frame in both modes is reported in Table 2.13.

Synchrotron mode	Introduced jitter (ns)	
	Stress signal	Strain signal
Uniform	254	570
Single Bunch	110	173

TABLE 2.13 – Total time shift and total jitter induced on the reconstructed stress and strain signals in both Synchrotron modes.

To reduce the jitter and its influence on the measurements, the choice was made to :

- cumulate strain gauge values (at a fixed delay over several thousands of cycles) to improve the statistics on the estimation of the total strain ;
- cumulate XRD frames to obtain XRD images with a sufficient SNR and better statistics to determine the diffraction peak position from the image ;
- fit the diffraction peak to determine its position (and width) in order to improve the resolution with which the peak position is estimated.

30. A jitter is a deviation from true periodicity of a periodic signal, in relation to a reference clock signal. This corresponds to a fluctuation of a signal in time. This fluctuation influences the phase of the signal. It is random but its maximum fluctuation can be measured : the envelope of the jitter.

2.4.4 Conclusion of the section

The estimation of the stress evolution during one cycle is achieved by conducting in-situ time-resolved X-ray Diffraction measurements. The estimation of the strain evolution is achieved by using strain gauge. Both evolutions are reconstructed as discrete signals, acquired point by point by using an intricate experimental setup developed and tested during the Ph.D. at the DiffAbs beamline, at Synchrotron SOLEIL.

The complete methodology enables the reconstruction of stress and strain time evolutions allowing to estimate their respective amplitudes and the time shift between both signals. With these three values, the mechanical work can be computed.

It is worth keeping in mind that the XRD measurements (as well as the strain gauge measurements) are subjected to important uncertainties in terms of jitter. The influence of these uncertainties is however reduced owing to the stroboscopic process that is employed to improve the statistics of the strain and stress measurements. A synchrotron X-ray source is also considered to improve the quality of the XRD images acquired. In addition, the beam drifts that were observed at DiffAbs beamline are to be kept in mind as it might act as an additional source of error on the reconstruction of the stress signal and on the determination of the time shift between stress and strain.

2.5 Measurement of the temperature to estimate the dissipated energy

2.5.1 Principle of experimental measurements

To complete the estimation of the dissipated energy, the temperature increase over time during an ultrasonic fatigue test is measured. Fatigue tests are interrupted after 10^7 cycles. Several tests were conducted at increasing stress amplitudes that were applied to the same specimen. The temperature increment was measured for each.
To do so, an experimental setup was developed. It relies on the use of an InfraRed (IR) camera FLIR^{TM}, along with a lens of 50 mm focal length mounted with rings between the CCD of the camera and the lens. It is settled in front of the tested specimen, itself fixed to the ultrasonic fatigue machine. The camera is settled at a distance of 70 mm of the specimen which corresponds to a pixel being representative of $0.04 \times 0.04\,\text{mm}^2$. Figure 2.41 shows the experimental setup used for dissipated energy measurements. The temperature is assessed over the whole specimen's surface in 2D field temperature measurements. The sampling frequency of the IR camera can reach at maximum 1 kHz but is usually settled to be close to 100 Hz (to avoid too large data files).

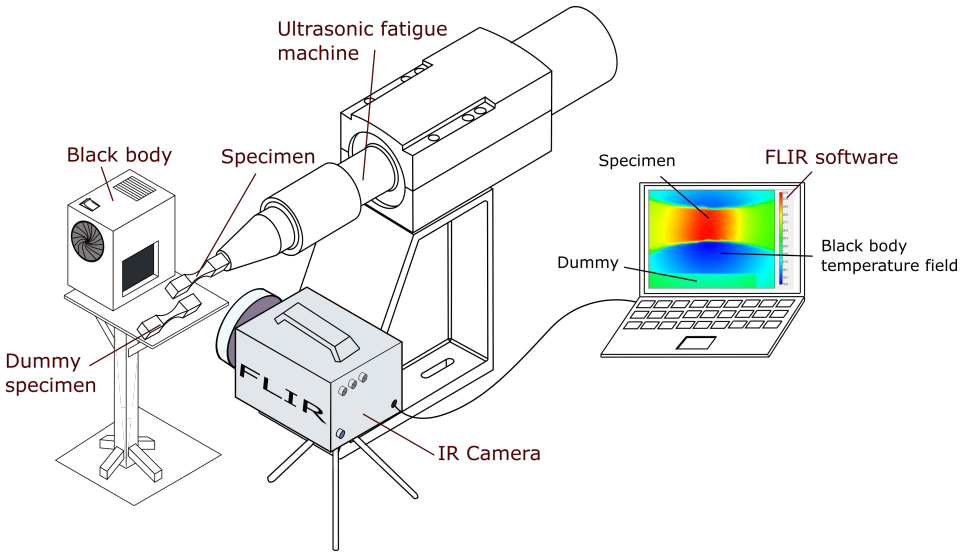


FIGURE 2.41 – Experimental setup developed to measure the dissipated energy from specimen under a fatigue loading.

A black body is added behind the specimen to improve the contrast on the recorded temperature field and distinguish the specimens with respect to the background. Also, a dummy specimen is placed in the field of view of the IR camera and plays the role of the reference temperature which varies with the room temperature. To maximize the emittance of the observed surface (i.e. to obtain an emissivity of 1) and facilitate the measurement of the temperature, the loaded and the dummy specimens were painted in matte black. The paint used is a special paint from Nextel® which can stand high temperature up to 400°C.

2.5.2 Temperature measurements during ultrasonic fatigue tests

Each image acquired with the IR camera can be post-processed with the software provided by FLIR^{TM}. Two zones are plotted respectively on the center of the loaded specimen and on the dummy, as it is shown by Figure 2.42 in the case of the C70 steel. They represent the temperature field over several hundreds of pixels. The mean temperature is computed in these two zones to make the temperature estimation statistically accurate and representative. The difference between the mean temperature of each zone is computed to deduce the variation in temperature of the specimen without the influence of the variations of the room temperature[31].

31. In practice, the temperature of the room changes by less than 0.1 °C during the 10^7 cycles of each test. This is thus negligible compared to the temperature increase of the specimen.

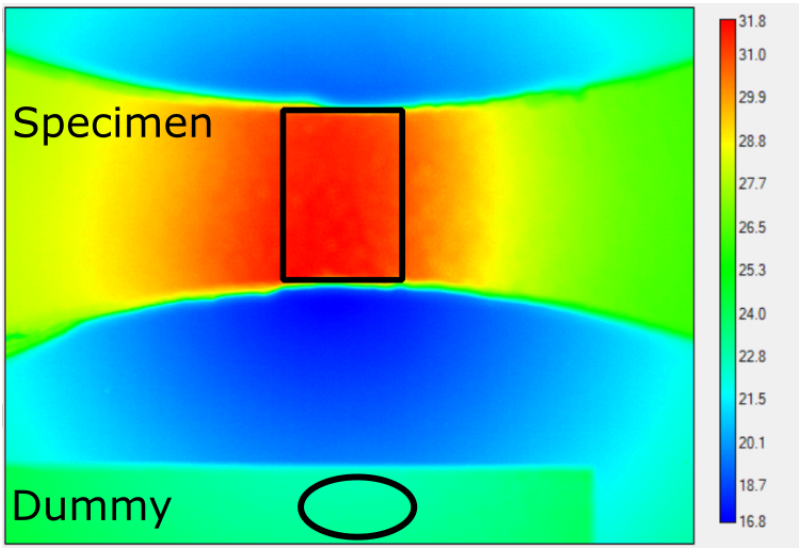


FIGURE 2.42 – Example of an image recorded by the IR camera during a fatigue test conducted on a steel specimen.

The temperature increase is plotted versus time in the case of steel in Figure 2.43 for a stress amplitude of 228 MPa maintained during 10^7 cycles. An increase of the self-heating is observed and a plateau is reached after at least 250 s or 5×10^6 cycles and is estimated at $\theta_s = 8.9\,°C$.

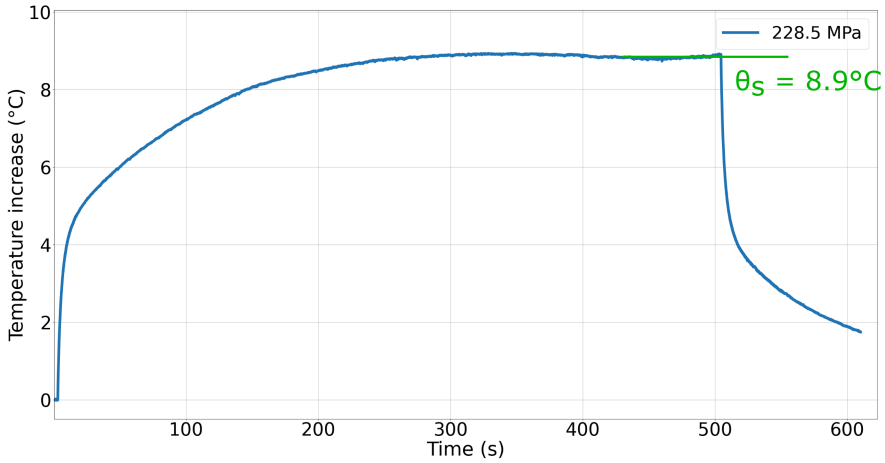


FIGURE 2.43 – Self-heating (temperature increment) curve versus time during an ultrasonic fatigue test at 228 MPa - case of the C70 steel.

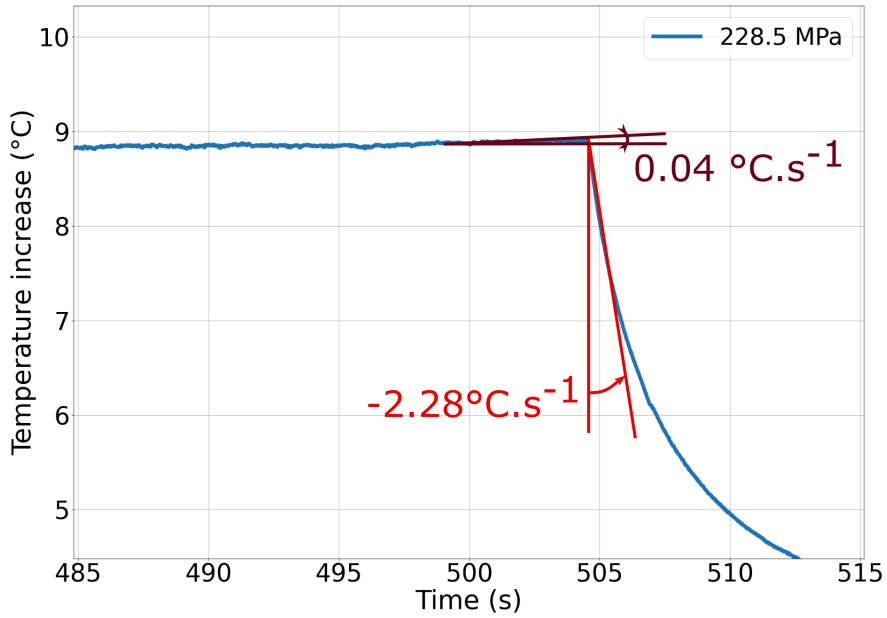


FIGURE 2.44 – Zoom on the self-heating curve of the C70 steel (Fig. 2.43). Calculation of the speed of cooling as the slope at the end of the test.

After the plateau, i.e. after 10^7 cycles, the test is stopped and the temperature decreases. The decreasing slope when the loading is stopped is calculated as shown in Figure 2.44 for the ultrasonic fatigue test conducted at 228 MPa. The slope is computed over the first four points after the temperature starts to decrease and was estimated at $d\theta/dt = -2.28\,^{\circ}\mathrm{C\,s^{-1}}$.

2.5.3 Estimation of the dissipated energy

The model used to compute the dissipated energy from temperature measurements at the surface of a specimen relies on the heat equation and the determination of the heat source owing to dissipation effects d_{int} (also referred to as intrinsic dissipation).

The heat equation is projected in a zero dimensionnal problem to obtain a straigthforward formulation as the time scale of the acquisitions is 200 times bigger than the time period of one loading cycle [Blanche, 2012]. The formulation is expressed in equation (2.18) :

$$\rho C \frac{\partial \theta}{\partial t} + \frac{\rho C}{\tau_{0D}} \theta = d_{int} + s_{the}. \tag{2.18}$$

where $\theta = T - T_0$ is the temperature increment with T_0 the initial temperature and T the temperature difference between the two areas shown in Figure 2.42. $\partial\vartheta/\partial t$ is the

variation of temperature with time. s_{the} corresponds to the overall heat sources due to thermoelastic effects. Heat losses are considered linear and are defined by a characteristic time τ_{0D}. The characteristic time constant, in 0D, accounts for the heat losses considering the contribution of convection and conduction.
By considering the mean temperature over one cycle, equation (2.18) is rewritten such that :

$$\rho C \frac{\partial \theta}{\partial t} + \frac{\rho C}{\tau_{0D}} \theta = < d_{int} + s_{the} >_{cycle} . \tag{2.19}$$

During one cycle, $< s_{the} >_{cycle}$ vanishes [Boulanger, 2004] [Chrysochoos et al., 2008]. Equation (2.19) thus becomes :

$$< d_{int} >_{cycle} = \rho C \left(\frac{\partial \theta}{\partial t} + \frac{\theta}{\tau_{0D}} \right) . \tag{2.20}$$

The calculation of the dissipated energy relies on the estimation of the mean of the intrinsic dissipation over one loading cycle, as exposed in equation (2.21) :

$$E_{diss} = \int_{cycle} d_{int} dt = \frac{< d_{int} >_{cycle}}{f} . \tag{2.21}$$

where f is the frequency of the loading.

To identify d_{int}, one considers two calculations [Blanche, 2012] [Jongchansitto et al., 2019] :

- First, the identification of the characteristic time τ_{0D} is possible by considering equation (2.20) at $t = t_{f+}$ (i.e. just after the test has stopped, when the temperature starts to drop), such that :

$$\left. \frac{\partial \theta}{\partial t} \right|_{t_{f+}} = - \frac{\theta_s}{\tau_{0D}} . \tag{2.22}$$

  After the test stops, the dissipative sources are inactive, and d_{int} becomes zero, allowing to identify τ_{0D} from the estimation of $\partial\theta/\partial t$ and θ_s at $t = t_{f+}$.

- Then, $< d_{int} >_{cycle}$ is estimated by considering equation (2.20) at $t = t_{f-}$ (i.e. just before the test is stopped, when the temperature is stabilized), such that :

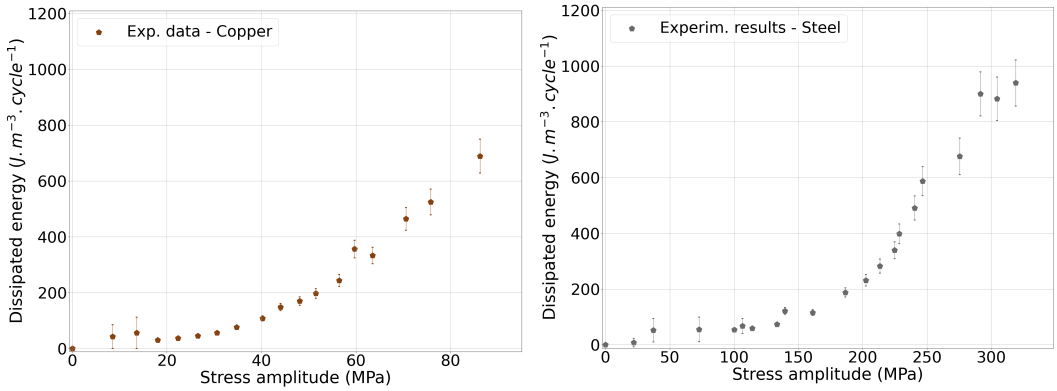
$$< d_{int} >_{cycle} = \rho C \left(\left. \frac{\partial \theta}{\partial t} \right|_{t_{f-}} + \frac{\theta_s}{\tau_{0D}} \right) . \tag{2.23}$$

From the self-heating curve presented in Figure 2.44, one can determine that $\tau_{0D} = 3.9$ s and thus that $< d_{int} >_{cycle} = 8.02 \times 10^6$ J m^{-3}. The disipated energy is

estimated at $E_{diss} = 398\,\mathrm{J\,m^{-3}\,cycle^{-1}}$, as the frequency of the fatigue test was 20 160 Hz.

The results obtained in terms of dissipated energy estimation are presented for both materials in Figure 2.45. The calculation was conducted over all the applied stress amplitudes. The vertical error bars are estimated to be in the order of 9% of the measured dissipated energy for both materials and arise from the accuracy of the temperature measurement and that of the estimation of the slope of the exponential temperature decrease.

The dissipated energy per cycle, estimated in $\mathrm{J\,m^{-3}\,cycle^{-1}}$ increases with the applied stress. At a similar stress amplitude, the dissipated energy is more important in the case of copper. This is associated with the higher thermal conductivity of copper.



(a) (b)

FIGURE 2.45 – Dissipated energy estimated with respect to the applied stress amplitudes to a) pure copper single crystal and b) C70 steel.

2.6 Conclusion of the chapter

In order to experimentally estimate the energy that is stored in a material during a fatigue loading in the VHCF regime, the choice was made to establish an energy balance. To complete this objective, a methodology was fully developed, applied and optimised to estimate independently the dissipated energy and the mechanical work from fatigue specimens loaded with an ultrasonic fatigue machine, working at 20 kHz.
An experimental setup, inspired by what is found in the literature was set up to estimate the intrinsic dissipation from short interrupted fatigue tests with an InfraRed camera. The dissipated energy can thus be calculated from this estimation.

As well, an in situ time-resolved X-ray diffraction based methodology was developed to permit the estimation of the mechanical work brought to a material that is loaded cyclically at 20 kHz. This estimation was performed on two pure copper single crystal specimens and several C70 pearlitic steel specimens. The particularity of these measurements lies in the different modes that are used. For the copper specimen, the uniform mode maximizing the energy of the X-ray beam was targeted and the setup was clearly efficient to perform accurate XRD measurements. However, the capacity of the measurements was limited when they were conducted on C70 steel in uniform mode, which induced the adaptation of the methodology to use a pulsed X-ray source to thus reach a finer time resolution.
Table 2.14 regroups the parameters that were selected to conduct XRD experiments on C70 steel and copper single crystal in both uniform and single-bunche modes.

TABLE 2.14 – Overview of the parameters selected to conduct XRD experiments on C70 steel (case of 110 diffraction ring of the ferrite phase) and copper single crystal (case of the $2\bar{2}6$ diffraction ring).

	Uniform mode		Single Bunch mode
Parameters	Copper	Steel	Steel
Number of cycles to reconstruct one point	8.46×10^6	3.6×10^7	1.1×10^8
Number of points to reconstruct one cycle	50	50	42
Aperture opening of XPAD detector (seconds)	0.1	0.5	2
Max. int. of the peak (case of aperture above)	230000	180000	220000

The results of the measurement of the dissipated energy and the computation of the mechanical work leading ultimately to the estimation of the stored energy will be presented and discussed in the next chapter.

Chapitre 3

Experimental results and discussions

Two materials were tested during this Ph.D. A pure copper single crystal from which one can directly determine evolutions of the dislocations structure because there is no effect of grains boundaries to account for. A polycrystalline C70 pearlitic steel that is a more complex material, composed of two phases, which is closer to metals that are commonly employed for industrial applications.

For the single crystal, the uniform mode of SOLEIL Synchrotron was sufficient to reach a time resolution in the order of a few tens of nanoseconds. This material is ideal to conduct XRD measurements because it provides a very intense diffracted beam which shortens the acquisition time and improves the SNR of the XRD images. This led to small uncertainties on the estimation of the stress and strain amplitudes as well as on the time shift between both quantities. In the case of our polycrystalline C70 steel, and because of its polycrystalline character, the time resolution provided in uniform mode was not sufficient to obtain XRD images with a high enough SNR. This is why the single bunch mode was employed to improve the time resolution of the methodology and allow an accurate reconstruction of the stress evolutions in that case.

The first section exposes and discusses the estimation of stress from in situ time-resolved XRD for both materials. Then, the results of the estimation of the stored energy respectively in copper and steel are reported and discussed in the second and third sections.

3.1 Estimation of the stress amplitude from in situ time-resolved X-ray diffraction

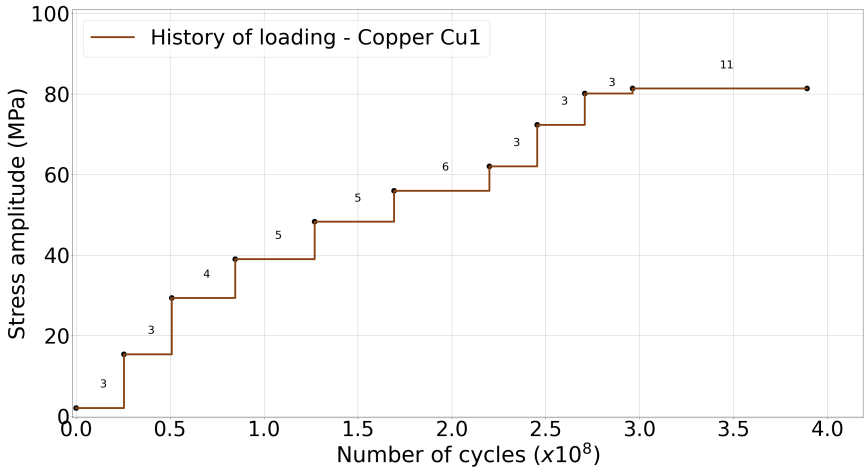
To link the longitudinal stress and the elastic lattice strain, the method requires the estimation of X-ray Elastic Constants (XEC) (see Section 2.4.2.4). However, these quantities are difficult to estimate. To retrieve experimentally the XEC, the total strain is measured by using strain gauge and is converted into longitudinal stress by considering an elastic behavior assumption (i.e. the plastic strain is neglected). In parallel, the elastic lattice strain (at the grain scale) is estimated from X-ray Diffraction.

3.1.1 Estimation of the stress - case of copper

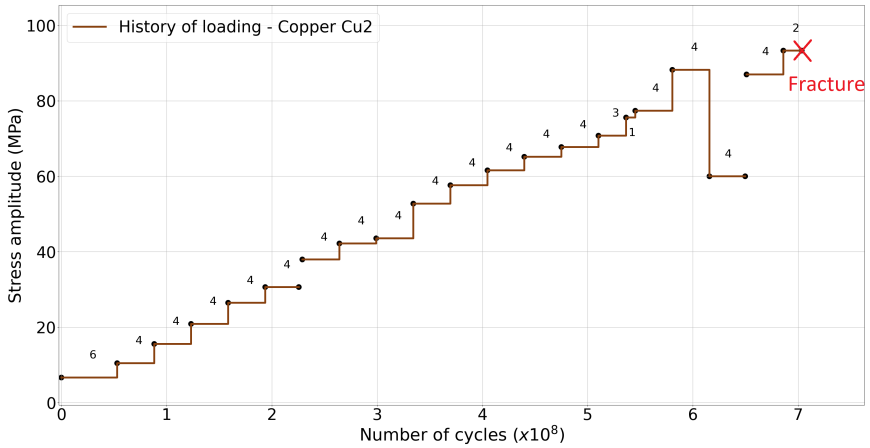
3.1.1.1 Experimental protocol of the tests - case of copper

Two copper specimens were used to estimate the stress that was applied to them with the methodology of in situ time-resolved XRD. The loading history of the two specimens is reported in Figure 3.1. Stress amplitudes as small as 2 MPa and as high

as 93 MPa were applied to copper specimens. Each stage of applied stress amplitude is called a loading step. In Figure 3.1, the number that appears above each loading step corresponds to the number of cycles that were reconstructed during the loading step. It is to be noted that specimen "Cu2" broke at a stress amplitude of 93 MPa after 2.5×10^7 cycles.



(a)



(b)

FIGURE 3.1 – Loading history of specimens put in vibration with the ultrasonic fatigue machine during XRD measurements : specimens a) "Cu1" and b) "Cu2". Measurements were conducted by using strain gauge.

Due to a self-heating of specimens, the acquisition was started at least 5×10^6 cycles after the machine was started to ensure that the temperature of the specimen has stabilized. It is worth noting that the specimen was placed under a blown nitrogen source to avoid its surface to oxidize and it also slightly reduced the influence of self-heating.

For both specimens, their longitudinal dimension was oriented along the crystallographic [110] direction. For specimen "Cu1", the face observed with XRD was oriented to be perpendicular to the $1\bar{1}3$ crystallographic direction. Thus, the $2\bar{2}6$ diffraction peak was observed. An example of the diffraction profile of this peak is shown in Figure 3.2, which has been obtained by using the procedure described in Section 2.4.2.2. For specimen "Cu2", the face observed with XRD was oriented to be perpendicular to the $1\bar{1}1$ crystallographic direction. Hence, the $5\bar{5}5$ diffraction peak was observed. The characteristics of both peaks are reported in Table 3.1.

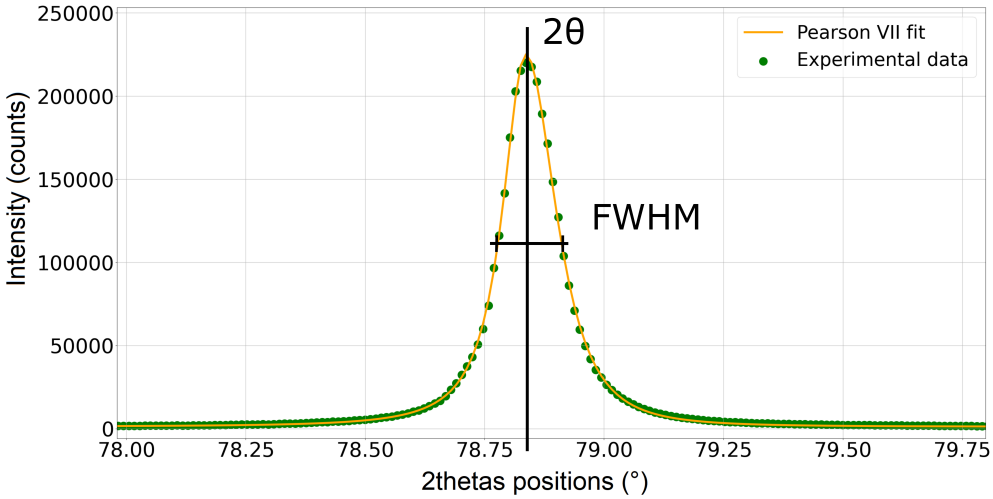


FIGURE 3.2 – Diffraction profile (intensity versus 2θ) of the diffraction ring $2\bar{2}6$ of copper - case of specimen "Cu1", not loaded.

For both specimens, measurements were conducted prior to the loading to determine the SNR of the diffraction peaks of both specimens. The uncertainties that are committed when estimating the peak angular position 2θ and width $FWHM$ from the fitting procedure were determined from these measurements. Those values are reported in Table 3.1.

TABLE 3.1 – Characteristic of "Cu1" and "Cu2" studied diffraction peaks in uniform mode. The uncertainties are computed as the standard deviation of 50 acquired diffraction peaks. Beam energy of 18 keV.

			Reference values		Standard deviations	
Specimen	Peak (hkl)	SNR	2θ (°)	FWHM (°)	2θ (°)	FWHM (°)
Cu1	$2\bar{2}6$	500	78.8	0.131	$8. \times 10^{-5}$	1.4×10^{-4}
Cu2	$5\bar{5}5$	75	111.5	0.128	1.2×10^{-4}	1.9×10^{-3}

3.1.1.2 Experimental estimation of the XEC for copper

The application of the in situ time-resolved XRD methodology on the pure copper single crystals allowed to reconstruct several cycles reproducing the evolution of stress and strain during the application of a fatigue loading with the ultrasonic fatigue machine. From the reconstructions of 3 to 6 cycles, the stress and strain amplitudes have been determined by fitting their respective evolutions with a sinusoidal function. Figure 3.3 shows the evolution of the lattice strain amplitude estimated from XRD with respect to the evolution of the stress amplitude estimated from strain gauge through Hooke's law. Each point on this curve represents the mean value of the amplitudes estimated on the different cycles reconstructed at each stress amplitude. The error bars on the plotted curves are computed from the dispersions of the results computed over several reconstructed cycles as a standard deviation. A linear trend is clearly identified between both quantities, corresponding to an equivalent elastic behavior of the material. This validates the hypothesis considered to estimate the longitudinal stress from total strain measurement.

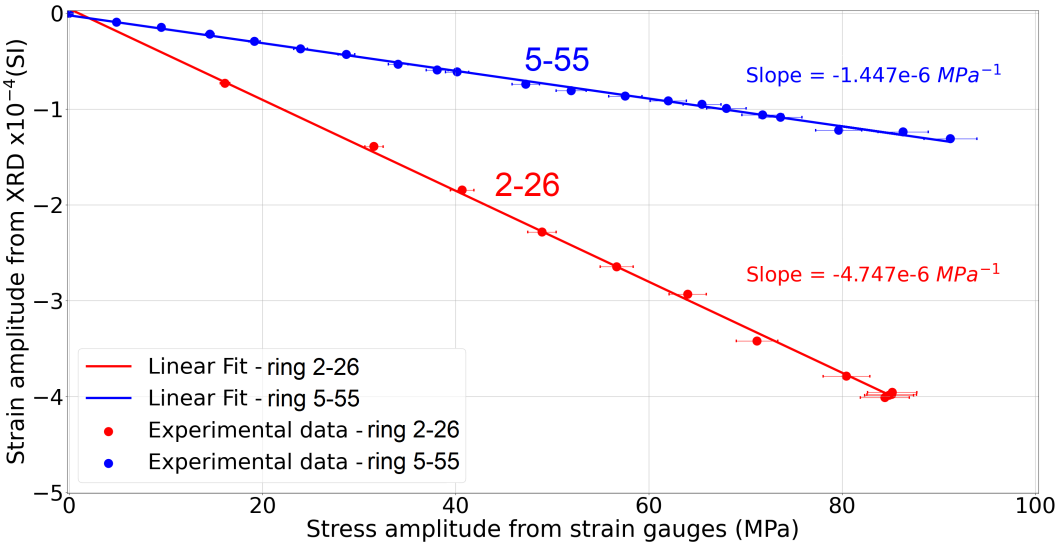


FIGURE 3.3 – Evolution of the strain amplitude measured from lattice deformation using XRD with respect to the stress amplitudes measured calculated from total strain measured using strain gauge - case of copper single crystal, specimens "Cu1" and "Cu2".

From a linear regression, the experimental X-ray elastic constants XEC_{exp} are estimated from both curves. For the diffraction peak $2\bar{2}6$ (i.e. specimen "Cu1"), $XEC_{2\bar{2}6,exp} = -4.742 \times 10^{-6} MPa^{-1}$ whereas $XEC_{2\bar{2}6,theo} = -4.966 \times 10^{-6} MPa^{-1}$. It corresponds to a relative difference of 4.3% between experimental and theoretical estimations (see Section 2.4.2.4). For the diffraction peak $5\bar{5}5$ (i.e. specimen "Cu2"),

$XEC_{5\bar{5}5,exp} = -1.447 \times 10^{-6} MPa^{-1}$ when $XEC_{5\bar{5}5,theo} = -1.403 \times 10^{-6} MPa^{-1}$. It corresponds to a relative difference of 3.1% of the experimental value with respect to the theoretical value. Thus, the XECs estimated by using the theoretical framework of a cubic symmetry and elastic behavior of copper at the crystal scale are reliable. It predicts the elastic behavior of a single crystal with a difference lower than 4% which is acceptable considering the 3% errors committed when estimating the total strain from strain gauge [Jacquemain et al., 2021]. The difference between theoretical and experimental XEC can be explained by the misorientations of the specimen longitudinal direction with respect to the [110] direction (in the order of 1 to 3°, see Section 2.2.1).

3.1.2 Estimation of the stress - case of steel

The XECs are estimated experimentally for steel following the same procedure as copper. The measurements were however conducted in both phases of the C70 steel. Thus, the XECs were estimated from several diffraction peaks measured in ferrite and cementite phases. These measurements were conducted in uniform mode.

3.1.2.1 Experimental protocol of the tests

In the same manner as presented previously for copper, steel specimens were cyclically loaded using the ultrasonic fatigue machine in its conventional mode of functioning. The loading history applied to two steel specimens (namely "C70-A9" and "C70-P9") is reported in Figure 3.4. The minimum stress was about 75 MPa for both specimens whereas the maximum applied stress reached 184 MPa for specimen "C70-A9" and 274 MPa for specimen "C70-P9".

The interest was directed towards diffraction peaks from ferrite and cementite phases. Both 110 and 220 diffraction peaks from the ferrite phase were studied. For the 220 peak, the procedure of treatment of the diffraction peak is the same as that presented in Section 2.4.2.2. For the 110 peak, there are diffraction peaks from the cementite phase that are very close to it. The top part of Figure 3.5 shows the C70 steel diffraction profile presenting the ferrite 110 diffraction peak as well as several cementite peaks. The procedure must thus be slightly modified ; it is depicted in Figure 3.5. 1) First, the 110 peak is fitted in the same manner as peak 220. 2) Its fit is then subtracted from the diffraction profile : only cementite peaks remain on the diffraction profile. 3) These peaks are thus fitted to follow their evolution in position. Only the cementite 102 peak was studied on the same diffraction profile as it shows the higher SNR of cementite peaks.

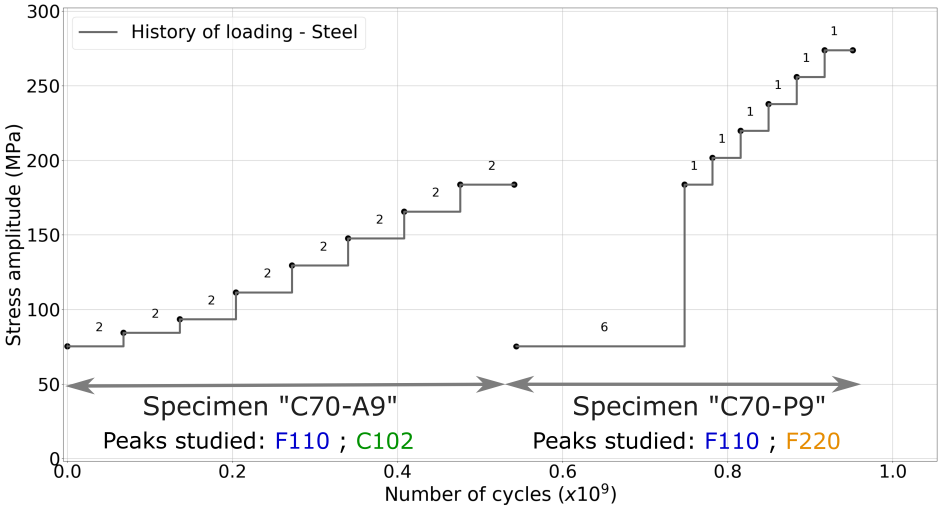


FIGURE 3.4 – Loading history of specimens put in vibration with the ultrasonic fatigue machine during XRD measurements : specimens a) "C70-A9" and b) "C70-P9".

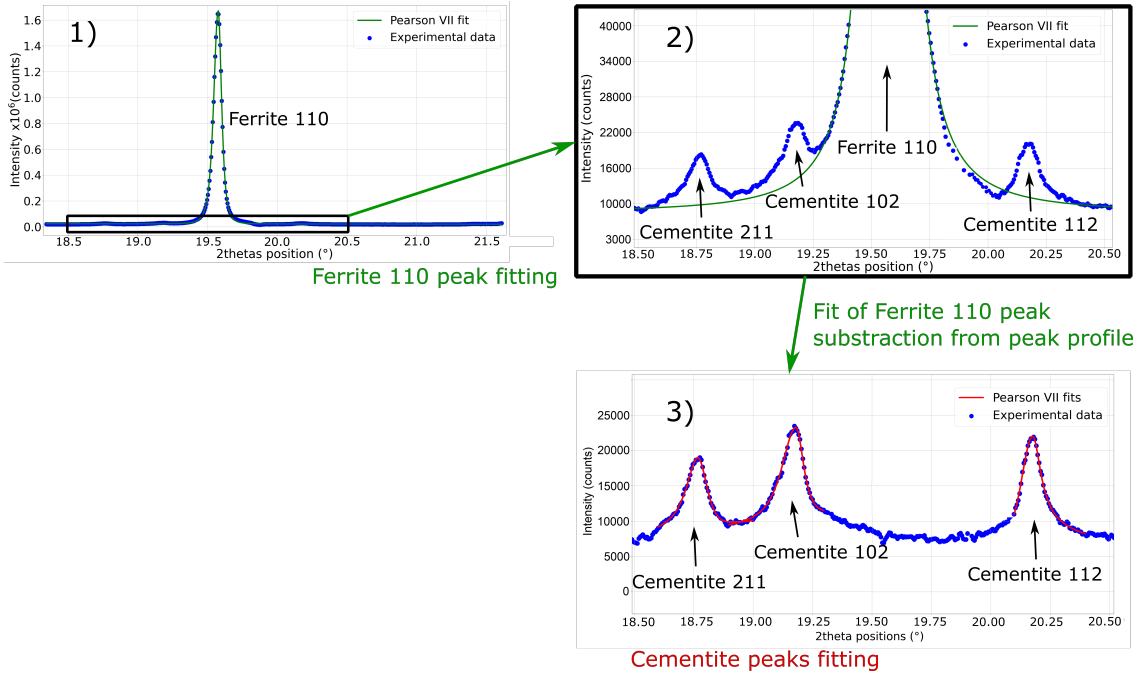


FIGURE 3.5 – Procedure of treatment of the ferrite 110 diffraction peak allowing the convenient study of the cementite 102 peak - case of specimen "C70-A9", not loaded.

Table 3.2 shows the estimation of the uncertainties committed on the estimation of the peaks' position and width from the fitting procedure. Similarly to what was done for copper, these uncertainties were estimated experimentally prior to the loading on the studied diffraction peaks. The SNR is very low for the cementite peak, which induces

important uncertainties. This is owing to the low intensity of the cementite peaks, as the volume proportion of cementite present in the steel is low.

TABLE 3.2 – Characteristic of C70 steel diffraction peaks in uniform mode. The uncertainties are computed as the standard deviation of 50 diffraction peaks. Beam energy of 18 keV.

			Reference values		Standard deviations	
Specimen	Peak (hkl)	SNR	2θ (°)	FWHM (°)	2θ (°)	FWHM (°)
C70-A9 + P9	110	105	19.6	0.0656	2.4×10^{-4}	3.2×10^{-4}
C70-P9	220	80	39.5	0.0944	5×10^{-4}	7.2×10^{-4}
C70-A9	102	2.2	19.2	0.1055	1.3×10^{-3}	2.2×10^{-3}

3.1.2.2 Estimation of the stress amplitude for steel specimens

Figure 3.6 shows the evolution of elastic lattice strain estimated by XRD with respect to the macroscopic stress amplitude estimated from strain gauge. Results are shown for the three *hkl* diffraction peaks of this study, namely ferrite 110 and 220 and cementite 102. The error bars of Figure 3.6 correspond to the dispersion of the measurements over several reconstructed cycles computed as a standard deviation.

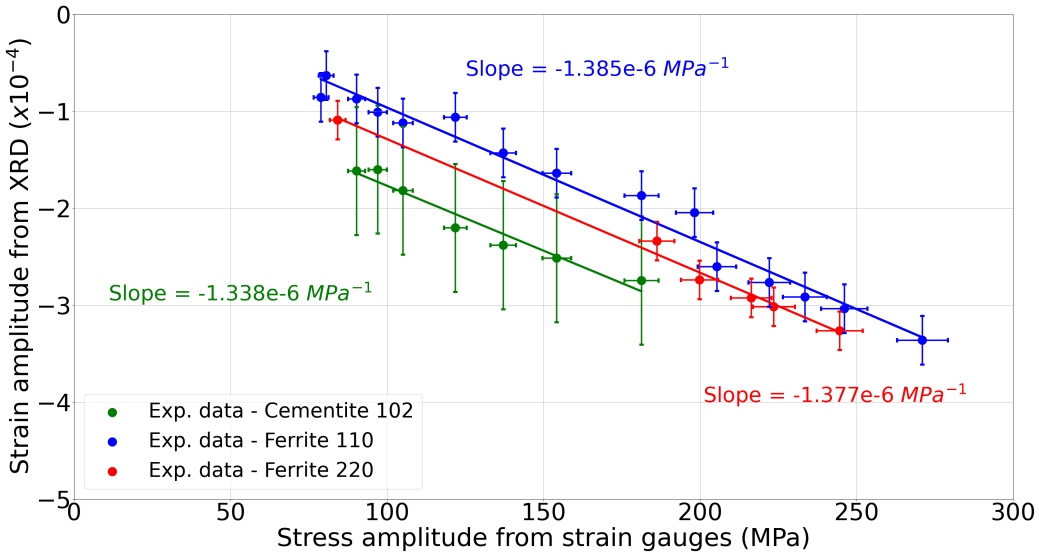


FIGURE 3.6 – Evolution of the strain amplitude measured from lattice deformation using XRD (from diffraction peaks of cementite and ferrite phases) with respect to the stress amplitudes measured calculated from total strain measured using strain gauge - case of C70 steel specimens "C70-19" and "C70-P9".

The XEC are found with a linear regression of the data obtained from the study of each diffraction peak. The linearity of the results is clear on the plots. For ferrite, the 110 and 220 peaks gave a $XEC_{exp,fer} = -1.38 \times 10^{-6} MPa^{-1}$ which is close to the theoretical value of $XEC_{theo,fer} = -1.32 \times 10^{-6} MPa^{-1}$. It corresponds to a 4.5% difference. For cementite, the 102 peak gave a $XEC_{exp,fer} = -1.338 \times 10^{-6} MPa^{-1}$ which is close to the theoretical value of $XEC_{theo,fer} = -1.29 \times 10^{-6} MPa^{-1}$, with a relative difference of 4%. These uncertainties are acceptable compared to the uncertainties committed from the measurements using strain gauge [Jacquemain et al., 2021] for instance.

3.1.2.3 Variability of the XEC for steel

The most studied peak was the 110 diffraction peak of the ferrite phase as it exhibits a higher intensity per pixel. The XEC of this peak was estimated at $-1.32 \times 10^{-6}\text{MPa}^{-1}$ (see Section 2.4.2.4). To verify if this value is retrievable experimentally in a repeatable way, the calculation was performed in a similar manner to what was exposed previously but by considering experimental results obtained from in-situ time-resolved XRD measurements applied to six specimens.

Table 3.3 gives the recap of all XEC values estimated experimentally from the six specimens. The relative difference are calculated as $(XEC_{exp} - XEC_{theo})/XEC_{theo}$. The mean value of experimental XEC is estimated at $-1.105 \times 10^{-6}\text{MPa}^{-1}$ with a standard deviation of $-0.247 \times 10^{-6}\text{MPa}^{-1}$. The value estimated experimentally shows a difference of $\pm 19\%$ with the theoretical XEC estimated from a SC model.

TABLE 3.3 – XEC of ferrite for 110 lattice strain, estimated from experimental results - case of C70 steel. Theoretical value is $XEC_{110} = -1.32 \times 10^{-6}\text{MPa}^{-1}$.

Specimen	XEC $\times 10^{-6}(\text{MPa}^{-1})$	Relative difference (%)
C70-P9	-1.468	+3%
C70-A9	-1.30	-1%
C70-P5	-0.820	-38%
C70-A1	-0.880	-33%
C70-A6	-1.049	-20%
Mean	-1.105	/
Standard deviation	0.247	/

The texture of the material was not considered in the self-consistent model used to estimate the XEC of both phases of C70 steel. The variability observed in the results might be explained by the difference of texture from one specimen to another. This assumption has been investigated by conducting texture measurements on several C70 steel specimens, but did not provide conclusive results.

3.1.3 Conclusion of the results

For both copper (resp. steel), longitudinal macroscopic stress evolves linearly with respect to the elastic lattice strain for stress amplitudes ranging from 0 to 93 MPa (resp.0 to 274 MPa). This indicates that the assumption of an elastic behavior is valid for this range of stresses and that conventional methods used to estimate the stress are reliable.

The quantification of the XEC is conducted by estimating the linear slope between stress and strain. Its quantification works well in the case of copper to validate the theoretical value obtained from elastic constants of the material. On the contrary, for steel, the XEC that is estimated shows a strong variability between specimens and with respect to the theoretical value. The texture of the material should be duly investigated by conducting EBSD measurements and the effect of the measured texture should thus be taken into account to reduce the variability.

3.2 Estimation of the stored energy : case of copper single crystal

This section is devoted to the estimation of the energy that is stored in pure copper single crystal loaded in fatigue at 20 kHz. The results of the evolution of the stored energy with respect to the applied stress and the number of loading cycles are discussed.

3.2.1 Estimation of the mechanical work evolution with the stress amplitude and number of cycles

The previous section proved the reliability of the linear elastic assumption to determine the longitudinal stress amplitude from total strain measurements with strain gauge. This allows us to free ourselves from the variability observed on the estimation of the XEC. Thus, the mechanical work can be computed from equation (3.1) solely from the estimation of the strain amplitude and of the time shift between stress and strain. Indeed, the estimation of the time shift still requires the reconstruction of both stress and strain signals with the time-resolved methodology presented in the previous chapter.

$$W_{mech} = -\pi \frac{\Delta\sigma}{2}\frac{\Delta\varepsilon}{2}\sin(\phi) = E\frac{\Delta\varepsilon^2}{4}\sin(\phi) \tag{3.1}$$

where E is the Young's modulus of the material.

3.2.1.1 Influence of the stress amplitude and number of cycles on the time shift

In this chapter, the estimation of the time shift between stress and strain is presented. Figure 3.7 recalls the measurement of the time shift from the reconstruction of stress and strain cycles.

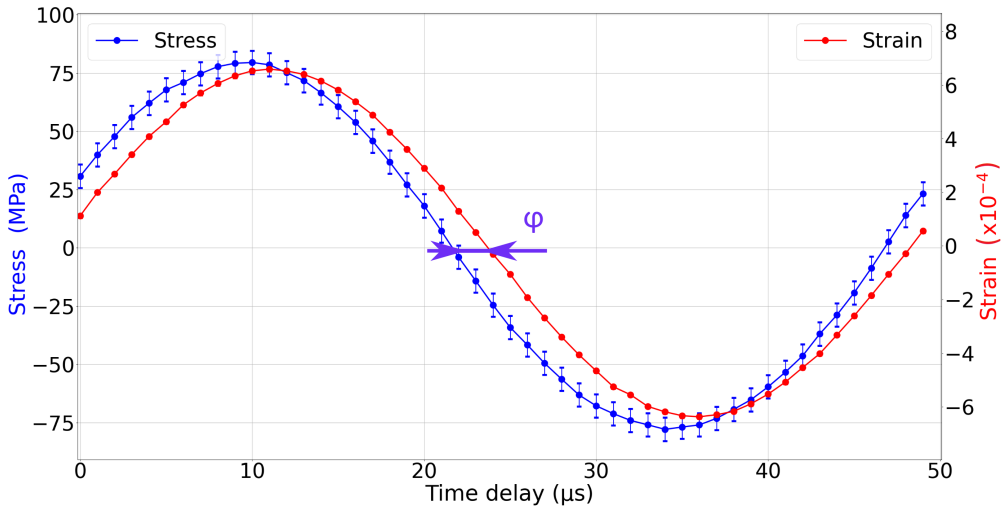


FIGURE 3.7 – Stress and strain cycle reconstructed with respect to the time delay of the acquisitions. The time shift is measured between stress and strain signals - case of copper single crystal, specimen "Cu1" at a stress amplitude of 80 MPa.

Figures 3.8 and 3.9 plot the relative time shift with respect to the stress amplitude (estimated by using strain gauge) for specimen "Cu1" and "Cu2" respectively. Each point corresponds to a value of the time shift that was estimated from one couple of reconstructed cycles of stress and strain. Error bars plotted in the figures are arising from the fitting procedure of both stress and strain sinusoidal reconstructions, with a stronger influence from the reconstruction of the stress signal. In fact, the quality of the fitting procedure of the stress signal is dependent on the noise on the XRD images and the beam drifts[1].

In both figures and for each stress amplitude, the time shift obtained for the three first reconstructed cycles are plotted. The reconstruction of stress and strain cyclic evolutions relies on a stroboscopic approach, which corresponds to a considerable duration of the reconstructions. For copper, the duration of one cycle reconstruction lasts 8.46×10^6 cycles. Thus, for a given stress amplitude, the three points plotted in Figures 3.8 and 3.9 correspond to values respectively estimated after 8.46×10^6, 1.69×10^7 and 2.54×10^7 cycles.

1. The influence of the beam drifts and the noise on XRD images is transmitted as vertical noise on the reconstructed cycles of the stress evolution.

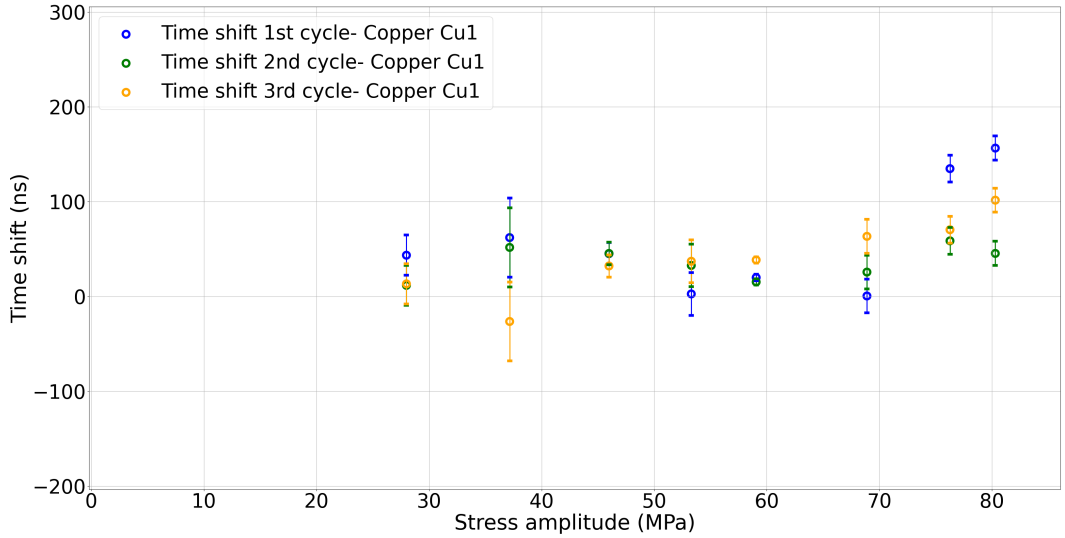


FIGURE 3.8 – Evolution of the time shift between stress and strain with respect to the applied stress amplitudes - case of copper single crystal, specimen "Cu1". For each stress amplitude, the values measured for three reconstructed cycles are reported. For one stress amplitude, the three points corresponds to the time shift evaluated for cycles respectively reconstructed after 8.46×10^6, 1.69×10^7 and 2.54×10^7 loading cycles.

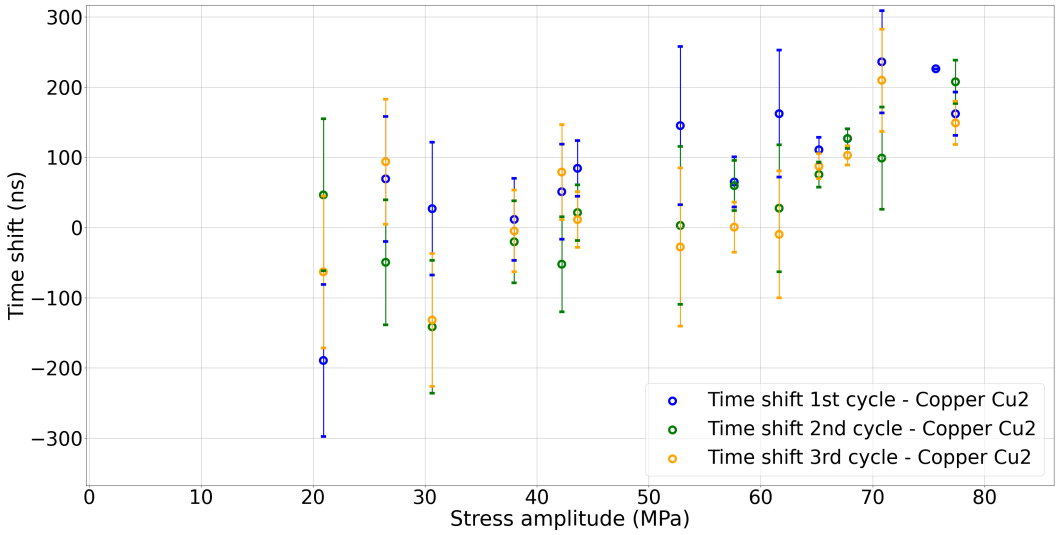


FIGURE 3.9 – Evolution of the time shift between stress and strain with respect to the applied stress amplitudes - case of copper single crystal, specimen "Cu2". For each stress amplitude, the values measured for three reconstructed cycles are reported. For one stress amplitude, the three points corresponds to the time shift evaluated for cycles respectively reconstructed after 8.46×10^6, 1.69×10^7 and 2.54×10^7 loading cycles.

An increase is identified with a change of approximately 100 ns (resp. 200 ns) between 20 and 80 MPa for specimen "Cu1" (resp "Cu2") with respect to stress. On the contrary, a slight decrease is observed with the number of cycles, for a given stress amplitude. The results obtained for specimen "Cu1" show a local maximum of the time shift for stress amplitudes between 30 and 55 MPa. It will be referred to as a hill. The time shift decreases after the hill before exhibiting an important increase for higher stress amplitudes. This observation is also true for specimen "Cu2" but is less marked, owing to the strong uncertainties on the estimation of the time shift in this case.

In the case of specimen "Cu1", the order of magnitude of the uncertainties associated with the estimation of the time shift is in the range of 5 to 30 ns for stress amplitudes higher than 25 MPa. In the case of specimen "Cu2", uncertainties are ranging between 20 to 75 ns. The variation of the time shift in the case of specimen "Cu2" is higher than for specimen "Cu1" owing to the smaller SNR of the XRD images of the studied diffraction peak. It is also due to the lower displacement of the studied peak of specimen "Cu2"[2], which increases the influence of the noise (of the XRD images) on the stress signal reconstruction.

As an overall observation, the time shift is positive, corresponding to the strain that is late compared to the stress. This is coherent with a mechanical behavior of the material that is visco-elastic and tends to become plastic.

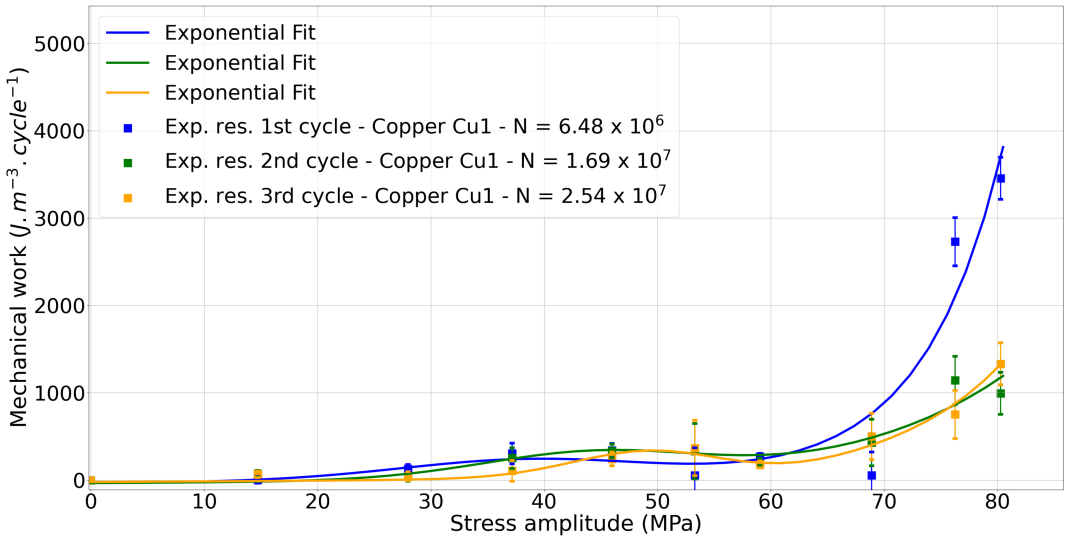
3.2.1.2 Influence of the stress amplitude and number of cycles on the mechanical work

From the measurements of both stress and strain amplitudes and the estimation of the relative time shift, the mechanical work W_{mech} measured per loading cycle is estimated from equation 3.1. The results obtained from the application of this calculation are shown in Figures 3.10 and 3.11 for both copper specimens. One value of W_{mech} is plotted per reconstructed cycle, similarly to what was done for the time shift. The values computed for the three first reconstructed cycles, at each stress amplitude, are plotted.

The mechanical work increases with the stress amplitude, from a few hundreds to a few thousands of $J.m^{-3}.cycle^{-1}$ between 20 and 80 MPa, for both specimens. The mechanical work estimated for specimen "Cu2" is higher than what is measured for specimen "Cu1".

For specimen "Cu1", the mechanical work decreases with respect to the number of loading cycles. It decreases after 6.48×10^6 cycles (corresponding to the first reconstructed cycle) and tends to stabilize after 1.69×10^7 cycles. For specimen "Cu2", the decrease

2. Being located at a higher 2θ position, the $5\bar{5}5$ peak should exhibit a higher displacement than the $2\bar{2}6$ peak, but its lower XEC value induces, in fact, a lower peak displacement.



$$\text{1st cycle:}\quad 781.4\left(e^{-\frac{(\sigma-41)^2}{289.1}}-\frac{1}{1.8}e^{-\frac{(\sigma-46)^2}{289.1}}\right)+e^{0.02\sigma^{1.4}}$$

$$\text{2nd cycle:}\quad 909.8\left(e^{-\frac{(\sigma-47)^2}{214.9}}-\frac{1}{1.8}e^{-\frac{(\sigma-52)^2}{214.9}}\right)+e^{0.16\sigma^{0.86}}$$

$$\text{3rd cycle:}\quad 811.4\left(e^{-\frac{(\sigma-51)^2}{99.5}}-\frac{1}{1.8}e^{-\frac{(\sigma-46)^2}{99.5}}\right)+e^{0.04\sigma^{1.17}}$$

FIGURE 3.10 – Evolution of the Mechanical work with respect to the applied stress amplitudes - case of copper single crystal, specimen "Cu1". For one stress amplitude, the three points correspond to the mechanical work evaluated for three cycles successively reconstructed.

is less distinct, which can be explained by the higher uncertainties on the measurements for this specimen. The error bars plotted on the curves are essentially induced by the uncertainty arising from the estimation of the time shift.

For specimen "Cu1", the mechanical work shows a local maximum between 30 to 55 MPa, similarly to what was observed on the time shift evolution. Above such stress amplitude, the mechanical work seems to decrease before increasing strongly above 60 MPa. This particular evolution of the mechanical work could have been attributed to the noise on the reconstruction or to an experimental artefact. However, the evolution of the mechanical work of the specimen "Cu2" shows a similar trend, at stress amplitudes in the same order of magnitude. This confirms that the particular evolution of the mechanical work does not experience a simple exponential growth with stress amplitude.

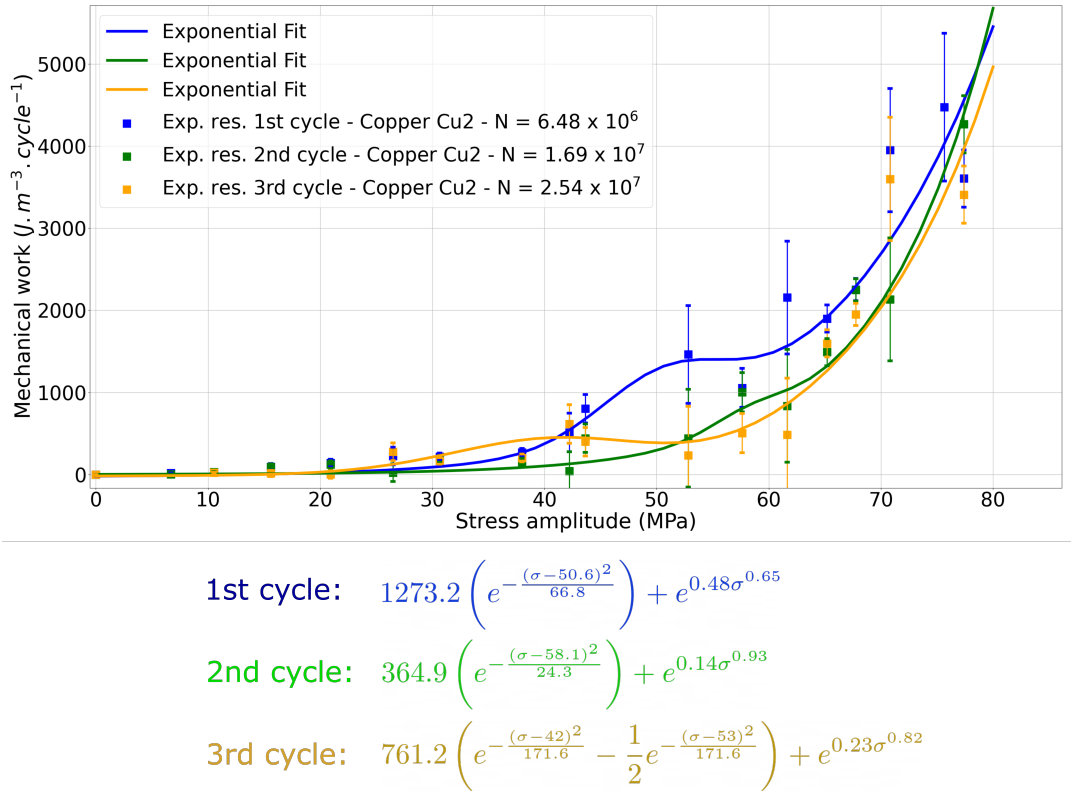


FIGURE 3.11 – Evolution of the Mechanical work with respect to the applied stress amplitudes - case of copper single crystal, specimen "Cu2". For one stress amplitude, the three points correspond to the mechanical work evaluated for three cycles successively reconstructed.

The equation used to fit the typical evolutions of the mechanical work, with respect to the stress amplitude, are reported on the respective figures for both specimens. The fit functions were chosen as the combination of an exponential growth with two small positive and negative (gaussian) hills. The fits allow identifying precisely the positions of the hills.

3.2.2 Estimation of the dissipated energy evolution with the stress amplitude

The energy that is dissipated by copper was measured during short interrupted tests. This section presents the evolution of the dissipated energy with the stress amplitude.

3.2.2.1 Experimental protocol for dissipative measurements

The experimental protocol that was applied aimed at sweeping stress amplitudes in the same order of magnitude as what was applied during the experiments conducted to estimate the mechanical work. Figure 3.12 shows the loading history for copper specimen "Cu1". The specimen that was used for temperature measurements is the same as the one loaded at SOLEIL Synchrotron for XRD measurements. Thus, the loading history exposed in this section happened after the loading history of Figure 3.1.

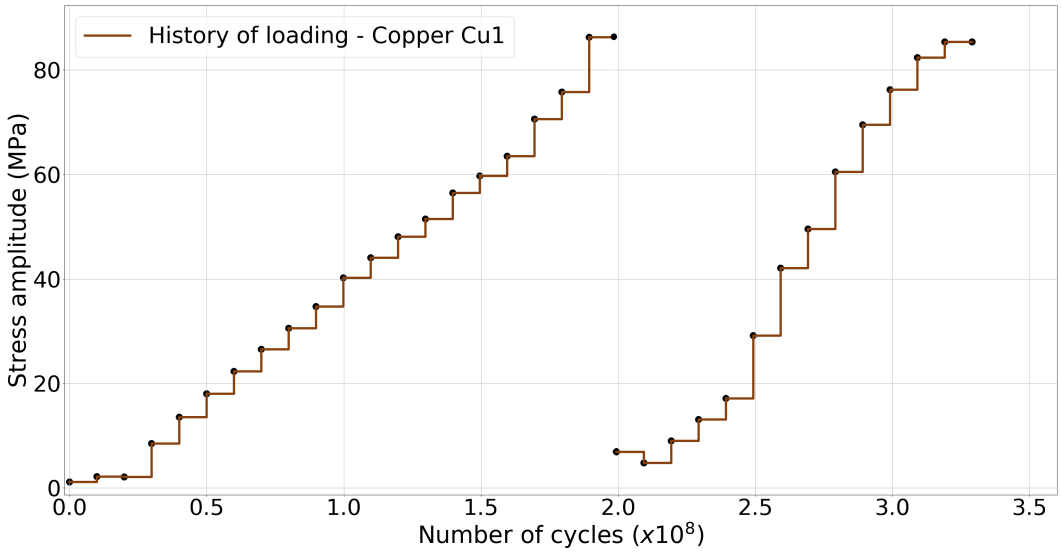


FIGURE 3.12 – Loading history of specimens put in vibration with the ultrasonic fatigue machine during temperature measurements - case of copper single crystal, specimen "Cu1".

Each loading step was maintained during blocks of 10^7 cycles during which the IR camera recorded the temperature at the surface of the specimen. Two increasing ramps (in stress amplitude) were applied to the specimen with slightly different stress amplitudes to increase the statistics of the self-heating curve. The stress amplitude that was applied to the specimen was estimated from the measurement of the displacement amplitude at the free end of the specimen (see Section 2.3.1.5).

3.2.2.2 Influence of the stress amplitude on the dissipated energy

During the ultrasonic fatigue interrupted tests conducted to estimate the dissipated energy, the temperature at the surface of the specimen was measured. This temperature increment was seen to reach a plateau after a few 10^6 cycles (see Section 2.5.2). The temperature increment corresponding to the plateau is defined as the saturation temperature θ_s. Its evolution with respect to the stress amplitude is shown in Figure 3.13.

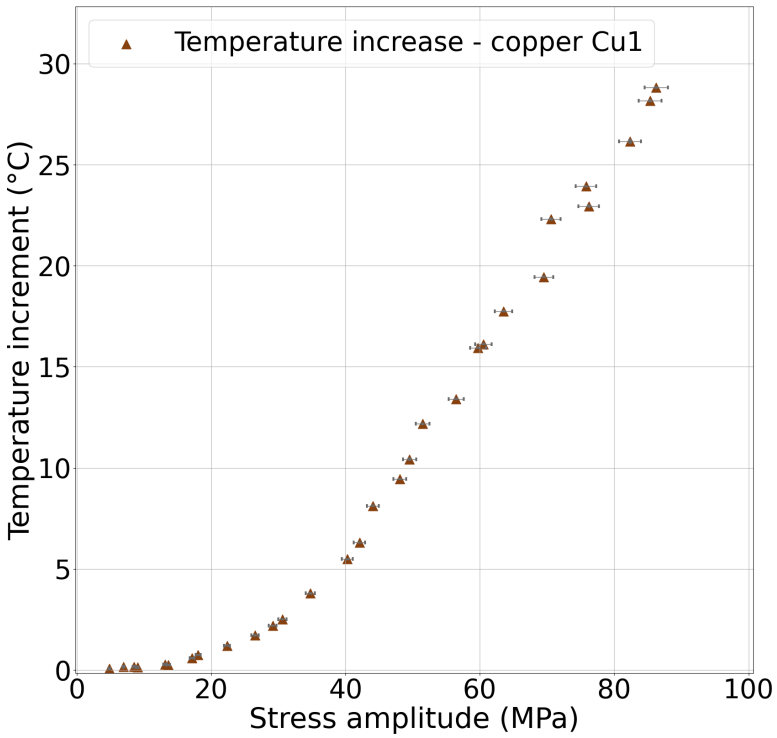


FIGURE 3.13 – Evolution of temperature imcrement (θ_s) with respect to the applied stress amplitudes - case of copper single crystal, specimen "Cu1".

The dissipated energy per cycle is computed by employing the 0-dimensional heat equation (see Section 2.5.3) from the temperature measurements. Figure 3.14 shows the evolution of the dissipated energy for the pure copper single crystal specimen that was subjected to the abovementioned loading history. Each dissipated energy measurement (each point on the curve) is thus associated with the energy that was dissipated by the specimen at a fixed stress amplitude at the end of the loading block (after 10^7 cycles).

The results show an increase following a quasi-quadratic evolution. The fitting of the results is reported on the figure and both evolutions show an exponent that is close to 2. The two increasing ramps provided results that lie very close. Thus, it can be observed

that the energy dissipated by our copper single crystal specimen is not dependent on the loading history. The assumption could thus be made that the loading applied to the specimen during the experiments conducted to estimate the mechanical work did not influence the amount of energy that was dissipated by the material, in the present measurement, at similar stress amplitudes.

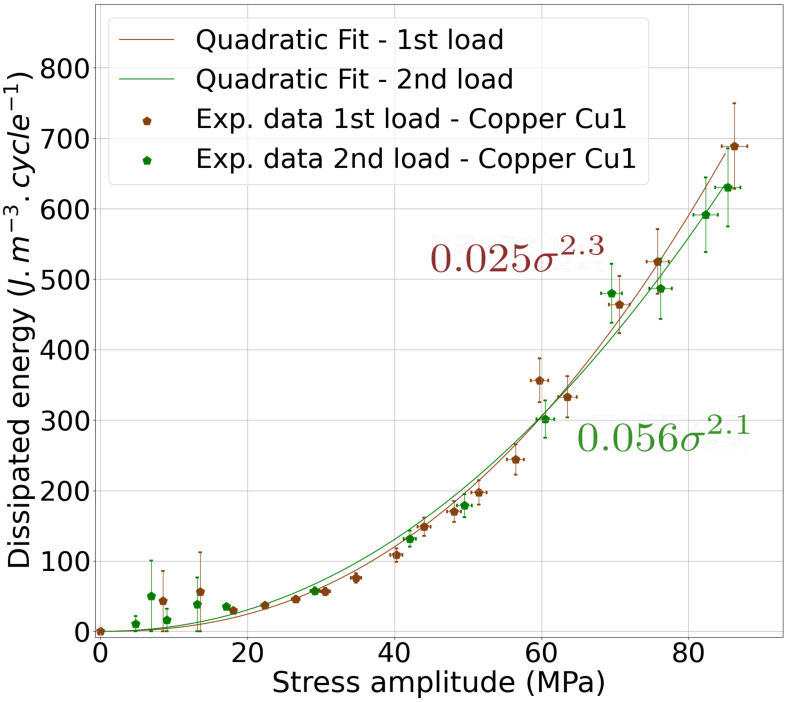


FIGURE 3.14 – Evolution of dissipated energy with respect to the applied stress amplitudes - case of copper single crystal, specimen "Cu1".

3.2.3 Evolution of the stored energy with the number of cycles and the stress amplitude

The stored energy can be computed from the estimations of the mechanical work and the dissipated energy that was conducted. This section is devoted to the analysis of the evolution of the stored energy with respect to the number of cycles and the stress amplitude.

3.2.3.1 Estimation of the stored energy

The dissipated energy and the mechanical work were estimated independently by applying two different loading histories. The computation of the energy balance as the difference between both quantities requires to use a fitting procedure. The evolutions of dissipated energy and mechanical work (with respect to stress amplitude) are fitted and the difference between their equivalent fit is computed to estimate the stored energy.

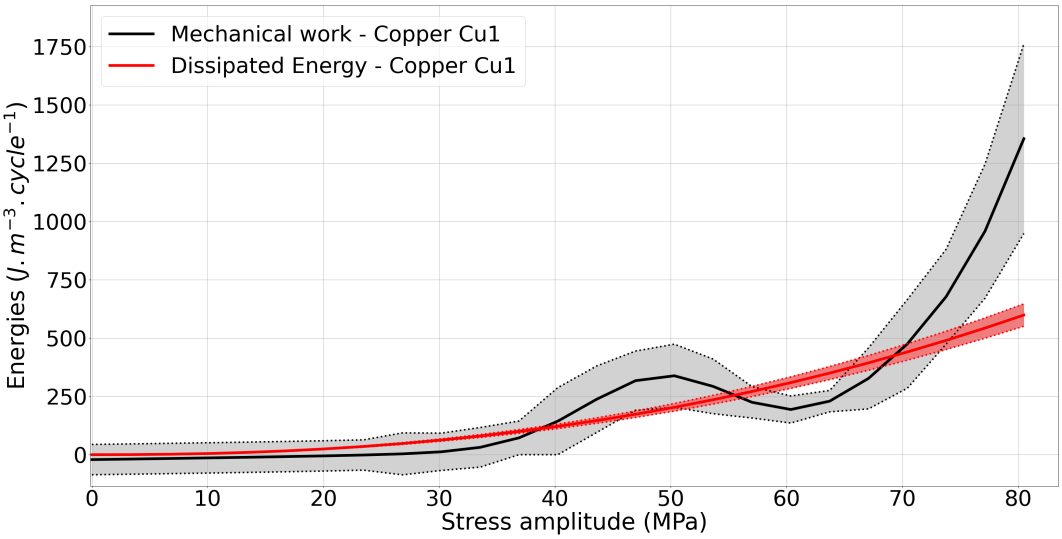


FIGURE 3.15 – Evolution of the both mechanical work (for the third reconstructed cycle) and dissipated energy with respect to the stress amplitude applied to the specimen - case of copper single crystal, specimen "Cu1".

Both fitted evolutions are reported on the same plot, in Figure 3.15. The mechanical work that is plotted in this figure corresponds to the third cycle that was reconstructed, i.e. when the mechanical work is considered stabilized after its initial decrease (see Section 3.2.1.2). The envelope added to the figure corresponds to the statistical uncertainties on the respective measurement of both quantities.

3.2.3.2 Influence of the number of cycles on the stored energy

The temperature of the material reached a plateau during the thermographic measurements that were conducted during at least 10^7 loading cycles. For longer fatigue lives, the temperature remains constant. Thus, the dissipated energy should be the same for a fatigue test conducted during 10^7 or 10^8 loading cycles. From this assumption, the estimation of the stored energy is possible for successive cycles reconstructed at a maintained stress amplitude : the same value of dissipated energy is retrieved to the values of mechanical work estimated for each reconstructed cycle.

At least eleven cycles were reconstructed at a stress amplitude that was maintained at 80 ± 1.5MPa during 10^8 loading cycles. This allows one to study the evolution of stored energy with respect to the number of loading cycles. The dissipated energy is estimated at $630 J.m^{-3}.cycle^{-1}$ (from Fig. 3.15) for a stress amplitude of 80 MPa and is found constant during the 10^8 cycles of the test.

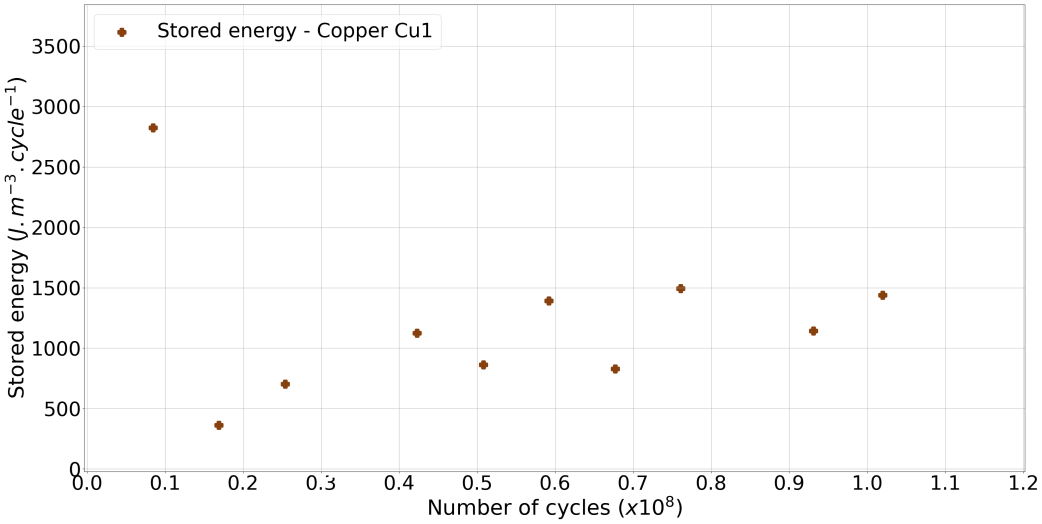


FIGURE 3.16 – Evolution of the stored energy with respect to the number of loading cycles applied to the specimen for a loading amplitude of 80 MPa maintained during 1.02×10^8 cycles - case of copper single crystal, specimen "Cu1".

Figure 3.16 shows the evolution of the stored energy with respect to the number of loading cycles applied to the specimen at the maintained amplitude. It is measured at $2850 J.m^{-3}.cycle^{-1}$ after 8.46×10^6 cycles, decreases down to $420 J.m^{-3}.cycle^{-1}$ after 1.69×10^7 cycles and then increases up to a plateau that lies around $1100 J.m^{-3}.cycle^{-1}$ after at least 2.4×10^7 cycles. Thus, the stored energy per cycle is considered stabilized after this number of cycles. Notwithstanding, the plateau that is reached shows a variation of the stored energy in the order of $\pm 250 J.m^{-3}.cycle^{-1}$. It is believed to be induced

by the uncertainty on the measurement of the time shift between stress and strain. The present results are consistent with what was reported by [Martins et al., 2020] (resp. [Zhang et al., 2019]) who studied the amount of stored energy per cycle with respect to the number of loading cycles in the case of steel (resp. shape memory alloys) in the LCF domain and found a decrease with respect to the number of loading cycles.

One can correlate the amount of cumulated stored energy with respect to the total number of loading cycles. From an integration of the curve shown in Figure 3.16, one can estimate that after the 10^8 cycles applied to the specimen at a stress amplitude of 80 MPa, the cumulated stored energy of the specimen is about $E_{st,cum}(79.5) = 9.88 \times 10^{10} J.m^{-3}$. This is 10000× higher than what was estimated by [Clarebrough et al., 1957] in LCF after 10^6 cycles applied to a polycrystalline copper (see Section 1.3.3). This could be explained by the 100× higher number of loading cycles applied to the specimen and possibly by the very high frequency at which these tests were conducted.

3.2.3.3 Estimation of the cumulative stored energy until the fracture of a specimen

The specimen "Cu2" was loaded for higher stress amplitudes than specimen "Cu1". It leads to a failure of the specimen "Cu2" at 93 MPa after 2.5×10^7 cycles. This corresponds to the last loading step shown in Figure 3.1b.

The amount of energy that was stored during this loading step could be estimated. First, we can consider the mechanical work that was estimated for the second (and only reliable) reconstructed cycle as $W_{mech}(93) = 11400 J.m^{-3}.cycle^{-1}$. In addition, the dissipated energy can be extrapolated from the fitted evolution shown in Figure 3.14 for specimen "Cu1". Both specimens have the same longitudinal orientation and are believed to exhibit the same thermographic behavior. Thus, from the fitting function $E_{diss} = 0.025\sigma^{2.3}$ one can extrapolate that $E_{diss}(93) = 842 J.m^{-3}.cycle^{-1}$. The stored energy per cycle at this stress amplitude is thus estimated at $E_{st}(93) = 10558 J.m^{-3}.cycle^{-1}$.

The loading being applied during 2.5×10^7 cycles, the cumulated stored energy until the fracture of the specimen is estimated at $E_{st,cum}(93) = 2.639 \times 10^{11} J.m^{-3}$. This value is considered to be a stored energy threshold of copper single crystal above which failure occurs.

3.2.3.4 Influence of the stress amplitude on the stored energy

The results of stored energy are plotted with respect to the applied stress amplitude in Figure 3.17 in the case of specimen "Cu1". Solely the results obtained from the third reconstructed cycle are reported, as the stored energy per cycle is considered stabilized. The envelope of the estimation is reported in the figure. It is calculated by the propaga-

tion of uncertainties arising from the estimation of both mechanical work and dissipated energy.

The variations of stored energy with respect to stress are observed to be rather small, but significant compared to the envelope of the evolution. The stored energy evolution with respect to the stress amplitude follows the evolution of the mechanical work evidenced previously.

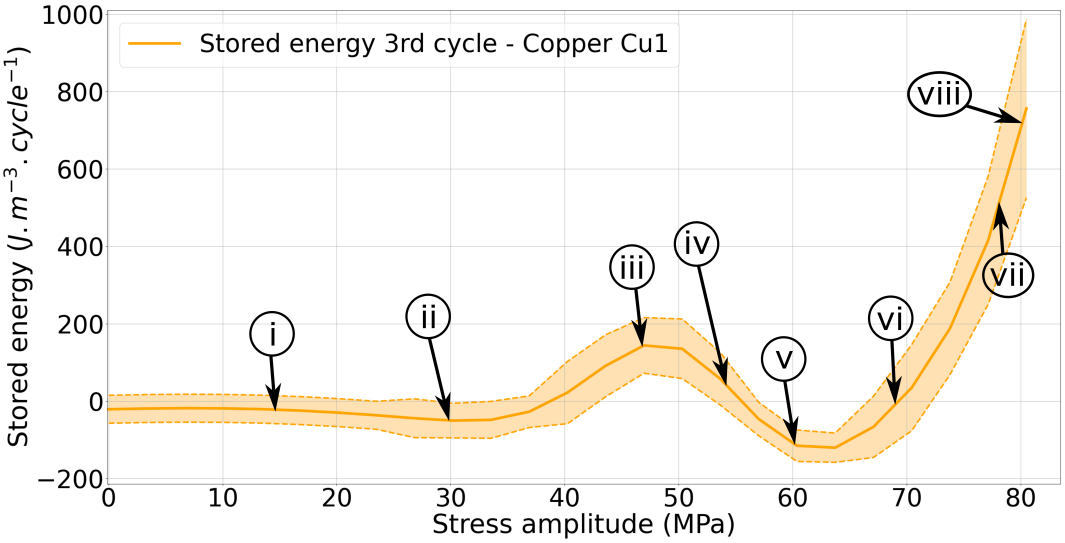


FIGURE 3.17 – Evolution of the stored energy with respect to the stress amplitude applied to the specimen - case of copper single crystal, specimen "Cu1". Results are shown for the third reconstructed cycle, for which the stored energy is considered stabilized.

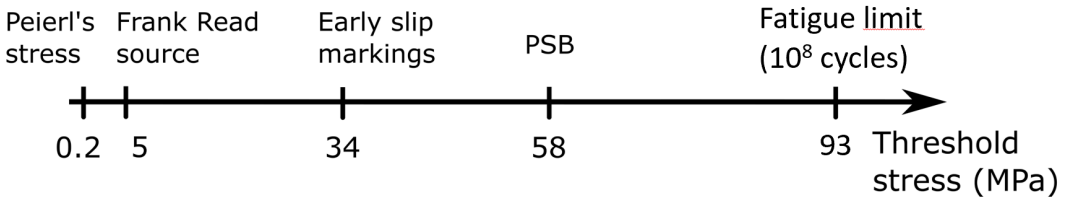


FIGURE 3.18 – Threshold (nominal macroscopic) stress for appearance of microstructural mechanisms in pure copper single crystals : Peierl's [Nabarro, 1997], Frank-Read [Madec et al., 2000], slip markings [Stanzltschegg et al., 2007], PSB [Mughrabi, 1978].

As a matter of fact, the stored energy amount that was estimated in the present study could be compared to the values that were displayed in Section 1.3.3. To be comparable, the amount of stored energy estimated for several materials will be compared with

respect to a unified quantity that is the ratio σ/R_m between the applied stress and the ultimate tensile stress. The stored energy per cycle, that was estimated in this study, ranges close to $7.7 \times 10^2 J.m^{-3}.cycle^{-1}$ for $\sigma/R_m = 0.38$[3] and is in the order of $1.5 \times 10^2 J.m^{-3}.cycle^{-1}$ for $\sigma/R_m = 0.24$. The comparison can be made with the results reported by [Hu et al., 2021] in the case of aluminum alloys as no results were found in the literature concerning copper. Hu *et al.* measured the stored energy per cycle to be about a few $10^4 J.m^{-3}.cycle^{-1}$ for $\sigma/R_m = 0.56$, i.e. in the LCF regime of the material. It is 10 to 100× higher than what we found in the case of a loading in the VHCF regime of copper.

The local maximum that was observed on the evolution of the mechanical work is observed as well on the evolution of the stored energy. The hill appears between 30 and 55 MPa. According to Figure 3.18, which recalls the threshold stress at which dislocation structures form in copper, this range of stress corresponds to the appearance of slip markings in the material. These slip markings are precursors to persistent slip bands (PSB) with ladder-like structure, representative of the slip irreversibility in the material. The diffraction peak width (FWHM) is correlated with the stress heterogeneity and the dislocation density (see Section 2.4.2.2). The study of the peak width evolution during a fatigue loading provides complementary information about the dislocation's content and its evolution. FWHMs were thus measured simultaneously to the estimation of stored energy for specimen "Cu1".

Figure 3.19 shows the reconstructed cyclic evolutions of the $2\bar{2}6$ diffraction peak FWHM for the three first reconstructed cycles, in the case of eight particular stress amplitudes[4]. The stress amplitudes at which the FWHM are presented corresponds to stress amplitudes at which the stored energy has specific values, as reported in Figure 3.17.

3. The ultimate tensile stress of copper single crystal is taken similar to polycrystalline copper, i.e. $R_m = 210$MPa.

4. It is worth noting that the FWHM evolution is in anti-phase with respect to the strain gauge signal reported on the figures, owing to the XRD study that is conducted in the direction perpendicular to the loading direction (along the specimen length). Thus, when a tensile load is measured by the strain gauge, it corresponds to a negative lattice strain in the perpendicular direction.

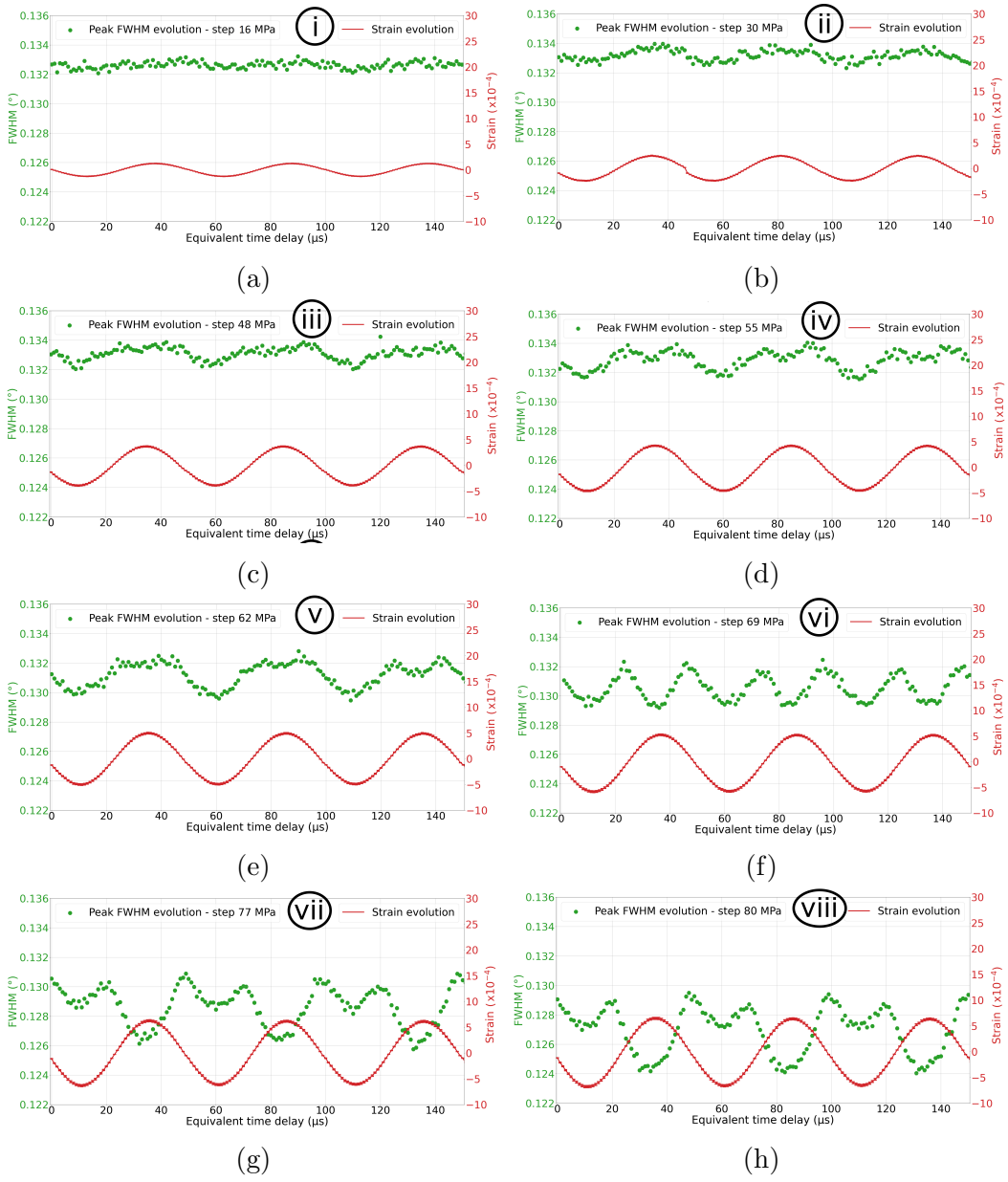


FIGURE 3.19 – Evolution of the FWHM of the $2\bar{2}6$ diffraction peak (copper single crystal) with respect to the applied delay to acquire the data. The cyclic evolution of the FWHM is acquired cycle per cycle. Their representation one after the other is made for sake of simplicity. Yet, it does not mean that these reconstructed cycles are successive as they are each reconstructed over 8.46×10^6 cycles. The strain measured by the strain gauge provide an element of comparison to the cyclic evolution of the FWHM. The FWHM are plotted for stress amplitudes of a) 16 MPa, b) 30 MPa, c) 48 MPa, d) 55 MPa, e) 61 MPa, f) 69 MPa, g) 77 MPa and h) 80 MPa.

The FWHM evolution of the $2\bar{2}6$ diffraction peak shows similar evolutions to what was presented in Section 2.4.3.5. A sinusoidal evolution is observed for stress amplitudes lower than 40 MPa. Above 48 MPa, the specific evolution of the FWHM is similar to what is observed for polycrystalline materials. Thus, we propose to fit their cyclic evolutions by the following function :

$$A_w + B_w \sin(\omega t) + C_w \sin(\omega t)^2 \tag{3.2}$$

where the signification of the three parameters A_w, B_w and C_w becomes different than typical models used for polycrystalline materials (see Section 2.4.3.5). Indeed, in the case of a single crystal, they could be described as :

Aw : corresponds to the "average" peak width (during one cycle), which is associated with the average dislocation density.

Bw : corresponds to the amplitude of the peak width evolution (during one cycle). It is linked with the intensity of fluctuation of the dislocation density.

Cw : is associated with the difference of behavior of the fluctuation of dislocation density between the tensile and compressive part of the cyclic loading[5]. This parameter remains difficult to interpret.

The evolution of the three parameters with respect to the stress amplitudes is represented in Figure 3.20.

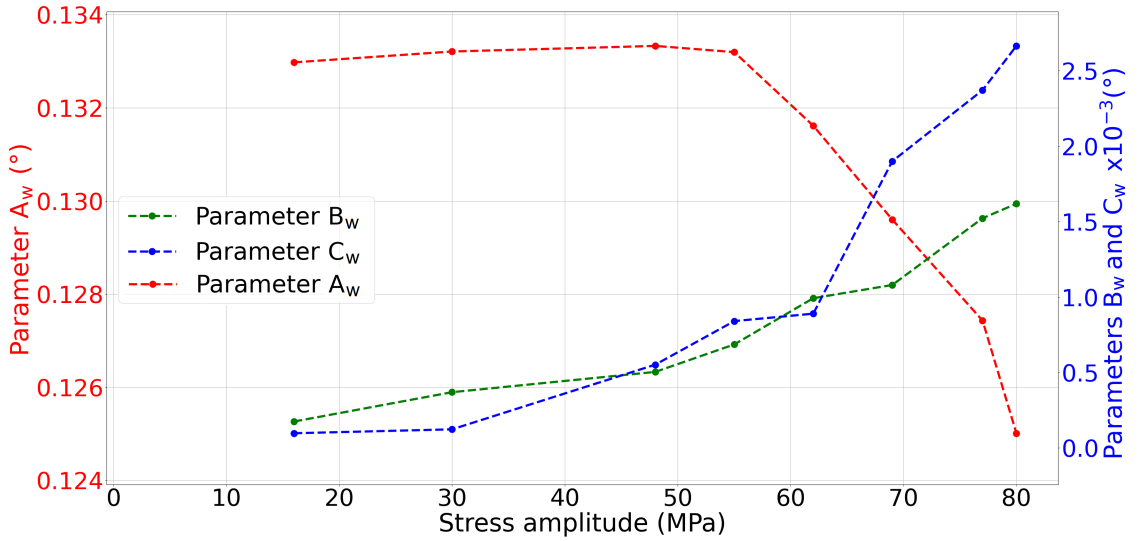


FIGURE 3.20 – Evolution of parameters A_w, B_w and C_w with respect to the stress amplitudes - case of copper single crystal, specimen "Cu1".

5. If C_w is null, it means that the fluctuation of dislocation density between the tensile and compressive states of the material is equivalent, except for the sign.

One can see that parameter A_w remains constant up to 56 MPa and drops above this stress amplitude. However, parameter B_w increases continuously with the stress amplitudes. Parameter C_w increases continuously with the stress amplitudes as well but shows a steep increase above 62 MPa.

The behavior exhibited by the evolution of the stored energy, with respect to the applied stress amplitude seems correlated to the variation of the parameters of the diffraction peak width evolutions. Four observations can be made :

- The increase of parameter B_w is continuous, which is associated with a higher fluctuation of the dislocation density during one loading cycle at a higher stress amplitude. Such fluctuation is consistent with the results reported by [Erel, 2015]. Dislocations can also be considered more mobile, which is correlated to the continuous increase in dissipated energy with the increasing stress amplitude (see Fig. 3.14).
- The local maximum observed in the stored energy per cycle evolution corresponds to parameter C_w starting to increase and becoming greater than parameter B_w. It might be representative of the appearance of slip markings.
- The stress amplitude at which PSB appears, i.e. above 55 MPa (see Fig. 3.18), corresponds to the decrease of parameter A_w. It is also correlated to the stored energy per cycle being negative. This might be due to a decrease of dislocation density associated with the formation of PSBs.
- The C_w parameter starts to increase steeply at a stress amplitude above 62 MPa. In parallel, the stored energy per cycle is increasing sharply as well and becomes positive again. The increase in parameter C_w could be attributed to a stronger difference of dislocation behavior under the tensile and compressive part of the cyclic loading. This could thus be a representation of the irreversibility of the dislocation movement in fatigue.

The present discussion concerning the correlation between stored energy and FWHM is open to questionning and further investigations of the evolution of FWHM would be required to obtain a knowledgeable answer. Such work is conducted by Doriana Vinci (Post-doctoral for the FastMat project) and will be the subject of an upcoming article about the evolution of the FWHM in the case of the present copper single crystal loaded in fatigue at 20 kHz.

3.3 Estimation of the stored energy : case of C70 pearlitic steel

The methodology applied to the uniform mode of SOLEIL Synchrotron was not providing a time resolution that was small enough to estimate the stored energy in C70 steel. The methodology was thus diverted to be applied in single-bunch mode to allow an acceptable estimation of stored energy in steel.

3.3.1 Estimation of the mechanical work evolution with the stress amplitude and number of cycles

In this section, the objective is to present and discuss the evolution of the mechanical work with the applied stress amplitude that was estimated in the case of our C70 steel.

3.3.1.1 Experimental protocol of the tests

The focus is made on specimen "C70-P6-SB" which was tested in single-bunch mode with the developed setup. The loading history applied to the steel specimen is reported in Figure 3.21. The minimum stress applied during the tests was in order of 35 MPa and the maximum applied stress reached 253 MPa.

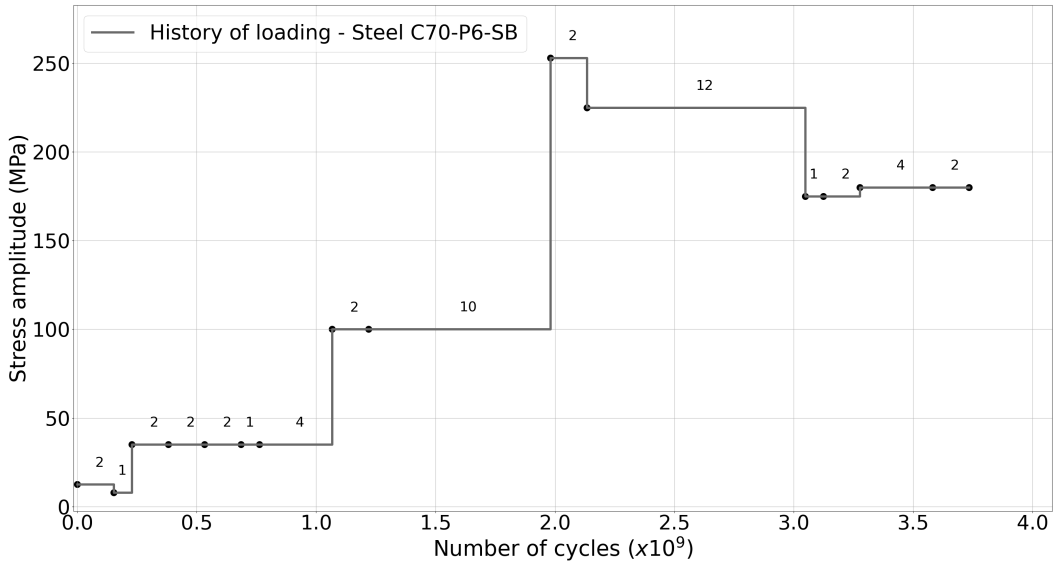


FIGURE 3.21 – Loading history of specimens put in vibration with the ultrasonic fatigue machine during XRD measurements : specimen "C70-P6-SB". Stress amplitudes has been estimated by using strain gauge.

XRD measurements focused on the 110 diffraction ring of the ferrite phase as it is the most intense. In the present case of the single-bunch mode, an SNR of 265 can be obtained on the diffraction peak, which guarantees a low influence of the photon noise on the reconstructed stress and strain evolution. Table 3.4 shows the uncertainties on the estimation of the diffraction peak position and the peak width. The uncertainties reported in the present table are at least 2.5× lower than what was evidenced for the tests conducted on the C70 steel in uniform mode (see Table 3.2), which underlines the improvement that the single bunch mode brought to the methodology.

TABLE 3.4 – Characteristic of ferrite 110 diffraction peak studied in single-bunch mode. The uncertainty is computed as the standard deviation of 50 acquired diffraction peaks - case of C70 steel, specimen "C70-P6-SB"; beam energy of 18 keV.

			Reference values		Standard deviations	
Specimen	Peak (hkl)	SNR	2θ (°)	FWHM (°)	2θ (°)	FWHM (°)
C70-P6-SB	110	265	19.6	0.0656	1.7×10^{-4}	1.7×10^{-4}

For steel in single-bunch mode, the intensity acquired on each frame during the frame accumulation process is small. Thus, the duration of the accumulation process is longer than that used for copper. The reconstruction of one cycle was seen to take 1.1×10^8 cycles. In fact, one cycle is reconstructed in 1.5 hour of test. It remains acceptable in terms of stability of the material state during the fatigue loading at stress amplitudes below 260 MPa as the material was seen to exhibit an elastic behavior (see Section 3.1.2.2).

3.3.1.2 Influence of the stress amplitude and number of cycles on the mechanical work

From the measurements of both stress and strain amplitudes and the estimation of the time shift between both signals, the mechanical work W_{mech} can be estimated. The results obtained are shown in Figure 3.22. The error bars represent roughly 40 to 70% of the measured value. This uncertainty arises specifically from the uncertainties of the estimation of the time shift between stress and strain, which is induced by the strong influence of the beam drift on the reconstructed cycles of the stress evolution (see Section 2.4.2.7).

The mechanical work per cycle decreases with the number of loading cycles. The decrease is shown to be about 66% from the first to the third reconstructed cycle, i.e. from 1.1×10^8 to 3.3×10^8 cycles. From these results, it is difficult to conclude on the potential stabilization of the mechanical work with respect to the number of cycles.

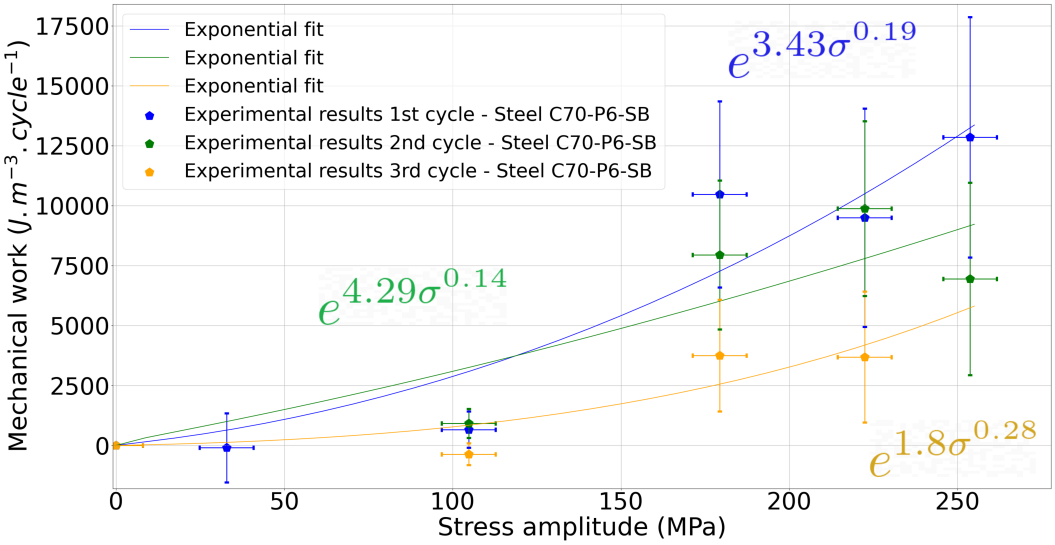


FIGURE 3.22 – Evolution of the Mechanical work with respect to the applied stress amplitudes - case of C70 steel. For each stress amplitude, the values measured for three reconstructed cycles are reported. For one stress amplitude, the three points corresponds to the mechanical work evaluated for cycles respectively reconstructed after 1.1×10^8, 2.2×10^8 and 3.3×10^8 loading cycles.

The mechanical work shows an exponential increase with respect to stress amplitudes. It reaches at least $10^4 J.m^{-3}.cycle^{-1}$ for the first reconstructed cycle and for stress amplitudes higher than 180 MPa. The order of magnitude estimated in the present work is consistent with the values obtained by [Connesson et al., 2011b] for a low carbon steel subjected to fatigue loading in HCF and VHCF domains.

3.3.2 Estimation of the dissipated energy evolution with the stress amplitude

This section presents and discusses the results of the evolution of the dissipated energy, with respect to the stress amplitude estimated from the C70 steel specimen.

3.3.2.1 Experimental protocol for dissipative measurements

Figure 3.23 shows the loading history of the steel specimen "C70-P6-SB" during the temperature measurements. The specimen that was used for temperature measurements is the same as the one loaded at SOLEIL Synchrotron for XRD measurements. Thus, the loading history exposed in this section happened after the loading history of Figure 3.21. Each loading step was maintained during blocks of 10^7 cycles.

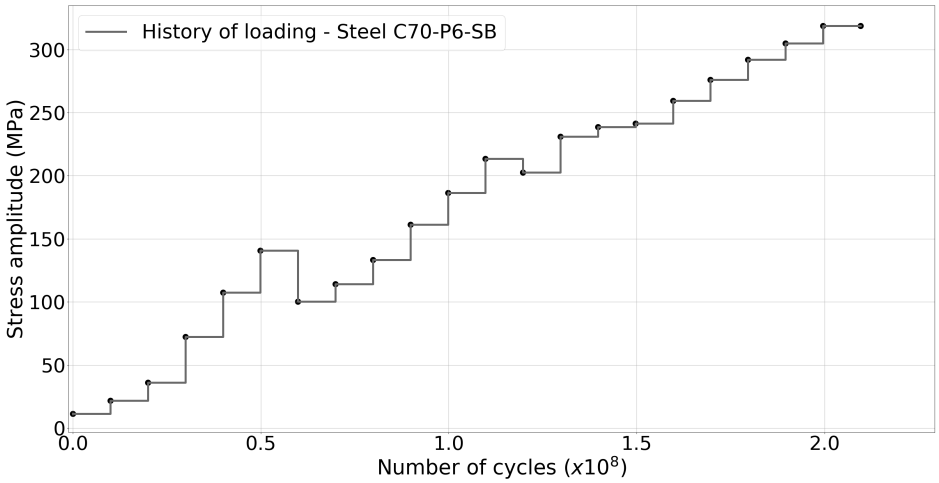


FIGURE 3.23 – Loading history of specimens for temperature measurements during ultrasonic fatigue tests - case of C70 steel, specimen "C70-P6-SB".

3.3.2.2 Influence of the stress amplitude on the dissipated energy

During the ultrasonic fatigue interrupted tests conducted to estimate the dissipated energy, the temperature at the surface of the specimen was measured. The temperature increment corresponding to the saturation temperature is plotted with respect to the stress amplitude in Figure 3.24.

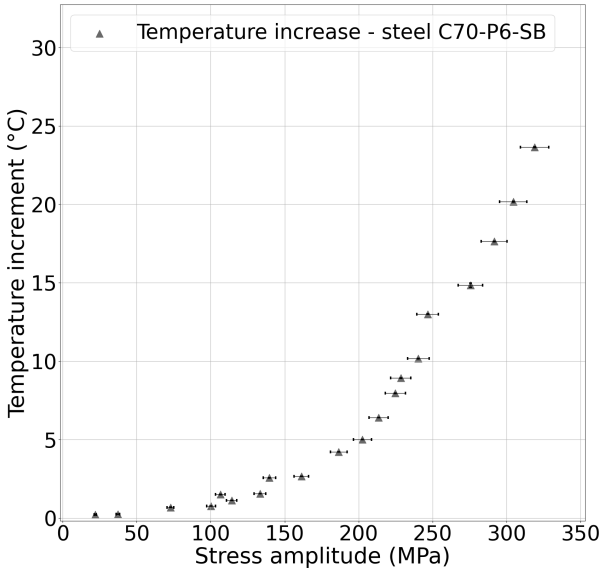


FIGURE 3.24 – Evolution of temperature imcrement (θ_s) with respect to the applied stress amplitudes - case of C70 steel, specimen "C70-P6-SB".

The dissipated energy was estimated from temperature measurements, as previously recalled for copper. Figure 3.25 shows the evolution of the dissipated energy with respect to the stress amplitude. The results show an increase following an almost quadratic law.

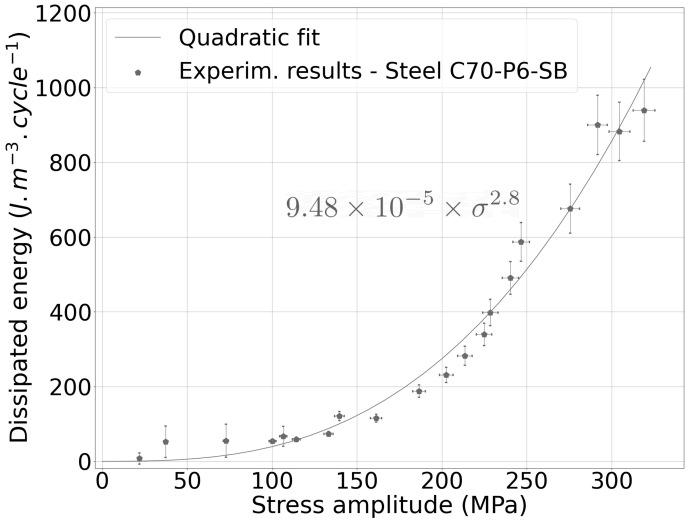


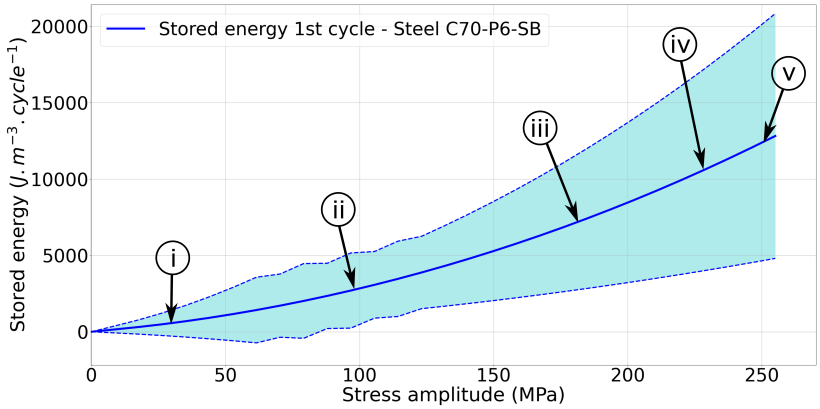
FIGURE 3.25 – Evolution of dissippated energy with respect to the applied stress amplitudes - case of C70 steel, specimen "C70-P6-SB".

The C70 steel shows a steep increase in its measured temperature increments for stress amplitudes above 150-200 MPa. The steep increase in the dissipated energy might indicate that dislocations are more mobile above such stress amplitude but it does not provide any intel on the irreversible character of the dislocation movements.

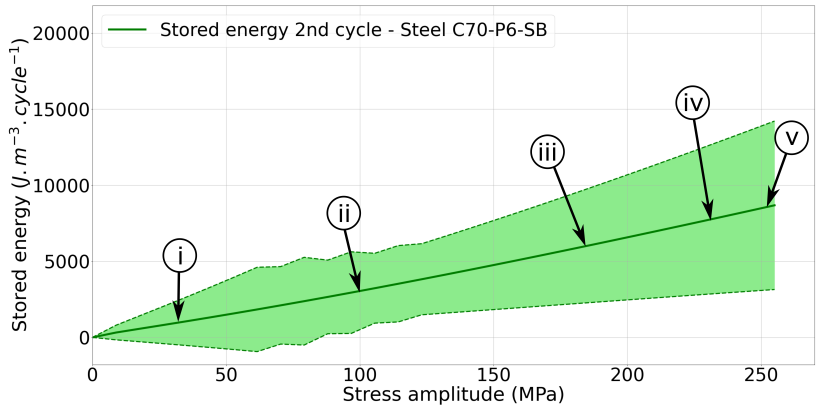
3.3.3 Estimation of the stored energy evolution with the stress amplitude and number of cycles

The results obtained for the estimation of the stored energy versus the stress amplitude are plotted in Figure 3.26. They show the evolution of stored energy in the case of the first three reconstructed cycles. The envelope plotted on the curves are calculated by the propagation of uncertainties arising from the estimation of both mechanical work and dissipated energy, with a stronger influence of the uncertainty made on the estimation of mechanical work.

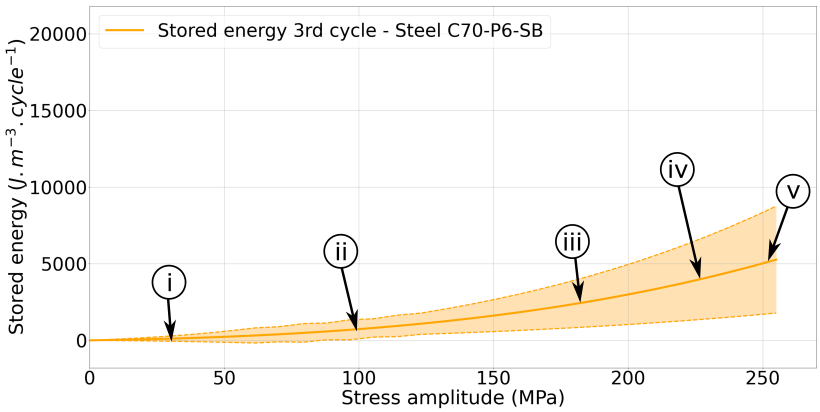
In the same manner as what was estimated in the case of copper single crystal, the stored energy that is estimated for steel is decreasing with the number of loading cycles. For instance, the stored energy decreased from $1.3 \times 10^4 J.m^{-3}.cycle^{-1}$ after 1.1×10^8 cycles down to $5 \times 10^3 J.m^{-3}.cycle^{-1}$ after 3.3×10^8 cycles.



(a)



(b)



(c)

FIGURE 3.26 – Evolution of the stored energy with respect to the stress amplitude applied to the specimen - case of C70 steel, specimen "C70-P6-SB". Results are shown for the a) first, b) second and c) third reconstructed cycles.

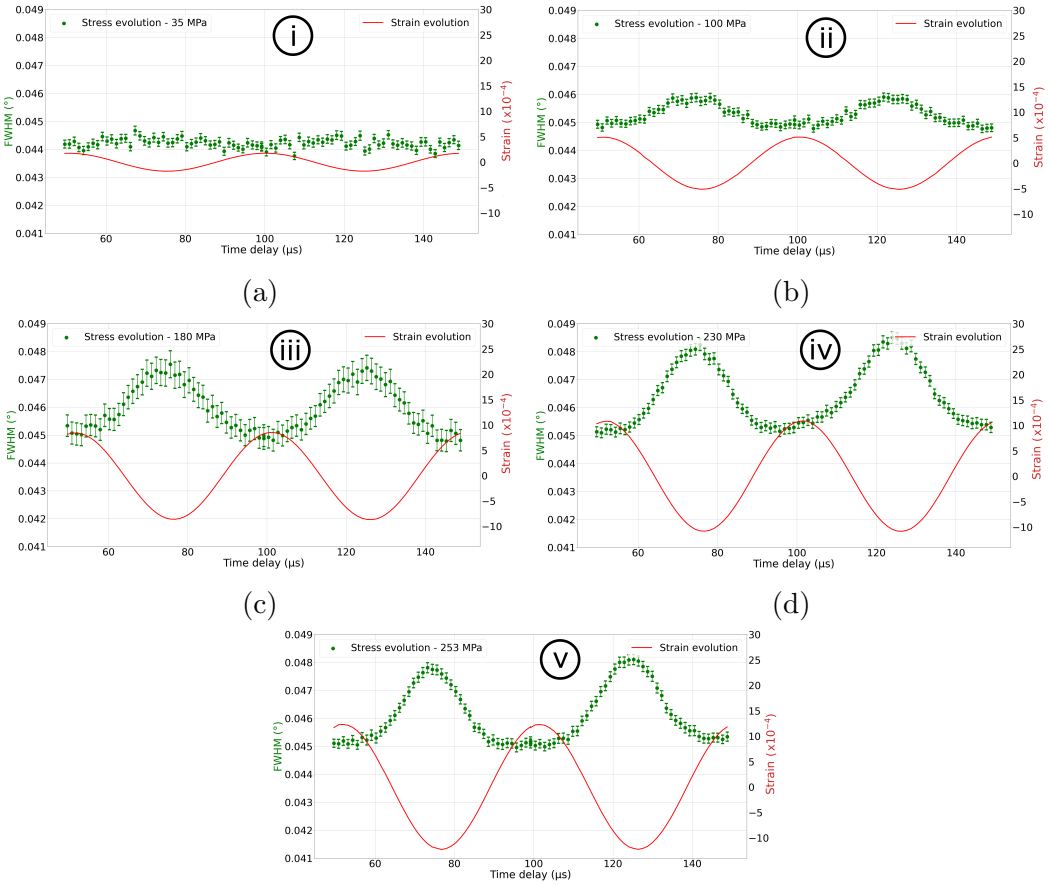


FIGURE 3.27 – Evolution of the FWHM of the 110 diffraction peak with respect to the applied delay to acquire the data. The cyclic evolution of the FWHM is acquired cycle per cycle. Their representation one after the other is made for sake of simplicity. Yet, it does not mean that these cycles are successive as they are each computed over 1.1×10^8 cycles. The strain measured by the strain gauge provides an element of comparison to the cyclic evolution of the FWHM. The FWHM are plotted for stress amplitudes of a) 35 MPa, b) 100 MPa, c) 180 MPa, d) 230 MPa and e) 253 MPa.

In addition, one can put the present results in front of the order of magnitude of the stored energy presented in Section 1.3.3. In a bainitic steel loaded at $\sigma/R_m = 0.76$, the results reported a stored energy of $6 \times 10^6 J.m^{-3}.cycle^{-1}$ [Martins et al., 2020]. Besides, a stored energy of $3 \times 10^5 J.m^{-3}.cycle^{-1}$ in a low carbon steel loaded at $\sigma/R_m = 0.88$ was evidenced by [Jirandehi and Khonsari, 2020]. In comparison to such results, the stored energy estimated in the present study is at least 100 to 1000× smaller (in the order of a few $10^3 J.m^{-3}.cycle^{-1}$). It is consistent when one considers the present fatigue loading conducted on the C70 steel in the VHCF domain at σ/R_m varying from 0.13 to 0.34.

The loading was held during 3×10^8 cycles at 253 MPa on the specimen "C70-P6-SB". The cumulated stored energy after this loading is estimated to be close to $2.7 \times 10^{12} J.m^{-3}$. This value is at least 200× higher than what was reported by [Martins et al., 2020] in the case of a bainitic steel loaded at $\sigma/R_m = 0.76$ (at low-frequency) after 10^4 cycles. It is thus highly probable that more energy has been stored in the present test as the loading was maintained during 3×10^8 cycles and the tests were carried out with an ultrasonic fatigue machine.

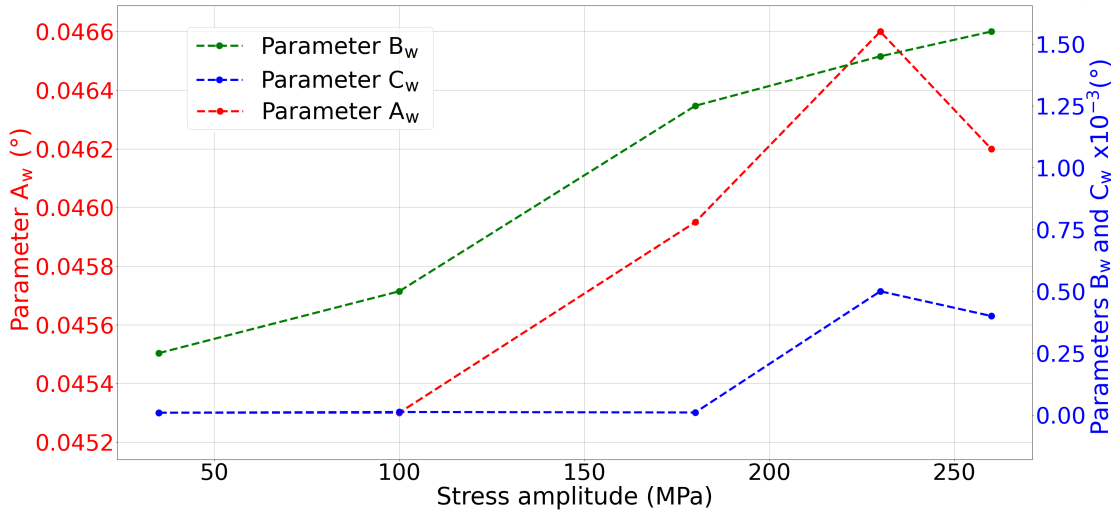


FIGURE 3.28 – Evolution of parameters A_w, B_w and C_w with respect to the stress amplitudes - case of C70 steel, specimen "C70-P6-SB".

A correlation between the FWHM evolutions and the evolution of the stored energy with stress amplitude in the steel specimen can be made. Similarly to what was presented for copper, Figure 3.28 shows the evolution of parameters A_w, B_w and C_w with respect to the stress amplitude. The following observations are reported :

- The amplitude of fluctuation of the FWHM (associated with parameter B_w mentioned previously) during one reconstructed cyclic evolution increases with stress amplitude. This means that dislocations are more mobile and that dislocation density is fluctuating largely at higher stress amplitudes. This corresponds to more energy stored in the specimen, and also to a higher amount of dissipated energy.
- Additionally, the average peak width (associated with parameter A_w) seems to be higher for higher stress amplitudes. This variation of the mean is associated with a substantial increase in dislocation density between 100 and 230 MPa. Additionally, a decrease is observed at a stress amplitude of 253 MPa.
- The specific variation of FWHM, following the "$\sin + \sin^2$" function, observed in the case of copper was not evidenced in the case of the steel, even at stress

amplitude of 253 MPa. However, the lower part of the FWHM evolution seems to be flatter than the upper part. In parallel, parameter C_w is increasing for stress amplitudes above 180 MPa. It could be associated with the tensile portion of the cycle that reaches a saturation of dislocation density.

3.3.4 Conclusion of the discussions

From the presented results, general tendencies can be extracted and expressed as follows :

- The stored energy per cycle is found to lie between a few hundreds and a few thousands of $J.m^{-3}.cycle^{-1}$ for both materials. This result is consistent with what is reported in the literature.
- For an increasing stress amplitude, the stored energy per cycle increases as well. This was shown for both materials.
- For a maintained stress amplitude, the stored energy per cycle decreases with the number of cycles applied to the material. It can reach a stable value after 2.5×10^7 cycles for copper.
- On the evolution of the stored energy per cycle with respect to the stress amplitude, a local maximum was observed between 30 and 55 MPa in the case of copper. It is believed to be correlated to the appearance of slip markings in the material. On the contrary, no local maximum was identified for steel.

The stored energy per cycle is estimated after the reconstruction of at least one cycle of stress and strain evolutions. Thus, the sampling frequency at which the stored energy is estimated during a fatigue loading is very small. In fact, one value of stored energy can be estimated every 7×10^6 cycles for copper (i.e. every 6 minutes) and every 1.1×10^8 cycles for steel (i.e. every 92 minutes)[6]. This rather low sampling frequency on the estimation of the stored energy depends on the accuracy of the measurements. For copper, the sampling frequency is higher because the SNR of the diffraction peaks studied is high and the reconstruction of the evolution of the stress is less influenced by the noise on the XRD images. This is not true for steel where the time required to reconstruct one cycle must be prolonged.

To explain the difference in accuracy of the measurements of stored energy between both materials, we must consider the noise on the XRD images but also the beam drifts. Beam drifts were seen to influence more the reconstructed stress signals measured on steel than on those measured on copper. This is owing to the smaller SNR of the studied

6. In the case of a loading at a lower frequency (at 10 Hz for instance), values of stored energy would be acquired more often (i.e. separated by a smaller number of loading cycles) but it would become too long to reach fatigue lives in the VHCF domain.

diffraction peaks of steel compared to copper, which in turn depends on the material to study, i.e. if it is a single crystal or a polycrystalline material. In addition, the beam drifts were seen to be even more influencing the reconstruction of the stress signal in the case of steel because the duration of one cycle reconstruction is at least 15× longer than for copper. It is thus more probable than the beam would drift during the reconstruction of one cycle in the case of steel than in the case of copper.

Conclusion and perspectives

General conclusions

This Ph.D. aimed at the development of an experimental methodology to determine fast the fatigue properties of metals in the VHCF domain. The fatigue loading was conducted with an ultrasonic fatigue machine, working at 20 kHz, to reduce the duration of the tests. The focus was directed toward the experimental estimation of the energy that is stored in metallic materials during a fatigue test. This quantity is believed to be representative of fatigue damage and its evolution throughout the cyclic loading. This work involved the development of a pump-probe methodology on a very large research instrument that is SOLEIL Synchrotron. This iterative development finally brought the methodology to reach a reliable state allowing the time-resolved methodology to be applied to two materials that are a pure copper single crystal and C70 pearlitic steel.

The major conclusions that are drawn from the developments conducted during this work are reported hereafter :

- The in situ time-resolved X-ray diffraction methodology enables one to estimate the longitudinal stress amplitude applied to a specimen (during an ultrasonic fatigue test conducted in the VHCF domain) from the measurement of the lattice strain underwent by grains, conditionally upon the correct estimation of the X-ray elastic constants of the studied material.
- It is possible to estimate the mechanical work during fatigue tests conducted at an ultrasonic frequency, from the reconstruction of stress and strain cyclic evolutions, by employing a method inspired from pump-probe techniques.
- The existing methodology of in-situ time-resolved XRD adapted to the uniform mode (continuous beam) of SOLEIL Synchrotron, was applied to estimate the mechanical work applied to a copper single crystal.
- A new approach was developed to be adapted to the single-bunch mode (pusled beam) of SOLEIL Synchrotron. It consists in synchronizing the vibration of the ultrasonic fatigue machine with the frequency of the X-ray pulses to carry out in situ XRD measurements. It was required to estimate the mechanical work brought to C70 steel.
- The uncertainties in the estimation of the time shift between stress and strain (which is the most influencing quantity when estimating the mechanical work) was estimated at 570 ns in uniform mode and 173 ns in single-bunch mode (arising from the total jitter of the experimental setup). However, the application of the stroboscopic approach led to statistical uncertainties that was brought to 5-30 ns in the case of copper in uniform mode and 30-75 ns in the case of steel in single-

bunch mode.

- The energy that is dissipated by the materials loaded cyclically was estimated from temperature measurements conducted during interrupted ultrasonic fatigue tests.
- Consequently, the energy that is stored in the material during the loading has been estimated from the establishment of an energy balance, after the dissipated energy and mechanical work were independently estimated experimentally.

Hereafter are reported the scientific contributions of this work :

- For both materials, and for a maintained fatigue loading at a given stress amplitude, the energy stored per cycle was seen to decrease with the number of cycles. After decreasing, the stored energy per cycle reaches a stabilized regime. The stabilized regime was reached after at least 2 to 3×10^7 cycles for copper single crystal.
- The energy stored per cycle increases with the stress amplitude for the two studied materials. For copper, it shows a local maximum at stress amplitudes between 30 and 55 MPa, followed by a small decrease leading to a negative stored energy per cycle. Finally, a steep increase is observed for the highest stress amplitudes applied. The local maximum appears for stress amplitudes corresponding to the possible appearance of early slip markings on the specimen surface and the negative stored energy per cycle is believed to be attributed to the formation of PSBs. Through its specific evolution, stored energy is believed to be a good marker of microstructural changes occuring during a fatigue loading. On the contrary, the evolution of dissipated energy with respect to stress did not allow one to draw such conclusions.
- Full width at half maximum (FWHM) of diffraction peaks are believed to be representative of the dislocation density. From the present work, the cyclic evolution of the FWHM, with respect to the stress amplitude, was seen to be correlated to the evolution of the stored energy and thus to the microstructural change possibly occurring in the material.

Perspectives

The methodology is not exempt from improvements and this section intends to give some leads to make the methodology even more efficient or to diversify its applications.

Refinement of the temporal resolution

The fluctuation observed in the estimation of the stored energy per cycle is constrained by the experimental methodology employed in this work. An additional decrease in the time resolution on the estimation of the time shift between stress and strain would reduce the uncertainties on the estimation of the stored energy. It could thus make the existence of the observed local maximum clearer on the evolution of stored energy with respect to stress (at least for copper).
Besides, investigating more levels of stress amplitude would also clarify the position of the local maximum with respect to stress. In addition, it would be interesting to investigate several more levels of stress amplitude, between 100 and 400 MPa for C70 steel, in order to determine if the local maximum can be observed for this material as well. This is possible by increasing the electrical power generated by the power supply that was developed during this work to allow the synchronisation of the ultrasonic fatigue machine with the synchrotron.

Extend the measurements to longer fatigue lives

An improvement of the time resolution with which the time shift is estimated would reduce the fluctuation of stored energy estimates from one cycle to another. This would help to confirm the exactitude of the stabilized regime that was highlighted in this work. Furthermore, the investigation of the behavior of the stored energy for higher fatigue lives would be necessary. Indeed, knowing how the stored energy per cycle behaves for very long fatigue lives, above several 10^9 cycles for instance, would provide crucial information on the corresponding occuring microstructural changes.

Reduce the influence of the beam drifts

The stability of the X-ray beam that is used to conduct such in situ time-resolved X-ray diffraction measurements is of great importance. According to the material chosen to conduct these measurements, the influence of the beam drifts can be either negligible (for copper) or detrimental (for steel) on the time accuracy with which the time shift is estimated. The influence of beam drifts is more important for complex materials that are closer to industrial applications.

A possibility would be to reduce the influence of the beam drifts by reducing the duration of the cycle reconstructions, owing to an X-ray beam with more energy for instance. This would be achievable through the employment of a X-ray source with a higher brilliance or by using 3D detectors with which it is possible to use polychromatic beams and thus acquire photons at several wavelengths.

Correlate stored energy evolution with dislocations activity

A scientific interest still lies in the correlation between the evolutions of stored energy per cycle and the cyclic evolutions of FWHM. Both quantities are associated with dislocations and could provide interesting information about their evolution during a fatigue loading.

To go further, the relation between both quantities should now be modeled to confirm the conclusions drawn in this work. This investigation could be conducted over three main axes :

- The proposition of a plasticity model that could explain the evolutions of the FWHM, based on the microstructural state of the material (and thus the dislocation content of this material) and its evolution.
- A complementary study would also be necessary. It could correspond to the simulation of disloctation systems and structures through Discrete Dislocations Dynamics (DDD) from which an equivalent stored energy could be estimated. The evolution of the simulated dislocations under a fatigue loading (typical of the VHCF domain) would provide an estimate of the evolution of the stored energy in VHCF.
- In addition, it would be interesting to try to retrieve the evolutions of the peak width that were experimentally observed through the simulation of the cyclic loading applied to a dislocation structure with DDD. It would constitute a complex simulation to recreate the equivalent diffraction peak of an RVE of grains that would be characteristic of a material submitted toa certain stress heterogeneity. Then, by applying different loading conditions to the RVE, the simulated diffraction peak would evolve in accordance with the evolution of the dislocation content and the material stress state.

If a correlation can be proven, the study of FWHM could be used on its own to follow the evolution of microstructural changes and the initiation of damage in metallic materials subjected to a fatigue loading. The convenience and ease with which FWHM can be studied on metals would allow one to diversify the methodology and conduct tests at low-frequency or with a more complex stress state. However, this requires the investigation of the evolution of the FWHM with respect to the number of cycles, to see if it does reach a stabilized regime, similarly to the stored energy.

Determination of fatigue properties from stored energy measurements

To allow the use of the methodology, the evolutions of stored and dissipated energies that were measured experimentally in this work could be retrieved through simulations at the scale of dislocations by using DDD. From such simulations, it would thus be possible to properly compare the evolution of stored energy and the increase in dislocation density or the formation of dislocation structures. It would thus be possible to determine the fatigue properties of metallic materials from stored energy evolutions and establish a fatigue design criterion.

References

[Albert, 1837] Albert, W. A. J. (1837). Uber treibseile am harz. *Archiv für Mineralogie, Georgnosie Bergbau und Hüttenkunde*, 10 :215–234.

[Antolovich and Armstrong, 2014] Antolovich, S. D. and Armstrong, R. W. (2014). Plastic strain localization in metals : origins and consequences. *Progress in Materials Science*, 59 :1–160.

[ASM et al., 2000] ASM, Kuhn, H., and Medlin, D. (2000). Ultrasonic fatigue testing. In *Mechanical Testing and Evaluation*, volume 8, page 717–729. ASM International.

[ASM-E466, 2021] ASM-E466 (2021). E466 - standard practice for conducting force controlled constant amplitude axial fatigue tests of metallic materials. ASM International - E08 Committee. Accessed 04 Apr. 2022.

[ASM-E468, 2011] ASM-E468 (2011). E468 - practice for presentation of constant amplitude fatigue test results for metallic materials. ASM International - E08 Committee. Accessed 29 Mar. 2022.

[ASM-E606, 2001] ASM-E606 (2001). E606 - test method for strain-controlled fatigue testing. ASM International - E08 Committee. Accessed 29 Mar. 2022.

[Bach et al., 2016] Bach, J., Möller, J., Göken, M., Bitzek, E., and Höppel, H. (2016). On the transition from plastic deformation to crack initiation in the high- and very high-cycle fatigue regimes in plain carbon steels. *International Journal of Fatigue*, 93 :281–291.

[Bailey, 1963] Bailey, J. E. (1963). The dislocation density, flow stress and stored energy in deformed polycrystalline copper. *Philosophical Magazine*, 8(86) :223–236.

[Baohua et al., 2018] Baohua, N., Chen, D., Zhao, Z., Zhang, J., Meng, Y., and Gao, G. (2018). Notch effect on the fatigue behavior of a tc21 titanium alloy in very high cycle regime. *Applied Sciences*, 8 :1614.

[Bargheer et al., 2006] Bargheer, M., Zhavoronkov, N., Woerner, M., and Elsaesser, T. (2006). Recent Progress in Ultrafast X-ray Diffraction. *Chemistry European Journal of Chemistry and Physics*, 7(4) :783–792.

[Basolo et al., 2008] Basolo, S., Bérar, J., Boudet, N., Breugnon, P., Chantepie, B., Clémens, J., Delpierre, P., Dinkespiler, B., Hustache, S., Medjoubi, K., Ménouni, M., Morel, C., Pangaud, P., and Vigeolas, E. (2008). A 20kpixels CdTe photon-counting imager using XPAD chip. *Nuclear Instruments and Methods in Physics Research Section A : Accelerators, Spectrometers, Detectors and Associated Equipment*, 589(2) :268–274.

[Bathias, 2006] Bathias, C. (2006). Piezoelectric fatigue testing machines and devices. *International Journal of Fatigue*, 28(11) :1438–1445.

[Bathias et al., 2013] Bathias, C., Field, D., Antolovich, S., and Paris, P. (2013). Microplasticity , microdamage, microcracking in ultrasonic fatigue. *13th International Conference on Fracture 2013, ICF 2013*, 6 :5048–5057.

[Bayraktar et al., 2006] Bayraktar, E., Garcias, I. M., and Bathias, C. (2006). Failure mechanisms of automotive metallic alloys in very high cycle fatigue range. *International Journal of Fatigue*, 28(11) :1590–1602.

[Benzerga et al., 2005] Benzerga, A., Bréchet, Y., Needleman, A., and Van der Giessen, E. (2005). The stored energy of cold work : Predictions from discrete dislocation plasticity. *Acta Materialia*, 53(18) :4765–4779.

[Berar et al., 2009] Berar, J.-F., Boudet, N., Breugnon, P., Caillot, B., Chantepie, B., Clemens, J.-C., Delpierre, P., Dinkespiller, B., Godiot, S., Meessen, C., Menouni, M., Morel, C., Pangaud, P., Vigeolas, E., Hustache, S., and Medjoubi, K. (2009). XPAD3 hybrid pixel detector applications. *Nuclear Instruments and Methods in Physics Research Section A : Accelerators, Spectrometers, Detectors and Associated Equipment*, 607(1) :233–235.

[Berera et al., 2009] Berera, R., van Grondelle, R., and Kennis, J. T. M. (2009). Ultrafast transient absorption spectroscopy : principles and application to photosynthetic systems. *Photosynthesis Research*, 101(2-3) :105–118.

[Berkum et al., 1996] Berkum, v., Delhez, R., Keijser, d., Th, H., and Mittemeijer, E. (1996). Diffraction-line broadening due to strain fields in materials ; fundamental aspects and methods of analysis. *Acta Crystallographica Section A*, 52 :730–747.

[Berthel et al., 2008] Berthel, B., Chrysochoos, A., Wattrisse, B., and Galtier, A. (2008). Infrared Image Processing for the Calorimetric Analysis of Fatigue Phenomena. *Experimental Mechanics*, 48(1) :79–90.

[Bever, 1973] Bever, M. B. (1973). The stored energy of cold work. *Progress in materials science*, 17.

[Blanche, 2012] Blanche, A. (2012). *Effets dissipatifs en fatigue à grand et très grand nombre de cycles*. PhD thesis. Thèse de doctorat dirigée par Chrysochoos, André Mécanique et Génie civil Montpellier 2 2012.

[Blanche et al., 2015] Blanche, A., Chrysochoos, A., Ranc, N., and Favier, V. (2015). Dissipation Assessments During Dynamic Very High Cycle Fatigue Tests. *Experimental Mechanics*, 55(4) :699–709.

[Bonneville and Escaig, 1979] Bonneville, J. and Escaig, B. (1979). Cross-slipping process and the stress-orientation dependence in pure copper. *Acta Metallurgica*, 27(9) :1477–1486.

[Boudet et al., 2003] Boudet, N., Berar, J.-F., Blanquart, L., Breugon, P., Caillot, B., Clemens, J.-C., Koudobine, I., Delpierre, P., Mouget, C., Potheau, R., and Valin, I. (2003). XPAD : a hybrid pixel detector for X-ray diffraction and diffusion. *Nuclear Instruments and Methods in Physics Research Section A : Accelerators, Spectrometers, Detectors and Associated Equipment*, 510(1-2) :41–44.

[Boulanger, 2004] Boulanger, T. (2004). Calorimetric analysis of dissipative and thermoelastic effects associated with the fatigue behavior of steels. *International Journal of Fatigue*, 26(3) :221–229.

[Brenner et al., 2009] Brenner, R., Lebensohn, R., and Castelnau, O. (2009). Elastic anisotropy and yield surface estimates of polycrystals. *International Journal of Solids and Structures*, 46(16) :3018–3026.

[Bruchhausen et al., 2013] Bruchhausen, M., Hähner, P., Fischer, B., and Cornu, D. (2013). Device for carrying out environmental very high cycle fatigue tests with ultrasonic excitation in asymmetric push–pull mode. *International Journal of Fatigue*, 52 :11–19.

[Brugger et al., 2017] Brugger, C., Palin-Luc, T., Osmond, P., and Blanc, M. (2017). A new ultrasonic fatigue testing device for biaxial bending in the gigacycle regime. *International Journal of Fatigue*, 100 :619–626.

[Buchinger et al., 1985] Buchinger, L., Stanzl, S., and Laird, C. (1985). Dislocation structures in copper single crystals fatigued at low amplitudes. *Philosophical Magazine A*, 50(2) :275–298.

[Buton et al., 2014] Buton, C., Dawiec, A., Graber-Bolis, J., Arnaud, K., Bérar, J., Blanc, N., Boudet, N., Clémens, J., Debarbieux, F., Delpierre, P., Dinkespiler, B., Gastaldi, T., Hustache, S., Morel, C., Pangaud, P., Perez-Ponce, H., and Vigeolas, E. (2014). Comparison of three types of XPAD3.2/CdTe single chip hybrids for hard X-ray applications in material science and biomedical imaging. *Nuclear Instruments and Methods in Physics Research Section A : Accelerators, Spectrometers, Detectors and Associated Equipment*, 758 :44–56.

[Callister, 1994] Callister, W. D. (1994). *Materials Science and Engineering : An Introduction*.

[Chen et al., 2019] Chen, B., Janssens, K., and Dunne, F. (2019). Multiaxial and non-proportional microstructure-sensitive fatigue crack nucleation. *MATEC Web Conferences*, 300 :01001.

[Chen et al., 2005] Chen, Q., Kawagoishi, N., Wang, Q., Yan, N., Ono, T., and Hashiguchi, G. (2005). Small crack behavior and fracture of nickel-based superalloy under ultrasonic fatigue. *International Journal of Fatigue*, 27(10-12) :1227–1232. Funding Information : This work was supported in partial by the Japan Science Promotion Society under Grant Nos 11750085 and 13650096. Special thanks are also due to Prof. C. Laird, Dr A.K. Vasudevan, and Prof. H. Mayer for insightful discussion. ; Fatigue Damage of Structural Materials V ; Conference date : 19-09-2004 Through 24-09-2004.

[Cheng and Laird, 1981] Cheng, A. S. and Laird, C. (1981). Mechanisms of fatigue hardening in copper single crystals : The effects of strain amplitude and orientation. *Materials Science and Engineering*, 51(1) :111–121.

[Chrysochoos et al., 2008] Chrysochoos, A., Berthel, B., Latourte, F., Pagano, S., Wattrisse, B., and Weber, B. (2008). Local Energy Approach to Steel Fatigue. *Strain*, 44(4) :327–334.

[Clarebrough et al., 1952] Clarebrough, L., Hargreaves, M., Michell, D., and West, G. (1952). The determination of the energy stored in a metal during plastic deformation. *Proceedings of the Royal Society of London. Series A*, 215(1123) :507–524.

[Clarebrough et al., 1957] Clarebrough, L. M., Hargreaves, M. E., West, G. W., Head, A., and Mott, N. (1957). The energy stored in fatigued metals. *Proceedings of the Royal Society of London. Series A. Mathematical and Physical Sciences*, 242(1229) :160–166.

[Connesson et al., 2011a] Connesson, N., Maquin, F., and Pierron, F. (2011a). Dissipated energy measurements as a marker of microstructural evolution : 316L and DP600. *Acta Materialia*, 59(10) :4100–4115.

[Connesson et al., 2011b] Connesson, N., Maquin, F., and Pierron, F. (2011b). Experimental Energy Balance During the First Cycles of Cyclically Loaded Specimens Under the Conventional Yield Stress. *Experimental Mechanics*, 51(1) :23–44.

[Couteau et al., 2011] Couteau, O., Kruml, T., and Martin, J.-L. (2011). About the activation volume for cross-slip in cu at high stresses. *Acta Materialia*, 59(10) :4207–4215.

[Crupi et al., 2016] Crupi, V., Guglielmino, E., Plekhov, O., Prokhorov, A., and Risitano, G. (2016). Theoretical Approach for Developing the Thermographic Method in Ultrasonic Fatigue. *Procedia Structural Integrity*, 2 :1221–1228.

[Dawiec et al., 2016] Dawiec, A., Garreau, Y., Bisou, J., Hustache, S., Kanoute, B., Picca, F.-E., Renaud, G., and Coati, A. (2016). Real-time control of the beam at-

tenuation with xpad hybrid pixel detector. *Journal of Instrumentation*, 11 :P12018–P12018.

[DIN-50100, 2016] DIN-50100 (2016). Load controlled fatigue testing - execution and evaluation of cyclic tests at constant load amplitudes on metallic specimens and components. page 111. Deutsche Institut für Normung e.V. (DIN). Accessed 29 Mar. 2022.

[Dollar et al., 1989] Dollar, M., Bernstein, I. M., Daeubler, M., and Thompson, A. (1989). The effect of cylclic loading on the dislocation structure of fully pearlitic steel. *Metallurgical Transations A*, 201 :447–451.

[Doudard et al., 2005] Doudard, C., Calloch, S., Cugy, P., Galtier, A., and Hild, F. (2005). A probabilistic two-scale model for high-cycle fatigue life predictions. *Fatigue & Fracture of Engineering Materials & Structures*, 28(3) :279–288.

[Doudard et al., 2010] Doudard, C., Calloch, S., Hild, F., and Roux, S. (2010). Identification of heat source fields from infrared thermography : Determination of 'self-heating' in a dual-phase steel by using a dog bone sample. *Mechanics of Materials*, 42(1) :55–62.

[Elzinga et al., 1987] Elzinga, P. A., Kneisler, R. J., Lytle, F. E., Jiang, Y., King, G. B., and Laurendeau, N. M. (1987). Pump/probe method for fast analysis of visible spectral signatures utilizing asynchronous optical sampling. *Applied Optics*, 26(19) :4303.

[Erel, 2015] Erel, C. (2015). Dislocation dynamics simulations of persistent slip bands during fatigue of fcc metals. *University of California*.

[Essmann and Mughrabi, 1981] Essmann, U.and Gösele, U. and Mughrabi, H. (1981). A model of extrusions and intrusions in fatigued metals i. point-defect production and the growth of extrusions. *Philosophical Magazine A*, 44(2) :405–426.

[Farren and Taylor, 1925] Farren, W. and Taylor, G. (1925). The heat developed during plastic extension of metals. *Proceedings of the Royal Society A : Mathetmatical, Physical and Engineering Sciences*, 107 :422–451.

[Faurie et al., 2009] Faurie, D., Castelnau, O., Brenner, R., Renault, P.-O., Le Bourhis, E., and Goudeau, P. (2009). *In situ* diffraction strain analysis of elastically deformed polycrystalline thin films, and micromechanical interpretation. *Journal of Applied Crystallography*, 42(6) :1073–1084.

[Favier et al., 2014] Favier, V., Blanche, A., Phung, N. L., Ranc, N., and Chrysochoos, A. (2014). Energy Dissipation and Self-Heating due to Microplastic Deformation Mechanisms at Very High Cycle Fatigue for Single-Phase Ductile Metals. *Materials Science Forum*, 783-786 :2278–2283.

[Favier et al., 2016] Favier, V., Blanche, A., Wang, C., Phung, N. L., Ranc, N., Wagner, D., Bathias, C., Chrysochoos, A., and Mughrabi, H. (2016). Very high cycle fatigue

for single phase ductile materials : Comparison between a-iron, copper and a-brass polycrystals. *International Journal of Fatigue*, 93 :326–338.

[Finney and Laird, 1975] Finney, J. M. and Laird, C. (1975). Strain localization in cyclic deformation of copper single crystals. *The Philosophical Magazine : A Journal of Theoretical Experimental and Applied Physics*, 31(2) :339–366.

[Fischer et al., 2011] Fischer, C., Wagener, R., Friedmann, A., Axt, C., and Melz, T. (2011). Piezoelectric driven testing facilities to research the very high cycle fatigue regime. pages 427–432. Berger C, Christ H-J, editors.

[French, 1996] French, P. M. W. (1996). Ultrafast solid-state lasers. *Contemporary Physics*, 37(4) :283–301.

[Fu et al., 2021] Fu, H., Dönges, B., Krupp, U., Pietsch, U., Fritzen, C.-P., bing Yun, X., and Christ, H.-J. (2021). Evolution of the residual stresses of types i, ii, and iii of duplex stainless steel during cyclic loading in high and very high cycle fatigue regimes. *International Journal of Fatigue*, 142 :105972.

[Furuya, 2011] Furuya, Y. (2011). Notable size effects on very high cycle fatigue properties of high-strength steel. *Materials Science and Engineering : A*, 528(15) :5234–5240.

[Furuya, 2019] Furuya, Y. (2019). A new model for predicting the gigacycle fatigue strength of high-strength steels. *Materials Science and Engineering : A*, 743 :445–452.

[Furuya et al., 2002] Furuya, Y., Matsuoka, S., Abe, T., and Yamaguchi, K. (2002). Gigacycle fatigue properties for high-strength low-alloy steel at 100 Hz, 600 Hz, and 20 kHz. *Scripta Materialia*, 46(2) :157–162.

[Gallard, 2019] Gallard, M. (2019). *Etude in situ de la cristallisation et des contraintes dans des nanostructures de GeTe par diffraction du rayonnement X synchrotron.* PhD thesis, Universite Aix-Marseille. Thèse de doctorat dirigée par Thomas, Olivier et Mocuta, Cristian Physique et sciences de la matière. Matière condensée et nanosciences Aix-Marseille 2019.

[George, 2004] George, T. (2004). Development of a novel vibration-based fatigue testing methodology. *International Journal of Fatigue*, 26(5) :477–486.

[Ghuzlan, 2001] Ghuzlan, K. A. (2001). *Fatigue Damage Analysis in Asphalt Concrete Mixtures Based Upon Dissipated Energy Concepts.* PhD thesis.

[Golovin, 2008] Golovin, I. S. (2008). Anelasticity of iron-based ordered alloys and intermetallic compounds. *Intermetallics Research Progress*, pages 65–133.

[Graber et al., 2011] Graber, T., Anderson, S., Brewer, H., Chen, Y.-S., Cho, H. S., Dashdorj, N., Henning, R. W., Kosheleva, I., Macha, G., Meron, M., Pahl, R., Ren, Z., Ruan, S., Schotte, F., Šrajer, V., Viccaro, P. J., Westferro, F., Anfinrud, P., and

Moffat, K. (2011). BioCARS : a synchrotron resource for time-resolved X-ray science. *Journal of Synchrotron Radiation*, 18(4) :658–670.

[Groma and Szekely, 2006] Groma, I. and Szekely, F. (2006). Evolution of the dislocation microstructure : A model based on x-ray line profile measurements. *Scripta Materialia*, 54 :553–757.

[Gu et al., 2017] Gu, T., Castelnau, O., Forest, S., Hervé-Luanco, E., Lecouturier, F., Proudhon, H., and Thilly, L. (2017). Multiscale modeling of the elastic behavior of architectured and nanostructured Cu–Nb composite wires. *International Journal of Solids and Structures*, 121 :148–162.

[Guardian, 2021] Guardian, T. (2021). Denver plane engine fire consistent with metal fatigue in fan blade, say investigators.

[Haasen et al., 1980] Haasen, P., Gerold, V., and Kostorz, G. e. (1980). *Microscopic mechanisms of metal fatigue*, volume 3. Pergamon Press.

[Hershey, 1954] Hershey, A. V. (1954). The elasticity of an isotropic aggregate of anisotropic cubic crystals. *Journal of Applied Mechanics*, 21 :236–240.

[Howard and Preston, 1989] Howard, S. A. and Preston, K. D. (1989). *Modern Powder Diffraction*, volume Vol. 20. The Mineralogical Society of America.

[Hu et al., 2021] Hu, Y., Shi, J., Cao, X., and Zhi, J. (2021). Low cycle fatigue life assessment based on the accumulated plastic strain energy density. *Materials (Basel, Switzerland)*, 14.

[Inogamov et al., 2010] Inogamov, N., Zhakhovsky, V., Ashitkov, S., Agranat, M., Komarov, P., Khokhlov, V., and Shepelev, V. (2010). Pump-probe method for measurement of thickness of molten layer produced by ultrashort laser pulse. *AIP Conference Proceedings*, 1278.

[ISO-12107, 2012] ISO-12107 (2012). Standard 12107 :2003 - metallic materials — fatigue testing — statistical planning and analysis of data. International ISO - Committee ISO/TC 164 - Mechanical testing of metals. Accessed 04 Apr. 2022.

[Jacek and Gieras, 2013] Jacek, F. and Gieras, J. (2013). Analysis of accidents of the tu-154 aircraft.

[Jacquemain et al., 2021] Jacquemain, V., Ranc, N., Cheuleu, C., Michel, V., Favier, V., Castelnau, O., Vinci, D., Thiaudiere, D., and Mocuta, C. (2021). Estimation of stress in specimens loaded with ultrasonic fatigue machines. *International Journal of Fatigue*, 153 :106474.

[Jirandehi and Khonsari, 2020] Jirandehi, A. P. and Khonsari, M. M. (2020). Microstructure-sensitive estimation of fatigue life using cyclic thermodynamic entropy as an index for metals. *Theoretical and Applied Fracture Mechanics*, 112 :102854.

[Jongchansitto et al., 2019] Jongchansitto, P., Douellou, C., Preechawuttipong, I., and Balandraud, X. (2019). Comparison between 0d and 1d heat source reconstruction for fatigue characterization. pages 1–6.

[Kieffer and Karkoulis, 2013] Kieffer, J. and Karkoulis, D. (2013). Pyfai, a versatile library for azimuthal regrouping. *Journal of Physics : Conference Series*, 425 :202012.

[Krapez et al., 2000] Krapez, J.-C., Pacou, D., and Gardette, G. (2000). Lock-in thermography and fatigue limit of metals. In *Proceedings of the 2000 International Conference on Quantitative InfraRed Thermography*. QIRT Council.

[Krivoglaz, 1996] Krivoglaz, M. (1996). *Theory of X-Ray and Thermal Neutron Scattering by Real Crystals*. Springer-Verlag, NewYork.

[Kröner, 1978] Kröner, E. (1978). Self-consistent scheme and graded disorder in polycrystal elasticity. *Journal of Physics F : Metal Physics*, 8 :2261–2267.

[Krupp et al., 2016] Krupp, U., Giertler, A., and Koschella, K. (2016). Microscopic damage evolution during very high cycle fatigue (vhcf) of tempered martensitic steel. *Procedia Engineering*, 160 :231–238. XVIII International Colloquium on Mechanical Fatigue of Metals (ICMFM XVIII), Gijón (Spain), September 5-7, 2016.

[Krupp et al., 2010] Krupp, U., Knobbe, H., Christ, H.-J., Köster, P., and Fritzen, C.-P. (2010). The significance of microstructural barriers during fatigue of a duplex steel in the high- and very-high-cycle-fatigue (hcf/vhcf) regime. *International Journal of Fatigue*, 32(6) :914–920. Selected Papers of the 17th European Conference of Fracture (ECF 17).

[Laird et al., 1981] Laird, C., Finney, J., and Kuhlmann-Wilsdorf, D. (1981). Dislocation behavior in fatigue VI : Variation in the localization of strain in persistent slip bands. *Materials Science and Engineering*, 50(1) :127–136.

[Laufer and Roberts, 1964] Laufer, E. and Roberts, W. N. (1964). Dislocation structures in fatigued copper single crystals. *The Philosophical Magazine : A Journal of Theoretical Experimental and Applied Physics*, 10(107) :883–885.

[Le Bourlot et al., 2012] Le Bourlot, C., Landois, P., Djaziri, S., Renault, P.-O., Le Bourhis, E., Goudeau, P., Pinault, M., Mayne-L'Hermite, M., Bacroix, B., Faurie, D., Castelnau, O., Launois, P., and Rouzière, S. (2012). Synchrotron X-ray diffraction experiments with a prototype hybrid pixel detector. *Journal of Applied Crystallography*, 45(1) :38–47.

[Lebedev, 1999] Lebedev, A. (1999). Amplitude-dependent elastic-modulus defect in the main dislocation-hysteresis models. *Physics of the Solid State*, 41(7) :1105–1111.

[Lebensohn et al., 2011] Lebensohn, R., Castañeda, P., Brenner, R., and Castelnau, O. (2011). *Computational Methods for Microstructure-Property Relationships*, chapter

Full-Field vs. Homogenization Methods to Predict Microstructure–Property Relations for Polycrystalline Materials, pages 393–441. Springer, ghosh, somnath and dimiduk, dennis edition.

[Ledbetter and Naimon, 1974] Ledbetter, H. M. and Naimon, E. R. (1974). Elastic properties of metals and alloys. ii. copper. *Journal of Physical and Chemical Reference Data*, 3(4) :897–935.

[Li et al., 2011] Li, P., Li, S., Wang, Z., and Zhang, Z. (2011). Fundamental factors on formation mechanism of dislocation arrangements in cyclically deformed fcc single crystals. *Progress in Materials Science*, 56(3) :328–377.

[Li et al., 2019] Li, Z.-d., Zhou, S., Yang, C.-f., and Yong, Q. (2019). High/very high cycle fatigue behaviors of medium carbon pearlitic wheel steels and the effects of microstructure and non-metallic inclusions. *Materials Science and Engineering : A*, 764 :138208.

[Llanes and Laird, 1992] Llanes, L. and Laird, C. (1992). The role of annealing twin boundaries in the cyclic deformation of f.c.c. materials. *Materials Science and Engineering A-structural Materials Properties Microstructure and Processing*, 157 :21–27.

[Llanes et al., 1993] Llanes, L., Laird, C., Rollett, A. D., and Bassani, J. L. (1993). Effect of grain size and annealing texture on the cyclic response and the substructure evolution of polycrystalline copper. *Acta Metallurgica et Materialia ; (United States)*, 41(9).

[Ludwig et al., 2010] Ludwig, W., Reischig, P., King, A., Herbig, M., Proudhon, H., Buffiere, J.-y., Rutishauser, S., and David, C. (2010). Thoughts about the optimum data acquisition geometry and time resolution of monochromatic beam x-ray diffraction microscopy experiments. In Hansen, N., Jensen, D. J., Nielsen, S., Poulsen, H., and Ralph, B., editors, *31st Risø International Symposium on Materials Science*, volume 31, pages 317–328. RISO.

[Lukás et al., 1974] Lukás, P., Klesnil, M., and Polák, J. (1974). High cycle fatigue life of metals. *Materials Science and Engineering*, 15 :239–245.

[Lukáš and Kunz, 2004] Lukáš, P. and Kunz, L. (2004). Role of persistent slip bands in fatigue. *Philosophical Magazine*, 84 :317–330.

[Luong, 1995] Luong, M. P. (1995). Nuclear Engineering and Design. *Nuclear Engineering and Design*, 158 :363–376.

[Luong, 1997] Luong, P. (1997). Fatigue limit evaluation of metals using an infrared thermographic technique. *Mechanics of Materials*, 28.

[Macdonald, 1976] Macdonald, D. E. (1976). ultrasonic frequency metal fatigue : a review of the investigations of the institute for the study of fatigue (fracture) and (structural) reliability. *Engineering Fracture Mechanics*, 8 :17–29.

[Madec et al., 2000] Madec, R., Devincre, B., and Kubin, L. (2000). New line model for optimized dislocation dynamics simulations. *Materials Research Society Proceedings*, 653.

[Manole et al., 2009] Manole, C., Déprés, C., and Tabourot, L. (2009). Developement of a dislocation-based constitutive law for fcc crystal on a wide range of deformation amplitude. In *X International Conference on Computational Plasticity COMPLAS X*, page 354, Barcelona, France.

[Maquin and Pierron, 2009] Maquin, F. and Pierron, F. (2009). Heat dissipation measurements in low stress cyclic loading of metallic materials : From internal friction to micro-plasticity. *Mechanics of Materials*, 41(8) :928–942.

[Mareau et al., 2009] Mareau, C., Favier, V., and Berveiller, M. (2009). Micromechanical modeling coupling time-independent and time-dependent behaviors for heterogeneous materials. *International Journal of Solids and Structures - INT J SOLIDS STRUCT*, 46 :223–237.

[Mareau et al., 2012] Mareau, C., Favier, V., Weber, B., Galtier, A., and Berveiller, M. (2012). Micromechanical modeling of the interactions between the microstructure and the dissipative deformation mechanisms in steels under cyclic loading. *International Journal of Plasticity*, 32-33 :106–120.

[Marines, 2003] Marines, I. (2003). An understanding of very high cycle fatigue of metals. *International Journal of Fatigue*, 25(9-11) :1101–1107.

[Marti et al., 2015] Marti, N., Favier, V., Saintier, N., and Gregori, F. (2015). Investigating Fatigue Frequency Effects on Single Phase Ductile Materials. *Procedia Engineering*, 133 :294–298.

[Martins et al., 2020] Martins, R. F., Branco, R., and Long, X. (2020). Fatigue life assessment in bainitic steels based on the cumulative strain energy density. *Applied Sciences*, 10(21).

[Mason, 1958] Mason, W. (1958). Physical acoustics and the properties of solids.

[Mayer, 1999] Mayer, H. (1999). Fatigue crack growth and threshold measurements at very high frequencies. *International Materials Reviews*, 44(1) :1–34.

[Morgan and Milligan, 1997] Morgan, J. M. and Milligan, W. W. (1997). A 1 khz servohydraulic fatigue testing system. *Materials Week '97*, pages 305–312.

[Mughrabi, 1978] Mughrabi, H. (1978). The cyclic hardening and saturation behavior of copper single crystals. *Materials Science and Engineering*, 33 :207–223.

[Mughrabi, 2002] Mughrabi, H. (2002). On 'multi-stage' fatigue life diagrams and the relevant life-controlling mechanisms in ultrahigh-cycle fatigue. *Fatigue & Fracture of Engineering Materials & Structures*, 25(8-9) :755–764.

[Mughrabi, 2006] Mughrabi, H. (2006). Specific features and mechanisms of fatigue in the ultrahigh-cycle regime. *International Journal of Fatigue*, 28(11) :1501–1508.

[Mughrabi, 2009] Mughrabi, H. (2009). Cyclic Slip Irreversibilities and the Evolution of Fatigue Damage. *Metallurgical and Materials Transactions B*, 40(4) :431–453.

[Mughrabi, 2012] Mughrabi, H. (2012). Fatigue behavior of ferritic-pearlitic-bainitic steel in loading with positive mean stress. *International Journal of Fatigue*, 39 :103–108.

[Mughrabi, 2013] Mughrabi, H. (2013). Cyclic slip irreversibility and fatigue life : A microstructure-based analysis. *Acta Materialia*, 61 :1197–1203.

[Mughrabi, 2015] Mughrabi, H. (2015). Microstructural mechanisms of cyclic deformation, fatigue crack initiation and early crack growth. *Philosophical Transactions of the Royal Society A : Mathematical, Physical and Engineering Sciences*, 373(2038) :20140132.

[Mughrabi et al., 1979] Mughrabi, H., Ackermann, F., and Herz, K. (1979). Persistentslipbands in fatigued face-centered and body-centered cubic metals. fatigue mechanisms. *Proceedings of ASTM-NBS-NSF Symposium*, 22(24) :69–105.

[Munier, 2012] Munier, R. (2012). *Etude de la fatigue des aciers laminés à partir de l'auto-échauffement sous sollicitation cyclique : essais, observations, modélisation et influence d'une pré-déformation plastique*. Theses, Université de Bretagne occidentale - Brest.

[Munier et al., 2014] Munier, R., Doudard, C., Calloch, S., and Weber, B. (2014). Determination of high cycle fatigue properties of a wide range of steel sheet grades from self-heating measurements. *International Journal of Fatigue*, 63 :46–61.

[Nabarro, 1997] Nabarro, F. (1997). Fifty-year study of the peierls-nabarro stress. *Materials Science and Engineering : A*, 234-236 :67–76.

[Neumann, 1986] Neumann, P. (1986). Low energy dislocation configurations : A possible key to the understanding of fatigue. *Materials Sciences and Engineering : A*, 81 :465–475.

[Neutze and Hajdu, 1997] Neutze, R. and Hajdu, J. (1997). Femtosecond time resolution in x-ray diffraction experiments. *Proceedings of the National Academy of Sciences*, 94(11) :5651–5655.

[Nicholas, 2002] Nicholas, T. (2002). Step loading for very high cycle fatigue. *Fatigue & Fracture of Engineering Materials & Structures*, 25(8-9) :861–869.

[Nishijima and Kanazawa, 1999] Nishijima, S. and Kanazawa, K. (1999). Stepwise s-n curve and fish-eye failure in gigacycle fatigue. *Fatigue & Fracture of Engineering Materials & Structures*, 22.

[Obrtlík et al., 1994] Obrtlík, K., Kruml, T., and Polák, J. (1994). Dislocation structures in 316l stainless steel cycled with plastic strain amplitudes over a wide interval. *Materials Science and Engineering : A*, 187(1) :1–9.

[Ono, 2020] Ono, K. (2020). A comprehensive report on ultrasonic attenuation of engineering materials, including metals, ceramics, polymers, fiber-reinforced composites, wood, and rocks. *Applied Sciences*, 10 :2230.

[Ors et al., 2019] Ors, T., Ranc, N., Pelerin, M., Michel, V., Favier, V., Castelnau, O., Mocuta, C., and Thiaudière, D. (2019). Microsecond time-resolved x-ray diffraction for the investigation of fatigue behavior during ultrasonic fatigue loading. *Journal of Synchrotron Radiation*, 26.

[Özdemir, 2012] Özdemir, Z. (2012). A metallographic examination of fracture splitting c70s6 steel used in connecting rods. *Marmara Üniversitesi Fen Bilimleri Dergisi*, 24 :45–58.

[Peierls, 1940] Peierls, R. (1940). The size of a dislocation. *Proceedings of the Physical Society*, 52(1) :34–37.

[Peralta et al., 1999] Peralta, P., Laird, C., and Mitchell, T. (1999). Fatigue fracture at copper bicrystal interfaces : Fractography. *Materials Science and Engineering A-structural Materials Properties Microstructure and Processing*, 264 :215–231.

[Phung et al., 2013] Phung, N., Marti, N., Blanche, A., Ranc, N., Favier, V., Chrysochoos, A., Saintier, N., Gregori, F., Bacroix, B., and Thoquenne, G. (2013). Very high cycle fatigue for single phase ductile materials : slip band appearance criterion. *Procedia Engineering*, 66 :615–625.

[Phung, 2012] Phung, N.-l. (2012). *Fatigue sous très faibles amplitudes de contrainte : Analyse des mécanismes précurseurs de l'amorçage de fissures dans le cuivre polycristallin*. PhD thesis, ENSAM Paris. Thèse de doctorat dirigée par Favier, Véronique et Ranc, Nicolas Mécanique Paris, ENSAM 2012.

[Polák and Man, 2015] Polák, J. and Man, J. (2015). Initiation of stage i fatigue cracks – experiments and models. *Procedia Engineering*, 101.

[Poncelet, 1841] Poncelet, J. (1841). *Introduction a la mecanique industrielle, physique ou experimentale*.

[Prokic, 2004] Prokic, M. (2004). Piezoelectric transducers modeling and characterization. page 266. MPI All international.

[Puškár, 1993a] Puškár, A. (1993a). Ultrasonic fatigue testing equipment and new procedures for complex material evaluation. *Ultrasonics*, 31(1) :61–67.

[Puškár, 1993b] Puškár, A. (1993b). Ultrasonic fatigue testing equipment and new procedures for complex material evaluation. *Ultrasonics*, 31(1) :61–67.

[Pyttel et al., 2011] Pyttel, B., Schwerdt, D., Brunner, I., and Berger, C. (2011). Fatigue strength and failure mechanisms in the vhcf-region. *Anales de Mecanica de la Fractura*, 28.

[Quinney and Taylor, 1937] Quinney, H. and Taylor, G. (1937). *Proceedings of the Royal Society, A163*, page 157.

[Ranc, 2014] Ranc, N. (2014). *Contribution à l'étude du comportement thermomécanique des solides et des structures.* PhD thesis. Habilitation a Ddiriger des Recherches, Université Paris VI - Pierre et Marie Curie 2014.

[Ranc et al., 2015] Ranc, N., Blanche, A., Ryckelynck, D., and Chrysochoos, A. (2015). Pod preprocessing of ir thermal data to assess heat source. *Experimental Mechanics*, 55(4).

[Rehn et al., 1990] Rehn, V., Rosenberg, R. A., and Williams, R. (1990). Pump-probe and other timing experiments in synchrotron radiation. *Nuclear Instruments and Methods in Physics Research Section A : Accelerators, Spectrometers, Detectors and Associated Equipment*, 291(1-2) :50–53.

[Ricaud et al., 2011] Ricaud, J.-P., Betinelli, P., Bisou, J., Elattaoui, X., Laulhé, C., Monteiro, P., and Nadolski, L. (2011). The timbel synchronization board for time resolved experiments at synchrotron soleil. pages 2036–2038.

[Risbet et al., 2003] Risbet, M., Xavier, F., Guillemer-Neel, C., and Clavel, M. (2003). Use of atomic force microscopy to quantify slip irreversibility in a nickel-base superalloy. *Scripta Materialia*, 49 :533–538.

[Rönnpagel and Schwink, 1978] Rönnpagel, D. and Schwink, C. (1978). Measurement of the stored energy of copper single crystals by means of a new deformation calorimetry method. *Acta Metallurgica*, 26 :319–331.

[Rosa and Risitano, 2000] Rosa, G. L. and Risitano, A. (2000). Thermographic methodology for rapid determination of the fatigue limit of materials and mechanical components. *International Journal of Fatigue*, page 9.

[Rössle et al., 2022] Rössle, M., Thomas, O., Mocuta, C., Rousset, R., Texier, M., Escoubas, S., Dubourdieu, C., Araújo, E. B., and Cornelius, T. W. (2022). Time-resolved piezoelectric response in relaxor ferroelectric (pb0.88la0.12)(zr0.52ti0.48)o3 thin films. *Journal of Applied Physics*.

[Sakai et al., 2002] Sakai, T., Sato, Y., and Oguma, N. (2002). Characteristic S-N properties of high-carbon-chromium-bearing steel under axial loading in long-life fatigue. *Fatigue & Fracture of Engineering Materials & Structures*, 25(8-9) :765–773.

[Schmidt et al., 2010] Schmidt, M., Friedman, A., Drögemüller, T., and Melz, T. (2010). Hybride prüftechnik zur dynamischen charakterisierung von elastomerbauteilen. pages 161–166.

[Seelan et al., 2020] Seelan, P., Dulieu-Barton, J., and Pierron, F. (2020). Microstructural assessment of 316l stainless steel using infrared thermography based measurement of energy dissipation arising from cyclic loading. *Mechanics of Materials*, 148.

[Sharma et al., 2020] Sharma, A., Oh, M. C., and Ahn, B. (2020). Recent Advances in Very High Cycle Fatigue Behavior of Metals and Alloys—A Review. *Metals*, 10(9) :1200.

[Shih et al., 2010] Shih, C.-C., Ho, N., and Huang, H.-L. (2010). Dislocation evolution in interstitial-free steel during constant and variable amplitude testing. *Journal of Materials Science, New York*, 45(7) :1809–1816.

[Sonsino, 2007] Sonsino, C. (2007). Course of s-n curves especially in the high-cycle fatigue regime with regard to component design and safety. *International Journal of Fatigue*, 29 :2246–2258.

[Stanzl-Tschegg, 2017] Stanzl-Tschegg, S. E. (2017). Fracture mechanical characterization of the initiation and growth of interior fatigue cracks. *Fatigue & Fracture of Engineering Materials & Structures*, 40(11) :1741–1751.

[Stanzl-Tschegg and Schönbauer, 2010] Stanzl-Tschegg, S. E. and Schönbauer, B. a. (2010). Mechanisms of strain localization, crack initiation and fracture of polycrystalline copper in the VHCF regime. *International Journal of Fatigue*, 32(6) :886–893.

[Stanzltschegg et al., 2007] Stanzltschegg, S., Mughrabi, H., and Schoenbauer, B. (2007). Life time and cyclic slip of copper in the VHCF regime. *International Journal of Fatigue*, 29(9-11) :2050–2059.

[Szczepiński, 2001] Szczepiński, W. (2001). The stored energy in metals and the concept of residual microstresses in plasticity. *Archives of Mechanics*, 53.

[Thiaudière et al., 2012] Thiaudière, D., Mocuta, C., Réguer, S., Alves, F., and Hennet, L. (2012). Diffabs - beam-line review - (report for 2008-2011).

[Thompson et al., 1956] Thompson, N., Wadsworth, N., and Louat, N. (1956). Xi. the origin of fatigue fracture in copper. *The Philosophical Magazine : A Journal of Theoretical Experimental and Applied Physics*, 1(2) :113–126.

[Tofique, 2016] Tofique, M. (2016). Initiation and early crack growth in vhcf of stainless steelsFIX ME!!!! : Experimental and theoretical analysis.

[Torabian et al., 2017] Torabian, N., Favier, V., Dirrenberger, J., Adamski, F., Ziaei-Rad, S., and Ranc, N. (2017). Correlation of the high and very high cycle fatigue response of ferrite based steels with strain rate-temperature conditions. *Acta Materialia*, 134 :40–52.

[Torabian et al., 2016] Torabian, N., Favier, V., Ziaei-Rad, S., Adamski, F., Dirrenberger, J., and Ranc, N. (2016). Self-heating measurements for a dual-phase steel under

ultrasonic fatigue loading for stress amplitudes below the conventional fatigue limit. *Procedia structural integrity*, 2 :1191–1198.

[Torkabadi et al., 2016] Torkabadi, A., Meinders, T., and Van den Boogaard, T. (2016). On the nonlinear anelastic behaviour of ahss. *Journal of Physics : Conference Series*, 734 :032100.

[Tridello et al., 2021] Tridello, A., Niutta, C. B., Berto, F., and Paolino, D. (2021). Size-effect in very high cycle fatigue : A review. *International Journal of Fatigue*, 153 :106462.

[Ungar et al., 1984] Ungar, T., Mughrabi, H., Rönnpagel, D., and Wilkens, M. (1984). X-ray line-broadening study of the dislocation cell structure in deformed [001]-orientated copper single crystals. *Acta Metallurgica*, 32(3) :333–342.

[Ungár, 2001] Ungár, T. (2001). Dislocation densities, arrangements and character from x-ray diffraction experiments. *Materials Science and Engineering : A*, 309-310 :14–22.

[Ungár, 2004] Ungár, T. (2004). Microstructural parameters from x-ray diffraction peak broadening. *Scripta Materialia*, 51(8) :777–781. Viewpoint set no. 35. Metals and alloys with a structural scale from the micrometer to the atomic dimensions.

[Vashista and Paul, 2012] Vashista, M. and Paul, S. (2012). Correlation between full width at half maximum (fwhm) of xrd peak with residual stress on ground surfaces. *Philosophical Magazine*, 92(33) :4194–4204.

[Vermeulen, 2001] Vermeulen, A. C. (2001). An elastic constants database and xec calculator for in use xrd residual stress analysis.

[Vermeulen et al., 2019] Vermeulen, A. C., Kube, C. M., and Norberg, N. (2019). Implementation of the self-consistent kröner–eshelby model for the calculation of x-ray elastic constants for any crystal symmetry. *Powder Diffraction*, 34(2) :103–109.

[Wagner et al., 2012] Wagner, D., Cavalieri, F., Bathias, C., and Ranc, N. (2012). Ultrasonic fatigue tests at high temperature on an austenitic steel. *Propulsion and Power Research*, 1(1) :29–35.

[Wang et al., 2012] Wang, Q., Khan, M. K., and Bathias, C. (2012). Current understanding of ultra-high cycle fatigue. *Theoretical and Applied Mechanics Letters*, 2(3) :031002.

[Wang et al., 2013] Wang, Y. T., Luo, C. W., and Kobayashi, T. (2013). Understanding Multiferroic Hexagonal Manganites by Static and Ultrafast Optical Spectroscopy. *Advances in Condensed Matter Physics*, 2013 :1–13.

[Wang and Laird, 1988] Wang, Z. and Laird, C. (1988). Cyclic stress—strain response of polycrystalline copper under fatigue conditions producing enhanced strain localization. *Materials Science and Engineering*, 100 :57–68.

[Wauthier-Monnin et al., 2015] Wauthier-Monnin, A., Chauveau, T., Castelnau, O., Réglé, H., and Bacroix, B. (2015). The evolution with strain of the stored energy in different texture components of cold-rolled IF steel revealed by high resolution X-ray diffraction. *Materials Characterization*, 104 :31–41.

[Weidner et al., 2010] Weidner, A., Amberger, D., Pyczak, F., Schönbauer, B., Stanzl-Tschegg, S., and Mughrabi, H. (2010). Fatigue damage in copper polycrystals subjected to ultrahigh-cycle fatigue below the PSB threshold. *International Journal of Fatigue*, 32(6) :872–878.

[Williams, 1964] Williams, R. (1964). *Acta Metallurgica*, 12 :745.

[Winter, 1974] Winter, A. T. (1974). A model for the fatigue of copper at low plastic strain amplitudes. *Philosophical Magazine*, 30(4) :719–738.

[Wöhler, 1867] Wöhler, A. (1867). Versuche über die festigkeit der eisenbahnwagenachsen. *Zeitschrift für Bauwesen 10. English Summary Eng.*, (4) :160–161.

[Wöhler, 1870] Wöhler, A. (1870). Über die festigkeitsversuche mit eisen und stahl. *Zeitschrift für Bauwesen*, 20 :73 – 106.

[Woods, 1973] Woods, P. J. (1973). An optical analysis of the dislocation structure in walls formed by fatigue. *Philosophical Magazine*, 28(1) :193–202.

[Wu et al., 1994] Wu, T., Ni, J., and Bathias, C. (1994). An Automatic Ultrasonic Fatigue Testing System for Studying Low Crack Growth at Room and High Temperatures. In Amzallag, C., editor, *Automation in Fatigue and Fracture : Testing and Analysis*, pages 598–607. ASTM International, West Conshohocken, PA.

[Xu, 2017] Xu, J. (2017). Effect of cyclic plastic strain and flow stress on low cycle fatigue of 316l(n) stainless steel. *Mechanics of Materials*, 114 :131–141.

[Yahiaoui, 2013] Yahiaoui, H. (2013). *Effet de l'espacement interlamellaire sur le comportement sous chargements monotone et cyclique de l'acier perlitique C70.* PhD thesis, ENSAM. Thèse de doctorat dirigée par Braham, Chedly Mécanique-matériaux Paris, ENSAM 2013 ; Thèse de doctorat Mécanique-matériaux ecole supérieure des sciences et technique de tunis 2013.

[Yang et al., 2010] Yang, D.-S., Mohammed, O. F., and Zewail, A. H. (2010). Scanning ultrafast electron microscopy. *Proceedings of the National Academy of Sciences*, 107(34) :14993–14998.

[Zettl et al., 2006] Zettl, B., Mayer, H., Ede, C., and Stanzl-Tschegg, S. (2006). Very high cycle fatigue of normalized carbon steels. *International Journal of Fatigue*, 28 :1583–1589.

[Zhang et al., 2019] Zhang, Y., You, Y., Moumni, Z., Anlas, G., Zhu, J., and Zhang, W. (2019). Stored-energy-based fatigue criterion for shape memory alloys. *Smart Materials and Structures*, 28(6).

[Zhigachev, 2013] Zhigachev, A. O. (2013). The effect of specimen surface curvature on x-ray diffraction peak profiles. *Review of Scientific Instruments*, 84(9) :095105.

[Zhu et al., 2017] Zhu, J., Wu, X., Lattery, D. M., Zheng, W., and Wang, X. (2017). The ultrafast laser pump-probe technique for thermal characterization of materials with micro/nanostructures. *Nanoscale and Microscale Thermophysical Engineering*, 21(3) :177–198.

[Zimmermann and Christ, 2007] Zimmermann, M. and Christ, H.-J. (2007). Experimentelle herausforderungen bei der versuchsführung zur charakterisierung des ermüdungsverhaltens im Übergang von hcf zu vhcf. pages 385–391. Verlag Stahleisen GmbH.

[Čebron and Kosel, 2014] Čebron, M. and Kosel, F. (2014). Stored Energy Predictions from Dislocation-Based Hardening Models and Hardness Measurements for Tensile-Deformed Commercial Purity Copper. *SV - Journal of Mechanical Engineering*, 60(7-8) :462–474.

Vincent Jacquemain

Fast determination of stored energy of metals during fatigue tests at 20kHz by using in situ time-resolved X-ray diffraction

Résumé : L'objectif de cette thèse est de développer une méthode de détermination rapide des propriétés des matériaux en fatigue, à partir de l'évolution de l'énergie stockée en fonction de l'amplitude de contrainte et du nombre de cycles appliqués. Cette évolution est estimée pendant des essais de fatigue menés à haute fréquence et pour des très grands nombres de cycles. La compréhension du lien entre l'évolution de l'énergie stockée et l'activation des mécanismes d'endommagement en fatigue permettrait de renforcer la crédibilité de la méthode. L'énergie stockée est estimée en réalisant un bilan d'énergie, qui correspond à la différence entre le travail mécanique apporté au matériau et l'énergie qu'il dissipe sous forme de chaleur. Le travail mécanique est estimé par diffraction des rayons X in situ résolue en temps et l'énergie dissipée par thermographie. Pour étudier le domaine des très grands nombres de cycles, un machine de fatigue ultrasonique fonctionnant à 20 kHz est utilisée. Les résultats des mesures montrent d'une part que l'énergie stockée décroit avec le nombre de cycles, jusqu'à atteindre un régime stabilisé et d'autre part qu'elle augmente avec l'amplitude de contrainte. Dans le cas du cuivre, l'évolution de l'énergie stockée en fonction de l'amplitude de contrainte semble également être corrélée à l'apparition de bandes de glissements, précurseurs de la formation d'endommagement en fatigue.

Mots clés : Fatigue à très grand nombre de cycles, Machine de fatigue ultrasonique, Bilan d'énergie, Travail mécanique, Diffraction des rayons X in situ résolue en temps, Énergie dissipée, Thermographie infrarouge, Cuivre monocristallin, Acier C70 perlitique

Abstract : The objective of this thesis is to develop a methodology to quickly determine the fatigue properties of materials, from the evolution of the stored energy with respect to the stress amplitude and number of cycles applied. This evolution is estimated during fatigue tests conducted at high frequency and for very high number of cycles. The understanding of the link between the evolution of stored energy and the activation of fatigue damage mechanisms would help to improve the credibility of the methodology. The stored energy is estimated by establishing an energy balance from the difference between the mechanical work that is brought to the material and the energy that is dissipated as heat. The mechanical work is estimated from in situ time resolved X-ray diffraction measurements and the dissipated energy from thermographic measurements. To study the very high fatigue lives, fatigue tests are conducted by using an ultrasonic fatigue machine working at 20 kHz. On the first hand, the results show that the stored energy decreases with the number of cycles, down to reach a stabilized regime. On the other hand, the stored energy increases with the stress amplitude. In the case of copper, the evolution of the stored energy with respect to the stress amplitude is also correlated to the appearance of slip bands, which are precursors of fatigue damage.

Keywords : Very high cycle fatigue, Ultrasonic fatigue machine, Energetic balance, Mechanical work, In situ time-resolved X-ray diffraction, dissipated energy, Infrared thermography, Copper single crystal, C70 pearlitic steel

HESAM UNIVERSITÉ

Arts et Métiers Sciences et Technologies

ÉCOLE DOCTORALE SCIENCES ET MÉTIERS DE L'INGÉNIEUR

PIMM - Campus de Paris

THÈSE

présentée par : **Vincent JACQUEMAIN**

défendue le : **07 Octobre 2022**

pour obtenir le statut de : **Docteur d'HESAM Université**

préparée à : **Ecole Nationale Supérieure des Arts et Métiers**

Spécialté : **Mécanique des matériaux**

Détermination rapide de l'énergie stockée dans les métaux pendant des essais de fatigue à 20kHz en utilisant la diffraction des rayons X in situ résolue en temps

Thèse supervisée par : Nicolas RANC

Jury

M. Pierre-Olivier RENAULT	University of Poitiers	Président
M. Cedric DOUDARD	ENSTA Brest	Rapporteur
M. Henry PROUDHON	MINES Paris	Rapporteur
M. Jonathan CORMIER	ENSMA Poitiers	Examinateur
M. Olivier CASTELNAU	ENSAM Paris	Examinateur
M. Cristian MOCUTA	Synchrotron SOLEIL	Examinateur
M. Nicolas RANC	ENSAM Paris	Examinateur

T H È S E

Résumé

L'objectif de cette thèse est de développer une méthode de détermination rapide des propriétés des matériaux en fatigue, à partir de l'évolution de l'énergie stockée en fonction de l'amplitude de contrainte et du nombre de cycles appliqués. Cette évolution est estimée pendant des essais de fatigue menés à haute fréquence et pour des très grands nombres de cycles. La compréhension du lien entre l'évolution de l'énergie stockée et l'activation des mécanismes d'endommagement en fatigue permettrait de renforcer la crédibilité de la méthode. L'énergie stockée est estimée en réalisant un bilan d'énergie, qui correspond à la différence entre le travail mécanique apporté au matériau et l'énergie qu'il dissipe sous forme de chaleur. Le travail mécanique est estimé par diffraction des rayons X in situ résolue en temps et l'énergie dissipée par thermographie. Pour étudier le domaine des très grands nombres de cycles, un machine de fatigue ultrasonique fonctionnant à 20 kHz est utilisée. Les résultats des mesures montrent d'une part que l'énergie stockée décroit avec le nombre de cycles, jusqu'à atteindre un régime stabilisé et d'autre part qu'elle augmente avec l'amplitude de contrainte. Dans le cas du cuivre, l'évolution de l'énergie stockée en fonction de l'amplitude de contrainte semble également être corrélée à l'apparition de bandes de glissements, précurseurs de la formation d'endommagement en fatigue.

Mots-clés : Fatigue à très grand nombre de cycles, Machine de fatigue ultrasonique, Bilan d'énergie, travail mécanique, Diffraction des rayons X in situ résolue en temps, Energie dissipée, Thermographie infrarouge, Cuivre monocristallin, Acier C70 perlitique.

Table des matières

Résumé **3**

Introduction **7**

1 État de l'art - dimensionnement en fatigue **11**

1.1 Tests à petite échelle - Courbes SN 11

1.2 Mesures énergétiques pendant des tests de fatigue interrompus 13

1.2.1 Estimation de l'énergie dissipée pour déterminer la limite de fatigue 13

1.2.2 L'énergie stockée, un marqueur de l'irréversibilité du glissement cyclique ? 14

1.3 Mécanismes d'endommagement en fatigue 14

1.3.1 Mécanismes d'endommagement en HCF 15

1.3.2 Mécanismes d'endommagement en VHCF 15

2 Contribution expérimentale - établissement d'un bilan énergétique pendant des essais de fatigue à 20kHz **17**

2.1 Objectifs de la thèse 17

2.2 Matériaux 18

2.3 Essais de fatigue ultrasonique 19

2.3.1 fonctionnement de la machine en mode standard 19

2.3.2 fonctionnement de la machine en mode synchronisé 20

2.4 Mesures du travail mécanique 21

2.4.1 Principe de diffraction des rayons X 21

2.4.2 Méthodologie développée pour l'estimation des évolutions de contrainte et de déformation cycliques 22

2.5 Mesures de l'énergie dissipée 25

3 Résultats et discussions **27**

3.1 Résultats Cuivre - uniforme 27

3.1.1 Estimation de l'évolution d'énergie stockée en fonction de la contrainte 27

3.1.2 Estimation de l'évolution d'énergie stockée en fonction du nombre de cycles 29

3.2 Résultats Acier - Single-Bunch 30

3.2.1 Estimation de l'évolution d'énergie stockée en fonction de la contrainte 30

Conclusions **33**

Introduction

Motivation de l'étude

La fatigue des matériaux est un phénomène qui préoccupe toujours de nombreux industriels dans les domaines des transports et de la production d'énergie. Ce phénomène correspond à l'action d'un chargement cyclique qui fragilise la matière du fait de sa répétition et conduit à sa rupture. Un exemple récent d'incident ayant eu lieu à cause de ce phénomène s'est produit en 2021. Le moteur d'un Boeing 777 a pris feu suite à la rupture d'une aube de turbine, du fait d'un chargement cyclique après près de deux milliards de cycles.

Le développement des structures vise à ce qu'elle soit à la fois plus résistantes dans le temps mais aussi à ce que leur suivi en maintenance soit efficace. Les structures atteignent donc de plus en plus communément des durées de vies supérieures à 10^7 cycles, i.e. correspondant au domaine de la fatigue à très grand nombre de cycles (VHCF). Pour garantir la sécurité de ces structures, il est nécessaire de bien contrôler la durée de vie des structures soumises à des charges cycliques. Pour ce faire, il est indispensable de bien connaitre les propriétés en fatigue des matériaux qui sont employés. Le comportement des matériaux en fatigue peut être déterminé par des essais mécaniques. Cependant, pour caractériser les matériaux en fatigue pendant de très grandes durées de vie, les moyens conventionnels utilisés pour faire des essais de fatigue sont limités.

Différentes méthodes furent développées et ont chacune leur avantage. L'objectif actuel est de réduire les temps de caractérisation des matériaux sous chargement cyclique pour être en mesure de maitriser rapidement leur comportement en fatigue et mieux prévoir le cycle de vie des structures. Des méthodes récentes proposent de réaliser des mesures énergétiques pendant le chargement en fatigue des matériaux. Cela semble prometteur, mais les quantités estimées ne sont pas toujours faciles à interpréter. Depuis plusieurs décennies, le focus est fait sur l'énergie dissipée par la matériau pendant un chargement cyclique. Cette quantité, facile à mesurer, est cependant difficile à interpréter en terme de changements microstructuraux et donc en terme d'endommagement en fatigue. L'énergie stockée quant à elle, est directement associée aux changements microstructuraux conduisant à l'endommagement de la matière. Cette quantité mérite donc

qu'on s'y intéresse.

Objectifs de la thèse

L'objectif de cette thèse est triple :

1. Déterminer rapidement les propriétés en fatigue des matériaux métalliques dans le domaine VHCF à partir de l'évolution de l'énergie stockée.
2. Estimer les évolutions d'énergie stockée en fonction de l'amplitude de contrainte et du nombre de cycles.
3. Comprendre le lien entre les évolutions d'énergie stockée et les changements microstructuraux, précurseur d'endommagement en fatigue.

Le travail conduit pendant cette thèse a été effectué dans le cadre du projet ERC H2020 FastMat ("Fast determination of fatigue properties of Materials beyond one billion cycles") financé par le Comité Européen de Recherche (*grant agreement No 725142*).

Approche scientifique

Le travail réalisé durant cette thèse s'est concentré sur le développement de la méthodologie d'estimation de l'énergie stockée. Cette dernière repose sur le calcul de la différence entre le travail mécanique apporté au matériau et l'énergie qu'il dissipe sous forme de chaleur. L'énergie dissipée est estimée par mesure de température à la surface du matériau. Le travail mécanique est quant à lui estimé à l'aide d'une méthode de diffraction des rayons X résolue en temps, appliquée in situ. Cette méthode, développée de manière itérative pendant de multiples campagnes d'essais tout au long de la thèse, est conduite sur un synchrotron. En l'occurrence, les travaux de cette thèse ont été réalisés en collaboration avec la ligne DiffAbs du synchrotron SOLEIL. Les essais sont conduits à l'aide d'une machine de fatigue ultrasonique qui permet d'atteindre le domaine VHCF rapidement.

Les deux méthodologies sont appliquées à deux matériaux : un cuivre monocristallin et un acier perlitique polycristallin C70.

Organisation du manuscrit

Ce manuscrit est divisé en trois chapitres :

- Le premier chapitre correspond à l'état de l'art en termes de dimensionnement en fatigue et reprend principalement les méthodes de dimensionnement basées sur des essais conduits jusqu'à rupture, et sur des essais courts interrompus avec mesure énergétique complémentaire. Il pose également les bases de l'endommagement en fatigue et de sa formation.
- Le deuxième chapitre présente la méthodologie expérimentale ainsi que le dispositif qui ont été tous deux développés pour permettre d'atteindre l'objectif de la

thèse, à savoir estimer l'énergie stockée dans un matériau pendant une sollicitation cyclique conduite dans le domaine VHCF, i.e. sur une machine ultrasonique fonctionnant à 20 kHz. Ce chapitre discute en détail les estimations de travail mécanique et d'énergie dissipée indispensable à la détermination de l'énergie stockée.

- Finalement, le troisième chapitre présente et discute les résultats obtenus en termes de mesures énergétiques (énergie dissipée, travail mécanique et énergie stockée) pour les deux matériaux de l'étude.

Chapitre 1

État de l'art - dimensionnement en fatigue

Il existe différentes méthodologies pour dimensionner une structure en fatigue :

- **Tests de structures à l'échelle 1 :1** : ces tests permettent de reproduire le chargement en conditions réelle d'une structure jusqu'à sa rupture pour déterminer sa durée de vie. Ce type de test est cependant couteux et très spécifique à une structure pour un cas de chargement.
- **Tests à petite échelle** : des tests peuvent être réalisés sur un échantillon de matière qui serait représentatif du matériau employé dans une structure pour déterminer les propriétés en fatigue de ce matériau. Cette méthode est probabiliste et nécessite de réaliser de nombreux tests (conduits jusqu'à rupture) pour s'assurer de la fiabilité des résultats. A partir de ces résultats, une simulation numérique de la réponse de la structure à une sollicitation de fatigue peut être calculée pour valider sa résistance.
- **Tests interrompus à petite échelle** : pour accélérer le dimensionnement en fatigue, une méthode permet de déterminer les propriétés en fatigue des métaux en réalisant des essais courts interrompus pendant lesquels la température de l'échantillon est mesurée. A partir de ces estimations, différentes approches ont été réalisées et différentes et modélisations employées pour lier l'augmentation de la température et le nombre de cycles à rupture.

1.1 Tests à petite échelle - Courbes SN

La seconde méthode basées sur des tests de fatigue, conduits à petite échelles, jusqu'à rupture est détaillée ici. Les courbes SN sont un outil permettant de visualiser les

propriétés en fatigue des matériaux en mettant en regard la contrainte appliquée en fonction du nombre de cycles à rupture. Cet outil est construit à partir de nombreux tests conduits jusqu'à rupture sur des éprouvettes d'un matériau donné.

Sur ce genre de courbes, plusieurs domaines peuvent être identifiés :

- LCF = fatigue à faible nombre de cycles caractérisé par des durées de vie inférieures à 10^4 cycles et des contraintes appliquées élevées.
- HCF = fatigue à grand nombre de cycles caractérisé par des durées de vie comprises entre 10^4 et 10^7 cycles.
- VHCF = fatigue à très grands nombre de cycles caractérisé par des durées de vie supérieures à 10^7 cycles.

Les courbes SN sont tracées en suivant des normes qui permettent de déterminer une limite de fatigue, correspondant à une horizontalité de la courbe SN observée sur les résultats expérimentaux, pour de nombreux matériaux, aux alentours de 10^7 cycles. C'est ainsi que furent dimensionnées de nombreuses pièces mécaniques, en se basant sur cette limite. La norme considère qu'à une contrainte inférieure à la limite en fatigue, la durée de vie du matériau est infinie. Cette considération de la norme est d'une part biaisée par le fait que de nombreuses applications considéraient 10^7 cycles comme une durée de vie infinie. D'autre part, les machines conventionnelles permettant de réaliser des essais de fatigue, qui furent utilisées à l'époque, sont limitées en terme de fréquence à plusieurs dizaines de hertz en général. De ce fait, l'étude expérimentale des durées de vie supérieures à 10^7 cycles par ces moyens est limitée. Depuis plusieurs décennies, les machines de fatigues ultrasonique fonctionnant à 20 kHz ont été développées. Ces machines permettent de solliciter un matériau pendant un milliard de cycle en 14 heures seulement, ce qui autorise une étude du domaine VHCF dans des durées d'essais raisonnables. Les essais menés dans le domaine VHCF ont permit d'étudier le comportement des matériaux pour des très grandes durées de vie. Il a été observé que pour certains matériaux, la limite en fatigue se prolonge du domaine HCF au domaine VHCF. Cependant, pour de nombreux matériaux, leur comportement diverge du comportement montrant une limite. En effet, certains matériaux présentent une croissance continue de la durée de vie pour une contrainte décroissante tandis que d'autres peuvent rompre pour des contraintes inférieures à limite de fatigue (identifiée à 10^7 cycles) et pour des durées de vie bien supérieures à 10^7 cycles.

En conséquence, la courbe SN est un outil puissant permettant de déterminer expérimentalement les propriétés en fatigue des matériaux métalliques. Cependant, la construction des courbes SN pour des durées de vie très importantes (de l'ordre de 10^11 cycles par exemple) est limitée par les moyens expérimentaux permettant de conduire des essais de fatigue, même dans le cas de l'emploi des machines de fatigue ultrasonique. Cependant, il est nécessaire de déterminer les propriétés des matériaux en fatigue de

manière expérimentale, soit pour des durées de vie très importantes, soit en accélérant la caractérisation des matériaux à 10^9 cycles. De ce fait, d'autres méthodes doivent être envisagées.

1.2 Mesures énergétiques pendant des tests de fatigue interrompus

La troisième méthode exposée plus haut est à son tour détaillée dans cette section. Elle constitue une alternative intéressante pour déterminer les propriétés en fatigue des matériaux métalliques rapidement en conduisant des essais courts interrompus !

1.2.1 Estimation de l'énergie dissipée pour déterminer la limite de fatigue

En mesurant l'échauffement de la matière lorsqu'elle est sollicitée cycliquement pendant un nombre de cycle donné[1], on peut construire une courbe d'auto-échauffement en fonction de la contrainte. A partir de cette courbe, on peut déterminer une limite en fatigue du matériau. Il s'agit du niveau de contrainte à partir duquel l'auto-échauffement s'intensifie clairement. Dans certains cas, cette limite en fatigue à celle identifiée sur la courbe SN du matériau. Dans d'autres cas, les évolutions de température, parfois particulières, ne permettent pas d'analyser aisément la courbe d'auto-échauffement. La température n'est en effet pas une grandeur intrinsèque du matériau, et son suivi ne permet pas de prendre en compte les changements microstructuraux ayant lieu dans la matière.

Pour mieux interpréter les résultats de l'échauffement du matériau (en étant indépendant de l'influence de l'environnement), il fut proposé de caractériser les sources thermiques à l'origine de l'augmentation de température dans le matériau sollicité. Ces mesures s'appuient sur la mesure de la température mais utilisent une équation de la chaleur pour déterminer l'énergie qui est dissipée par le matériau. Ces mesures sont très adaptées aux essais de fatigue conduits dans les domaines LCF et HCF. Cependant, pour des essais dans le domaine VHCF, les niveaux de contraintes faibles entrainent une très légère dissipation qui n'est pas toujours mesurable facilement expérimentalement. Pour améliorer ces mesures, les machines de fatigue ultrasonique peuvent être employées pour faire croitre l'augmentation de température par unité de temps lors de l'essai.

1. On considère des essais interrompus durant entre 10^4 et 10^7 cycles en général, pendant lesquels la température à la surface de l'éprouvette sollicitée est mesurée en continu.

L'aspect très intéressant de ce type de méthodes est associé au gain de temps qu'elles proposent. De plus, cela permet d'obtenir une estimation d'une limite de fatigue en quelques essais réalisés sur très peu d'échantillons. Cependant, ce type de méthode ne permet par une interprétation aisée des résultats. En effet, le lien entre l'énergie qui est dissipée au cours du chargement et les mécanismes microstructuraux à l'œuvre dans la matière (i.e. les mouvements, multiplications et arrangement des dislocations) n'est pas bien compris.

1.2.2 L'énergie stockée, un marqueur de l'irréversibilité du glissement cyclique ?

L'énergie stockée correspond à l'énergie qui est accumulée dans la matière lorsqu'elle se déforme de manière irréversible. Elle est représentative des mécanismes microstructuraux qui se développent au sein du matériau. Ainsi, il est plus aisé d'interpréter une évolution d'énergie stockée qu'une évolution d'énergie dissipée en fonction de la contrainte appliquée. Il est possible d'associer l'énergie stockée aux mouvements non recouvrables des dislocations (appelé "irréversibilité du glissement"). De ce fait, cette énergie peut faire office de marqueur des changements microstructuraux ayant lieu dans la matière, qui est à l'origine de la formation de fissure et donc de l'endommagement en fatigue.

Des estimations expérimentales d'énergie stockée ont été réalisées par plusieurs groupes de recherche. Cependant, très peu de résultats sont reportés dans la littérature dans le cas d'essais de fatigue et les résultats reportés sont relativement discordants. De plus, aucune étude n'a été réalisé sur des essais de fatigue dans le domaine VHCF.
Cependant, plusieurs consensus sont observés dans la littérature. D'une part, l'énergie stockée augmente avec la contrainte appliquée. Cela vient du fait que pour une contrainte suffisamment importante, les niveaux de plasticité sont suffisant pour permettre aux dislocations de se multiplier et de s'arranger sous le forme de structures. D'autre part, l'énergie stockée diminue avec le nombre de cycles appliqués lorsque l'on maintient un chargement cyclique à une amplitude donnée. Cela peut venir du fait que l'irréversibilité du glissement atteint un stade de saturation et qu'il faut augmenter la contrainte pour la faire s'accroitre encore.

1.3 Mécanismes d'endommagement en fatigue

Les fissures de fatigue dans les matériaux cristallins s'initient à partir de l'activité non recouvrable des dislocations à l'intérieur de la matière. Cette non recouvrabilité est associée à une évolution microstructurale pouvant elle-même être irréversible. L'accu-

mulation d'irréversibilités même de faible ampleur conduit à la formation d'un endommagement. En effet, les mécanismes associés à la fissuration de fatigue dans les domaines HCF et VHCF sont tous deux associés à l'irréversibilité du glissement cyclique.

1.3.1 Mécanismes d'endommagement en HCF

L'irréversibilité du mouvement des dislocations est associée à l'activité plastique ayant lieu à l'intérieur de la matière. Diverses structures de dislocations se forment pour différents niveaux de déformations plastiques. La structure de dislocations responsable de l'initiation de fissures dans le domaine HCF est associée aux bandes de glissement permanentes (appelées PSB) et se forment pour un niveau de déformation plastique conséquent. Ces bandes ont une structure dite "en échelle" dans laquelle les dislocations se regroupent sous la forme de murs. Ces structures sont stables et accommodent facilement la déformation plastique. Les dislocations sont très mobiles dans les PSBs. Lorsque ces bandes rencontrent la surface, elles laissent une marche irréversible appelée une marque de glissement. L'accumulation de la déformation plastique irréversible conduit à une rugosité de surface qui s'accroit. Cette rugosité est caractérisée par la formation d'extrusions et d'intrusions qui favorisent la formation d'une fissure de fatigue. Ainsi, la rupture dans le domaine HCF est très majoritairement due à l'action des PSBs. La limite de fatigue communément identifiée sur les courbes SN est environ deux fois supérieure au seuil d'apparition des PSBs. Dans le cuivre, ce seuil à été déterminé à 56 MPa.

1.3.2 Mécanismes d'endommagement en VHCF

En VHCF, les mécanismes à l'origine de la formation des fissures sont eux aussi dépendant du caractère irréversible du glissement. Cependant, la rupture se produit pour des niveaux de contrainte qui sont inférieurs au seuil d'apparition des PSB.

Il est possible de considérer deux types de matériaux dans ce domaine. Ceux qui présentent une initiation de fissure en surface et ceux présentant une initiation interne. On peut distinguer deux types de matériaux, pour lesquels les modes d'initiation de fissures sont différents :

- **type I :** matériaux homogènes, constitués d'une phase cristalline et sans défauts interne. Le cuivre en est un exemple.
- **type II :** matériaux non homogènes, constitués potentiellement de plusieurs phases et contenant des défauts microstructuraux de type inclusions non métalliques, pores ou précipités.

Pour les matériaux de type I, c'est la formation tardives de bandes de glissements

(n'étant pas des PSB) qui est à l'origine de la fissuration en surface, même dans le domaine VHCF. Lorsqu'un matériau est soumis à une contrainte plus faible que la limite en fatigue à 10^7 cycles, ce dernier voit une partie de la déformation plastique qui lui est appliquée être irréversible. Cependant, cette déformation plastique n'est pas assez importante pour former des PSBs directement. En effet, les structures de dislocations qui se forment dans le domaine VHCF (en veines ou en patchs) évoluent avec le nombre de cycles pour former des bandes de glissement primaires (qui n'ont pas la structure en échelle des PSBs) en surface. Ces bandes de glissements induisent une déformation plastique en surface qui conduit à une rugosité croissante de la surface. Cette rugosité de surface entraine ensuite une concentration de contrainte localement qui conduit à la formation de PSBs. Celles-ci, avec l'accumulation de la déformation plastique, même de faible amplitude, pendant les très nombreux cycles appliqués au matériau, peuvent conduire à la formation de fissures. Ces mécanismes ont été observés expérimentalement. On observe la présence de bandes de glissement (sans la structure en échelle) pour des amplitudes de contrainte à peine supérieure à 30 MPa dans le cas du cuivre par exemple.

Les matériaux de type II quant à eux, rompent après la formation de fissure internes, pour des durées de vies caractéristiques du domaine VHCF. Ces dernières se forment généralement au niveau des défauts microstructuraux autour desquels la déformation plastique se concentre. Suite à cette plasticité très localisée, des micro-fissures peuvent apparaitre et lentement se propager au cours du chargement cyclique.

Chapitre 2

Contribution expérimentale - établissement d'un bilan énergétique pendant des essais de fatigue à 20kHz

2.1 Objectifs de la thèse

L'objectif de cette thèse est de permettre l'estimation de l'énergie stockée dans les métaux sollicités en fatigue dans le domaine VHCF. Pour estimer cette quantité, on propose d'établir un bilan d'énergie tel que l'on estime la différence entre le travail mécanique apporté au matériau lors de sa sollicitation et l'énergie dissipée sous forme de chaleur.

L'énergie dissipée est estimée par cycle, à partir de la variation de dissipation intrinsèque. Pour estimer cette dernière, on utilise sur une équation de la chaleur et en mesurant la variation de température de la surface de l'éprouvette, pendant sa sollicitation, avec une caméra InfraRouge. L'énergie dissipée est mesurée indépendamment du travail mécanique lors d'essais indépendants.

Le travail mécanique, apporté par cycle, est estimé à partir de la détermination des évolutions respective de la contrainte et du taux de déformation du matériau pendant un cycle de chargement. Cela correspond à estimer le travail mécanique comme l'air sous la courbe d'hystérésis contrainte-déformation. La déformation totale peut être estimée directement par des jauges de déformation. Pour estimer le contrainte, on utilise une loi de Hooke qui requiert la mesure de la déformation élastique. Une méthode qui permet de mesurer expérimentalement la déformation élastique est la diffraction des rayons X (DRX). La DRX permet de s'affranchir de l'hypothèse d'un comportement du matériau élastique macroscopique et autorise ainsi l'estimation d'un décalage temporel

entre contrainte et déformation. Ce décalage temporel est associé au temps caractéristiques de l'amortissement visqueux des matériaux et est estimé à quelques dizaines de nanosecondes pour les métaux.

Pour estimer l'évolution cyclique de la déformation totale, la mesure des jauges suffit. Cependant, estimer l'évolution dans le temps de la contrainte et du décalage temporel entre contrainte et déformation, pendant un essai de fatigue à 20 kHz, est la principale difficulté dans l'estimation du travail mécanique. Il est nécessaire d'employer une méthode résolue en temps pour laquelle plusieurs conditions doivent être réunies :

- Le nombre de valeurs de contrainte acquises doit être suffisant pour reconstruire une évolution cyclique correcte ;
- Le positionnement temporel des points doit être très précis ;
- L'acquisition d'une valeur doit durer peu de temps pour limiter la variation du signal de contrainte pendant son acquisition. On considère des durées d'acquisitions de l'ordre de 1 µs jusqu'à 0.1 ns ;
- Le niveau de bruit doit être limité par rapport à l'amplitude de variation du signal de contrainte.

Pour remplir ces conditions, cela revient à maximiser le ratio signal-sur-bruit des images de DRX (à partir desquelles la contrainte est estimée). Pour ce faire, il est nécessaire d'utiliser une source de rayons X à très haute brillance telle que celle d'un Synchrotron par exemple. Cela n'étant en réalité pas suffisant, une approche stroboscopique a également été envisagée pour améliorer la qualité des clichés de diffraction qui sont traités.

2.2 Matériaux

Deux matériaux ont été choisis pour conduire ces travaux de thèse :

- un cuivre monocristallin, qui permet d'étudier la réponse d'un matériau à l'échelle d'un grain, en se concentrant sur les structures de dislocations et leurs évolutions en fatigue en s'affranchissant de l'effet des joints de grains.
- un acier perlitique C70. ce matériau biphasé est plus complexe que le cuivre monocristallin et est plus proche des matériaux employés dans l'industrie. Pour cet acier, une caractérisation à été effectuée pendant la thèse pour déterminer sa limite de fatigue par le tracé d'une courbe SN. Une limite de fatigue a été déterminée à 400 MPa pour des durées de vie allant de 10^7 à 10^{10} cycles.

2.3 Essais de fatigue ultrasonique

Durant cette thèse, c'est une machine de fatigue ultrasonique qui est utilisée pour solliciter cycliquement des éprouvettes. Son fonctionnement peut être divisé en deux modes :

- le mode standard, pour lequel la fréquence de vibration de la machine est asservie en continu pour garantir un fonctionnement en consommation minimale de puissance ;
- le mode synchronisé, pour lequel la machine fonctionne à une fréquence fixe imposée par une source extérieure (telle que l'horloge d'un synchrotron).

2.3.1 fonctionnement de la machine en mode standard

Le fonctionnement standard des machines de fatigue ultrasonique a été largement étudié et reporté dans la littérature. Elles reposent sur l'action d'un convertisseur piézoélectrique qui convertit une tension électrique alternative en vibration à une fréquence qui est en général de l'ordre de 20 kHz. Pour ce type de machine, le dimensionnement des éléments constitutifs du système vibrant est nécessaire pour assurer leur vibration à une fréquence particulière. Il s'agit de la fréquence d'anti-résonance du système. Cette dernière dépend des propriétés mécaniques et des dimensions des éléments constitutifs du système vibrant. Ainsi, dans son fonctionnement standard, la machine règle en continu la fréquence à laquelle elle vibre pour matcher la fréquence d'anti-résonance du système mécanique en vibration. Cela lui permet ainsi de consommer le moins de puissance électrique possible.

Pour solliciter un matériau, il faut dimensionner une éprouvette pour que la fréquence de son premier mode propre longitudinal de vibration libre soit similaire à la fréquence d'anti-résonance de la machine. Ainsi, la machine fonctionnera dans son régime nominal de vibration en sollicitant l'éprouvette dans son mode propre. Cela permet de découpler la vibration de la machine et celle de l'éprouvette et garanti une contrainte nulle à la jonction des deux. Les éprouvettes sont dimensionnées dans une forme de type Hourglass, et présentent ainsi une répartition de contrainte en gaussienne le long de l'éprouvette. Pour conduire le dimensionnement, on considère un modèle 3D en éléments-finis (type Abaqus^{TM}) de l'éprouvette pour lequel on conduit un calcul modal. On impose les propriétés matériaux déterminées préalablement et on fait varier la longueur des fûts de l'éprouvette. Les autres dimensions sont fixées. On détermine ensuite la longueur pour laquelle le mode propre de l'éprouvette est à une fréquence qui correspond à la fréquence d'anti-résonance de la machine.

L'estimation des contraintes appliquées lors d'essais en fatigue ultrasonique est une étape complexe de l'utilisation de ces machines. Deux méthodes conventionnelles sont utilisées dans la littérature, et s'appuient toutes les deux sur l'hypothèse du comportement élastique macroscopique du matériau :

- la première repose sur la mesure de la déformation totale par des jauges de déformation ;
- la seconde requiert l'utilisation d'un vibromètre laser avec lequel on estime l'amplitude de déplacement à l'extrémité libre de l'éprouvette. Ensuite, on reprend le modèle 3D de l'éprouvette sous la forme d'un calcul harmonique, avec lequel on peut prédire l'amplitude de contrainte dans l'éprouvette pour une amplitude de déplacement donnée (appliquée à l'extrémité de l'éprouvette qui est fixée à la machine).

Avec la seconde méthode, on peut estimer l'hétérogénéité de contrainte dans la section de l'éprouvette et le long de cette dernière. Il est observé que le maximum de contrainte est situé au centre de l'éprouvette, dans les coins de sa section centrale.

L'un des objectifs du dimensionnement est de déterminer le coefficient reliant l'amplitude de déplacement et l'amplitude de contrainte, noté k. Ce coefficient a été déterminé à partir des mesures conduites avec le vibromètre laser et des calculs éléments finis. A noter que les calculs éléments finis ont bien pris en compte l'anisotropie du comportement du monocristal dans le cas du dimensionnement des éprouvettes de cuivre.

2.3.2 fonctionnement de la machine en mode synchronisé

En mode synchronisé, la machine fonctionne à une fréquence imposée par une source externe. La machine utilise une alimentation électrique qui lit un signal d'entrée, et génère un signal électrique sinusoïdal. Le signal généré est initialement synchronisé en fréquence avec le signal externe et il est ensuite synchronisé en phase puis enfin amplifié pour fournir une tension suffisamment importante afin d'alimenter le convertisseur piézoélectrique de la machine de fatigue. Ce fonctionnement spécifique de la machine a été possible grâce au développement d'un générateur de tension permettant la génération d'un signal sinusoïdal et sa synchronisation avec une source externe. Le signal externe est l'horloge du synchrotron dans notre cas. Dans ce mode de fonctionnement, la machine vibre à une fréquence fixe imposée. Pour qu'elle consomme une quantité limitée de courant (donc de puissance), la machine doit être adaptée pour que son système vibrant ait une fréquence d'anti-résonance qui soit similaire à la fréquence externe qui est imposée. Pour ce faire, un système vibrant et des éprouvettes particulières doivent être dimensionnées spécifiquement pour vibrer à la bonne fréquence.

2.4 Mesures du travail mécanique

Pour mesurer le travail mécanique, il est nécessaire d'estimer les évolutions temporelles de la déformation et de la contrainte au cours d'un cycle. L'estimation du travail mécanique peut même être réalisée à partir de seulement 3 quantités en considérant les évolutions de contrainte et déformation comme sinusoïdales : les amplitudes de contrainte et de déformation ainsi que le décalage temporel entre contrainte et déformation. La déformation totale est mesurée par les jauges de déformations. Cette mesure étant relativement répandue, nous ne la détaillerons pas d'avantage. Quant à la mesure des contraintes cependant, celle-ci va être détaillée dans le suite puisqu'elle repose sur le développement d'une méthode originale de diffraction des rayons X résolue en temps, *in-situ*.

Le développement de la méthodologie pendant les travaux de thèse a été très itératif. Il a nécessité la préparation et la réalisation de pas moins de 10 campagnes d'essais sur la ligne DiffAbs du synchrotron SOLEIL ! Cela a finalement permis la maitrise du processus d'acquisition des données ainsi que l'estimation du travail mécanique pour les deux matériaux étudiés.

2.4.1 Principe de diffraction des rayons X

Le principe de diffraction des rayons X repose sur la loi de Bragg. Cette loi donne la relation entre la distance inter-réticulaire entre les plans de la maille cristalline et l'angle qui doit exister entre le rayon X incident et les plans inter-réticulaires du cristal pour que la diffraction ait lieu.
Lorsque l'on soumet un matériau à un chargement externe, il se déforme. La maille de chacun des grains qui constitue ce matériau se déforme donc de même. La déformation locale est appelée la déformation élastique de maille. Cette déformation induit un rapprochement ou un éloignement des plans de la maille selon son caractère de tension ou de compression. Par la loi de Bragg, on sait que l'angle avec lequel le rayon X diffracte évolue en fonction de la distance entre les plans (donc de la déformation élastique de maille). Dans le cas d'un chargement cyclique, le faisceau diffracté évolue de manière cyclique et synchrone par rapport à l'écartement entre les plans de la maille.

Pour estimer la variation des plans et donc la déformation de la maille, il est possible de suivre l'évolution de la position angulaire du rayon diffracté à l'aide d'un détecteur 2D. Ce dernier l'intercepte et capture une portion du cone de diffraction appelée anneau. En étudiant les évolutions des positions de l'anneau, sur l'image capturée par le détecteur, on peut retrouver la déformation de maille.
Le suivi de la position de l'anneau de diffraction se fait pas traitement des images de

diffraction pour tracer un pic de diffraction. Les mouvements du pic sont facilement mesurable puisque la détermination de la position du pic se fait par un fit, qui utilise une fonction de Pearson VII asymétrique. Le principe de fit d'un pic permet d'obtenir à la fois sa position angulaire mais aussi sa largeur. Cette largeur donne une information sur l'hétérogénéité de contrainte présente dans le matériau.

Pour estimer la contrainte macroscopique par DRX, il reste une étape à réaliser : la conversion de la déformation élastique de maille en contrainte macroscopique. Pour ce faire, il est nécessaire d'employer des modèles de considérer les constantes radiocristallographiques (CRC). Ces grandeurs permettent de relier, par des lois de comportement élastique, la déformation de maille à la contrainte macroscopique, dans plusieurs directions. Elles sont estimées pour les deux matériaux tel que :

- Pour le monocristal de cuivre, ses CRC sont estimées à partir de lois de comportements élastiques (pour une symétrie cubique) et de projections de la déformation et de la contrainte selon la même direction, i.e. la direction du chargement longitudinal macroscopique. Ces CRC dépendent de l'orientation du cristal.
- Dans le cas de l'acier C70, le matériau étant polycristallin, ce type de loi de comportement n'est représentative que du comportement d'un grain isolé. Or, la DRX est en général appliquée à un volume diffractant qui comprend de nombreux grains. De ce fait, des modèles auto-cohérents permettent de simuler un ensemble aléatoire de gains pas une technique d'homogénéisation numérique.

A l'aide de ces modèles et des lois de comportement élastique de chaque matériau à l'échelle du grain, on peut estimer les CRC des différentes orientations de grains pour les diverses mailles étudiées par diffraction sur les deux matériaux.

2.4.2 Méthodologie développée pour l'estimation des évolutions de contrainte et de déformation cycliques

Pour conduire une mesure de la contrainte avec une précision temporelle suffisamment fine, il est nécessaire d'utiliser un rayonnement X provenant d'une source synchrotron. Cela garanti une meilleure qualité des images DRX acquises de manière ponctuelle au cours d'un cycle de chargement (qui ne dure que 50 µs dans le cas d'essais conduits à 20 kHz). Durant cette thèse, le rayonnement synchrotron qui a été choisit est celui de la ligne DiffAbs sur le Synchrotron SOLEIL[1]. Il est important de noter que, sur la ligne DiffAbs, il a été constaté pendant les campagnes d'essais que le fasiceau dérive

1. En pratique, la machine de fatigue ultrasonique est montée sur le diffractomètre de la ligne DiffAbs. Le faisceau X illumine la zone centrale de l'éprouvette qui est sollicitée, là où les contraintes sont maximales et considérées homogènes. Un détecteur 2D à pixels hybrides (XPAD s140) intercepte les cônes de diffractions pour acquérir des images DRX.

verticalement, ce qui induit une variation de la position du pic de diffraction acquis par DRX dont les mesures sont tributaires.

Pour acquérir ponctuellement l'état de contrainte d'un matériau pendant un essai de fatigue à 20 kHz, les images de diffraction présentent donc une exposition de l'ordre de quelques microsecondes seulement. Il s'avère que même en employant un rayonnement synchrotron, les clichés de diffraction ne sont pas assez résolu en intensité. De ce fait, il est nécessaire de développer une stratégie pour améliorer la résolution des clichés de diffraction.
Une méthodologie de diffraction des rayons X résolue en temps appliquée *in situ* pendant des essais de fatigue ultrasoniques à été développée. Celle-ci s'inspire des techniques pompe-sonde. Ces dernières reposent sur un principe de synchronisation temporelle entre l'application d'un chargement (par un pompe : souvent un laser) et l'observation de la réponse du matériau (par la sonde : également un laser ou faisceau X) déclenché avec un très court délai par rapport à la pompe. Ce type de méthodologie permet de reconstruire la réponse d'un matériau à un phénomène physique et/ou chimique, considéré répétable, avec une résolution temporelle qui peut atteindre la femtoseconde.
De ce fait, nous nous sommes inspiré de ces méthodes pompe-sonde pour développer une méthode originale de reconstruction des signaux d'évolution cyclique de la contrainte (et de la déformation) : on utilise la machine de fatigue ultrasonique comme pompe pour appliquer une sollicitation cyclique continue à un matériau. Pendant cette sollicitation, on vient observer ponctuellement l'état de contrainte pendant une durée très courte avec une sonde : à savoir un détecteur 2D pendant que le matériau est irradié par un rayon X. On acquiert alors une image DRX correspondant à un état de contrainte du matériau, à une position temporelle donnée sur le cycle de chargement. Puis, en appliquant un délai très précis sur les acquisitions, on va pouvoir obtenir une reconstruction échantillonnée, point par point, du signal de contrainte. On considèrera des reconstructions avec un cinquantaine de points par cycle. Une approche stroboscopique est également employée pour accumuler les clichés de DRX sur plusieurs milliers de cycles afin de maximiser le rapport signal sur bruit des images DRX qui seront traitées. Pour reconstruire les évolutions de la déformation, on réalise des acquisitions de valeurs de jauges en parallèles des acquisitions d'images DRX, pour les mêmes positions temporelles sur les cycles de chargement.

Cette technique de reconstruction peut s'appuyer sur l'utilisation de deux modes du synchrotron soleil :

- le mode uniforme pour lequel le faisceau est considéré continu. Il correspond à

416 paquets d'électrons en révolution dans l'anneau de stockage.
- le mode single-bunch du synchrotron pour lequel le faisceau est considéré pulsé. Dans ce mode là, un seul paquet d'électron gravite dans l'anneau de stockage.

Avec un faisceau continu, la résolution temporelle est déterminée par la durée d'ouverture du détecteur 2D pour l'acquisition des images DRX. Ces images sont acquises pendant 1 µs, ce qui correspond à la précision temporelle de la mesure. Cette courte durée assure la faible variation de la contrainte pendant les acquisitions ainsi que la possibilité de reconstruire 50 points par cycles (du fait de la période de chargement qui est de 50 µs). Cette méthode est particulièrement adaptée au matériaux simples, tels que le cuivre monocristallin étudié.
Cependant, il a été constaté que cette méthode, et sa résolution temporelle, n'étaient pas assez performante pour permettre la reconstruction précise des évolutions cycliques de contrainte dans le cas de matériaux complexes comme l'acier C70. Pour palier à cette limitation, la méthodologie de DRX résolue en temps a été adaptée au mode single-bunch du Synchrotron SOLEIL. Cela permet ainsi de réduire la résolution temporelle à 91 ps, ce qui correspond à la durée d'un pulse du rayon X. Cette durée est prédominante sur l'ouverture du détecteur et correspond à la précision temporelle de la méthodologie en mode pulsé.

Le déclenchement des acquisitions est différent en fonction du mode Synchrotron employé :

- dans le cas du mode uniforme, les acquisitions sont déclenchées lorsque le signal de tension qui alimente le convertisseur piézo-électrique dépasse un seuil (réglé manuellement). A cet instant, une capture DRX et une acquisition de valeur de jauge sont déclenchés. Les acquisitions (accumulées) sont réalisées successivement 50 fois à différents délais par rapport au déclenchement de référence pour reconstruire les évolutions de la déformation et de la contrainte au cours d'un cycle.
- Dans le cas du mode single-bunch, le déclenchement des acquisitions est contrôlé par une carte électronique de synchronisation qui agit comme une horloge maitre au sein de la ligne DiffAbs. C'est cette carte qui synchronise le déclenchement des acquisitions des images DRX avec l'instant où le paquet d'électron passe devant la ligne DiffAbs et provoque l'illumination de l'échantillon par le rayon X. L'application de la méthodologie dans ce mode de fonctionnement du synchrotron requiert que la machine fonctionne dans son mode synchronisé. Cette synchronisation est réalisée à partir du signal de la carte électronique de synchronisation

de la ligne DiffAbs. La machine vibre ainsi à une fréquence qui est un multiple de la période de révolution du paquet d'électron dans l'anneau[2]. En définitive, une acquisition est donc déclenchée tous les 42 pulses. Ces acquisitions permettent donc de reconstruire un couple de cycles d'évolution de contrainte et de déformation qui sont définis par 42 points.

Le déclenchement de l'acquisition d'une image DRX par le détecteur XPAD et d'une valeur de jauges sont influencés par les appareils électroniques qui constituent la chaine de mesure. Ces derniers induisent un offset et une incertitude (due à la jigue des signaux électroniques et aux dérives du faisceau[3]) sur les données acquises. Ces quantités ont été quantifiées expérimentalement et leur influence est bien prise en compte dans le traitement des données. On peut ainsi reconstruire les évolutions de contrainte et déformation dont on peut estimer les amplitudes et le décalage temporel entre contrainte et déformation dont la contribution est purement associée à l'évolution du comportement du matériau.

2.5 Mesures de l'énergie dissipée

L'énergie dissipée est calculée à partir de la variation de dissipation intrinsèque pendant un cycle. Cette dernière peut être estimée à partir d'une équation de la chaleur en mesurant continuellement l'évolution de température du matériau sollicité de manière cyclique. Les essais sont conduits pendant 10^7 cycles puis interrompus. La mesure est réalisée pour une multitude de niveaux de contraintes pendant des essais de fatigue ultrasonique. Cela permet de caractériser l'évolution de l'énergie dissipée en fonction du niveau de chargement, même pour des amplitudes de contraintes très faibles, caractéristiques du domaine VHCF.

2. Pour être exact, la période de la sollicitation cyclique sera de 42 fois la période de révolution du paquet d'électron.

3. Les dérives du faisceau déforment la reconstruction des évolutions cycliques de contrainte par la méthodologie développée, ce qui influence le décalage temporel estimé entre les signaux reconstruits de contrainte et de déformation.

Chapitre 3

Résultats et discussions

3.1 Résultats Cuivre - uniforme

La méthodologie développée pour le mode continu du Synchrotron SOLEIL est parfaitement adaptée au cuivre monocristallin. En effet, ce matériau diffracte sous la forme d'un spot très intense du fait qu'un seul grain contribue au faisceau diffracté. De ce fait, il est à la fois possible d'accumuler peu d'images (et donc réduire la durée des acquisitions). De plus, avec une grande intensité observée sur le pic de diffraction étudié, il est possible de considérer des pics situés à des grands angles 2θ, en obtenant une qualité d'image suffisante ! En étudiant ce type de pic, cela permet d'obtenir une évolution de la position angulaire du pic très ample et ainsi réduire l'effet du bruit sur les images DRX ainsi que l'influence des dérives faisceau. L'influence des dérives faisceau étant plus ou moins continue mais très aléatoire dans le temps, la courte durée d'acquisition des images, dans le cas du cuivre, aide à moins exposer les résultats à ces dérives. Les estimations des amplitudes et du décalage temporel entre contrainte est déformation a donc pu être réalisé dans de bonnes conditions.

3.1.1 Estimation de l'évolution d'énergie stockée en fonction de la contrainte

Dans un premier temps, concentrons nous sur le cas du cuivre monocristallin. L'application de la méthodologie a permis l'estimation du travail mécanique en fonction de l'amplitude de contrainte appliquée. En reconstruisant l'évolution de la contrainte et de la déformation en fonction du temps, on peut estimer sur ces signaux leur amplitude respective et le décalage temporel entre les deux signaux. Pour chaque cycle reconstruit, on obtient donc une valeur de travail mécanique. A chaque amplitude, plusieurs cycles

ont été reconstruits. En ce qui concerne les résultats, on note une évolution particulière qui présente une première croissance légère, suivie d'une baisse légère puis enfin d'une augmentation franche du travail mécanique en fonction de l'amplitude de contrainte. Cette évolution est retrouvée pour les deux éprouvette testées, ce qui signifie qu'elle est associée au comportement du matériau et non à un artefact de mesure.

Dans un second temps, on estime l'énergie dissipée en appliquant une rampe d'augmentation de contrainte à l'une des éprouvettes. L'augmentation d'énergie dissipée avec la contrainte suit une loi quadratique. On observe que l'augmentation de l'énergie dissipée par cycle se fait plus marquée au delà de 30 MPa.

A partir de ces deux estimations indépendantes, on peut calculer l'énergie stockée en réalisant un bilan d'énergie. Par souci de correspondance, on considèrera les résultats d'estimation de l'énergie stockée sur l'une des deux éprouvettes uniquement (car les mesures d'énergie dissipée et de travail mécanique furent réalisées sur la même éprouvette, mais pas en même temps). Cela permet de tracer la courbe d'évolution de l'énergie stockée en fonction de l'amplitude de contrainte. On retrouve la première légère augmentation suivie d'une baisse puis d'une augmentation plus marquée. Les évolutions d'énergies stockées sont corrélées aux évolutions de microstructure du matériau pouvant avoir lieu pour des contraintes similaires : le maximum local observé sur la courbe (entre 35 et 55 MPa) peut correspondre à l'apparition de bande de glissement primaire tandis que le minimum local de la courbe (entre 55 et 70 MPa), pour lequel l'énergie stockée par cycle est négative, est associé à l'apparition de bandes de PSB présentant une structure en échelle. Ces corrélations n'ont pas encore été validées par observations microscopiques.

En parallèle de l'estimation des contraintes par le suivi de la position d'un pic de diffraction, on peut suivre l'évolution des largeurs du pic de diffraction étudié. cette dernière est représentative de l'hétérogénéité de contrainte du matériau. Dans le cas d'un monocristal, l'hétérogénéité n'est possiblement affectée que par la densité de dislocation du matériau. On remarque une évolution des largeurs qui est sinusoïdale pour de faibles amplitudes de contrainte (i.e. inférieure à 35 MPa) et finit par avoir une évolution asymétrique au delà. Cette évolution cyclique de la largeur du pic de diffraction étant proche des évolutions observées pour un matériau polycristallin, on se propose de la fitter par une fonction du type : "$A + B \times \sin(\omega t) + C \times \sin(\omega t)^2$" où les paramètres A, B et C du modèle sont associés à l'évolution des dislocations.
On remarque alors une corrélation des évolutions des largeurs de pics et des évolutions d'énergie stockée en fonction de la contrainte :

- Pour des contraintes inférieures à 30 MPa, l'énergie stockée par cycle est nulle et l'évolution de la largeur évolue très peu et de manière réversible.

- Au delà de 35 MPa, l'évolution de la largeur du pic semble augmenter en amplitude et cela correspond à une augmentation de l'énergie stockée par cycle. Cela peut être associé à une augmentation de l'irréversibilité du déplacement des dislocations et potentiellement à la formation de bandes de glissement primaires.
- Pour des amplitudes de contraintes de l'ordre de 55 à 70 MPa, l'énergie stockée est négative : le matériau ne stocke pas d'énergie. La valeur moyenne de l'évolution de la largeur de pic quant à elle semble décroitre pour ces amplitudes. La décroissance est plus marquée pour une contrainte plus importante. Cette diminution de la valeur moyenne de l'évolution de la largeur est accompagnée par une augmentation marquée de l'asymétrie des évolutions cyclique de largeur de pic. Ces deux variations semblent indiquer que la densité de dislocations diminue, surement à cause de la formation de PSBs pour lesquelles, de nombreuses dislocations s'annihilent. Ce type de structure se forme pour minimiser l'énergie du système, ce qui justifierait que l'énergie stockée par cycle soit négative lors de leur formation.
- Pour des amplitudes de contrainte plus importante, de l'ordre de 70 à 80 MPa, l'énergie stockée est de nouveau positive et augmente beaucoup avec la contrainte. L'évolution de la largeur du pic semble augmenter en amplitude de variation par cycle, ce qui est surement associée à la plasticité qui se développe dans l'éprouvette à de telles amplitudes, qui sont proche de la limite en fatigue identifiée pour ce matériau à 93 MPa après 10^8 cycles. De plus, la valeur moyenne de cette variation poursuit sa décroissance, pouvant être associée à la formation continue de PSBs et à leur développement qui induit une réduction de la densité de dislocations dans le matériau.

Cette corrélation qui a été identifiée dans ce travail n'est pas encore parfaitement comprise, et mérite d'être plus approfondie, notamment par le développement d'un modèle basé sur les évolutions des densités de dislocations.

3.1.2 Estimation de l'évolution d'énergie stockée en fonction du nombre de cycles

Dans un second temps, on peut considérer l'évolution de l'énergie stockée en fonction du nombre de cycles appliqués. Par exemple, l'énergie stockée a été mesurée pour une contrainte de 80 MPa maintenue pendant 10^8 cycles. Cette contrainte maintenue a permis d'estimer 11 valeurs d'énergie stockée. On observe une première valeur très importante suivie d'une forte décroissance. Puis l'énergie stockée augmente pour atteindre un plateau. Ce qui souligne le fait qu'elle finit par saturer après un certain du nombre de cycles mais de l'énergie est toujours stockée pendant chaque cycle.

3.2 Résultats Acier - Single-Bunch

Cependant, la méthodologie destinée au mode continu n'est pas adaptée à l'acier C70. En effet, ce matériau est polycristallin, et présente donc des anneaux de diffraction continus mais peu intenses. De ce fait, il est préférable de se concentrer sur l'étude des pics situés aux faibles angles 2θ, qui sont les plus intenses. Cependant, même avec leur intensité plus importante que les autres pics, il est nécessaire de cumuler de nombreuses images pour obtenir une qualité d'image suffisante. De plus, les pics situés aux faibles 2θ se déplacent moins que les autres, ce qui rend les évolutions cycliques plus sensibles aux dérives faisceau mais aussi au bruit. En effet, cela induit donc une plus grande incertitude de mesure des amplitudes des évolutions et du décalage temporel entre les signaux.
Pour palier à la mauvaise prédisposition de l'acier pour ce type de mesures, il a été nécessaire d'adapter la méthode au mode single-bunch du Synchrotron SOLEIL. Le mode pulsé permet d'atteindre une résolution de l'ordre de 0.1 ns sur les acquisitions en DRX, ce qui autorise ainsi des reconstructions des évolutions cycliques de contrainte qui sont bien plus précises d'un point de vue position temporelle des points constituants les signaux. Cette amélioration de la méthode a permis son application à notre acier et a donné des résultats qui sont présentés dans cette section. Ces derniers ne sont pas aussi concluants que pour le cuivre mais sont très encourageants.

3.2.1 Estimation de l'évolution d'énergie stockée en fonction de la contrainte

En appliquant la méthodologie à l'acier, cette fois avec un faisceau de rayons X pulsé, on peut estimer le travail mécanique apporté à l'éprouvette testée. On obtient une évolution du travail mécanique par cycle en fonction de l'amplitude de contrainte qui présente une croissance exponentielle.
En appliquant la même méthodologie que pour le cuivre, on peut également estimer l'énergie dissipée par cycle. La croissance de cette énergie ne fonction de la contrainte est quadratique.

A partir de ces deux mesures, on estime l'énergie stockée dans le matériau à chaque cycle. Les résultats obtenus pour l'acier présentent des larges barres d'erreurs qui rendent difficile l'établissement d'observations claires. On ne peut qu'observer une augmentation de l'énergie stockée avec l'amplitude de contrainte. De plus, aucune variation spécifique d'énergie stockée n'est observée pour l'acier, ce qui peut être expliqué d'une part par les importantes incertitudes de mesure et d'autre part à cause des faibles amplitudes

de contraintes atteintes pendant les essais expérimentaux[1]. Une corrélation avec les évolutions cycliques des largeurs de pics de diffraction est assez difficile dans le cas de l'acier, d'une part car ces évolutions ne permettent pas de tirer de conclusion claires et d'autre par car le matériau étant polycristallin, l'interprétation des largeurs de pics est plus délicate.

1. Les niveaux de contraintes appliquées sont limités par la puissance de l'alimentation électrique développée pour synchroniser le fonctionnement de la machine de fatigue avec le synchrotron, dans le cas de l'utilisation du mode single-bunch. Cette alimentation n'était encore qu'au stade de prototype à l'époque

Conclusions

Principales conclusions

Les conclusions à tirer de ce travail de thèse sont associées à deux aspects. Le premier aspect concerne les développements réalisés pendant la thèse :

- La méthodologie de diffraction des rayons X résolue en temps *in situ* permet l'estimation des évolutions de contraintes avec une résolution temporelle suffisamment fine pour permettre l'estimation du travail mécanique et d'observer ses variations en fonction de la contrainte et du nombre de cycles.
- Le développement de la méthode a permis son application à deux modes de fonctionnement du synchrotron soleil pour permettre l'estimation du travail mécanique pour les deux matériaux étudiés.
- Les incertitudes de mesures observées dans le cas de l'application de la méthodologie dépend du mode du synchrotron utilisé et du matériau étudié. On observe une différence conséquente des incertitudes de mesures entre le cuivre et l'acier : le cuivre monocristallin permettant des mesures dont la précision temporelle est bien meilleure.
- L'énergie stockée dans le matériau pendant un essai de fatigue conduit dans le domaine VHCF a été estimée et ce de manière suffisament précise pour dégager des conclusions scientifiques intéressantes.

Le second aspect est associé aux mesures et résultats obtenus d'un point de vue avancées scientifique :

- Pour les deux matériaux, et pour une amplitude de contrainte donnée, l'énergie stockée décroit avec le nombre de cycle. Dans le cas du cuivre, l'énergie stockée par cycle atteint un régime stabilisé après 2 à 3×10^7 cycles.
- L'énergie stockée par cycle semble également augmenter avec l'amplitude de contraintes pour les deux matériaux. Dans le cas du cuivre, on observe des variations spécifiques de l'énergie stockées, qui sont associées à la formation de structure de dislocations précurseurs de l'endommagement en fatigue. L'énergie stockée est donc un marqueur qui semble pertinent pour étudier les propriétés des matériaux en fatigue, dans le domaine VHCF.

- Les évolutions cycliques de la largeur de pic semblent être corrélées aux évolutions d'énergie stockée, directement liées aux évolutions de densité de dislocations dans le cas du cuivre monocristallin. Cela renforce donc l'intérêt que l'on peut porter à cette énergie pour suivre les changements microstructuraux de la matière. Cependant, une corrélation basée sur un modèle physique manque encore pour vérifier cette corrélation.

Principales perspectives

Le travail réalisé met également en avant certains points d'améliorations :

- Nous avons constaté que les dérives faisceau sont un réel problème pour l'estimation du déphasage entre contrainte et déformation dans le cas de l'acier. Du fait que ces dérives sont très aléatoires et difficiles à suivre précisément, nous pouvons seulement réduire la durée de la reconstruction des cycles en augmentant l'intensité du faisceau. Cela requiert d'employer un faisceau dont la brillance est bien plus importante ou d'employer un détecteur 3D qui permet l'utilisation d'un faisceau polychromatique.
- Aussi, les niveaux de contraintes appliquées à l'acier n'ont pas pu être aussi importants que souhaités parce que l'alimentation électrique de la machine de fatigue développée pendant ma thèse pour utiliser le mode single bunch était encore au stade de prototype. Les tensions et ampérages que nous avons pu atteindre sont de l'ordre de $\pm$150V et 0.5 A. L'alimentation électrique doit alors être améliorée pour atteindre des tensions et ampérages de l'ordre de $\pm$300V et 1 A.
- Pour établir un lien concret entre les évolutions cycliques des largeurs de pics et la formation de structures de dislocation dans le cas du cuivre, il faut développer des simulations numériques à l'échelle des dislocations. A partir de ces simulations, nous envisageons de recalculer un cliché de diffraction équivalent pour recouper ça avec les évolutions expérimentales constatées.
- Pour aller plus loin, on souhaite également développer des modèles de simulation numérique basés sur des simulations de dynamique des dislocations pour retrouver les évolutions de l'énergie dissipée et de l'énergie stockée à l'échelle des dislocations. Cela pourrait permettre le développement d'un critère de détermination des propriétés en fatigue des matériaux à partir des mesures d'énergie stockée.